Laser spectroscopic shock tube studies on NO$_x$ and CO forming bimolecular reactions of NCN, HNO and HCO

Dissertation

zur Erlangung des Doktorgrades
der Mathematisch-Naturwissenschaftlichen Fakultät
der Christian-Albrechts-Universität zu Kiel

vorgelegt von
Dipl.-Chem. Nancy Faßheber

Kiel 2015

Abstract

Five rate constant expressions for combustion relevant bimolecular reactions of NCN, HNO and HCO have been measured directly behind shock waves. NCN and HNO are known as short-lived flame intermediates that are involved in the formation of nitrogen oxide (NO_x) pollutants. HCO is a key radical on the main oxidation pathway of hydrocarbons yielding CO. Accurate knowledge of the rate constants of all involved reactions in the ensuing complex reaction mechanisms makes it possible to develop strategies to (at least) reduce the problem of pollutant formation in combustion processes.

Concentration-time profiles of NCN radicals have been detected via UV laser absorption spectroscopy to measure the rate constants of the reactions NCN + H, NCN + H_2, and NCN + O_2. The thermal decomposition of cyanogen azide (NCN_3) was used as quantitative NCN source behind shock waves. The extremely toxic and highly explosive NCN_3 had to be directly synthesized from the reaction of NaN_3 with BrCN since it could not be purified. The thermal decomposition of ethyl iodide (C_2H_5I) has been used as high temperature H atom source. The rate constant of the reaction NCN + H, which critically determines the formation of HCN along the prompt-NO formation pathway, has been directly measured for the first time. From the measured rate constant data, conclusions could be drawn for the product channel branching ratios and the disputed value of the enthalpy of formation of NCN. The reaction NCN + H_2, which has so far always been neglected for NCN modeling in flames, turned out to be comparatively fast and hence gains some importance under H_2 rich flame conditions. From the consideration of possible reaction product sets, the abstraction reaction NCN + $H_2 \rightarrow$ HNCN + H turned out to be the most reasonable reaction channel.

Using the sensitive absorption based frequency modulation spectroscopy, HNO has been detected for the first time behind shock waves. A reaction mechanism for the simulation of HNO formation from the 193 nm photolysis of glyoxal/NO mixtures was compiled from available literature data and has been validated experimentally. HNO detection was performed at three different absorption lines of the $(\tilde{A}^1A'' \leftarrow \tilde{X}^1A')(100 \leftarrow 000)$ transition. HNO and HCO concentration-time profiles have been measured at similar reaction conditions at room temperature and behind shock waves. From the consistent modeling of the two species profiles, the HNO absorption cross section has been obtained for the transition at $\tilde{\nu} =$16173.86 cm^{-1}. Based on these analyses high temperature rate constant values for the reaction HNO + $O_2 \rightarrow$ NO + HO_2 were obtained for the first time. The resulting rate expression is up to five orders of magnitude higher than frequently used k_{HNO+O_2} expressions in existing combustion mechanisms.

HCO formation from the thermal decomposition of glyoxal has been observed by frequency modulation spectroscopy. By adding oxygen to the reaction mixtures, the rate constant of the reaction HCO + $O_2 \rightarrow HO_2$ + CO could be directly measured. These experiments significantly extend the range of available rate constant data towards higher temperatures of 1285 - 1760 K and were also used to test the capability of an extensive glyoxal oxidation mechanism for intermediate and high temperatures.

Zusammenfassung

Die Geschwindigkeitskonstanten von fünf verbrennungsrelevanten bimolekularen Reaktionen von NCN, HNO und HCO wurden hinter Stoßwellen direkt gemessen. Bei NCN und HNO handelt es sich um kurzlebige Zwischenprodukte in Flammen, die an der Stickoxid- (NO_x-) Bildung beteiligt sind. Das HCO-Radikal ist ein zentrales Intermediat während der Oxidation von Kohlenwasserstoffen, die zur CO-Bildung führt. Komplexe Reaktionsmechanismen sind nötig, um die Schadstoffbildung in Verbrennungsprozessen zu beschreiben. Durch genaue Kenntnis der Geschwindigkeitskonstanten aller beteiligten Reaktionen, können Strategien entwickelt werden, um diese Schadstoffbildung zu verringern.

Konzentrations-Zeit-Profile von NCN-Radikalen wurden mittels UV Laser-Absorptions-Spektroskopie aufgenommen. Auf diese Weise gelang es, die Geschwindigkeitskonstanten der Reaktionen NCN + H, NCN + H_2 und NCN + O_2 erstmals bei hohen Temperaturen direkt zu messen. Als quantitative Quelle für NCN-Radikal hinter Stoßwellen wurde der thermische Zerfall von Cyanazid (NCN_3) verwendet. Das sehr giftige und hochexplosive NCN_3 wurde aus NaN_3 und BrCN direkt synthetisiert, da es nicht aufgereinigt werden konnte. Als Quelle für H-Atome diente der Zerfall von Ethyliodid (C_2H_5I). Die Geschwindigkeitskonstante der Reaktion NCN + H, die entscheidend für die HCN-Bildung und damit für die prompt-NO-Bildung ist, wurde zum ersten Mal direkt experimentell bestimmt. Aus den gemessenen Geschwindigkeitskonstanten für NCN + H konnten Rückschlüsse auf die Produktverteilung der Reaktion und die nach wie vor umstrittene Bildungsenthalpie des NCN-Radikals gezogen werden. Zusätzlich wurde die Reaktion NCN + H_2, die bisher für die Simulation von Flammen vernachlässigt wurde, hinsichtlich ihrer Reaktionsprodukte betrachtet. Als wahrscheinlichster Reaktionskanal wurde der Abstraktionskanal NCN + H_2 → HNCN + H ermittelt.

Mittels der sehr empfindlichen Frequenz-Modulations-Spektroskopie ist es erstmals gelungen HNO hinter Stoßwellen nachzuweisen. Zunächst wurde ein Reaktionsmechanismus zur Simulation der HNO Bildung aus der 193 nm Photolyse von Glyoxal/NO-Mischungen aus Literaturdaten zusammengestellt und danach experimentell überprüft. Für die HNO-Detektion wurden drei verschiedene Linien des $(\tilde{A}^1 A'' \leftarrow \tilde{X}^1 A')(100 \leftarrow 000)$ Übergangs ausgewählt. Durch Kombination von HNO- und HCO-Experimenten bei ähnlichen Reaktionsbedingungen hinter Stoßwellen und bei Zimmertemperatur konnte der HNO Absorptionsquerschnitt bei $\tilde{\nu} = 16173.86$ cm^{-1} bestimmt werden. Basierend auf diesen Ergebnissen wurden erstmals Geschwindigkeitskonstanten für die Reaktion HNO + O_2 → NO + HO_2 bei hohen Temperaturen gemessen. Die ermittelten Ergebnisse liegen bis zu fünf Größenordnungen über den bisher in Verbrennungsmechanismen enthaltenen Ausdrücken für k_{HNO+O_2}.

Weiterhin wurde die HCO-Bildung aus dem thermischen Zerfall von Glyoxal mittels FM-Spektroskopie beobachtet. Durch den Zusatz von Sauerstoff zu den Reaktionsmischungen wurde zusätzlich die Geschwindigkeitskonstante der Reaktion HCO + O_2 → HO_2 + CO direkt gemessen. Diese Messungen haben den zugänglichen Temperaturbereich der Geschwindigkeitskonstante auf 1285 bis 1760 K erweitert. Außerdem wurde mit den Messungen ein umfangreicher Mechanismus zur Oxidation von Glyoxal bei mittleren und hohen Temperaturen validiert.

Contents

1 Introduction

The global requirement for energy, heat, and electricity is continually growing since the industrial revolution. Even though the effort of making regenerative energy sources accessible is considerable, the combustion of fossil fuels like coal, oil, and gas is still required to cover the high energy demand of all industrial nations. Fig. 1.1a summarizes the mix of primary energy supply. The graph shows that about 82% of the worlds energy requirement is currently (status 2012) covered by fossil materials and only 13% by renewable sources. In addition, parts of renewable sources, namely bio-fuels and waste, are also based on combustion. As pointed out in Fig. 1.1b, Global Future scenarios assume that combustion will still play the leading role in energy supply in the conceivable future.[1]
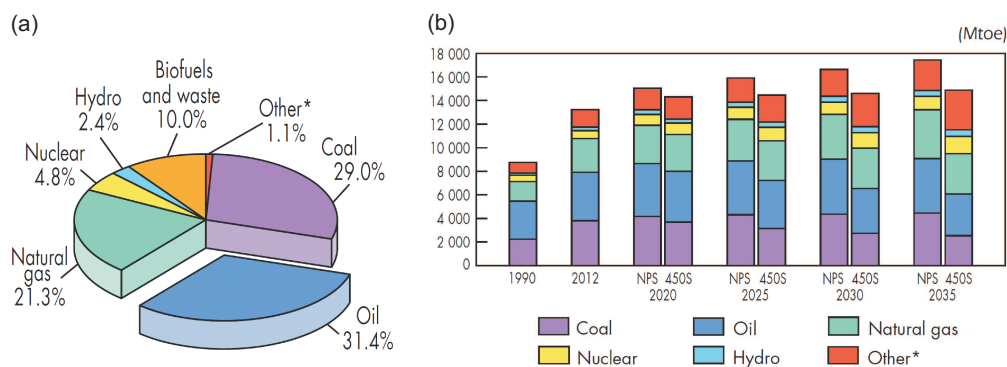
Figure 1.1: a) Fuel share of the world total primary energy supply in 2012 in mega tonnes of oil equivalents (Mtoe). b) Outlook on world total primary energy supply based on New policies Scenario (NPS) and on a post-2012 climate-policy framework (450S). Adopted from Ref. 1. *: geothermal, solar, wind, heat, etc.

Alternative energy sources to fossil fuels are required because there are several problems connected with their use. Not only are they slowly running out and are expected to become more and more expensive on the long run, also toxic substances are released into the environment by burning of the fuels. The most prominent pollutant gas is carbon dioxide (CO_2), which is known as a major green house gas causing global warming. And in fact the traceable impact of anthropogenic CO_2 on the environment is constantly growing.[2,3] Furthermore, sulfates (SO_2, responsible for acid rain), nitrogen oxides (NO_x, see section 1.1), polycyclic aromatic hydrocarbons (PAH), and soot particles are formed during combustion.[4]

1

Since combustion will remain crucial for our energy supply, extensive studies are required to promote effective use of fossil fuels and to optimize the combustion processes in general. For a full characterization of combustion processes, a combination of chemical and physical quantities need to be considered. Within flames, mixing (fuel-fuel or fuel-air), transportation, and streaming processes take place that affect the distribution of the reacting species. Also the heat transport and the heat distribution are important factors. Furthermore, myriads of elementary chemical reactions proceed simultaneously in flames and they are strongly coupled to these physical factors.[5] A proper reaction mechanism for the combustion of only one combustible easily includes several hundreds of elementary reactions and their temperature and pressure dependencies have to be known. Especially the kinetics of very reactive, mostly radical-like intermediates are important. Different reactive species are formed under different conditions affecting the amount of harmful substances that are produced. A detailed knowledge of the elementary reactions and their rate constants provides the background for the construction of more effective combustors and thereby lower pollutant emissions.

1.1 Formation mechanisms and environmental impact of nitrogen oxides (NO_x)

Subject to combustion conditions different amounts of environmentally harmful nitrogen oxides such as NO, NO_2, and N_2O (NO_x) are generated from the burning of fossil fuels. Released into the atmosphere all nitrogen oxides have diverse, dangerous impacts on the environment over a variety of mostly radical reactions. Which kind of reactions take place is dependent on the particular conditions like temperature, solar radiation, humidity and concentration as well as the nature of the surrounding reactants.[6,7,8]

For example, through the photochemical process (1), NO_2 provides atomic oxygen that contributes to the (undesired) formation of the so called "urban ozone" in the troposphere (first layer of the atmosphere, ~ 10 km height).[7]

$$NO_2 + h\nu \ (\lambda < 400\,nm) \rightarrow NO + O \tag{1}$$

$$O + O_2 \rightarrow O_3 \tag{2}$$
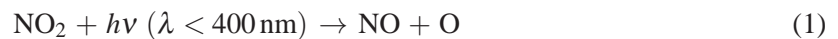
In contrast, in the stratosphere (between 10 - 50 km above the ground) overall ozone concentrations are higher and NO_x is responsible for the destruction of the ozone layer over a catalytic cycle:

$$NO + O_3 \rightarrow NO_2 + O_2 \tag{3}$$

$$NO_2 + O \rightarrow NO + O_2 \tag{4}$$

$$\overline{}$$

net reaction $\quad\quad O + O_3 \rightarrow O_2 + O_2 \tag{5}$
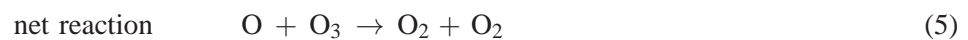
At high humidity levels, NO_x species will be washed out of the atmosphere and lead to generation of nitric acid according to reaction (6). This elution of nitrogen oxides from the atmosphere contributes

to the formation of acid rain.[8]

$$N_2O_5 + H_2O \rightarrow 2\,HNO_3 \rightarrow 2\,H^+ + 2\,NO_3^- \tag{6}$$
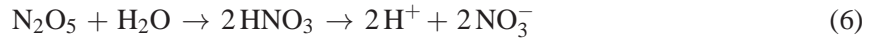
Depending on the combustion conditions, for example the fuel air ratio ϕ, and the type of fuel, four main pathways of NO_x formation can occur.[5,9,10]
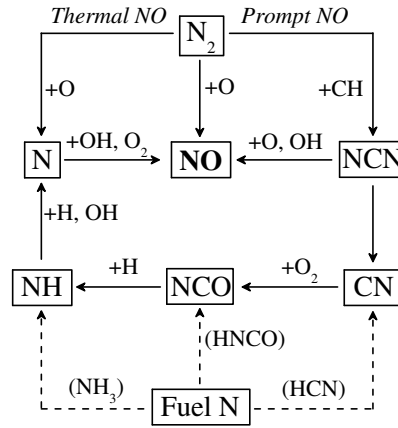
Figure 1.2: Reaction path diagram abstracting fuel-, thermal-, and prompt-NO formation pathways, according to Glarborg.[11]

(*i*) Fossil fuels like coal naturally contain a certain amount of nitrogen that can be oxidized to NO over several reaction steps (see Fig. 1.2). This so-called fuel-N-conversion especially takes place under fuel-air equivalent ratios below $\phi < 1.3$.

(*ii*) Even if the fuel itself does not contain any nitrogen, NO_x formation takes place due to the oxidation of atmospheric nitrogen, called *thermal-NO*. For this pathway, the combustion temperature needs to be very high such that O atoms from the atmospheric oxygen can oxidize the very stable N$\equiv$N triple bond according to the following mechanism.

$$O + N_2 \rightarrow NO + N \tag{7}$$

$$N + O_2 \rightarrow NO + O \tag{8}$$

$$N + OH \rightarrow NO + H \tag{9}$$

This is the so-called Zeldovich mechanism.[12]

(*iii*) Another way to form NO, especially under leaner combustion conditions and at lower temperatures, proceeds through N_2O. According to Wolfrum,[13] N_2O can be formed by the recombination reaction (10).

$$N_2 + O + M \rightarrow N_2O + M \tag{10}$$

$$N_2O + O \rightarrow NO + NO \tag{11}$$

Due to the need for a collision partner M, this mechanism is favored at high pressures.

(*iv*) The fourth way of NO$_x$ formation, the *prompt-NO*, was supposed to proceed according to the Feni-more mechanism for a long time. This mechanism describes the reaction of small hydrocarbon radicals with nitrogen molecules stemming from the combustion air over the spin-forbidden reaction:[14]

$$CH\left(^2\Pi\right) + N_2\left(^1\Sigma^+\right) \rightarrow N\left(^4S\right) + HCN\left(^1\Sigma^+\right) \tag{12a}$$

Although there has not been any experimental evidence of this elementary reaction step, it has been widely accepted for a very long time. The required intersystem crossing (ISC) probability from the doublet to the quartet potential energy surface is actually very low, causing a huge deviation between experimental flame modeling work[15,16] and theoretically[17] determined rate constants. The measured rate constant data for the reaction CH + N$_2$ are about two orders of magnitude higher than the theoretical estimates for the rate constant of reaction channel (12a).[18,19] A solution for this dilemma was found by Moskaleva and Lin in 2000.[20,21,22] They introduced a new prompt-NO initiation pathway over the spin-allowed formation of NCN radicals:

$$CH\left(^2\Pi\right) + N_2\left(^1\Sigma^+\right) \rightarrow H\left(^2S\right) + NCN\left(^3\Sigma^-\right). \tag{12b}$$

Based on quantum chemical methods, Lin and coworkers[20,23], Berman et al.[24], and Harding et al.[25] calculated the potential energy surface (PES) diagram for the reaction CH + N$_2$ shown in Fig. 1.3. It can be seen that the formation of NCN + H is thermodynamically unfavorable compared to HCN + H formation, but does not require an ISC process. As the overall energy thresholds for both reaction pathways (12a) and (12b) are similar and, additionally, the first reaction step forming NCN is a simple bond fission process compared to the activation-controlled HCN formation, the spin-allowed reaction channel is dominating the overall reaction. However for the reverse reaction NCN + H, the ISC point is energetically lower than the energy of the educts such that it is likely to produce HCN + N.[23,26] The rate constant of the reaction NCN + H has been directly measured in this work for the first time. The accessible reaction channels and the product branching ratios are discussed in chapter 4.
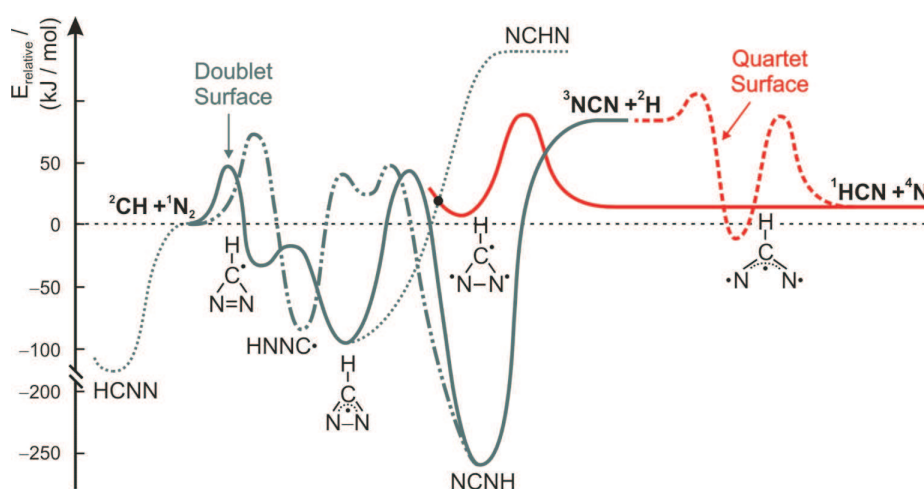
Figure 1.3: Potential energy surface for the reaction CH + N$_2$, according to Lin and coworkers,[20,21,23] Berman et al.,[24] and Harding et al.[25]

In the meantime, the formation of NCN and its correlation with CH and NO concentrations in flames has been experimentally proven by several laser-induced fluorescence (LIF) studies.[27,28,29] Moreover, a shock tube study by Vasudevan et al.[26] finally verified that NCN is the main product (> 70%) of the reaction CH + N_2. Consequently, NCN high-temperature kinetics has been implemented into prompt-NO mechanism for flame simulations. Prominent examples are the detailed mechanisms by Konnov (Konnov 0.6 mechanism)[30] and Lamoureux et al. (GDFkin3.0_NCN mechanism)[31,32]. Until now, however, due to the lack of experimental data, NCN reaction rates are mostly taken from theoretical predictions and estimations provided by the M. C. Lin group. It was a main objective of this work to make accurate high-temperature bimolecular rate constants available that should improve NCN flame modeling mechanisms.

1.2 High temperature cyanonitrene (NCN) kinetics

After Moskaleva and Lin[20] proposed NCN to be the main product of the initial prompt-NO reaction CH + N_2, several studies have been performed to detect NCN formation in flames and to provide first high-temperature NCN rate constant data. In 2006 El Bakali et al.[33] embedded the prompt-NO pathway and NCN chemistry in the GDF-Kin 3.0 mechanism. Rate constant expressions were adopted from the early estimates of Glarborg et al.[34] Already by using these roughly estimated rate constant data they obtained much better agreements between simulated and measured CH and NO concentration profiles for low-pressure methane, ethane, and propane flames than for the mechanism without NCN chemistry, especially under fuel rich conditions. Gersen et al.[35] implemented the new prompt-NO reaction (12b) into the combustion mechanism GRI-Mech 3.0[36] and could also show significant improvements simulating HCN profiles under fuel rich conditions for a methane-air flame. As expected, the rate constant for reaction (12b) turned out to be crucial and the value from the calculations by Moskaleva and Lin had to be adjusted to improve the simulation results.

Vasudevan et al.[26] studied the reaction CH + N_2 behind shock waves using NCN and CH laser absorption. They determined the total rate constant for the overall reaction (12) and branching ratios $\phi = k_{12b}/(k_{12a} + k_{12b})$ at temperatures between 1943 and 3543 K. Their obtained rate constant for the NCN formation is in very good agreement with the results of multi-reference quantum chemical calculations performed by Harding et al. for temperatures between 1000 K and 3000 K.[25] Their ab initio calculations also revealed that an accurate value of the enthalpy of formation of NCN is crucial for the resulting rate constant. A work by Goos et al.[37] highlighted this issue and reviewed experimental and calculated values for $\Delta_f H^{\circ}_{298\,K}$(NCN). Values in-between 445 and 501 kJ/mol have been reported in the literature. Most recent studies favor a theoretical value of about 459 kJ/mol,[23,25] whereas experiments differ between 452 kJ/mol[38] and 467 kJ/mol.[39]

A set of rate constants for NCN consumption reactions including NCN + H, NCN + N, NCN + C and NCN + CN, calculated using ab initio data and Rice-Ramsperger-Kassel-Marcus (RRKM) theory, was published by Lin and coworkers already in the year 2000.[20,21] Later, Lin and coworkers expanded their NCN submechanism by NCN decomposition[40] and the reactions NCN + O_2,[41] NCN + NO[42] and NO_2,[43] NCN + O,[44] and NCN + OH.[45]. Very recently, they updated their predictions for

the reaction NCN + H.[23] In 2008 Sutton et al.[28,46] modeled NO and NCN profiles measured by laser-induced fluorescence (LIF) in low-pressure rich, stoichiometric, and lean methane flames. Their simulations of the experimental data could be improved using the NCN rate constant data published by Lin et al. instead of the estimated data from Glarborg et al.[34] In a similar study, Konnov[30] also adopted the NCN data from Lin and coworkers to work out a mechanism for NCN/NO modeling in lean and rich flames of CH_4, C_2H_4, C_2H_6 and C_3H_8.
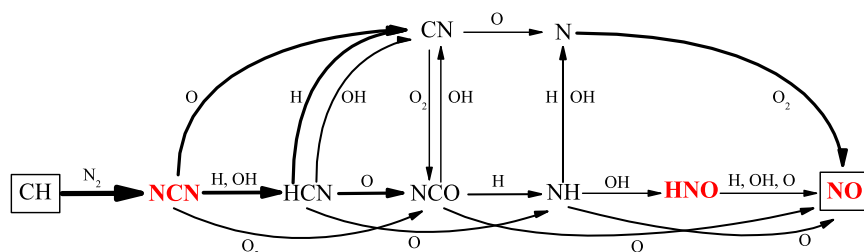
Figure 1.4: Reaction scheme for prompt-NO formation in a rich CH_4-O_2-N_2 flame, according to Lamoureux et al.[31]

Lamoureux et al.[31] combined LIF and cavity ring-down spectroscopy (CRDS) to measure absolute concentration profiles of CH, NCN and NO in methane and ethylene flames. By simulating the measured profiles with the GDFkin 3.0 mechanism, again extended by NCN chemistry taken from Lin and coworkers, the new prompt-NO reaction mechanism was established. The reaction scheme is illustrated in Fig. 1.4. It reveals that the reactions NCN + H, NCN + OH, NCN + O and NCN + O_2 are the most important NCN reactions along the prompt-NO pathway. It also highlights the fact that the reactions NCN + H and NCN + OH generate HCN, which is the product initially assumed for reaction (12), CH + N_2, in the *traditional* Fenimore mechanism. HCN is further oxidized to NO. Overall, complemented by the intermediate NCN formation, this reaction sequence resembles a straightforward *extended* Fenimore pathway. This finding explains why the *traditional* Fenimore mechanism, despite the wrongly assumed initial products, was actually quite suitable to model experimental findings. However, due to the direct oxidation of NCN by O atoms and O_2, CN and NCO are formed, respectively. The most favored reaction process always depends on the combustion conditions and hence the implementation of NCN chemistry is essential.

Other flame modeling groups came to the conclusion that even with the new NCN reaction pathway NO concentrations in flames are still underestimated. Therefore, Konnov[30] and Williams and Fleming[47] proposed another NCN forming reaction, $C_2O + N_2 \rightarrow NCN + CO$, to account for the missing NO. At this point, it remains unclear if the persisting discrepancies are real or only reflect uncertainties in the used NCN submechanism. Direct measurements of NCN rate constants are therefore needed to update and validate the proposed NCN mechanisms.

So far, experimental work on NCN high temperature kinetics is scarce and has been accomplished mainly in the Kiel shock tube lab. Dammeier et al. developed the NCN_3 decomposition behind shock waves in combination with narrow-bandwidth UV laser absorption to generate and detect NCN radicals.[48,49] Following a thorough characterization of NCN_3 thermal decomposition as a source

of NCN radicals,[48] in 2011 Dammeier and Friedrichs published direct shock tube studies for the reactions NCN + NO and NCN + NO$_2$, which are important for the combustion of nitrogen containing fuels.[50] Moreover the unimolecular decomposition NCN + M, and the reactions NCN + NCN and NCN + O have been investigated.[51] Besides our work, only two other shock tube studies on the reaction NCN + H by Vasudevan et al.[26] and NCN + M by Busch et al.[52,53] have been performed. In the Arrhenius plot in Fig. 1.5, previous rate constant determinations for NCN reactions (excluding results of this work) are summarized.
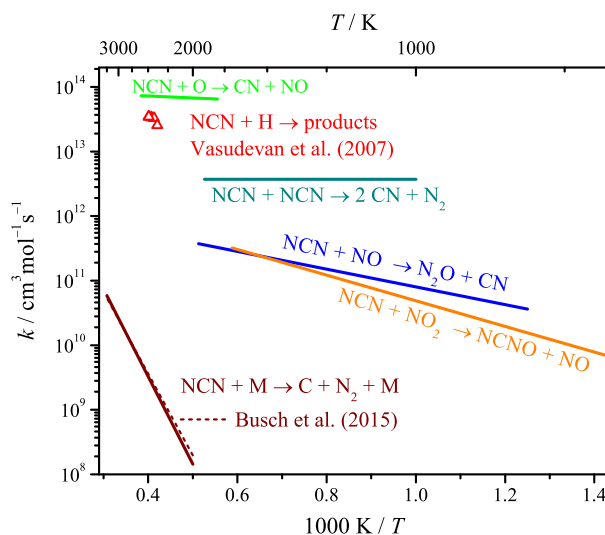
Figure 1.5: Summary of Arrhenius expressions for NCN reactions previously studied by Vasudevan et al.,[26] Busch et al.,[53] and in our working group at the Kiel shock tube lab.[50,51]

1.3 High temperature nitrosyl hydride (HNO) kinetics

HNO (nitrosyl hydride also called azanone or nitroxyl) is a combustion intermediate that can directly be oxidized to NO and is therefore closely linked to the total NO$_x$ concentration (see Fig. 1.4 as well). Most important for combustion modeling are the bimolecular reactions with highly reactive combustion intermediates like H, OH and O, the reaction with O$_2$ stemming from the combustion air and the unimolecular decomposition HNO (+ M) $\rightleftharpoons$ H + NO (+ M). NO is one of the main product of all this reactions. Very early (1964 - 1972) experimental rate constant data from measurements in flames are available for the two NO forming hydrogen abstraction reactions

$$HNO + H \rightarrow H_2 + NO \tag{13}$$

$$HNO + OH \rightarrow H_2O + NO \tag{14}$$
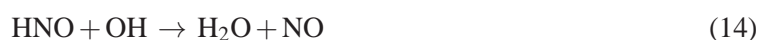
at temperatures between 1600 K $< T <$ 2100 K.[54,55,56] The results of these studies differ by a factor of about 2.6 for reaction (13) and 8.3 for reaction (14). All three analyses show that the reaction with OH radicals is faster than the reaction with H atoms. Rate constant ratios k_{14}/k_{13} are between 5 and 15, which is consistent with the general trend that OH radicals are more reactive than H atoms for abstracting hydrogen from hydrocarbon molecules. In contrast, more recent theoretical studies

by Soto et al.[57,58] and Nguyen et al.[59] predicted opposite k_{14}/k_{13} ratios. The ab initio calculations provide HNO + OH rate constant data close to the experimental data, but significantly higher reaction rates for HNO + H. Clearly, further experimental investigations of this two fundamental NO forming reactions at high temperatures are required.

In 2004, the first study for HNO + O reaction rates at combustion relevant temperatures have been published by Du et al.[60] They performed B3LYP density functional calculations for temperatures between 500 and 2500 K and revealed three possible reaction channels with OH + NO being the most favored reaction products. Since no experimental high temperature rate constant data for HNO + O are available, combustion mechanisms often rely on the rate expression from Inomata and Washida measured at temperatures below 473 K.[61] For the reaction

$$HNO + O_2 \rightarrow HO_2 + NO \tag{15}$$

there is also only one experimental expression available in the literature, which has been measured at temperatures between 296 K - 421 K.[62] Even though this reaction is a major NO source under reducing combustion conditions, only estimated rate expressions are included in most flame modeling mechanisms.[36,63,64] The equilibrium between HNO and NO is also an important factor for overall NO concentrations in flames. Especially under oxy-fuel conditions (e.g., under O_2/CO_2 atmosphere) the reaction HNO (+ M) $\rightleftharpoons$ H + NO (+ M) plays a key role for the removal of NO, which is exploited in reburning processes.[65] Three recent experimental studies on this reaction, which are in reasonable agreement, have been performed up to temperatures of $T = 1170$ K.[66,67,68] For the combustion of nitrogen containing fuels, existing mechanisms were expanded by the reactions HNO + NO,[69] NO_2,[70] and NH_2.[71] The used rate expressions have been estimated mostly. Overall the existing HNO high temperature kinetic data are not very consistent. Moreover, there is only one study reporting on HNO detection in flames, published by Lozovsky et al.[72,73] in 2000. They applied the sensitive intracavity laser absorption spectroscopy (ICLAS) to monitor HNO spectra in low-pressure hydrocarbon flames. So far, HNO has not been detected in shock tube experiments due to low absorption coefficients (see section 2.3.2.). It was the aim of this work to establish a high temperature HNO source, an HNO detection system as well as to directly measure HNO rate constants at high temperatures for the first time.

1.4 High temperature kinetics of the formyl radical (HCO)

The formyl radical (HCO) is a key intermediate along the direct CH_4 oxidation pathway of hydrocarbon (see Fig. 1.6). The bimolecular reactions of HCO with the most important oxygen species O, OH, and O_2, the HCO thermal decomposition, and the reaction HCO + H[74] result in the direct formation of CO. Measured rate constant data for these reactions, crucial for accurate modeling of the overall oxidation process in flames, are mostly stemming from low temperature studies. For example, the reaction HCO + O $\rightarrow$ CO + OH has only been measured up to temperatures of $T = 425$ K.[75] For the reaction HCO + OH $\rightarrow$ CO + H_2O only temperature independent, estimated rate constant values are

available.[76] A few studies have been performed on the reaction

$$HCO + O_2 \rightarrow CO + HO_2 \tag{16}$$

providing barely consistent results for the activation energy and overall rate constant.[36,77,78,79] A recent direct measurement on the rate constant of reaction (16) was performed behind shock waves by Colberg and Friedrichs.[80] Their study was carried out at temperatures between 769 K < T < 1108 K, so below average flame temperatures. A pronounced positive temperature dependence was found indicating a dominating direct abstraction channel. This is in contrast to theoretical work of Hsu et al.[79] who predicted an indirect abstraction channel, which is initiated by $HCO-O_2$ complex formation with a slightly negative temperature dependence, to dominate up to temperatures of 1000 K. Rate constant measurements at temperatures above 1100 K are needed to finally clarify the role of the indirect versus the direct abstraction channel for flame modeling. More direct measurements on rate constants of bimolecular HCO reactions at combustion relevant temperatures would be highly desirable.
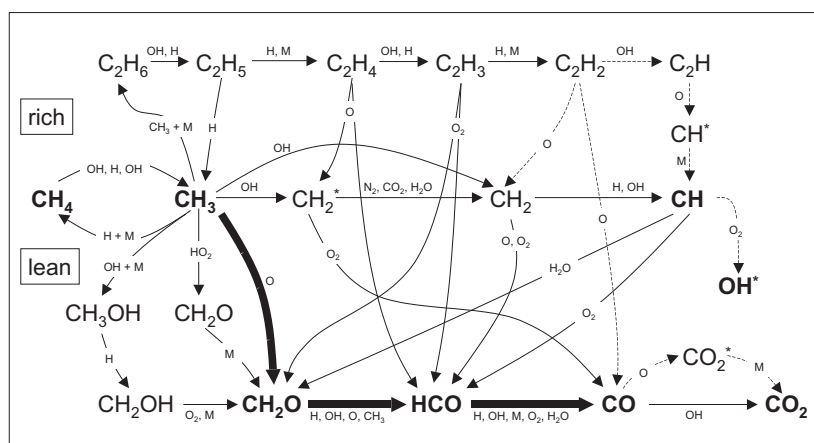
Figure 1.6: Reaction scheme of a methane oxidation pathway, according to Najm et al.[81]

1.5 Aim and structure of this work

To model the overall formation of atmospheric pollutants stemming from combustion processes, high temperature kinetics of many species have to be considered. The experimental studies of this work focus on bimolecular reactions of the two nitrogen containing species NCN and HNO and the key reaction $HCO + O_2$ of the flame intermediate HCO under combustion relevant conditions. These compounds are important intermediates for nitrogen oxide formation and to properly model the overall hydrocarbon oxidation process.

The shock tube method is well established for experimental studies on high temperature rate constants. Combustion relevant experimental conditions are easily accessible behind shock waves and in combination with sensitive absorption measurements, time-resolved concentration profiles of reactive intermediates can be detected. Building on previous studies in our working group, especially of the PhD thesis of J. Dammeier,[82] the reactions NCN + H, $NCN + H_2$ and $NCN + O_2$ should be

measured for the first time. Preliminary measurements of the rate constants of NCN + H and NCN + H$_2$, performed in the Diploma thesis of the author,[83] had to be considerably extended to allow for a thorough analysis including product branching ratios and the unsettled value of the enthalpy of formation of NCN. In addition to the experimental work, first flame modeling work was performed in collaboration with N. Lamoureux and P. Desgroux (Université Lille 1, France).

First detection of HNO behind shock waves has been achieved by applying the sensitive frequency modulation (FM) spectroscopy. The 193 nm photolysis of glyoxal/NO mixtures served as HNO source. Detecting the also formed HCO as a reference substance, quantitative HNO detection was possible. Further the rate constants of the reaction HNO + O$_2$ and HCO + O$_2$ should be directly measured. Updated rate constant data were implemented into a detailed glyoxal oxidation mechanism in collaboration with P. Glarborg (Technical University of Denmark) and P. Marshall (University of North Texas).

This thesis is structured as follows: The basic theoretical background and experimental details of the performed shock tube measurements, applied spectroscopic methods and sample preparation are outlined in chapter 2 and 3. Five papers reporting on the experimental results and their implications follow in separate chapters. For NCN, concentration-time profiles have been measured at $\tilde{\nu} = 30383.11 \text{ cm}^{-1}$ ($\lambda = 329.1302$ nm) by difference laser absorption spectroscopy. Rate constants for the reactions NCN + H (chapter 4), NCN + H$_2$ (chapter 5), and NCN + O$_2$ (chapter 6) could be obtained for temperatures of about 1000 K to 2500 K. HNO and HCO have been detected by FM spectroscopy at wavelengths of about $\lambda = 618.28$ nm and $\lambda = 614.76$ nm, respectively. The formation of HNO from the photolysis of glyoxal/NO mixtures as well as the HNO absorption cross section and the rate constant of the reaction HNO + O$_2$ are investigated in chapter 7. Finally, in chapter 8 the results of rate constant measurements on the reaction HCO + O$_2$ are presented.

References

[1] *Key World Energy Statistics*. International Energy Agency, 2014, www.iea.org, last accessed 13.04.2015.

[2] K. W. Thoning, P. P. Tans, and W. D. Komhyr. Atmospheric Carbon Dioxide at Mauna Loa Observatory 2. Analysis of the NOAA GMCC Data, 1974-1985. *J. Geophys. Research*, 94:8549–8565, 1989.

[3] J. G. Canadell, C. Le Que, M. R. Raupach, C. B. Field, E. T. Buitenhuis, P. Ciais, T. J. Conway, N. P. Gillett, R. A. Houghton, and G. Marland. Contributions to accelerating atmospheric CO$_2$ growth from economic activity, carbon intensity, and efficiency of natural sinks. *Proc. Natl. Acad. Sci.*, 104:18866–18870, 2007.

[4] J. Warnatz, R. W. Dibble, and U. Maas. *Combustion: Physical and Chemical Fundamentals, Modeling and Simulation, Experiments, Pollutant Formation*. Springer, 2006.

[5] J. Griffiths and J. Barnard. *Flame and Combustion*. Blackie Academic and Professional, London, 1995. ISBN: 0751401994.

[6] M. J. McEwan and L. F Phillips. *Chemistry of the Atmosphere*. Edward Arnold, 1975.

[7] C. Baird. *Environmental Chemistry*. W. H. Freeman and Company, 1995.

[8] A. Behnke and B.-M. Kemper. *Heizen mit Holz*. Umweltbundesamt, Dessau-Roßlau, 2010. www.umweltbundesamt.de, last accessed: 20.04.2015.

[9] H. B. Singh-Hrsg. *Combustion, Chemistry, and Climate of the Atmosphere*. Van Nostrand Reinhold, New York u. a., 1995, ISBN: 0-442-01264-0.

[10] J. Warnatz, R. W. Dibble, and U. Maas. *Verbrennung*. Springer-Verlag Berlin, 2006.

[11] P. Glarborg. Hidden interactions-Trace species governing combustion and emissions. *Proc. Combust. Inst.*, 31:77–98, 2007.

[12] Y. B. Zeldovich. The oxidation of nitrogen in combustion and explosions. *Acta. Physiochim. URSS*, 21:577–628, 1946.

[13] J. Wolfrum. Bildung von Stickstoffoxiden bei der Verbrennung. *Chemieingenieurtechnik*, 44:656–659, 1972.

[14] C. P. Fenimore. Formation of nitric oxide in premixed hydrocarbon flames. *Proc. Combust. Inst.*, 13:373–380, 1971.

[15] D. Lindackers, M. Burmeister, and P. Roth. Perturbation studies of high temperature carbon and CH reactions with nitrogen and nitrogen oxide (NO). *Proc. Combust. Inst.*, 23:251–257, 1991.

[16] A. J. Dean, R. K. Hanson, and C. T. Bowman. High temperature shock tube study of reactions of CH and carbon-atoms with nitrogen. *Proc. Combust. Inst.*, 23:259–265, 1991.

[17] M. R. Berman and M. C. Lin. Kinetics and Mechanism of the CH + N_2 Reaction. Temperature- and Pressure-Dependence Studies and Transition-State-Theory Analysis. *J. Phys. Chem.*, 87:3933–3942, 1983.

[18] Q. Cui, K. Morokuma, J. M. Bowman, and S. J. Klippenstein. The spin-forbidden reaction CH($^2\Pi$) + N_2 $\longrightarrow$ HCN + N(^{4}S) revisited. II. Nonadiabatic transition state theory and application. *J. Chem. Phys.*, 110:9469–9482, 1999.

[19] Q. Cui and K. Morokuma. The spin-forbidden reaction CH($^2\Pi$) + N_2 $\longrightarrow$ HCN + N(^{4}S) revisited. I. Ab initio study of the potential energy surfaces. *Theoretical Chemistry Accounts*, 102:127–133, 1999.

[20] L. V. Moskaleva and M. C. Lin. The spin-conserved reaction CH + N_2 $\longrightarrow$ H + NCN: A major pathway to prompt NO studied by quantum/statistical theory calculations and kinetic modeling of rate constant. *Proc. Combust. Inst.*, 28:2393–2401, 2000.

[21] L. V. Moskaleva, W. S. Xia, and M. C. Lin. The CH + N_2 reaction over the ground electronic doublet potential energy surface: a detailed transition state search. *Chem. Phys. Lett.*, 331:269–277, 2000.

[22] L. V. Moskaleva. *Computational studies of combustion systems pertinent to nitrogen oxides and incipient soot formation*. PhD thesis, Emory University, 2001.

[23] W.-S. Teng, L. V. Moskaleva, H.L. Chen, and M. C. Lin. Ab Initio Chemical Kinetics for H + NCN: Prediction of NCN Heat of Formation and Reaction Product Branching via Doublet and Quartet Surfaces. *J. Phys. Chem. A*, 117:5775–5784, 2013.

[24] M. R. Berman, T. Tsuchiya, A. Gregusova, S. A. Perera, and R. J. Bartlett. HNNC Radical and Its Role in the CH + N_2 Reaction. *J. Chem. Phys. A*, 111:6894–6899, 2007.

[25] L. B. Harding, S. J. Klippenstein, and J. A. Miller. Kinetics of CH + N_2 Revisited with Multireference Methods. *J. Phys. Chem. A*, 112:522–532, 2008,.

[26] V. Vasudevan, R. K. Hanson, C. T. Bowman, D. M. Golden, and D. F. Davidson. Shock Tube Study of the Reaction of CH with N_2: Overall Rate and Branching Ratio. *J. Phys. Chem. A*, 111:11818–11830, 2007.

[27] G. P. Smith. Evidence of NCN as a flame intermediate for prompt NO. *Chem. Phys. Lett.*, 367:541–548, 2003.

[28] J. A. Sutton and J. W. Fleming. Towards accurate kinetic modeling of prompt NO formation in hydrocarbon flames via the NCN pathway. *Combust. Flame*, 154:630–636, 2008.

[29] R. J. H. Klein-Douwel, N. J. Dam, and J. J. ter Meulen. Laser-Induced Fluorescence of NCN in Low and Atmospheric Pressure Flames. *Optics Letters*, 33:2620–2622, 2008.

[30] A. A. Konnov. Implementation of the NCN pathway of prompt-NO formation in the detailed reaction mechanism. *Combust. Flame*, 156:2093–2105, 2009.

[31] N. Lamoureux, P. Desgroux, A. El Bakali, and J.F. Pauwels. Experimental and numerical study of the role of NCN in prompt-NO formation in low-pressure CH_4-O_2-N_2 and C_2H_2-O_2-N_2 flames. *Combust. Flame*, 157:1929–1941, 2010.

[32] N. Lamoureux, H. El Merhubi, L. Gasnot, C. Schoemaecker, and P. Desgroux. Measurements and modelling of HCN and CN species profiles in laminar $CH_4/O_2/N_2$ low pressure flames using LIF/CRDS techniques. *Proc. Combust. Inst.*, 35:745–752, 2015.

[33] A. El Bakali, L. Pillier, P. Desgroux, B. Lefort, L. Gasnot, J. F. Pauwels, and I. da Costa. NO prediction in natural gas flames using GDF-Kin 3.0 mechanism. NCN and HCN contribution to prompt-NO formation. *Fuel*, 85:896–909, 2006.

[34] P. Glarborg, M. U. Alzueta, K. Dam-Johansen, and J. A. Miller. Kinetic Modeling of Hydrocarbon/Nitric Oxide Interactions in a Flow Reactor. *Combust. Flame*, 115:1–27, 1998.

[35] S. Gersen, A. V. Mokhov, and H. B. Levinsky. Diode laser absorption measurement and analysis of HCN in atmospheric-pressure, fuel-rich premixed methane/air flames. *Combust. Flame*, 155:267–276, 2008.

[36] G. P. Smith, D. M. Golden, M. Frenklach, N. W. Moriarty, B. Eiteneer, M. Goldenberg, C. T. Bowman, R. Hanson, S. Song, W. C. Gardiner Jr., V. Lissianski, and Z. Qiu. *GRI-Mech Version 3.0*, 1999. http://www.me.berkeley.edu/gri_mech, last accessed: 15.04.2015.

[37] E. Goos, C. Sickfeld, F. Mauß, L. Siedel, B. Ruscic, A. Burcat, and T. Zeuch. Prompt NO formation in flames: The influence of NCN thermochemistry. *Proc. Combust. Inst.*, 34:657–666, 2013.

[38] E. P. Clifford, P. G. Wenthold, W. C. Lineberger, G. A. Petersson, and G. B. Ellison. Photoelectron Spectroscopy of the NCN^- and $HNCN^-$ Ions. *J. Phys. Chem. A*, 101:4338– 4345, 1997.

[39] R. T. Bise, H. Choi, and D. M. Neumark. Photodissociation dynamics of the singlet and triplet states of the NCN radical. *J. Chem. Phys.*, 111:4923–4932, 1999.

[40] L. V. Moskaleva and M. C. Lin. Computational Study on the Energetics of NCN Isomers and the Kinetics of the C + $N_2 \rightleftharpoons$ N + CN Reaction. *J. Phys. Chem. A*, 105:4156–4163, 2001.

[41] R. S. Zhu and M. C. Lin. Ab Initio Study of the Oxidation of NCN by O_2. *Int. J. Chem. Kinet.*, 37:593– 598, 2005.

[42] C.-L. Huang, S. Y. Tseng, T. Y. Wang, N. S. Wang, Z. F. Xu, and M. C. Lin. Reaction mechanism and kinetics of the NCN+NO reaction: Comparison of theory and experiment. *J. Chem. Phys.*, 122:184321, 2005.

[43] T.-J. Yang, N. S. Wang, L. C. Lee, Z. F. Xu, and M. C. Lin. Kinetics and Mechanism of the NCN + NO_2 Reaction Studied by Experiment and Theory. *J. Phys. Chem. A*, 112:10185–10192, 2008.

[44] R. S. Zhu and M. C. Lin. Ab Initio Study on the Oxidation of NCN by O (^{3}P): Prediction of the Total Rate Constant and Product Branching Ratios. *J. Phys. Chem. A*, 111:6766–6771, 2007.

[45] R. S. Zhu, Hue M. T. Nguyen, and M. C. Lin. Ab Initio Study on the Oxidation of NCN by OH: Prediction of the Individual and Total Rate Constants. *J. Phys. Chem. A*, 113:298–304, 2009.

[46] J. A. Sutton, B. A. Williams, and J. W. Fleming. Laser-induced fluorescence measurements of NCN in low-pressure $CH_4/O_2/N_2$ flames and its role in prompt NO formation. *Combust. Flame*, 153:465–478, 2008.

[47] B. A. Williams and J. W. Fleming. Experimental and modeling study of NO formation in 10 torr methane and propane flames: evidence for additional prompt-NO precursors. *Proc. Combust. Inst.*, 31:1109–1117, 2007.

[48] J. Dammeier and G. Friedrichs. Thermal Decomposition of NCN$_3$ as a High-Temperature NCN Radical Source: Singlet-Triplet Relaxation and Absorption Cross Section of NCN($^3\Sigma$). *J. Phys. Chem. A*, 114:12963–12971, 2010.

[49] J. Dammeier, B. Oden, and G. Friedrichs. A consistent model for the thermal decomposition of NCN$_3$ and the singlet-triplet relaxation of NCN. *Int. J. Chem. Kinet.*, 45:30–40, 2013.

[50] J. Dammeier and G. Friedrichs. Direct Measurements of the Rate Constants of the Reactions NCN + NO and NCN + NO$_2$ Behind Shock Waves. *J. Phys. Chem. A*, 115:14382–14390, 2011.

[51] J. Dammeier, N. Faßheber, and G. Friedrichs. Direct measurements of the high temperature rate constants of the reactions NCN + O, NCN + NCN, and NCN + M. *Phys. Chem. Chem. Phys.*, 14:1030–1037, 2012.

[52] A. Busch and M. Olzmann. Shock-Tube Study of the Thermal Decomposition of NCN. *Proc. Eur. Combust. Meeting*, Paper P810138, Vienna, Austria, 2009.

[53] A. Busch, N. González-García, G. Lendvay, and M. Olzmann. Thermal Decomposition of NCN: Shock-Tube Study, Quantum Chemical Calculations, and Master-Equation Modeling. *J. Phys. Chem. A*, 2015, DOI: 10.1021/acs.jpca.5b01347.

[54] E. M. Bulewicz and T. M. Sugden. Flame Photometric Studies of Reactions Induced by Nitric Oxide in Hydrogen-Oxygen-Nitrogen Flames. I. The Catalyzed Recombination of Atomic Hydrogen and Hydroxyl Radicals. *Proc. R. Soc. London A*, 277:143–154, 1964.

[55] C. J. Halstead and D. R. Jenkins. Catalysis of recombination reactions in flames by nitric oxide. *Chem. Phys. Lett.*, 2:281–282, 1968.

[56] M. Y. Smith. The effect of nitric oxide on the recombination of H atoms in fuel-rich propane-oxygen-nitrogen flames. *Combust. Flame*, 18:293–295, 1972.

[57] M. R. Soto, M. Page, and M. L. McKee. Theoretical study of the reaction of OH with HNO. *Chem. Phys.*, 153:415–426, 1991.

[58] M. R. Soto and M. Page. Ab initio variational transition-state-theory reaction-rate calculations for the gas-phase reaction H + HNO → H$_2$ + NO. *J. Chem. Phys.*, 97:7287–7296, 1992.

[59] H. M. T. Nguyen, S. Zhang, J. Peeters, T. N. Truong, and M. T. Nguyen. Direct ab initio dynamics studies of the reactions of HNO with H and OH radicals. *Chem. Phys. Lett.*, 388:94–99, 2004.

[60] B. Du, W. C. Zhang, C. J. Feng, and Z. Y. Zhou. Thermodynamic and kinetic investigations on the reaction of O(^{3}P) with HNO. *J. Mol. Struct.*, 712:101–107, 2004.

[61] S. Inomata and N. Washida. Rate Constants for the Reactions of NH$_2$ and HNO with Atomic Oxygen at Temperatures Between 242 and 473 k. *J. Phys. Chem. A*, 103:5023–5031, 1999.

[62] M. G. Bryukov, A. A. Kachanov, R. Timonnen, J. Seetula, J. Vandoren, and O. M. Sarkisov. Kinetics of HNO reactions with O$_2$ and HNO. *Chem. Phys. Lett.*, 208:392–398, 1993.

[63] J. A. Miller and C. T. Bowman. Kinetic Modeling of the Reduction of Nitric Oxide in Combustion Products by Isocyanic Acid. *Int. J. Chem. Kinet.*, 23:289–313, 1991.

[64] P. Klaus and J. Warnatz. A contribution towards a complete mechanism for the formation of NO in flames. *Joint meeting of the French and German Sections of the Combustion Institute*, Mulhouse, 1995.

[65] B. Wang, L.S. Sun, S. Su, J. Xiang, S. Hu, and H. Fei. A kinetic study of NO formation during oxy-fuel combustion of pyridine. *Applied Energy*, 92:361–368, 2012.

[66] P. Glarborg, M. Østberg, M. U. Alzueta, K. Dam-Johansen, and J. A. Miller. The recombination of hydrogen atoms with nitric oxide at high temperatures. *Proc. Combust. Inst.*, 27:219–226, 1998.

[67] M. T. Allen, R. A. Yetter, and F. L. Dryer. Hydrogen/nitrous oxide kinetics–Implications of the N_xH_y species. *Combust. Flame*, 112:302–311, 1998.

[68] P. S. Riley, B. Cosic, and A. Fontijn. The H + NO Recombination Reaction Over a Wide Temperature Range. *Int. J. Chem. Kinet.*, 35:374–380, 2003.

[69] P. Glarborg, K. Dam-Johansen, J. A. Miller, R. J. Kee, and M. E. Coltrin. Modeling the Thermal $DENO_x$ Process in Flow Reactors. Surface Effects and Nitrous Oxide Formation. *Int. J. Chem. Kinet.*, 26:421–436, 1994.

[70] A. M. Mebel, M. C. Lin, and K. Morokuma. Ab Initio MO and TST Calculations for the Rate Constant of the HNO + $NO_2 \rightarrow$ HONO + NO Reaction. *Int. J. Chem. Kinet.*, 30:729–736, 1998.

[71] A. M. Mebel, E. W. G. Diau, M. C. Lin, and K. Morokuma. Theoretical Rate Constants for the $NH_3 + NO_x \rightarrow NH_2 +$ HNO_x) (x=1, 2) Reaction by ab Initio MO/VTST Calculations. *J. Phys. Chem.*, 100:7517–7525, 1996.

[72] V. A. Lozovsky and S. Cheskis. Intracavity laser absorption spectroscopy study of HNO in hydrocarbon flames dopted with N_2O. *Chem. Phys. Lett.*, 332:508–514, 2000.

[73] V. A. Lozovsky, I. Rahinov, N. Ditzian, and S. Cheskis. Laser absorption spectroscopy diagnostics of nitrogen-containing radicals in low-pressure hydrocarbon flames doped with nitrogen oxides. *Faraday Discuss.*, 119:321–335, 2002.

[74] G. Friedrichs, J. T. Herbon, D. F. Davidson, and R. K. Hanson. Quantitative detection of HCO behind shock waves: The thermal decomposition of HCO. *Phys.Chem. Chem. Phys.*, 4:5778–5788, 2002.

[75] I. M. Campbell and B. J. Handy. Studies of reactions of atoms in a discharge flow stirred reactor. Part 2. - O + H_2 + CO system. *J. Chem. Soc., Faraday Trans.*, 74:316–325, 1978.

[76] D. L. Baulch, C. J. Cobos, R. A. Cox, C. Esser, P. Frank, Th. Just, J. A. Kerr, M. J. Pilling, J. Troe anr R. W. Walker, and J. Warnatz. Evaluated kinetic data for combustion modelling. *J. Phys. Chem. Ref. Data*, 21:411– 429, 1992.

[77] M. A. Cherian, P. Rhodes, R. J. Simpson, and G. Dixon-Lewis. Kinetic modelling of the oxidation of carbon monoxide in flames. *Proc. Combust. Inst.*, 18:385, 1981.

[78] J. Vandooren, L. Oldenhove de Guertechin, and P. J. Van Tiggelen. Kinetics in a lean formaldehyde flame. *Combust. Flame*, 64:127–139, 1986.

[79] C.-C. Hsu, M. Mebel, and M.C. Lin. Ab initio molecular orbital study of the HCO + O_2 reaction: Direct versus indirect abstraction channels. *J. Chem. Phys.*, 105:2346–2352, 1996.

[80] M. Colberg and G. Friedrichs. Room Temperature and Shock Tube Study of the Reaction HCO + O_2 Using the Photolysis of Glyoxal as an Efficient HCO Source. *J. Phys. Chem. A*, 110:160–170, 2006.

[81] H. N. Najm, P. H. Paul, C. J. Müller, and P. S. Wyckoff. On the adequacy of certain experimental observables as measurements of flame burning rate. *Combust. Flame*, 113:312–332, 1998.

[82] J. Dammeier. *A Shock Tube Study of NCN and HCO Radical Reactions Related to the NO_x Formation in Combustion Processes*. PhD thesis, Christian-Albrechts-Universität zu Kiel, 2011.

[83] Nancy Faßheber. *Stoßwellenuntersuchungen zur Bestimmung der Hochtemperatur-Geschwindigkeitskonstanten der Reaktionen NCN + H und NCN + H_2*, Diploma thesis, Christian-Albrechts-Universität zu Kiel, 2010.

2 Theoretical background

2.1 The shock tube method

In 1808 Poisson[1] published first theoretical considerations on shock waves in ideal gases. The first apparatus for shock wave generation was built in 1899 by Paul Vieille.[2] A schematic picture of a shock tube is shown in Fig. 2.1. In principle the design of this first shock tube, consisting of a high and a low pressure section divided by a membrane, is still common.[2,3] At the beginning, shock tubes were applied to study shock wave propagation and reflection behavior.[4,5] Later they were also used for experimental studies on high temperature chemical kinetics.[6] Today the generation of shock waves is a very well established method to investigate fast gas phase reactions at combustion relevant temperatures. Temperatures between 500 and 15000 K and pressures of 0.1 bar $\leq p \leq$ 1000 bar are accessible. The over-adiabatic compression and, therefore, the heating of the test gas takes place in less than 1 μs. The reaction conditions can be accurately predicted, provided that the shock wave velocity and the initial conditions of the test gas are known. But they are only stable for a few milliseconds, depending on the shock tube design. Due to spontaneous burst of the membrane and the non-ideal flow behavior of the gas, two experiments will never result in exactly the same reaction conditions. Hence, averaging of several single-shot experiments is not easily possible.[7]

2.1.1 Shock wave theory

Shock waves are generated in a closed tube shown schematically in Fig. 2.1. The tube consists of a high pressure (driver) and a low pressure (driven) section divided by a diaphragm (aluminum foil). The low pressure section is filled with the test gas. To generate a shock wave, the high pressure section is filled with an inert driver gas (hydrogen or mixtures of hydrogen and nitrogen) until the diaphragm bursts due to the pressure difference between both sections. Due to the spontaneous rupture of the membrane compression waves are formed which propagate through the test gas section with sonic speed a.

$$a = \sqrt{\frac{\gamma R T}{M}} \qquad (2.1)$$

Where $\gamma = c_p/c_V$ is the adiabatic coefficient and M is the average molecular mass of the gas, T is the absolute temperature and R the gas constant. Due to the adiabatic compression the test gas heats up by a succession of compression waves. Therefore later compression waves travel with higher velocities than the early waves. In addition, the gas starts to flow in the same direction as the compression wave propagation. As a result, the compression waves form a single shock front propagating through the test gas with supersonic speed (about three times the velocity of sound) with respect to the resting, pre-shock gas. The shock wave causes a sudden increase in temperature, pressure and density due to over-adiabatic compression.
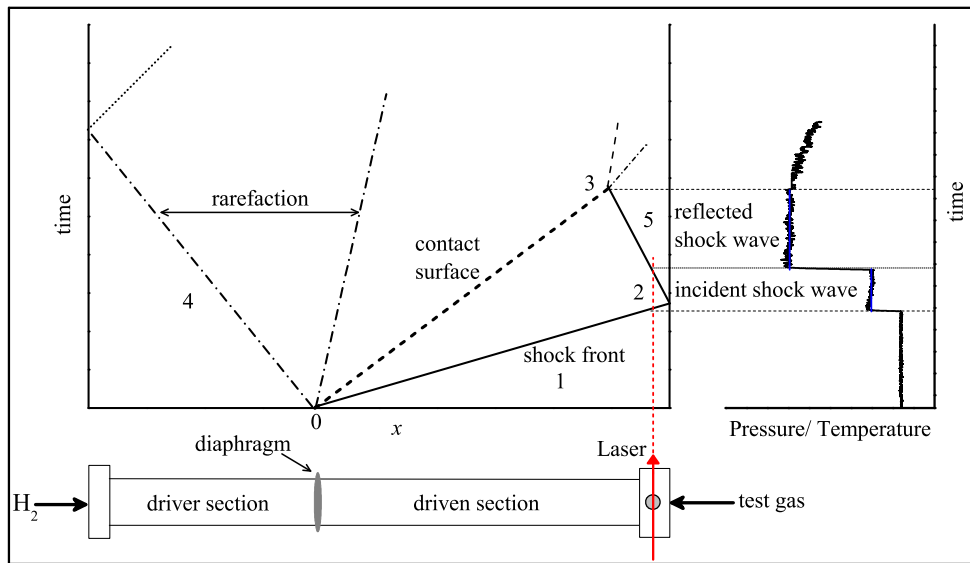
Figure 2.1: Schematics of shock wave propagation.

Fig. 2.1 illustrates the wave propagation through a shock tube after the burst of the membrane in a t-x-diagram. The initial conditions are labeled with the index 1 and the test gas conditions behind the incident shock with index 2. For measurements behind incident shock waves it must be taken into account that the test gas is in motion. When the shock front is reflected at the end plate of the shock tube, the shock wave proceeds through the already compressed (and pre-heated) test gas, brings the test gas to a rest and results in a second temperature and pressure jump. Typically, the temperature T and pressure p behind the reflected shock are about two times higher than behind the incident shock. The reaction conditions after the reflected shock wave are labeled with the index 5. Fig. 2.1 also shows the t-x-traces of the rarefaction waves spreading through the driver section and the contact surface between the driver gas and the test gas following the shock front. If one of these waves reach the measurement point, the measurement conditions are no longer constant and the experiment is over (point 3 in Fig. 2.1).

The measurement point is located close to the end of the low pressure section. The typical pressure (and temperature) profile at this point is shown in a p/T-t diagram in the right plot of Fig. 2.1. Constant measurement conditions are only achieved for a certain time. Incident shock wave conditions (stable for about 0.5 ms) are limited by the arrival of the reflected shock wave. Temperature and pressure

16

behind the reflected wave are stable for about 2 ms (for this work).

The temperatures and pressures during shock tube experiments cannot be easily measured directly because they rise abruptly and are constant on short timescales only. So the conditions (temperature T, pressure p, and density ρ) behind the incident and reflected shock waves have to be calculated. By assuming an ideal flow behavior of the test gas (ideal shock wave), this can be readily accomplished based on the conservation equations of mass, momentum and energy:

$$\text{Mass flow: } \Phi_m = \rho_1 u_1 = \rho_2 u_2 \tag{2.2}$$

$$\text{Momentum flow: } \Phi_i = p_1 + \rho_1 u_1^2 = p_2 + \rho_2 u_2^2 \tag{2.3}$$

$$\text{Energy flow: } \frac{\Phi_e}{\Phi_m} = H_1 + \frac{1}{2}u_1^2 = H_2 + \frac{1}{2}u_2^2. \tag{2.4}$$

Here, H is the specific enthalpy of the gas and u is the flow velocity. To determine the shock wave velocity, four fast piezoelectronic pressure transducers are mounted flush into the tube wall in the low pressure section at defined distances. The pre-shock wave conditions (index 1) are also needed, but can be easily measured before every experiment.

The so called *Rankine-Hugoniot*-equations 2.5 - 2.7 for calculation of incident shock wave conditions can be derived from the conservation equations 2.2 - 2.4 by assuming ideal gas behavior. In the case of argon for example the temperature dependence of the enthalpy can be characterized by the caloric equation of states ($H_2 - H_1 = c_p \times (T_2 - T_1)$) and the state variables are connected by the ideal gas law ($p = \rho RT$).

$$\frac{p_2}{p_1} = \frac{2\gamma M_1^2 - (\gamma - 1)}{\gamma + 1} \tag{2.5}$$

$$\frac{\rho_2}{\rho_1} = \frac{(\gamma + 1) \times M_1^2}{(\gamma - 1) \times M_1^2 + 2} \tag{2.6}$$

$$\frac{T_2}{T_1} = \frac{\left(\gamma M_1^2 - \frac{\gamma - 1}{2}\right) \times \left(\frac{\gamma - 1}{2}M_1^2 + 1\right)}{\left(\frac{\gamma + 1}{2}\right)^2 M_1^2} \tag{2.7}$$

Resulting temperatures, pressures, and densities behind the reflected shock waves can then be calculated based on the conditions behind the incident shock waves.[8,9]

$$\frac{p_5}{p_2} = \frac{\frac{\gamma + 1}{\gamma - 1} + 2 - \frac{p_1}{2}}{1 + \frac{\gamma + 1}{\gamma - 1} \times \frac{p_1}{p_2}} \tag{2.8}$$

$$\frac{T_5}{T_2} = \frac{p_5}{p_2} \times \left(\frac{\frac{\gamma + 1}{\gamma - 1} + \frac{p_5}{p_2}}{1 + \frac{\gamma + 1}{\gamma - 1} \times \frac{p_5}{p_2}}\right). \tag{2.9}$$

When using polyatomic gases in shock tube experiments, real gas effects have to be taken into account. The heat capacity c_p can no longer be treated as temperature independent and the calculated experimental conditions have to be determined by numerical procedures.[9] When rotational and vibrational

motions of the molecules are excited, the heat capacity increases and in the end the temperature is lower than for a monoatomic gas. Moreover, as the heating of the vibrational degrees of freedom is slow, at first the temperature is higher than expected for a vibrationally equilibrated system. Then, caused by vibrational relaxation, the temperature decreases exponentially and finally reaches the state of the fully equilibrated system. The resulting temperature profile can be approximately calculated by assuming that the pressure is nearly constant.[9] In order to minimize relaxation effects, the concentrations of polyatomic reactants should always be kept as low as possible. An example for the need of a significant temperature correction due to the addition of up to 17% O_2 is further outlined in chapter 6.

2.2 UV difference laser absorption spectroscopy

To detect NCN radicals in very low concentrations behind shock waves a fairly sensitive spectroscopic method had to be applied. For this work NCN was detected by difference amplification laser absorption spectroscopy at a wavelength of $\lambda = 329.1302$ nm.

2.2.1 NCN spectroscopy

The pyrolysis of NCN_3 manly leads to the generation of electronically excited ^{1}NCN radicals. Due to fast collision induced intersystem crossing (CIISC) NCN is subsequently converted into its electronic triplet ground state. Under incident shock wave conditions stable plateau concentrations of ^{3}NCN could be observed subsequently.

$$NCN_3 + M \rightarrow {}^1NCN + N_2 + M \rightarrow {}^3NCN + N_2 + M \tag{1}$$

A detailed kinetic study on ^{3}NCN formation has been published by Dammeier et al.[10,11]

The first two electronic states of the linear NCN radical are the $\tilde{X}^3\Sigma_g^-(010)$ and the $\tilde{A}^3\Pi_u(010)$ state. In case of the (010) vibration level, the Born-Oppenheimer approximation breaks down and the $^3\Pi_u$ state splits due to coupling of electron and vibration motion (Renner-Teller effect). Additionally, spin-orbit interactions are observed. The electronic ground state $\tilde{X}^3\Sigma_g^-$ with quantum numbers $\Lambda = 0$ and $l = 1$ is converted into a vibronic Π state according to $K = |\pm\Lambda\pm l|$. The former Π state with $\Lambda = 1$ and $l = 1$ splits into three vibronic Renner-Teller components, the $^3\Sigma_g^+$ and $^3\Sigma_g^-$ states with $K = 0$ and the degenerated $^3\Delta_g$ state ($K = 2$).[12,13,14]

NCN has been detected by narrow-bandwidth laser absorption at overlapping transitions belonging to the Q_1 branch of the $^3\Sigma^+ - ^3\Pi$ subband and the vibrationally hot $\tilde{A}^3\Pi_u(010) - \tilde{X}^3\Sigma_g^-(010)$ system at $\tilde{\nu} = 30383.11$ cm^{-1}. The spectrum is illustrated in Fig. 2.2. The corresponding absorption cross section

$$\log\left(\frac{\sigma}{\text{cm}^2/\text{mol}}\right) = 8.9 - 8.3 \times 10^{-4} \times T/K \tag{2.10}$$

has been adopted from Dammeier and Friedrichs.[10] The stated uncertainty was $\Delta\sigma = \pm 25\%$. Under typical experimental conditions applied in this work ($T = 1500$ K, $p = 500$ mbar, electronic time-

resolution $\Delta t \approx 1\ \mu$s), minimum detectable NCN concentrations were about 4×10^{-12} mol/cm^3 (corresponding to mole fractions of a few ppm).
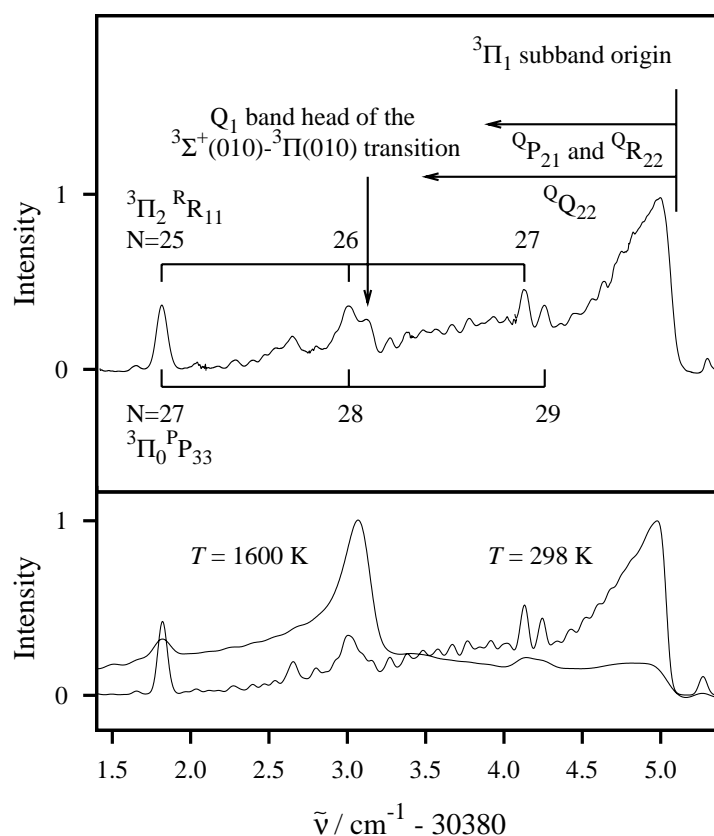
Figure 2.2: High resolution spectra of ^{3}NCN. Upper graph: Measured room temperature spectrum. Lower graph: Comparison between simulated spectra at $T = 298$ K and $T = 1600$ K, adopted from Dammeier and Friedrichs.[10]

2.3 Frequency modulation (FM) spectroscopy

Frequency modulation (FM) spectroscopy is an absorption based spectroscopic method, which was used for HNO and HCO detection in this work. Bjorklund[15] developed this measurement technique and demonstrated its capability of highly sensitive detection of absorption and dispersion of narrow spectral features. Since then FM spectroscopy has been applied and described in many publications.[16,17,18,19,20,21,22] In comparison with conventional absorption methods, FM spectroscopy is more sensitive and can therefore be used for time-resolved detection of small radicals and highly reactive atoms behind shock waves as firstly demonstrated by Friedrichs.[23,24]

2.3.1 Theory of FM spectroscopy

To perform frequency modulation spectroscopy the light of a narrow bandwidth cw-laser beam has to be phase modulated by an electrooptical modulator (EOM). The principle of FM spectroscopy is illustrated in Fig. 2.3, adopted from Friedrichs.[21] The phase modulation at frequency ω_m induces first

order (and higher order) sidebands, which are $1 \times \omega_m$ ($n \times \omega_m$) apart from the center frequency ω_0 of the laser. The modulated signal is monitored by a scanning etalon, which is necessary to properly set the modulation strength and to determine the modulation index $M = \Delta\omega/\omega_m$, with $\Delta\omega$ corresponding to the maximum frequency shift induced by the modulation. By using stronger modulation fields and therefore higher modulation indexes more energy is transferred to the sidebands leading to the generation of higher order sidebands that are displaced by higher integer multiples of ω_m from the center frequency ω_0. Meanwhile the intensity at center frequency gets lower and disappears at a modulation index of $M \approx 2.4$.

In a purely phase (or frequency) modulated beam, the upper and lower sidebands are exactly out-of-phase (phase shift of $180°$). Detecting the light by a photodetector will result in a constant DC signal (null signal), which is proportional to the square of the total light intensity. However, if the two sidebands in Fig. 2.3 are attenuated to a different extent by an absorbing sample, the balance of upper and lower sideband is broken. As a result an amplitude modulated beam with a modulation frequency of $\omega_m = 2\pi\nu_m$ is observed, which can be detected with a fast photodetector. The amplitude of the corresponding AC signal is proportional to the absorption and hence to the concentration of the absorbing species.
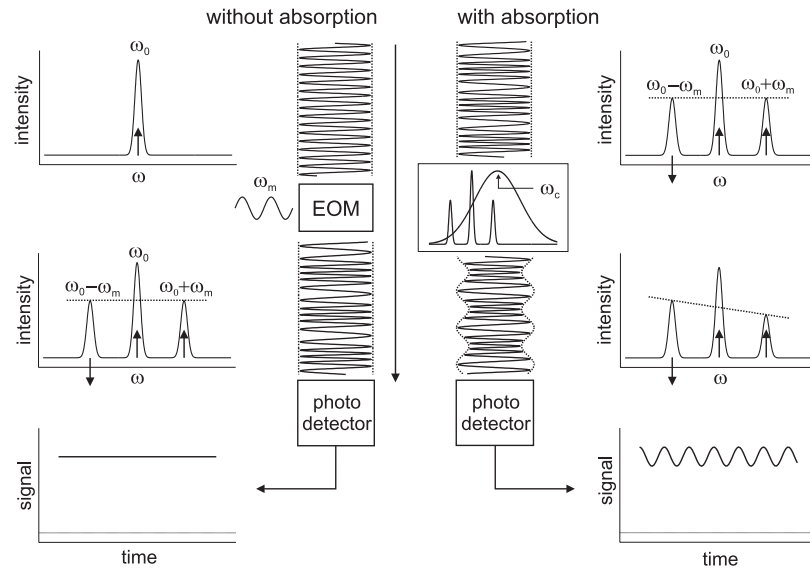
Figure 2.3: Scheme of FM spectroscopy, according to Friedrichs.[21]

For quantitative detection of an absorbing species, the relation between the AC FM signal intensity and the concentration of the species has to be known. Sinusoidal phase modulation with the modulation frequency ω_m, the center frequency ω_0, and the modulation index $M = \Delta\omega/\omega_m$ yields an electric field of the modulated laser beam, which can be expressed as:[18]

$$E(t) = E_0 \exp\left[\mathrm{i}\left(\omega_0 t + M\sin\omega_m t\right)\right] \tag{2.11}$$

$$= E_0 \exp(\mathrm{i}\omega_0 t) \sum_{n=-\infty}^{+\infty} J_n(M)\exp(\mathrm{i}n\omega_m t) \tag{2.12}$$

If the FM light passes through a gas sample, the absorption and dispersion experienced by the center frequency and the side bands can be described by a transmission function $T(\omega_n)$ resulting in the transmission field:

$$E_T(t) = E_0 \exp(i\omega_0 t) \sum_{n=-\infty}^{+\infty} T(\omega_n) J_n(M) \exp(in\omega_m t) \qquad (2.13)$$

The intensity $I_T(t)$, detectable by a photodetector, is proportional to $|E_T(t)|^2$. Considering only the components with a frequency of ω_m, and assuming a weak absorption, the measured FM signal intensity I_{FM} can be related to the concentration of the absorbing species by the equation:

$$I_{FM} = \frac{I_0}{2} \times \Delta f \times \sigma c l \times G \qquad (2.14)$$

with the total light intensity I_0, the narrow-bandwidth absorption cross section at line center σ, the absorption path length l, the gain factor G and the FM factor Δf. The factor G subsumes the total electronic gain factor of the used FM spectrometer (see section 3.2.2.2). The FM factor Δf accounts for the summation over the contributions of all frequency components contained in the frequency spectrum of the modulated light and can be calculated with the knowledge of the line shape data of the probed absorption feature, the modulation frequency ω_m and modulation index M as well as the demodulation phase angle.[21]

2.3.2 HNO spectroscopy

The 193 nm photolysis of glyoxal/NO mixtures has been used as a source for HNO molecules according to the reaction sequence:[25]

$$(CHO)_2 + h\nu \ (\lambda = 193 \, \text{nm}) \rightarrow HCO, H, H_2, CO, CH_2O \qquad (2)$$

$$HCO + NO \rightarrow HNO + CO \qquad (3)$$
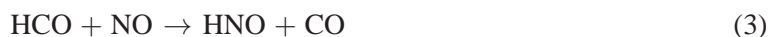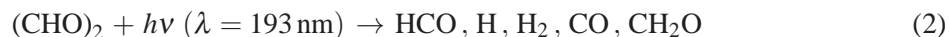
HNO is a bent molecule with a bond angle of about ~ 120°. Its electronic ground state is a singlet (closed shell configuration), which makes HNO a more stable flame species compared to radical-like intermediates. The $(\tilde{A}^1 A'' \leftarrow \tilde{X}^1 A')(100 \leftarrow 000)$ transition of HNO has been very well characterized in previous absorption measurements.[26,27,28,29] The only detection of HNO at high temperatures has been reported by Lozovsky et al.,[29] who measured HNO spectra by ICLAS in flames and compared the absorption intensities of the $(100 \leftarrow 000)$ transition, around 618 nm, and the $(011 \leftarrow 000)$ transition, around 643 nm. Although it turned out that the spectra in the $(011 \leftarrow 000)$ transition range are more intense than in the $(100 \leftarrow 000)$ range, we used the $(100 \leftarrow 000)$ transition because its wavelength region is closer to the HCO $(\tilde{A}^2 A'' \leftarrow \tilde{X}^2 A')(09^0 0 \leftarrow 00^1 0)$ transition at ~ 615 nm. HNO and corresponding HCO measurements have been performed to determine the HNO absorption cross section. In order to find the most suitable absorption line for HNO detection three selected lines of the $(100 \leftarrow 000)$ transition have been characterized (see chapter 7). The measurements of this work represent the first detection of HNO behind shock waves. The minimum detectable HNO concentrations under typical

experimental conditions of $T = 1000$ K and $p = 1000$ mbar were about 1×10^{-10} mol/cm^3 (corresponding to a mole fraction of 50 ppm).

2.3.3 HCO spectroscopy

HCO radicals were generated from the 193 nm glyoxal photolysis[30] or from the thermal decomposition of glyoxal[31] and were detected by means of FM spectroscopy. HCO detection behind shock waves has been thoroughly described by Colberg and Friedrichs.[30] In accordance with this work, HCO detection was performed at the Q(6)P(1) absorption line of the $(\tilde{A}^2A'' \leftarrow \tilde{X}^2A')(09^00 \leftarrow 00^10)$ transition at $\tilde{\nu} = 16266.61$ cm^{-1} (corresponding to the maximum of the FM signal).

For quantitative HCO detection the narrow-bandwidth absorption cross section

$$\ln\left(\frac{\sigma}{\text{cm}^2/\text{mol}}\right) = 6.57 - 1.39 \times 10^{-3}(T/\text{K}) + 3.16 \times 10^{-7}(T/\text{K})^2 - 4.08 \times 10^{-11}(T/\text{K})^3 \quad (2.15)$$

has been adopted from Friedrichs et al.[32] The stated uncertainty of σ is about $\pm 30\%$. The adopted absorption cross section has been determined for the Q(9)P(2) transition (see Fig. 2.4). With respect to the slightly different absorption features of the actually used Q(6)P(1) line, the absorption cross section from Friedrichs et al. was increased by a factor of ~ 1.18.[33] Under typical experimental conditions of this work ($T = 1500$ K, $p = 1300$ mbar), minimum detectable HCO concentrations were about 5×10^{-10} mol/cm^3 (corresponding to a mole fraction of 50 ppm).
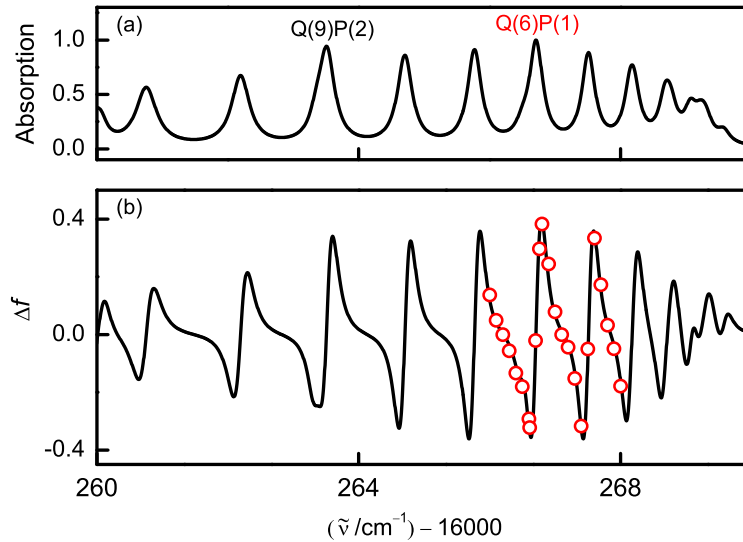
Figure 2.4: a) Simulated absorption spectrum of the $(\tilde{A}^2A'' \leftarrow \tilde{X}^2A')(09^00 \leftarrow 00^10)$ transition of HCO at room temperature. b) Comparison of measured and simulated HCO FM spectra, adopted from Ref. 33.

References

[1] S. D. Poisson. Mémoire sur la théorie du son. *J. École Polytech. (Paris)*, 7:319–392, 1808.

[2] P. Vieille. Sur les discontinuités produites par la détente brusque des gaz comprimés. *C. R. Acad. Sci. Paris*, 129:1228–1230, 1899.

[3] P. Vieille. Étude sur le rôle des discontinuités dans les phénomènes de propagation. *Mém. Poudres Salpêtres*, 10:177–260, 1900.

[4] W. Payman and W. C. F. Shepherd. Explosion waves and shock waves; the disturbance produced by bursting diaphragms with compressed air. *Proc. R. Soc. Lond. A Math. Phys. Sci.*, 186:293–321, 1946.

[5] W. Bleakney and A. H. Taub. Interaction of shock waves. *Rev. Mod. Phys.*, 21:584–605, 1949.

[6] H. S. Glick, W. Squire, and A. Hertzberg. Shock-tube technique for the study of high-temperature gas-phase reactions. *Proc. Combust. Inst.*, 5:393–402, 1954.

[7] K. A. Bhaskaran and P. Roth. The shock tube as wave reactor for kinetic studies and material systems. *Progress in Energy and Combustion Science*, 28:151–192, 2002.

[8] E. F. Greene, J. P. Toennies, and H. Gg. Wagner. *Chemische Reaktionen in Stoßwellen*. Steinkopff Verlag, Darmstadt, 1959.

[9] H. Oertel. *Stoßrohre / Shock Tubes / Tubes á choc*. Springer-Verlag, Wien, 1966, ISBN: 3211807748.

[10] J. Dammeier and G. Friedrichs. Thermal Decomposition of NCN_3 as a High-Temperature NCN Radical Source: Singlet-Triplet Relaxation and Absorption Cross Section of $NCN(^3\Sigma)$. *J. Phys. Chem. A*, 114:12963–12971, 2010.

[11] J. Dammeier, B. Oden, and G. Friedrichs. A consistent model for the thermal decomposition of NCN_3 and the singlet-triplet relaxation of NCN. *Int. J. Chem. Kinet.*, 45:30–40, 2013.

[12] G. Herzberg and D. N. Travis. The Spectrum and Structure of the free NCN Radical. *Canadian Journal of Physics*, 42:1658–1675, 1964.

[13] G. Herzberg. *Molecular Spectra and Molecular Structure, Volume III-Electronic Spectra and Electronic Structure of Polyatomic Molecules*. Krieger Publishing Company, Florida, 1966, ISBN: 0-89464-270-7.

[14] S. A. Beaton and J. M. Brown. Laser Excitation Spectroscopy of the $A^3\Pi_u$- $X^3\Sigma_g^-$ Transition of the NCN Radical. 2. The ν_2 Hot Band. *J. Mol. Spectrosc.*, 183:347–359, 1997.

[15] G. C. Bjorklund. Frequency-modulation spectroscopy: A new method for measuring weak absorptions and dispersions. *Optics Letters*, 5:15–17, 1980.

[16] G. C. Bjorklund, M. D. Levenson, W. Lenth, and C. Ortiz. Frequency Modulation (FM) Spectroscopy - Theory of Lineshapes and Signal-to-Noise Analysis. *Applied Physics B*, 32:145–152, 1983.

[17] J. A. Silver. Frequency-modulation spectroscopy for trace species detection: theory and comparison among experimental methods. *Applied Physics*, 31:707–717, 1992.

[18] J. M. Supplee, E. A. Whittaker, and W. Lenth. Theoretical description of frequency modulation and wavelength modulation spectroscopy. *Applied Optics*, 33:6294–6302, 1994.

[19] M. W. Crofton and E. L. Petersen. Frequency modulation spectroscopy in a particle-forming environment for the detection of SiH_2. *Proc. Combust. Inst.*, 30:1583–1589, 2005.

[20] G. E. Hall and S. W. North. Transient Laser Frequency Modulation Spectroscopy. *Annu. Rev. Phys. Chem.*, 51:243–274, 2000.

[21] G. Friedrichs. Sensitive Absorption Methods for Quantitative Gas Phase Kinetic Measurements. Part 1: Frequency Modulation Spectroscopy. *Zeitschrift für Physikalische Chemie*, 222:1–30, 2008.

[22] S. W. North, X. S. Zheng, R. Fei, and G. E. Hall. Line shape analysis of Doppler broadened frequency-modulated line spectra. *J. Chem. Phys.*, 104:2129–2135, 1996.

[23] G. Friedrichs. *Frequenzmodulierte Spektroskopie zur Untersuchung von Reaktionen des Amino- und Methylenradikals hinter Stoßwellen*. PhD thesis, Georg-August-Universität zu Göttingen, 1999, Cuvillier Verlag, Göttingen, ISBN: 3897127415.

[24] G. Friedrichs and H. Gg. Wagner. Quantitative FM Spectroscopy at High Temperatures: The Detection of $^1CH_2$ behind Shock Waves. *Zeitschrift für Physikalische Chemie*, 12:1723–1746, 2000.

[25] J. Dammeier, Colberg, and G. Friedrichs. Wide temperature range ($T = 295$ K and 770 - 1305 K) study of the kinetics of the reactions HCO + NO and HCO + NO_2 using frequency modulation spectroscopy. *Phys.Chem. Chem. Phys.*, 9:4177–4188, 2007.

[26] J. L. Bancroft, J. M. Hollas, and D. A. Ramsay. The absorption spectra of the HNO and DNO. *Can. J. Phys.*, 40:322–347, 1962.

[27] R. N. Dixon and M. Noble. The dipole moment of hno in its $\tilde{a}^1$a" excited state determined using optical–optical double resonance stark spectroscopy. *Chem. Phys.*, 50:331–339, 1980.

[28] J. Pearson, A. J. Orr-Ewing, M. N. R. Ashfold, and R. N. Dixon. Spectroscopy and predissociation dynamics of the $\tilde{A}^1A$" state of HNO. *J. Chem. Phys.*, 106:5850–5873, 1997.

[29] V. A. Lozovsky, I. Rahinov, N. Ditzian, and S. Cheskis. Laser absorption spectroscopy diagnostics of nitrogen-containing radicals in low-pressure hydrocarbon flames doped with nitrogen oxides. *Faraday Discuss.*, 119:321–335, 2002.

[30] M. Colberg and G. Friedrichs. Room Temperature and Shock Tube Study of the Reaction HCO + O_2 Using the Photolysis of Glyoxal as an Efficient HCO Source. *J. Phys. Chem. A*, 110:160–170, 2006.

[31] G. Friedrichs, M. Colberg, J. Dammeier, T. Bentz, and M. Olzmann. HCO Formation in the Thermal Unimolecular Decomposition of Glyoxal: Rotational and Weak Collision Effects. *Phys.Chem. Chem. Phys.*, 10:6520–6533, 2008.

[32] G. Friedrichs, J. T. Herbon, D. F. Davidson, and R. K. Hanson. Quantitative detection of HCO behind shock waves: The thermal decomposition of HCO. *Phys.Chem. Chem. Phys.*, 4:5778–5788, 2002.

[33] M. Colberg. *Aufbau und Charakterisierung einer Stoßwellenapparatur zur Untersuchung von Hochtemperaturreaktionen des Formylradikals*. PhD thesis, Christian-Albrechts-Universität zu Kiel, 2006.

3 Experimental

Several experimental methods have been applied to study the high temperature kinetics of NCN, HNO, and HCO. The shock tube method was used to heat up the test gases in $t < 1$ μs and to achieve stable reaction conditions for about 1 ms. Pressure and temperature values due to shock compression were calculated reliably based on a 1-dimensional shock tube code. NCN, HNO, and HCO have been generated in-situ from precursor molecules which had to be synthesized before the experiments. As the concentrations of the precursors and of all molecules that have been added as reactants have to be known for quantitative measurements, a mixing system with calibrated mass flow controllers was used to prepare reaction gas mixtures. A difference laser absorption setup and an FM spectrometer were used to detect time-resolved concentration profiles of different species in the gas phase. Rate constants were obtained from the experiments by fitting numerical simulations to the measured concentration-time profiles. Under the applied reaction conditions, the respective target reaction was always the most important one for the simulations.

The different experimental setups and numerical methods for the investigation of NCN, HNO, and HCO reactions in the gas phase are described in this chapter.

3.1 Shock tube setup

All high temperature measurements have been carried out in an overall 8.35 m long stainless steel shock tube with an inner diameter of 81 mm and a 10 mm thick wall. The 3.65 m long driver (high pressure) section was slightly shorter than the 4.05 m long, electro-polished test (low pressure) section. By a combination of an oil-free turbomolecular (Pfeiffer Vacuum, TMU261) and a membrane pump (Pfeiffer Vacuum, MVP055-3) the test section could be evacuated down to a pressure of $p \approx 10^{-7}$ mbar. A cold-cathode ionization gauge (Pfeiffer Vacuum, IKR 261) was used for pressure measurements in the test section. The pressure of the test gas in the low pressure section before shock compression could be measured by a second pressure gauge (MKS 622AX12MBE). The leak rate of the metal sealed test section was 1.6×10^{-6} mbar L/s.

The high pressure section was mounted on wheels such that the aluminum foil dividing the high pressure section from the test section (low pressure section) could be easily exchanged. The driver section was filled with a driver gas until the foil burst spontaneously. Either 30, 80 or 100 μm thick aluminum foils were used. In combination with the used driver gases hydrogen (Air Liquide, $\geq$

99,999%), helium (Air Liquide, $\geq 99,999\%$), or different mixtures of hydrogen and nitrogen (Air Liquide, $\geq 99,99\%$) temperatures between 700 and 2500 K after incident shock waves were accessible. Also a wide pressure range of 0.2 bar $\leq p \leq 2.1$ bar was within reach. The mixing of two different driver gases was accomplished by two magnetic valves (Danfoss, BA024A), which could be separately opened for particular times between 25 and 475 μs by an electronic controller. After an experiment the shock tube could be flushed with nitrogen to remove remaining pieces of aluminum foil. The test gas was passed into the test section by a tubing system that connected the shock tube head with the gas mixing system. Before an experiment the test gas mixture was flushed through the test section for about 3 min to minimize possible effects due to adsorption effects on the shock tube wall.

To determine the shock wave velocities needed for the calculations of experimental pressures and temperatures, four fast pressure transducers (PCB Piezotronics M 113A21) were embedded flush to the shock tube walls of the test section at defined positions. They were connected to a fast count unit. For spectroscopic measurements the laser beam was coupled into the shock tube head through two quartz windows. The observation time behind the incident wave was determined by the distance between the observation plane and the end plate of the shock tube head. This distance could be varied between 19 mm and 60 mm by installing an additional tube part, resulting in observation times of approximately 200 μs $\leq t \leq 600$ μs behind the incident shock wave.

3.1.1 Flow cell

FM measurements of HNO and HCO at room temperature were carried out in a 45 cm long glass flow cell that could be integrated into the shock tube setup. The two quartz windows at both ends of the cell were mounted in Brewster angle. To avoid depositions of reaction products, the windows could be flushed with nitrogen during the experiments. During the FM measurements the detection laser beam and the photolysis beam, with a much larger diameter, were collinearly coupled into the cell from opposite sides. The large diameter of the photolysis laser guaranteed that diffusional processes could be neglected. Two pressure gauges (5 mbar and 100 mbar) were attached to the cell to adjust the test gas flow during the experiments.

3.1.2 Gas mixing system

For the preparation of well defined gas mixtures the gas mixing system shown schematically in Fig. 3.1 was used. The prepared gas mixtures were stored in different tanks and passed into the test section of the shock tube through a valve in the shock tube head. Since the test section was evacuated near the membrane (end of test section) the test gas could be flushed through the whole section to compensate for possible wall adsorption effects. Alternatively the test gas was led to the flow cell. The mixing system mainly consisted of stainless steel tubing. For the storage and preparation of gas mixtures by the partial pressure method, gas bottles, glass flasks and tanks of stainless steel could be connected to the system. It was possible to purify gases like NO and NO_2 by freeze-pump-thaw cycles performed in a 5 L flask equipped with a cooling finger. The NCN_3 was only diluted in argon and not further

purified due to its tendency to explode in condensed phase. The prepared gas mixtures were passed through four different mass flow controllers (Aera, FC-7700CU 10, 50, 100 and 1000 sccm) for further mixing and dilution (mostly in argon) directly before entering the shock tube. A rotary vane pump with a cooling trap was used for fast evacuation of the gas mixing system and the test section of the shock tube. To avoid condensation of NCN_3 in the cooling trap it could be evacuated over a bypass (see Fig. 3.1). For evacuation down to pressures of $\sim 10^{-6}$ mbar, a turbomolecular pump (Pfeiffer Vacuum, TMH071-P) together with a diaphragm pump (Pfeiffer Vacuum, MVP 015-2) was used. Three different pressure gauges (MKS 722AMCE2FA, MKS 622AX12MBE, Pfeiffer Vakuum PKR 251) allowed to measure the pressure in the range of 5 bar $\geq p \geq 10^{-7}$ mbar.
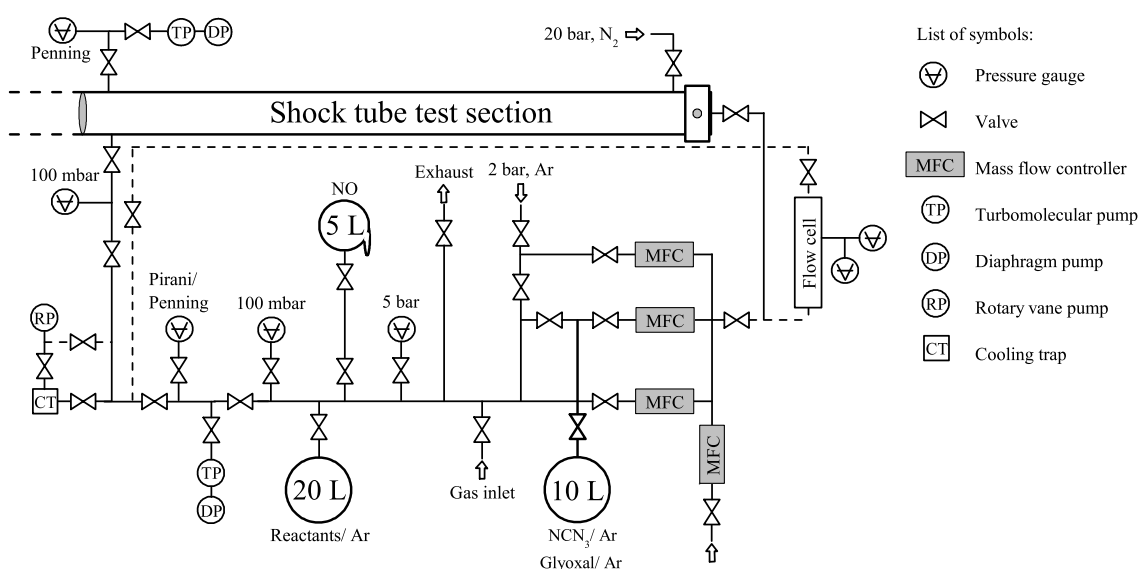
Figure 3.1: Scheme of the gas mixing system, which could either be connected to the shock tube head or a flow cell.

3.2 Absorption spectrometer

UV/VIS spectroscopy was used for the detection of HNO, HCO, and NCN radicals. By absorption based measurements of selected electronic transitions the different species could be directly observed. Assuming that the particular absorption cross sections are known it was possible to determine the concentrations of the species in the reaction mixture. In the visible spectral region, frequency modulation (FM) spectroscopy was used for highly sensitive detection of HNO and HCO ($(\alpha cl)_{\min} = 5 \times 10^{-5}$). Since FM spectroscopy cannot be used in the UV region, NCN was detected by narrow-bandwidth difference laser absorption (DLA) spectroscopy ($(\alpha cl)_{\min} = 5 \times 10^{-4}$) instead.

3.2.1 UV difference absorption spectrometer

Fig. 3.2 illustrates the schematic setup for the UV absorption experiment. The UV light ($\lambda \approx 330$ nm) was generated by intra-cavity frequency doubling of a continuous-wave ring-dye laser (Coherent 899

series), which was optically pumped by a solid state Nd:YVO$_4$ laser (Coherent Verdi V10). A LiIO$_4$ crystal, which was constantly flushed with boil-off nitrogen, was inserted in the laser cavity to achieve the frequency doubling. Typically, at 10 W pumping power, 1.5 mW UV light were generated. About 2 mW of the laser fundamental were coupled out of the cavity through a highly reflective mirror for wavelength measurements by an interferometric wavemeter (MetroLux WL200) referenced to a HeNe laser. By this means, taking into account a small wavemeter offset of $\Delta\tilde{\nu} = 0.02\,\mathrm{cm}^{-1}$, the wavelength could be determined with an accuracy of about 5×10^{-7} ($\Delta\tilde{\nu} = 0.015\,\mathrm{cm}^{-1}$). Using DCM-Spezial (4-Dicyanomethylen-2-methyl-6-p-dimethyl-aminostyryl-4H-pyran, Radiant Dyes) as a laser dye the wavelength of the fundamental could be set to $\tilde{\nu} = 15191.56\,\mathrm{cm}^{-1}$, hence the frequency-doubled laser beam was centered at $\tilde{\nu} = 30383.11\,\mathrm{cm}^{-1}$ to observe the $^3\Sigma^+(010) - {}^3\Pi(010)$ ^{3}NCN transition.
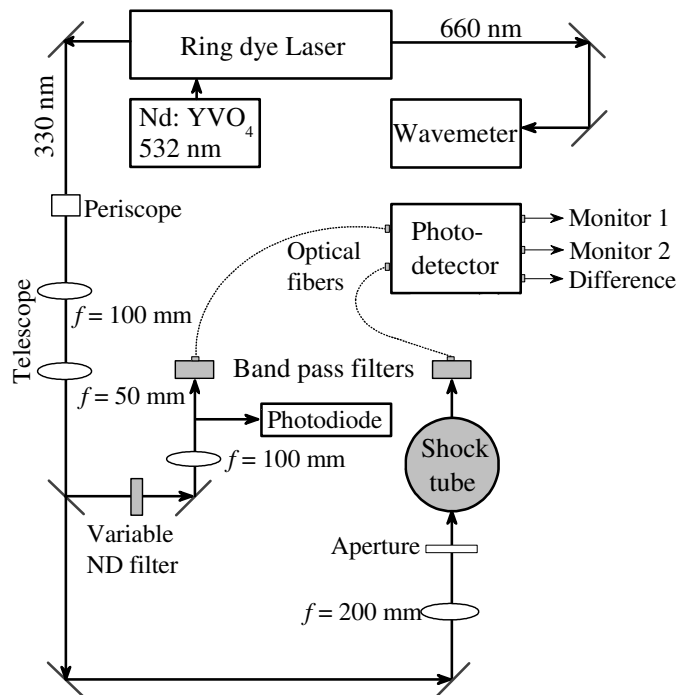
Figure 3.2: Scheme of the difference laser absorption spectroscopy setup.

The generated UV laser beam was deflected by a periscope to adjust the height of the laser beam to the height of the shock tube and collimated to a diameter of about 2 mm by a telescope. A 50:50 beam splitter plate was used to split the laser beam into a probe and a reference beam. The detection beam was focused by a quartz lens ($f = 200$ mm) and passed through the shock tube windows. After passing the shock tube the beam was band-pass filtered (Andover, 326FS25-12.5) and coupled into a quartz optical fiber (Thorlabs BF H22-550) connected to a balanced photodetector and difference amplifier (Thorlabs PDB 150A-EC). The reference beam was passed through a circular variable neutral density filter to match the intensity of the reference beam with the intensity of the probe beam. The intensities of the two separated beams (Monitor 1 and 2 in Fig. 3.2) were monitored on a digital oscilloscope (Hameg, HM 507, 50 MHz, 8 Bit). As the monitor exhibit a low time response, in order to check the stability of the laser beam, about 10% of the reference beam were split off the main beam by a quartz plate and were focused on a fast Si photodiode (Hamamatsu S5973-2). The finaly resulting amplified

difference signal from the balanced photodetector was low-pass-filtered (1.4 MHz), further amplified (Ortec Fast Preamp 9305, 18 dB) and stored by an analog input board (Measurement Computing, PCI-DAS4020/12, 20 MHz, 12 bit).
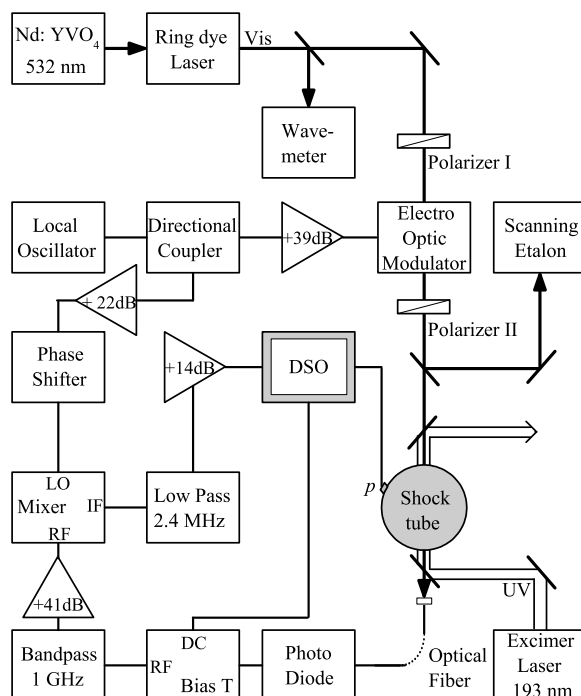
Figure 3.3: Block diagram of the used FM setup.

3.2.2   FM spectrometer

The basic FM setup for the HNO and HCO detection is schematically shown in Fig. 3.3. The ring-dye laser (Coherent 899 series) was operated with the dye Kiton Red (Sulforhodamine B, Radiant Dyes), thereby wavelength between 600 and 650 nm were accessible. The narrow-bandwidth laser beam was focused by a telescope, passed through a first polarizer (New Focus Inc., 5524), was phase-modulated by an external electro-optical modulator (EOM, New Focus Inc., 4421) and then passed a second polarizer. The two polarizer setup was necessary to properly set the input polarization with respect to the EOM crystal axis and to conveniently set the demodulation phase angle (see Section 1.2.2.1).

The EOM was driven by a part of the power of a local oscillator (Hewlett Packard, 8657B) providing the modulation frequency of 1000 MHz. The initial output power of the oscillator was divided by a bidirectional coupler (Mini Circuits ZFDC-10-5). The power for the EOM was amplified by 39.4 dB (Hughes 10 W Series) and could be varied by additional attenuators (between -1 dB and -3 dB) to obtain different modulation indices up to $M = 1.7$. To monitor the exact modulation index, a small part of the laser beam was split of and analyzed by a scanning etalon (Coherent, Typ SM 240-1).

The frequency modulated detection beam was focused ($f = 300$ mm) before passing the shock tube head and was then coupled into an optical fiber right after the shock tube window. The fiber output was strongly refocused ($f = 25$ mm) onto a fast Si photodiode (Hamamatsu, S5973) with a photo active

diameter of 0.4 mm. The signal collected by the photodiode was divided into its AC and DC component by a Bias Tee (Mini Circuits, ZFBT-4R2G). The DC component was directly monitored with a digital oscilloscope (Lecroy, Wavesurfer 454) without further amplification. The AC component, on the other hand, was filtered by a tunable bandpass filter (Trilithic) at 1 GHz, amplified by 41 dB (Mini Circuits, ZHL 0812 HLN) and fed into the signal input of a double balanced frequency mixer (Mini Circuits, 5542-ZFM-2000) for demodulation. The reference signal input for the frequency mixer came from the coupled line of the bidirectional coupler, which was connected to the local oscillator (Hewlett Packard, 8657B). The phase and thereby the demodulation angle of the resulting demodulated signal was adjusted by a variable phase shifter (Knick, J45). The demodulated signal was low pass filtered (2.5 MHz, Mini Circuits, SLP-2.5), amplified by 14 dB (Stanford Research System, SR445A) and stored in the digital oscilloscope (Lecroy, Wavesurfer 454).

3.2.2.1   Setting of the demodulation angle   For a strong FM signal reflecting the pure absorption of the sample, the demodulation phase angle θ had to be set to $0°$ or $180°$ degrees. This setting could be accomplished by the two-polarizer setup as described by Friedrichs and Wagner.[1] For normal operation the polarization of the two polarizers in front and behind the EOM was set vertically to the axis of the modulation crystal. By rotating one of the polarizers by a few degrees a small amplitude modulation was induced in addition to the phase or frequency modulation. This amplitude modulation is out-of-phase with respect to an absorption signal and causes an offset of the FM baseline. Rotating the second polarizer back and forth resulted in a strong positive and negative FM baseline shift if the phase angle was far from pure absorption ($0°$ or $180°$). Then, by changing the demodulation phase angle, by the voltage controlled phase shifter (Knick, J45) until the observed baseline shifts virtually disappeared, it was possible to set the demodulation electronics to a phase angle, which is close to the pure absorption case ($\pm 2°$). Finally, the polarizers were rotated back to normal operation.

3.2.2.2   Gain factor determination   For quantitative FM measurements the FM factor Δf and the gain factor G of the particular experimental setup had to be known. On the one hand, the gain factor as a value for the overall electronic amplification of the used FM spectrometer needed to be determined experimentally prior to the actual measurements.[1] On the other hand, the FM factor could be calculated based on the value of the modulation index and the line shape data for the absorbing species. In this work the gain factor G has been determined according to the scanning etalon method resulting in $G = 184 \pm 14$. This value was in good agreement with the gain factor estimated from the used electronic components and quantitative measurements of HCO radical concentrations.

Scanning etalon method: A scanning etalon in reflective mode was integrated into the beam path of the usual FM setup.[2,3] In this mode, the etalon acted like a narrow-bandwidth absorber resulting in a measurable FM spectrum. As an example, a typically measured FM spectrum and the corresponding absorption spectrum (measured by monitoring the attenuation of the total light intensity using the DC output of the Bias Tee) are depicted in Fig. 3.4. From these spectra the G factor could be directly

calculated using the equation

$$G = \frac{2 \times I_{\mathrm{FM}}}{A \times I_0 \times \Delta f}. \tag{3.1}$$

Here, A is the absorption measured at the center of the peaks corresponding to the first upper and lower sidebands, and I_0 is the intensity of the DC output of the Bias Tee.
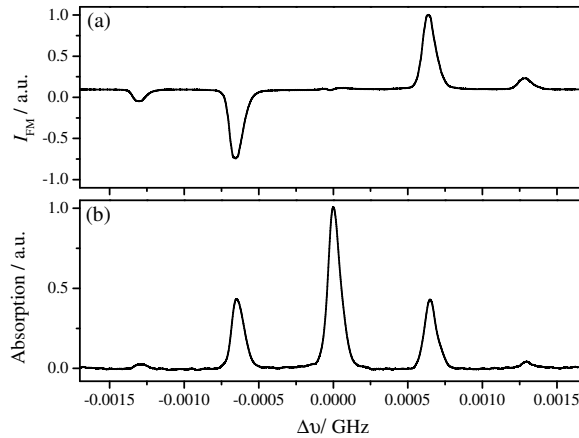
Figure 3.4: a) Measured FM signal and b) corresponding absorption signal from the scanning etalon used as narrow-bandwidth absorber.

FM electronic setup: In principle, it is possible to calculate the gain factor from the amplifications (attenuations) of all the used electronic components and the characteristics of the photodiode. Instead of using the data specified by the manufactures, the actual amplification and attenuation values have been determined experimentally. For it, a first frequency generator (Hewlett Packard, 8657B) was used to provide a signal with a frequency of $\nu = 1.000$ GHz and a defined amplitude. This signal and a second signal with a frequency of $\nu = 1.001$ GHz from a second frequency generator (Marconi Instruments, 2023) were connected to the inputs of the frequency mixer and its output has been displayed with an oscilloscope. From the amplitude of the resulting 1 MHz sinusoidal signal and the amplitude of the 1.00 GHz signal the attenuation of the frequency mixer was determined. Next, the other electronic devices were integrated in-between the first frequency generator and the frequency mixer. The resulting signal amplitudes measured with the oscilloscope with and without the integrated device directly reflected the attenuation or amplification resulting from this specific device. Tab. 3.1 shows the results for the electronic devices of the used FM setup. The only thing that could not be quantified for the determination of the gain factor was the exact frequency-dependence of the responsivity of the used photodiode. This value had to be estimated from technical data. The sum of all specific amplifications, taking a small loss due to the cables and connections into account, resulted in a maximum gain factor of $G_{\mathrm{max}} = 238$. Together with $G_{\mathrm{Diode}} = 0.8$ estimated for the used photodiode an overall gain factor of $G = 190$ could be determined. Taking into account the uncertainties, this estimate was in very good agreement with the result from the scanning etalon method.

Table 3.1: Measured amplification of FM electronic components.

Component	Model	Amplification / dB
Frequency mixer	Mini Circuits 5542-ZFM-2000	−6.4
Amplifier	Mini Circuits ZHL 0812 HLN	+40.8
	Hughes 10 W Series	+39.4
	Mini Circuits ZFL 2000	+22.4
	Stanford Research System SR445A	+14.3
Bias Tee	Mini Circuits ZFBT-4R2G	−0.5
Bidirectional-Coupler	Mini Circuits ZFDC-10-5	Main line −1.4
		Coupled line −10.5
Filter	Trilithic	est. −0.5
Cables and connections		est. −0.5
Si photodiode	Hamamatsu, S5973	est. −2.0

HCO absorption measurements: Concentration-time profiles of HCO, a species with a known absorption cross section[4,5] which has been previously measured with an accuracy of ±30%, have been detected to test the determined gain factor. HCO was generated from the thermal decomposition of glyoxal, which has been studied extensively in previous work.[6] Shock tube experiments with well known mole fractions of glyoxal (about 1% in argon) were performed at temperatures between 1299 and 1757 K (see chapter 8). The measured HCO profiles and maximum intermediate HCO concentrations could be very well reproduced by simulations using the adopted HCO cross section and glyoxal mechanism from Friedrichs et al.[6] together with the determined gain factor of $G = 184$. In fact, the HCO concentration maxima could be reproduced with an accuracy of about 10%. This is well within the uncertainty of the method and indicates an accurate gain factor.

3.3 Numerical Methods

3.3.1 Data analysis

Extensive reaction mechanisms containing a huge number of elementary reaction steps are necessary to describe combustion processes. Although the number of reactants in shock tube experiments is comparably small numerical procedures are required to simulate the measured concentration-time profiles.

The fitting procedures for all the experimental data of this work have been performed by the Chemkin-II program package.[7] The program performs the numerical integration of a high number of reactions with rate constants given in terms of the extended Arrhenius expression:

$$k_i = A_i T^{n_i} \exp\left[-E_{a,i}/RT\right]. \tag{3.2}$$

The core mechanism as well as a feasible set of rate constants were adopted from previous results of the working group Friedrichs and recent literature data. An additional background mechanism was

added to the core mechanism to take possibly important secondary chemistry into account. The core reaction mechanisms for NCN, HNO and HCO simulations are presented in chapters 4 - 8, respectively. Either the GRI-Mech 3.0[8] or the GDFkin3.0_NCN[9,10] have been used as background mechanisms. For the simulation of HCO concentration-time profiles measured during the thermal decomposition of glyoxal, a new glyoxal oxidation mechanism has been developed in collaboration with P. Glarborg, Technical University of Denmark, and P. Marshall, University of North Texas, (see chapter 8). To run the Chemkin-II program and to calculate the reverse rate constants the thermodynamic data for all involved species had to be included in form of NASA-polynomials. Thermodynamic data have been adopted from the databases of Goos et al.[11] and Konnov.[12] Additionally, the initial reaction conditions had to be specified. For the determination of a rate constant k_x, its value has been changed during the fitting procedure until the simulated and the measured profile were in good agreement. By using the Senkin routine sensitivity analyses have been performed.[7] Sensitivity coefficients σ provide informations about how much the resulting simulation was influenced by the rate constant of a certain reaction. Sensitivity analyses allows one to design the experiments in a way that they are most sensitive to the rate constant under study. In a sensitivity analysis the rate constants of all reactions are individually varied by a factor a_i (starting with $a_i = 1$)

$$k_{i,\,\text{varied}} = a_i \times A_i T^{n_i} \exp\left[-E_{a,\,i}/RT\right] \tag{3.3}$$

To get comparable values of sensitivity coefficients $\sigma(i, j, t)$, they were normalized as follows

$$\sigma(i, j, t) = \frac{\partial c(i, j, t)}{\partial a_i} \tag{3.4}$$

$$\sigma^{\circ}_{\text{max}}(i, j, t) = \sigma(i, j, t) \times \frac{a_i}{c_{\text{max}}(j)}. \tag{3.5}$$

Home-written Gnuplot[13] routines were used for further processing of the experimental and simulated data. Fitting of analytical functions was performed with the program Origin.[14]

3.3.2 Quantum chemical calculations

Quantum chemical calculations on the reaction NCN + H$_2$ $\rightarrow$ HNCN + H were carried out using the Gaussian 09 suite of programs.[15] Formation enthalpies were calculated on the G4 level of theory and the transition state of the reaction was located and verified by using a synchronous transit-guided quasi-Newton method (QST3 option) and intrinsic reaction coordinate following.

3.4 Synthesis of precursor molecules

HNO, HCO, and NCN are short-lived species and had to be generated directly during the experiments by photolysis and/or pyrolysis of precursor molecules. The used precursors are not stable, not commercially available and therefore they were synthesized in the following manner.

3.4.1 Cyanogen azide (NCN_3) synthesis
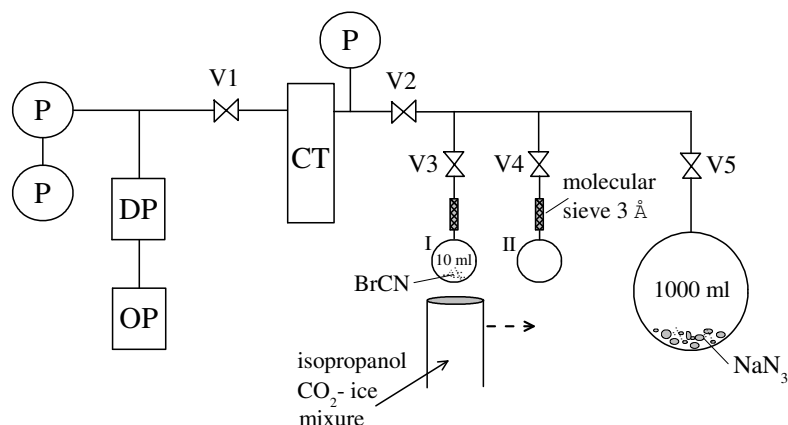
Figure 3.5: Schematic setup of the equipment for the NCN_3 synthesis. DP: Diffusion pump, CT: Cooling trap, OP: Oil pump, P: Pressure gauge, V: Valve.

The NCN radicals were generated from the 193 nm pyrolysis of NCN_3 molecules behind shock waves according to the reaction sequence:

$$NCN_3 + M \rightarrow {}^1NCN + N_2 + M \tag{1}$$

$$^1NCN + M \rightarrow {}^3NCN + M \tag{2}$$

The initial thermal decomposition of NCN_3 yields NCN in its first electronically excited singlet state, it is converted into the triplet ground state by a collision induced inter system crossing (CIISC) process.[16,17] According to studies of Bock and Dammel[18] as well as Benard et al,[19] cyanogen azide (NCN_3) pyrolysis quantitatively yields ^3NCN. Since cyanogen azide is known to be a toxic and, especially in condensed phase, a highly explosive substance, it was synthesized in the gas phase by a variation of a method from Milligan et al.[20] For safety reasons, no attempt was made to purify NCN_3 after synthesis. Instead, the reactants were applied in very high purity. In the glass apparatus illustrated in Fig. 3.5, gaseous cyanogen bromide was passed into a 1000 mL flask containing a huge excess of solid sodium azide.

$$NaN_3 \text{ (s)} + BrCN \text{ (g)} \rightarrow NCN_3\text{(g)} + NaBr \text{ (s)} \tag{3}$$
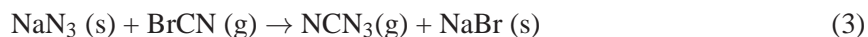
About 10 g (150 mmol) of very finely pestled sodium azide were degassed *i. vac.* at 2×10^{-4} mbar overnight to remove impurities of H_2O and CO_2. Directly before the start of the reaction, 0.25 g (2.4 mmol, mass before purification) BrCN were also degassed *i. vac.* (2×10^{-4} mbar) at $T = -78°$ C for about 10 min and were passed through a molecular sieve (3 Å) to remove H_2O. This procedure was repeated after BrCN was re-sublimed in a second flask. The purified BrCN was then evaporated into the sodium azide containing flask and the flask was closed vacuum tight. The reaction mixture was allowed to stand for 8 h and was carefully shaken every 30 min to guarantee a complete mixing of the reactants, which is important for a high yield of NCN_3. The amount of the initially applied BrCN

was chosen in a way that the resulting partial pressure of NCN_3 never exceeded 50 mbar (the reported approximate vapor pressure of NCN_3 at room temperature). Hence, care was taken that the highly explosive compound would never condense in the reaction flask. Immediately after the end of the reaction time, the gaseous reaction product was analyzed by FT-IR spectroscopy to control the purity. The described synthesis procedure typically yields NCN_3 in purities of > 97%. NCN_3 decomposes due to bimolecular reactions slowly forming dimers and polymers. It was directly diluted with Argon ($x(NCN_3) \leq 0.1\%$) in a 10 L glass flask and was used within 3 days. The NCN_3 loss in the mixture was about 10% per day.

3.4.2 FT-IR spectra of NCN_3

The yield of the synthesized NCN_3 was always checked by FT-IR analysis to detect possible impurities of H_2O, CO_2 and to determine the fraction of unreacted BrCN. The used spectrometer (Bruker, IFS 66V, resolution: 0.25 cm^{-1}) has been calibrated using different BrCN concentrations beforehand.[21] BrCN absorption at $\widetilde{\nu} = 2530$ cm^{-1} served as an indicator for the quantification of BrCN impurity when the total pressure in the probe cell was known.
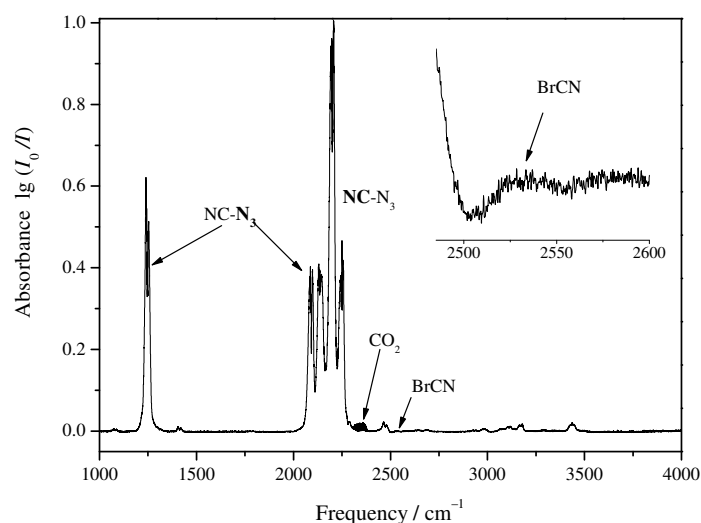
Figure 3.6: IR spectrum of the reaction products of a typical NCN_3 synthesis with a yield of $x(NCN_3) \approx 99\%$ measured at $p = 2.5$ mbar and $T = 298$ K in a 10 cm long measuring cell.

Fig. 3.6 shows a typical IR spectrum of a NCN_3 sample. Three fundamental vibration bands of NCN_3 occur in the observed wavelength region, assignment of the NCN_3 transitions is listed in Tab. 3.2 and was taken from Bak et al.[22] The spectrum also shows a very weak CO_2 peak (mole fraction < 0.2%) but almost no visible signs of H_2O. The wavelength region around $\widetilde{\nu} = 2530$ cm^{-1} where a BrCN signal would be expected to be visible in the spectrum is magnified in the inset. Almost no signal is detectable corresponding to BrCN impurities well below 1%.

Table 3.2: Band position for NCN_3 and impurities of the reaction product obtained from synthesis.

NCN_3	This work/ cm^{-1}	Literature data/ cm^{-1}
$-N_3$ (sym. str.)	1232-1262	1246[22]
$-N_3$ (asym str.)	2079-2155	2198[22]
$-C\equiv N$ (str.)	2181-2261	2248[22]
Impurities		
H_2O (sym + asym. str.)	3564-3925	3570-3760[23]
H_2O (bending)	1400-1770	1600-1630[23]
BrCN (combination band)	2520-2535	2495-2565[24]
CO_2 (asym. str.)	2313-2367	2349[25]

For comparison, a second IR spectrum is shown in Fig. 3.7. Here, a large amount of H_2O and CO_2 is present most likely due to a leakage in the synthesis apparatus. Additionally the clearly visible BrCN peak, corresponding to a mole fraction of $\sim 50\%$, indicates that to much BrCN was used or that the reaction time was too short. Such a poor result of the synthesis was an exception. For the kinetic measurements only mixtures with an NCN_3 yield of at least 97% have been used.
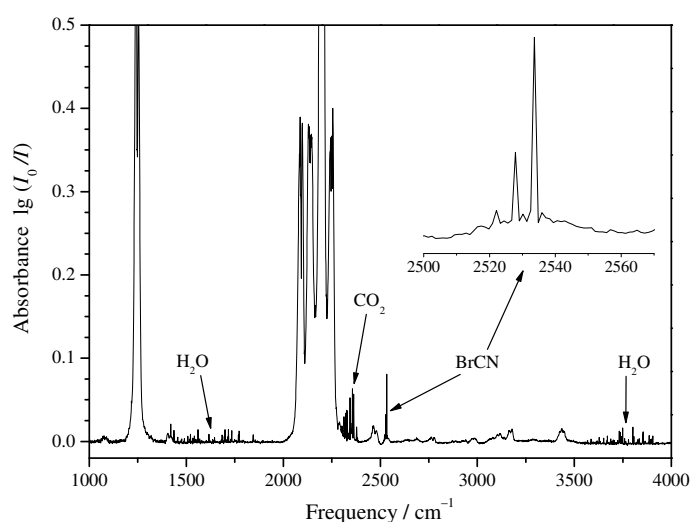
Figure 3.7: IR spectrum of an NCN_3 synthesis with significant amounts of impurities measured at $p = 2.3$ mbar and $T = 298$ K in a 10 cm long measuring cell.

3.4.3 Glyoxal synthesis

The glyoxal monomer $((CHO)_2)$ has been prepared by dehydration of the trimer dehydrate $((CHO)_2)_3 \times 2H_2O$ according to reaction (4).

36

$$3 \quad \text{(structure)} \quad + \quad 2 \ P_2O_5 \quad \longrightarrow \quad 9 \quad \text{(structure)} \quad + \quad 4 \ H_3PO_4 \qquad (4)$$

FT-IR analysis showed that this procedure yielded glyoxal monomers without the impurities of H_2O and CO_2.[5] One eq. of the trimer was mixed with 3 eq. of phosphoric anhydride (P_2O_5) and some silica sand. The mixture was slowly heated to a temperature of $T = 155°C$ *i. vac.* (2×10^{-2} mbar). A slight pressure rise indicated the formation of the gaseous reaction products, which were passed through a first cooling trap ($T = 0°C$) to remove impurities, for example water. The yellow $(CHO)_2$ crystals were re-sublimated in a second cooling trap ($T = -78°C$). The solid glyoxal crystals could be stored in liquid nitrogen over a longer time period. When preparing the mixtures of $\sim 1 - 2\%$ glyoxal in argon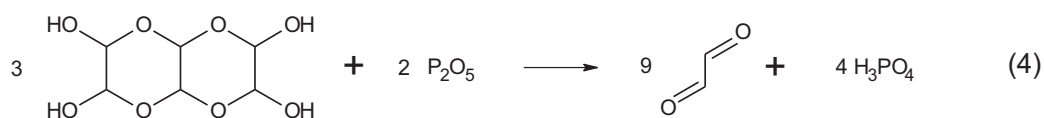, the first few mbar of sublimating $(CHO)_2$ were always pumped off. The glyoxal/argon mixtures were used within a few days because glyoxal tend to form polymeres that deposit on the walls of the storage tank.

References

[1] G. Friedrichs and H. Gg. Wagner. Quantitative FM Spectroscopy at High Temperatures: The Detection of $^1CH_2$ behind Shock Waves. *Zeitschrift für Physikalische Chemie*, 12:1723–1746, 2000.

[2] G. C. Bjorklund. Frequency-modulation spectroscopy: A new method for measuring weak absorptions and dispersions. *Optics Letters*, 5:15–17, 1980.

[3] M. Votsmeier, S. Song, D. F. Davidson, and R. K. Hanson. Sensitive Detection of NH_2 in Shock Tube Experiments Using Frequency Modulation Spectroscopy. *Int. J. Chem. Kinet.*, 31:445–453, 1999.

[4] G. Friedrichs, J. T. Herbon, D. F. Davidson, and R. K. Hanson. Quantitative detection of HCO behind shock waves: The thermal decomposition of HCO. *Phys.Chem. Chem. Phys.*, 4:5778–5788, 2002.

[5] M. Colberg and G. Friedrichs. Room Temperature and Shock Tube Study of the Reaction HCO + O_2 Using the Photolysis of Glyoxal as an Efficient HCO Source. *J. Phys. Chem. A*, 110:160–170, 2006.

[6] G. Friedrichs, M. Colberg, J. Dammeier, T. Bentz, and M. Olzmann. HCO Formation in the Thermal Unimolecular Decomposition of Glyoxal: Rotational and Weak Collision Effects. *Phys.Chem. Chem. Phys.*, 10:6520–6533, 2008.

[7] R. J. Kee, F. M. Ruply, and J. A. Miller. *Chemkin- II: A Fortran Chemical Kinetics Package for the Analysis of Gas-Phase Chemical Kinetics, Sandia Report SAND89-8009, Sandia National Laboratories, Livermore, California (Sept. 1989).*

[8] G. P. Smith, D. M. Golden, M. Frenklach, N. W. Moriarty, B. Eiteneer, M. Goldenberg, C. T. Bowman, R. Hanson, S. Song, W. C. Gardiner Jr., V. Lissianski, and Z. Qiu. *GRI-Mech Version 3.0*, 1999. http://www.me.berkeley.edu/gri_mech, last accessed: 15.04.2015.

[9] N. Lamoureux, P. Desgroux, A. El Bakali, and J.F. Pauwels. Experimental and numerical study of the role of NCN in prompt-NO formation in low-pressure CH_4-O_2-N_2 and C_2H_2-O_2-N_2 flames. *Combust. Flame*, 157:1929–1941, 2010.

[10] N. Lamoureux, H. El Merhubi, L. Gasnot, C. Schoemaecker, and P. Desgroux. Measurements and modelling of HCN and CN species profiles in laminar $CH_4/O_2/N_2$ low pressure flames using LIF/CRDS techniques. *Proc. Combust. Inst.*, 35:745–752, 2015.

[11] E. Goos, A. Burcat, and B. Ruscic. *Extended Third Millenium Ideal Gas and Condensed Phase Thermochemical Database for Combustion with Updates from Active Thermochemical Tables.* (2009) http://garfield.chem.elte.hu/Burcat/burcat.html, last accessed 10.01.2015.

[12] A. A. Konnov. Detailed reaction mechanism for small hydrocarbons combustion. Release 0.5 (2000, updated 2007).

[13] T. Williams and C. Kelley. gnuplot- An Interactive Plotting Program, Version 3.7. http://www.gnuplot.info/, last accessed 23.04.2015.

[14] Microcal^{TM} Software Inc. Origin^{TM}, Version 8.6. http://originlab.de, last accessed 23.04.2015.

[15] M. J. Frisch, G. W. Trucks, H. B. Schlegel, G. E. Scuseria, M. A. Robb, J. R. Cheeseman, G. Scalmani, V. Barone, B. Mennucci, G. A. Petersson, H. Nakatsuji, M. Caricato, X. Li, H. P. Hratchian, A. F. Izmaylov, J. Bloino, G. Zheng, J. L. Sonnenberg, M. Hada, M. Ehara, K. Toyota, R. Fukuda, J. Hasegawa, M. Ishida, T. Nakajima, Y. Honda, O. Kitao, H. Nakai, T. Vreven, J. A. Montgomery, Jr., J. E. Peralta, F. Ogliaro, M. Bearpark, J. J. Heyd, E. Brothers, K. N. Kudin, V. N. Staroverov, R. Kobayashi, J. Normand, K. Raghavachari, A. Rendell, J. C. Burant, S. S. Iyengar, J. Tomasi, M. Cossi, N. Rega, J. M. Millam, M. Klene, J. E. Knox, J. B. Cross, V. Bakken, C. Adamo, J. Jaramillo, R. Gomperts, R. E. Stratmann, O. Yazyev, A. J. Austin, R. Cammi, C. Pomelli, J. W. Ochterski, R. L. Martin, K. Morokuma, V. G. Zakrzewski, G. A. Voth, P. Salvador, J. J. Dannenberg, S. Dapprich, A. D. Daniels, Ö. Farkas, J. B. Foresman, J. V. Ortiz, J. Cioslowski, and D. J. Fox. Gaussian 09 Revision D.01. Gaussian Inc. Wallingford CT 2009.

[16] J. Dammeier and G. Friedrichs. Thermal Decomposition of NCN$_3$ as a High-Temperature NCN Radical Source: Singlet-Triplet Relaxation and Absorption Cross Section of NCN($^3\Sigma$). *J. Phys. Chem. A*, 114:12963–12971, 2010.

[17] J. Dammeier, B. Oden, and G. Friedrichs. A consistent model for the thermal decomposition of NCN$_3$ and the singlet-triplet relaxation of NCN. *Int. J. Chem. Kinet.*, 45:30–40, 2013.

[18] H. Bock and R. Dammel. The Pyrolysis of Azides in the Gas Phase. *Angew. Chem. Inter. Ed.*, 26:504–526, 1987.

[19] D. J. Benard, C. Linnen, A. Harker, H. H. Michels, J. B. Addison, and R. Ondercin. Dissociation of Cyanogen Azide: An Alternative Route to Synthesis of Carbon Nitride. *J. Phys. Chem. B*, 102:6010–6019, 1998.

[20] D. E. Milligan, M. E. Jacox, and A. M. Bass. Matrix Isolation Study of the Photolysis of Cyanogen Azide. The Infrared and Ultraviolet Spectra of the Free Radical NCN. *J. Chem. Phys.*, 43:3149–3160, 1965.

[21] J. Dammeier. *A Shock Tube Study of NCN and HCO Radical Reactions Related to the NO$_x$ Formation in Combustion Processes.* PhD thesis, Christian-Albrechts-Universität zu Kiel, 2011.

[22] B. Bak, O. Bang, F. Nicolaisen, and O. Rump. Assignment of vibrational frequencies in the infrared and Raman spectra of cyanogen azide. *Spectrochimica Acta, Part A: Molecular and Biomolecular Spectroscopy*, 27:1865–1871, 1971.

[23] G. Socrates. *Infrared and Raman Characteristic Group Frequencies: Tables and Charts.* 3. Auflage, WILEY & SONS, Chichester u. a., 2001, ISBN: 0470093072.

[24] A. Fayt, J. Demaison, G. Wlodarczak, and H. Buerger. Millimetre-wave and Fourier transform infrared spectra between 325 cm^{-1} and 4720 cm^{-1} of BrCN and global rovibrational analysis of the main isotopomers. *Molecular Physics*, 101:675–695, 2003.

[25] M. Hesse, H. Meier, and B. Zeeh. *Spektroskopische Methoden in der organischen Chemie.* Thieme, Mainz, 2005. ISBN: 3-13-576107-X.

4 Direct Measurements of the total rate constant of the reaction NCN + H and implications for the product branching ratio and the enthalpy of formation of NCN

Nancy Faßheber, Johannes Dammeier, and Gernot Friedrichs*

Institute für Physikalische Chemie, Christian-Albrechts-Universität zu Kiel
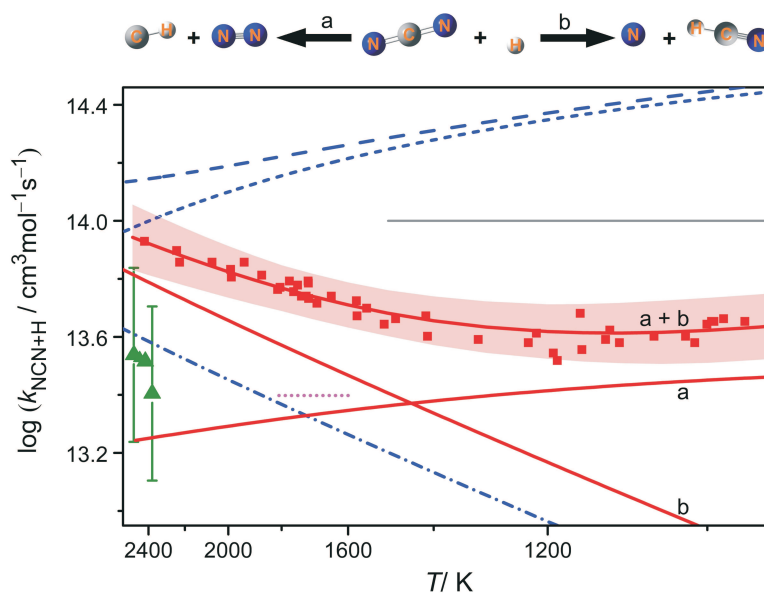
Own contributions:

Prior to dissertation:

- Shock tube experiments.

- Preliminary data analysis.

During the dissertation:

- Complete re-Analysis of the experimental data considering multiple product channels for the reaction NCN + H and new data for C_2H_5I decomposition

- Discussion on product branching ratio and NCN enthalpy of formation.

- Writing of paper draft.

Abstract

The overall rate constant of the reaction (2), NCN + H, which plays a key role in prompt-NO formation in flames, has been directly measured at temperatures 962 K $< T <$ 2425 K behind shock waves. NCN radicals and H atoms were generated by the thermal decomposition of NCN_3 and C_2H_5I, respectively. NCN concentration-time profiles were measured by sensitive narrow-line-width laser absorption at a wavelength of $\lambda = 329.1302$ nm. The obtained rate constants are best represented by the combination of two Arrhenius expressions, $k_2/(cm^3mol^{-1}s^{-1}) = 3.49 \times 10^{14} \exp(-33.3 \, kJ \, mol^{-1}/RT) + 1.07 \times 10^{13} \exp(+10.0 \, kJ \, mol^{-1}/RT)$, with a small uncertainty of $\pm$ 20% at $T =$1600 K and $\pm$ 30% at the upper and lower experimental temperature limits.The two Arrhenius terms basically can be attributed to the contributions of reaction channel (2a) yielding CH + N_2 and channel (2b) yielding HCN + N as the products. A more refined analysis taking into account experimental and theoretical literature data provided a consistent rate constant set for k_{2a}, its reverse reaction k_{1a} (CH + $N_2 \rightarrow$ NCN + H), k_{2b} as well as a value for the controversial enthalpy of formation of NCN, $\Delta_f H^\circ_{298\,K} = 450$ kJ/mol. The analysis verifies the expected strong temperature dependence of the branching fraction $\phi = k_{2b}/k_2$ with reaction channel (2b) dominating at the experimental high-temperature limit. In contrast, reaction (2a) dominates at the low-temperature limit with a possible minor contribution of the HNCN forming recombination channel (2d) at $T <$1150 K.

4.1 Introduction

Nitrogen oxides, NO and NO_2 (NO_x), are major atmospheric pollutants formed by different reaction mechanisms in combustion processes. Especially under fuel rich combustion conditions, the so-called prompt-NO formation pathway becomes significant. According to Fenimore,[1] prompt-NO formation is initiated by the reaction of small hydrocarbon radicals with molecular nitrogen from the combustion air. Although it has been proven both theoretically[2,3,4] and experimentally[5,6] that the key initiation reaction CH + N_2 yields the spin-allowed products H + NCN,

$$CH(^2\Pi) + N_2(^1\Sigma^+) \rightarrow H(^2S) + NCN(^3\Sigma_g^-), \tag{1a}$$

instead of the previously assumed spin-forbidden products N + HCN,

$$CH(^2\Pi) + N_2(^1\Sigma^+) \rightarrow N(^4S) + HCN(^1\Sigma^+), \tag{1b}$$

so far NCN chemistry has only been implemented in two detailed kinetic mechanisms for combustion modeling, namely konnov0-6 and GDFkin3.0_NCN.[7,8] Adopted NCN reaction rate constant parameters are largely based on the theoretical work of the M. C. Lin group who reported rate constant values for the most important bimolecular NCN consumption reactions NCN + H,[2,4] O,[9] OH,[10] and others.[11,12,13] Experimental high-temperature data for NCN reactions are scarce. Next to the early shock

tube detection of NCN and indirect rate constant measurements of the reaction NCN + H performed by Vasudevan et al.,[6] Busch and Olzmann investigated the thermal decomposition of NCN by means of C-ARAS detection behind shock waves.[14,15] All other direct high-temperature measurements are based on work performed in the Kiel shock tube laboratory operated by us. We use the thermal decomposition of cyanogen azide (NCN_3) as a quantitative source of NCN radicals.[16] So far, we were able to report rate constant data for the bimolecular NCN reactions with O, NCN, NO, NO_2, and its unimolecular decomposition $NCN + M \rightarrow C + N_2 + M$.[17,18] The purpose of this paper is to provide the first direct high-temperature measurements of the total rate constant of the reaction NCN + H. At combustion temperatures, the reaction exhibits two main reaction channels:

$$NCN + H \rightarrow CH + N_2, \tag{2a}$$

$$NCN + H \rightarrow HCN + N. \tag{2b}$$

Depending on the reaction conditions, two additional minor reaction channels forming HNC + N and HNCN are accessible (see discussion section 4.4). The rate of reaction (2) and its exact branching ratio turned out to be crucial factors for modeling the fate of NCN in hydrocarbon flames.[7,8,19] On the one hand reaction (2a) constitutes the reverse of the prompt-NO initiation reaction (1a) and can be calculated from k_{1a} via the thermochemical equilibrium constant $K(CH + N_2 \rightleftharpoons NCN + H) = k_{1a}/k_{2a}$. On the other hand the products of reaction (2b) are the same as the products of the formerly assumed spin-forbidden reaction (1b), which brings the new NCN chemistry back to the old Fenimore NO_x formation route.

Reported rate constant values for reaction NCN + H have been included in the Arrhenius diagram shown in Fig. 4.1. An early rate constant estimate of Glarborg et al.[20] assumed reaction (2b) to proceeds with a temperature independent rate constant close to the collisional rate, $k_{2b} = 1 \times 10^{14}$ $cm^3 mol^{-1}s^{-1}$ (upper solid line). Shortly after, the reaction NCN + H has been theoretically analyzed by Moskaleva and Lin.[2] As a side note in their paper on the overall rate constant of the reaction $CH + N_2 \rightarrow NCN + H$, but unfortunately without giving much details on the underlying theoretical model, they reported a pressure independent rate constant expression of $k_{2b} = 1.89 \times 10^{14} \times \exp(-35.3 \text{ kJ/mol}/RT)$ $cm^3 mol^{-1}s^{-1}$ revealing that the reaction takes place over a sizable barrier (lower dash-dotted line). Hence, with $k_{2b} = 1.1 \times 10^{13}$ $cm^3 mol^{-1}s^{-1}$ at $T = 1500$ K, the reaction is one order of magnitude slower than the initial estimate. Experimentally, Vasudevan et al.[6] indirectly determined the rate constant of reaction (2b) in the temperature range of 2378 K $< T < 2492$ K by measuring absorption-time profiles of NCN in ethane/N_2 mixtures behind shock waves (triangles with error bars). Following fast NCN generation by reaction (1a), the observed slow decays of the NCN radical concentration profiles were found to be consistent with k_{2b} values close to the ones reported by Moskaleva and Lin.

In an indirect experimental and numerical study of the role of NCN formation in low pressure flames, Lamoureux et al.[8] reported the value $k_{2b} = 2.5 \times 10^{13}$ $cm^3 mol^{-1}s^{-1}$ (dotted line), which was also adopted for the GDFkin3.0_NCN mechanism. Essentially, this value had been chosen to match the experimentally measured NCN and NO concentration profiles in methane and acetylene flames with peak

flame temperatures of $T = 1600$ K - 1835 K. Therefore, this reported value is highly dependent on the value of the assumed absorption cross section for NCN, which is subject to ongoing discussion.[21] Furthermore, the assumed enthalpy of formation of NCN, here $\Delta_f H^\circ_{298\,K} = 452$ kJ/mol, is a critical quantity as k_{2a} is calculated from k_{1a} via thermochemical equilibrium in their simulations. The crucial role of NCN thermochemistry for modeling prompt-NO formation in flames has been recently highlighted in a paper by Goos et al.[22] They nicely demonstrated that the modeled branching ratio of the overall reaction (2) heavily depends on the assumed enthalpy of formation value for NCN. For example, by switching the enthalpy of formation from the low value $\Delta_f H^\circ_{298\,K} = 444.5$ kJ/mol (representative for theoretical estimates based on single-reference computations)[16,23] to the high value 466.5 kJ/mol (experimental result based on photodissociation experiments)[24] both the simulated NCN peak mole fraction and final NO yield varied by a factor of about 3 for a fuel rich low-pressure CH_4-O_2-N_2 flame. In view of this large variation it becomes clear that also the indirect k_{2b} value of Lamoureux et al. is uncertain.
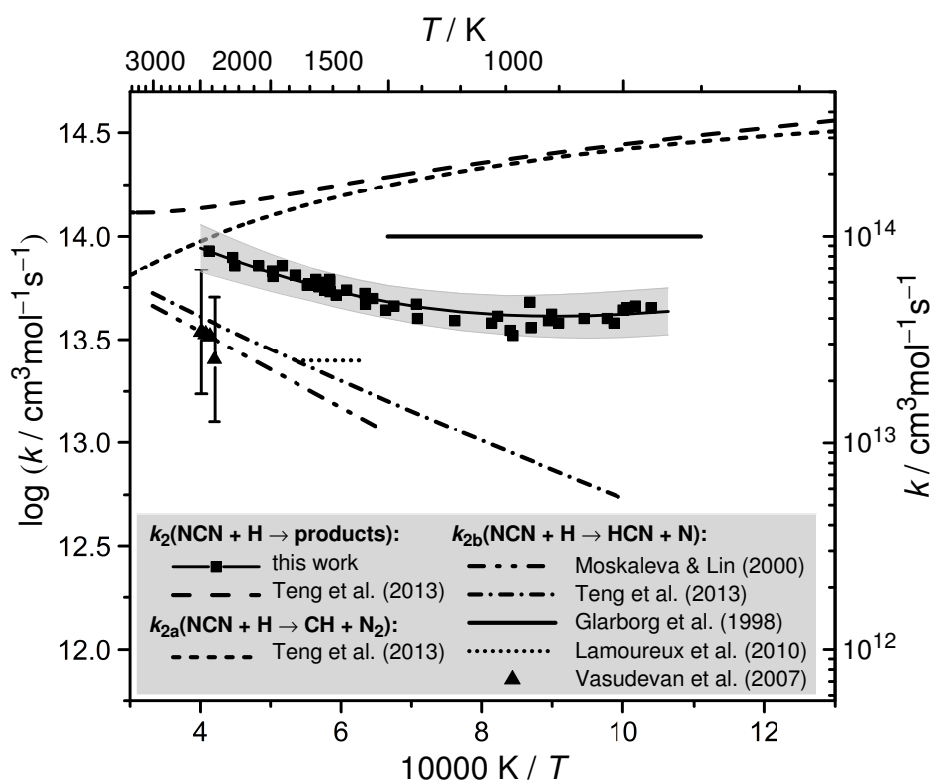
Figure 4.1: Experimental and theoretical literature rate constant data for the reaction NCN + H in comparison with the results of this work. Estimate of Glarborg et al.[20], shock tube data of Vasudevan et. al.[6], flame data of Lamoureux et al.,[8] and theoretical predictions of Teng et al.[4] and Moskaleva and Lin[2] are illustrated as outlined in the legend. The squares depict the experimental data of this work; the shaded area and the thick solid curve correspond to the range of uncertainty and a fit of the experimental data, respectively.

Very recently the M.C. Lin group[4] updated their theoretical prediction of the rate constants of the reactions $CH + N_2$ and NCN + H based on (i) high-level *ab initio* calculation (CCSD(T) with complete basis set limit) of the underlying quartet and doublet potential energy surfaces and (ii) by correct-

ing a previous coding error in a program used in their original paper[2] from the year 2000. Teng et al.[4] clearly showed that reaction (2b) is a spin-allowed process predominantly taking place on a quartet surface, in contrast to reaction (2a) taking place only on a doublet surface. In comparison with their previous work, they now recommend the rate expression $k_{2b} = 4.96 \times 10^{12} \times T^{0.41} \times \exp\left(-22.8 \text{ kJ/mol}/RT\right)$ cm^{3}mol^{-1}s^{-1} yielding 20% to 40% higher k_{2b} values at temperatures from 1500 K to 2000 K (upper dash-dotted line in Fig. 4.1). Another important finding was that an alternative reaction channel yielding HNC + N is minor and that the recombination reaction yielding HNCN, which dominates at room temperature, contributes to less than 5% at combustion relevant temperatures of $T > 1000$ K at 1 bar total pressure. Remarkably high total rate constant values with a shallow minimum of $k_2 \approx 1.3 \times 10^{14}$ cm^{3}mol^{-1}s^{-1} at $T = 3180$ K have been reported in their work as well (long-dashed curve), which we consider unfeasible. As it turns out in this work, the recommendation of Teng et al. for reaction channel (2a) alone is already up to 6 times higher (short-dashed curve) than our experimentally determined total rate constant k_2 (see also Discussion Section 4.4).

From this short overview of existing literature data we conclude that a reliable modeling of NCN chemistry in flames is not possible so far. Clearly, experimental data on the rate constant of the reaction NCN + H are needed to constrain the rate constant uncertainties and to advance current prompt-NO formation models.

4.2 Experimental

4.2.1 Shock tube apparatus

All experiments were carried out in an electropolished stainless steel shock tube with inner diameter of 81 mm. A more detailed description can be found elsewhere.[25] Briefly, hydrogen or mixtures of hydrogen and nitrogen were used as driver gas; diaphragms were made from 80 or 100 μm thick aluminum foil. The experimental conditions behind the incident and reflected shock waves were calculated from pre-shock conditions and the shock wave velocity, which was measured by four fast piezo-electric sensors (PCB Piezotronics M113A21). A frozen-chemistry code was applied taking into account real gas effects and the measured shock wave damping, which was on the order of 1% per meter. Storage gas mixtures of 500-750 ppm NCN$_3$ and 1000 ppm C$_2$H$_5$I in argon were prepared using the partial pressure method and were further diluted with argon using calibrated mass flow controllers (Aera, FC-7700CU). The low pressure section of the shock tube was flushed for about 5 min at $p \approx 30$ mbar to reduce possible adsorption effects on the shock tube wall.

4.2.2 NCN precursor

The thermal decomposition of cyanogen azide (NCN$_3$)

$$\text{NCN}_3 + \text{M} \rightarrow {}^1\text{NCN} + \text{N}_2 + \text{M} \tag{3}$$
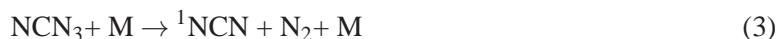
has been used as a quantitative source of NCN radicals.[26,27] It was shown in previous publications[16,28] that the thermal decomposition initially yields NCN in its first electronically excited singlet state. Under the experimental conditions applied in this work with total densities $\rho > 2 \times 10^{-6}$ mol/cm^3 and temperatures $T > 962$ K, the subsequent collision induced intersystem crossing (CIISC) is rate limiting for triplet NCN formation according to

$$^1\text{NCN} + \text{M} \rightarrow {}^3\text{NCN} + \text{M} \tag{4}$$

The CIISC efficiency is strongly dependent on the nature of the collider, reveals a non-linear pressure dependence due to a pressure saturation effect, and increases with increasing temperature.[18,28] In order to accurately model the initial formation rate of ^{3}NCN (denoted NCN in the following), the CIISC rate constant has been allowed to vary within the error limit reported by Dammeier et al.[28]

The highly toxic and explosive precursor molecule NCN$_3$ has been directly synthesized using a procedure described previously.[29,30] Briefly, a small amount of gaseous cyanogen bromide (BrCN, $\sim$20 mbar) was passed into an evacuated 1 L glass flask containing a huge excess of solid sodium azide (NaN$_3$). After a 8 - 10 h reaction time, the gaseous products were analyzed by FTIR spectroscopy. Almost no water and carbon dioxide ($\sim 0.01\%$), which serves as an indicator for a potential gas leak, were present in the reaction samples and the impurities of remaining cyanogen bromide were well below 4%, in some cases $< 0.1\%$. A slow decomposition of about 10% NCN$_3$ per day took place in the storage flask, therefore mixtures were used up within 3 days. Accurate initial NCN$_3$ mole fraction in the actual reaction mixtures were determined by modeling the maximum NCN yield in the experiments and were found to be consistent with the expected NCN$_3$ content in the storage gas mixtures in all cases.

4.2.3 H precursor

Hydrogen atoms were generated by the thermal unimolecular decomposition of ethyl iodide (C$_2$H$_5$I). Under typical experimental conditions behind shock waves, the reaction can be assumed to take place close to the high pressure limit[31] and exhibits two main reaction channels:

$$\text{C}_2\text{H}_5\text{I} \rightarrow \text{C}_2\text{H}_5 + \text{I} \tag{5a}$$

$$\text{C}_2\text{H}_5\text{I} \rightarrow \text{C}_2\text{H}_4 + \text{HI} \tag{5b}$$

H atom formation proceeds through the fast subsequent decomposition of the ethyl radical,

$$\text{C}_2\text{H}_5 + \text{M} \rightarrow \text{C}_2\text{H}_4 + \text{H} + \text{M}. \tag{6}$$

Although ethyl iodide has been widely used as an H atom precursor, until recently the assumed absolute values and temperature dependences of the H atom yield were uncertain and often represented the most significant source of error in such studies. Selected values of reported branching ratios $\phi = k_{5a}/(k_{5a} + k_{5b})$ are collected in Fig. 4.2. The most frequently used value of $\phi = 0.87 \pm 0.11$ is based

on direct H and I atom resonance absorption spectroscopic (ARAS) measurements performed by Kumaran et al.[32] at temperatures of 946 K $< T <$ 1303 K. Also based on ARAS experiments, Herzler and Roth[33] reported a coinciding value, Yamamori et al.[34] used lower values of $\phi < 0.78$ at overall higher temperatures, Miyoshi et al.[35] determined a higher value of $\phi = (0.92 \pm 0.06)$, and Giri et al.[36] assumed $\phi = 1$ by considering the hydrogen forming pathway only. Recently, Weber et al.,[37] Yang and Tranter,[38] and Bentz et al.[39] revisited the ethyl iodide pyrolysis. Whereas Yang and Tranter found excellent agreement with their laser-schlieren densitometry shock tube measurements by assuming $\phi = 0.87$, Weber et al. report a significantly lower value of $\phi = (0.7 \pm 0.1)$ from a mass spectrometric investigation of the flash pyrolysis of ethyl iodide. However, Bentz et al. could show by a combination of H- and I-ARAS measurements and statistical rate calculations that the abstraction reaction $H + C_2H_5I \rightarrow C_2H_5 + HI$, which had been neglected in former studies, needs to be taken into account for an accurate analysis of the branching ratio. Their experimental data, together with other available literature data, have been very recently reanalyzed by Varga et al.[31] in a follow-up publication using a new global optimization method developed by Turányi.[40] The simultaneous optimization of the rate constant expressions of all relevant reactions yielded a considerably temperature dependent branching ratio decreasing from $\phi(T = 962\,\text{K}) = 0.96$ to $\phi(T = 2450\,\text{K}) = 0.71$ over the temperature range of this study. A very low 3σ uncertainty level of ± 0.035 has been specified by Varga et al. at a temperature of $T = 1200$ K. As can be seen in Fig. 4.2 the recommended branching ratios are consistent with most of the previous literature data. We consider these results to be most reliable and therefore adopted the ethyl iodide decomposition mechanism as reported by Varga et al. It is included in the list of reactions in Table 4.1.
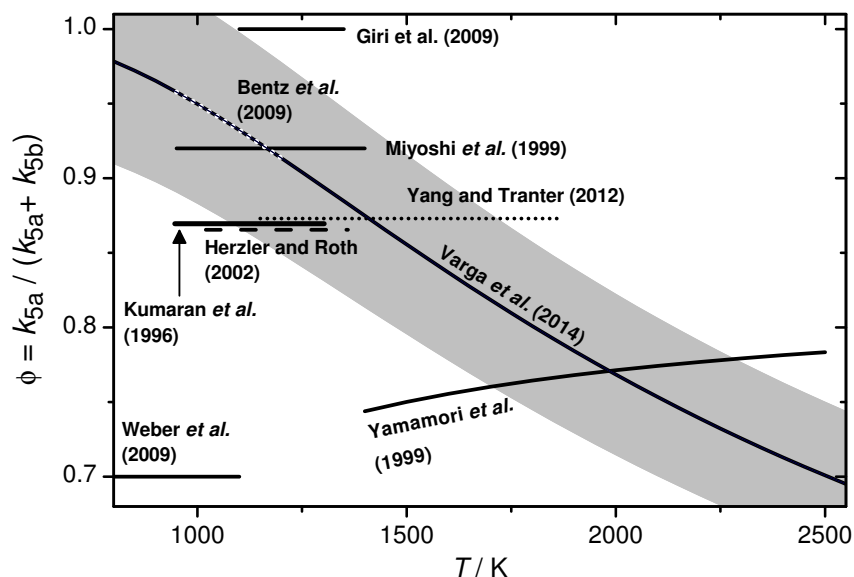
Figure 4.2: Selected literature values for the branching ratio ϕ of the thermal decomposition of ethyl iodide yielding C_2H_5 + I (channel 5a) and C_2H_4 + HI (channel 5b), respectively. H and/or I atom resonance absorption measurements: Kumaran et al.,[32] Yamamori et al.,[34] Miyoshi et al.,[35] Herzler and Roth,[33] Giri et al.,[36] and Bentz et al.;[39] laser schlieren technique: Yang and Tranter;[38] mass spectrometry: Weber et al.;[37] global optimization: Varga et al.[31] The gray area represents the assumed uncertainty range of $\pm 7\%$.

45

We have recommended the use of a different expression with opposite temperature dependence of ϕ in a previous paper dating back to the year 2002.[41] That recommendation was based on a theoretical treatment of the unimolecular decomposition of ethyl iodide with barrier heights taken from the paper of Kumaran et al. Then, the energy barrier E_0 of the I atom forming C-I bond fission channel (5a) was assumed to be about 15 kJ/mol higher than of the HI elimination channel (5b). However, the recent accurate CCSD(T) ab initio data of Bentz et al.[39] showed that both barriers are more or less energetically equal, which is more consistent with the reported decrease of ϕ with increasing temperature. For a more detailed treatment of the unimolecular decomposition reactions of alkyl iodides in the framework of statistical rate theories we refer to the work of Kumaran et al., Miyoshi et al., and Bentz et al.[32,35,39]

Table 4.1: Rate constant parameters for important NCN reactions and the ethyl iodide submechanism. Rate constants are given in terms of $k = A T^n \exp(-E_a/RT)$ in units of cm^3, mol^{-1}, s^{-1} and kJ. The listed rate constants for NCN (representing ^{3}NCN) reactions have been duplicated for ^{1}NCN to approximately take into account ^{1}NCN secondary chemistry. In addition to the reactions listed here, the GRI-Mech 3.0 has been used as base mechanism[42] supplemented by iodine chemistry adopted from our previous work.[41]

No.	Reaction	A	n	E_a	Ref.
3	$NCN_3 \rightleftharpoons {}^1NCN + N_2$	4.9×10^9		71	[28]
4	$^1NCN \rightarrow NCN$	2.0×10^6		31	[28]
2	$NCN + H \rightarrow$ products				see text
2a	$NCN + H \rightleftharpoons CH + N_2$	4.2×10^{15}	-0.69	2.0	this work[b]
2b	$NCN + H \rightleftharpoons HCN + N$	7.9×10^{12}	0.41	22.8	this work[a]
7	$NCN + M \rightleftharpoons C + N_2 + M$	8.9×10^{14}		260	[17]
8	$NCN + NCN \rightleftharpoons CN + CN + N_2$	3.7×10^{12}			[17]
9	$NCN + C \rightleftharpoons CN + CN$	1.0×10^{14}			[17]
10	$NCN + N \rightleftharpoons N_2 + CN$	1.0×10^{13}			[2]
11	$NCN + CN \rightleftharpoons C_2N_2 + N$	1.3×10^{14}		33.5	[2]
11	$NCN + CH \rightleftharpoons HCN + CN$	3.2×10^{13}		-3.6	[2]
13	$NCN + CH_2 \rightleftharpoons H_2CN + CN$	8.0×10^{13}		26.9	[2]
5a	$C_2H_5I \rightleftharpoons C_2H_5 + I$	3.4×10^{13}		203	[31]
5b	$C_2H_5I \rightleftharpoons C_2H_4 + HI$	4.7×10^{13}		226	[31]
6	$C_2H_5 + M \rightleftharpoons C_2H_4 + H + M$	1.0×10^{18}		140	[31]
14	$C_2H_5I + H \rightleftharpoons C_2H_5 + HI$	1.0×10^{15}		21.6	[31]
15	$C_2H_5I + I \rightleftharpoons C_2H_5 + I_2$	4.0×10^{13}		69.9	[43]
16a	$C_2H_5 + H \rightleftharpoons CH_3 + CH_3$	4.2×10^{13}			[44]
16b	$C_2H_5 + H \rightleftharpoons C_2H_4 + H_2$	1.2×10^{12}			[45]
17	$H + HI \rightleftharpoons H_2 + I$	6.6×10^{13}		4.1	[31]

[a] Rate expression of Teng et al.[4] scaled by a factor of 1.6.

[b] Assuming $\Delta_f H^\circ_{298\,K}(NCN) = 450$ kJ/mol; this corresponds to $k_{1a}(CH + N_2 \rightarrow NCN + H) = 2.3 \times10^{10} \times T^{0.53} \times \exp(-71.2\,kJ/mol/RT)$.

4.2.4 NCN detection

Triplet NCN radicals were detected by time-resolved difference amplification laser absorption spectroscopy at $\tilde{\nu} = 30383.11$ cm^{-1} ($\lambda = 329.1302$ nm). The absorption feature at this wavelength mainly

stems from a superposition of the $^3\Pi_1$ sub band of the $\tilde{A}^3\Pi_u(000) - \tilde{X}^3\Sigma_g(000)$ and the Q_1 band head of the $^3\Sigma^+(010) - {}^3\Pi(010)$ transition.[21] About 1 mW UV laser radiation was generated by intra-cavity frequency doubling of a continuous-wave ring-dye laser (Coherent, 899) with DCM-Special as dye pumped with a solid state Nd:YVO$_4$ laser using 8 W at $\lambda = 532$ nm (Coherent Verdi V10). The wavelength of the laser fundamental was measured interferometrically by a wavemeter (MetroLux) with an accuracy of $\Delta\tilde{\upsilon} \approx \pm 0.015$ cm^{-1}. The UV laser beam was split into a detection and a reference beam by a (50:50) beam splitter plate. The detection beam was passed through the shock tube and coupled into an optical fiber (Thorlabs BF H22-550) connected to a balanced photodetector and amplifier (Thorlabs PDB 150A-EC). The intensity of the reference laser beam was fine-tuned by a variable neutral density filter to match the intensity of the detection beam. The resulting difference signals were low-pass-filtered (1.4 MHz), amplified (Ortec Fast Preamp 9305, 18 dB), and stored by an analog input board (Measurement Computing, PCI-DAS4020/12, 20 MHz, 12 bit). The NCN concentration-time profiles were calculated from the detected absorption profiles based on NCN absorption cross sections $\log\left(\sigma(\text{base e})/(\text{cm}^2\text{mol}^{-1})\right) = 8.9 - 8.3 \times 10^{-4} \times T/\text{K}$ previously measured with an accuracy of $\pm$ 25% using the same apparatus at similar temperatures and pressures.[16]

Table 4.2: Experimental conditions and results.

$T/$ K	$\rho \times 10^6/$ mol cm^{-3}	$x(\text{NCN}_3)$ ppm	$x(\text{C}_2\text{H}_5\text{I})$ ppm	$k_2 \times 10^{-13}/$ cm^{3}mol^{-1}s^{-1}	$T/$ K	$\rho \times 10^6/$ mol cm^{-3}	$x(\text{NCN}_3)$ ppm	$x(\text{C}_2\text{H}_5\text{I})$ ppm	$k_2 \times 10^{-13}/$ cm^{3}mol^{-1}s^{-1}
1186	3.78	7.4	75	3.3	962	3.52	3.8	185	4.5
1714	3.43	19.0	72	6.1	1000	3.57	4.0	185	4.4
1720	3.43	21.0	72	5.5	1192	3.77	4.6	185	3.5
1813	3.46	21.8	72	5.8	1230	3.80	5.2	185	3.8
1870	3.46	22.8	72	6.5	1552	4.03	9.5	185	5.0
1936	4.20	9.0	76	7.2	1747	3.44	27.5	184	6.0
1991	3.51	27.8	72	6.8					
2070	3.54	23.5	72	7.2	1482	3.99	5.0	299	4.6
2227	3.57	25.0	72	7.2	1509	4.01	3.0	104	4.4
2242	3.55	26.0	72	7.9	1578	3.37	24.5	712	5.3
2425	2.89	28.0	72	8.5	1714	3.41	23.7	40	6.2
					1774	3.31	31.0	363	6.2
996	3.56	7.0	138	4.5	1988	2.11	11.9	155	6.4
1013	3.59	4.6	137	3.8					
1023	3.60	6.9	138	4.0	983	7.10	7.0	138	4.6
1101	3.69	3.2	137	3.8	993	7.13	6.5	138	4.5
1113	3.70	5.3	138	4.2	1059	7.25	5.8	138	4.0
1151	3.73	8.5	136	3.6	1119	7.41	6.4	138	3.9
1217	3.80	12.5	138	4.1	1153	7.48	6.5	138	4.8
1314	3.88	4.0	137	3.9	1646	7.19	4.0	185	5.5
1413	3.95	6.3	136	4.0	1760	7.43	7.4	138	5.7
1416	3.94	4.6	137	4.7	1805	7.50	3.9	137	5.9
1576	4.05	6.3	136	4.7					
1688	3.41	16.4	131	5.2	1713	14.7	5.0	138	5.4
					1735	14.8	5.0	138	5.5

4.3 Results

The reaction of NCN radicals with hydrogen atoms has been investigated behind incident and reflected shock waves in the temperature and pressure ranges 962 K $< T <$ 2425 K and 290 mbar $< p <$ 2130 mbar, respectively, at three different total densities of $\rho \approx 3.5 \times 10^{-6}$, 7.4×10^{-6}, and 1.5×10^{-5} mol/cm^3. Reaction gas mixtures contained 72-363 ppm ethyl iodide and 3-31 ppm NCN$_3$ in argon. In most cases, a large excess of ethyl iodide with $[C_2H_5I]_0/[NCN_3]_0$ ratios up to 60 was applied, hence the hydrogen atom was used as the excess species. Experimental conditions are listed in Table 4.2.
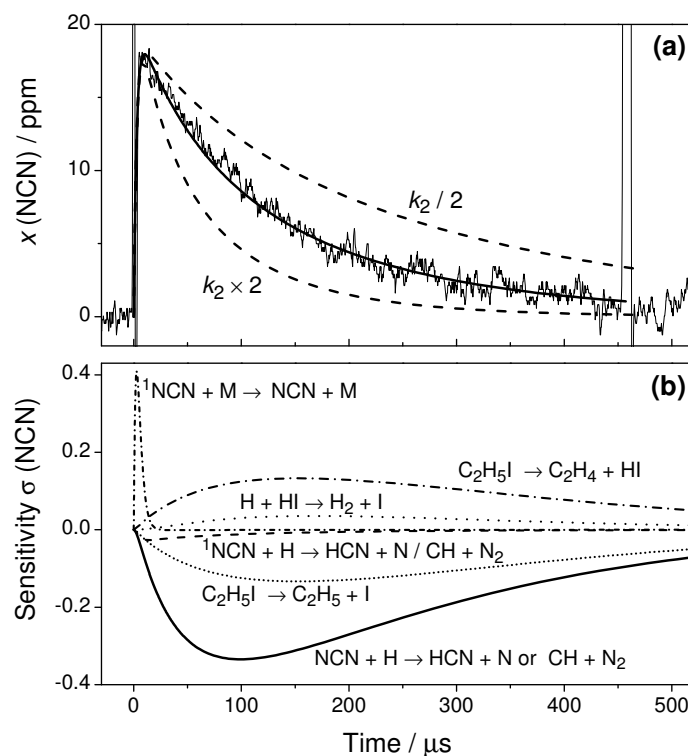
Figure 4.3: (a) Experimental NCN profile in comparison with numerical simulations. $T = 1720$ K, $\rho = 3.43 \times 10^{-6}$ mol/cm^3, $p = 490$ mbar, $x(NCN_3) = 21$ ppm, $x(C_2H_5I) = 72$ ppm, $k_2 = 5.5 \times 10^{13}$ cm^{3}mol^{-1}s^{-1}. (b) Sensitivity analysis.

Fig. 4.3a illustrates a typical experiment behind the incident shock wave at a temperature $T = 1720$ K and a total density $\rho = 3.43 \times 10^{-6}$ mol/cm^3 with initial mole fractions of $x(NCN_3) = 21$ ppm and $x(C_2H_5I) = 72$ ppm. After the arrival of the incident shock wave, the NCN signal increases within 20 μs. Obviously, both the thermal decomposition of NCN$_3$ and the singlet-triplet relaxation of NCN are fast. The subsequent NCN decay is well resolved and is more or less complete at the end of the experimental time window set by the Schlieren signal of the reflected shock wave at $t = 460$ μs.

In order to extract rate constants for reaction (2), NCN + H $\rightarrow$ products, the NCN profiles were numerically simulated using the CHEMKIN-II package.[46] The GRI-Mech 3.0 was used as a base mechanism[42] supplemented by an iodine submechanism adopted from our previous work[41] and the reactions outlined in Table 4.1. The mechanism for NCN secondary chemistry was assembled from

literature data, in particular from our previous measurements that have been validated to reproduce NCN concentration-time profiles of pure NCN_3/argon mixtures over a wide range of experimental conditions. The ethyl iodide decomposition has been modeled by including the recently optimized submechanism reported by Varga et al.[31] (vide supra). In order to identify potential contributions of [1]NCN secondary chemistry, all triplet NCN reactions have been duplicated for singlet NCN. Although this treatment neglects the presumably different [1]NCN reactivity, it can be safely assumed that [1]NCN secondary chemistry is dominated by its relaxation reaction forming triplet NCN within the first few μs of the experiments. Thermodynamic data were taken from Burcat's thermodynamic database[47] with updated NASA polynomial parameters for NCN from Goos et al.[22] Note that the assumed value for the enthalpy of formation of NCN, although of utmost importance for the discussion of the branching ratio of reaction (2) (vide infra), is not important for the determination of the total rate constant from the experimental profiles.

The solid curve in Fig. 4.3a reflects the best fit of the data using k_2 as an adjustable parameter. Two additional simulations using k_2 varied by a factor of two (dashed curves) are shown as well. They deviate strongly from the experimental profile demonstrating the high sensitivity of reaction (2). Assuming either the products of reaction channel (2a), $CH + N_2$, or reaction channel (2b), $HCN + N$, did not change the extracted k_2 value within error limits. The high sensitivity of reaction (2) is further outlined in the sensitivity analysis shown in Fig. 4.3b. Here, the sensitivity coefficient $\sigma(i,t)$ for reaction i at time t was normalized with respect to the maximum concentration $[NCN]_{max}$ over the time history, $\sigma(i,t) = 1/[NCN]_{max} \times (\partial[NCN]/\partial \ln k_i)$. For the analysis, a branching ratio of $\phi = k_{2b}/k_2 = 0.5$ has been assumed. Following the initial increase of the signal, which is determined by the NCN relaxation reaction (4), reaction (2) dominates the NCN decay. The relatively high sensitivity coefficients for reactions (5a) and (5b) directly reflect the influence of the branching ratio of reaction (5) and hence the assumed H atom yield from ethyl iodide pyrolysis. Presuming that this branching ratio is accurate, the sensitivity analysis reveals that the rate constant of reaction (2) could be directly measured under nearly pseudo first-order conditions.

Whereas the highest feasible experimental temperature was limited by the increasingly fast thermal decomposition of NCN, towards lower temperatures non-NCN secondary chemistry becomes significant as well. This is illustrated by the $T = 1150$ K experiment and sensitivity analysis shown in Fig. 4.4. Both reaction (14), $H + C_2H_5I$, and the assumed products of reaction (2) become important. Assuming the products of channel (2a), $HCN + N$, at longer reaction times the reaction $N + NCN$ significantly consumes NCN. Similarly, assuming the products of channel (2b), $CH + N_2$, the reaction $C + NCN$ gains importance. Here, C atoms are efficiently generated by the reaction $CH + H \rightarrow C + H_2$. Consistent with the expected diminishing role of the activation controlled channel (2b), somewhat better agreement with the experiment is obtained by assuming channel (2a). However, as the remaining differences between simulation and experiment could not be clearly attributed to a specific secondary reaction, no attempt was made to further improve the simulation at longer reaction times. Instead, the rate of reaction (2) was extracted from the NCN decay by fitting the transient at short reaction times where secondary chemistry did not yet exert a significant influence.

All measured rate constants k_2 are listed in Table 4.2 and are shown in Arrhenius form in Fig. 4.5.
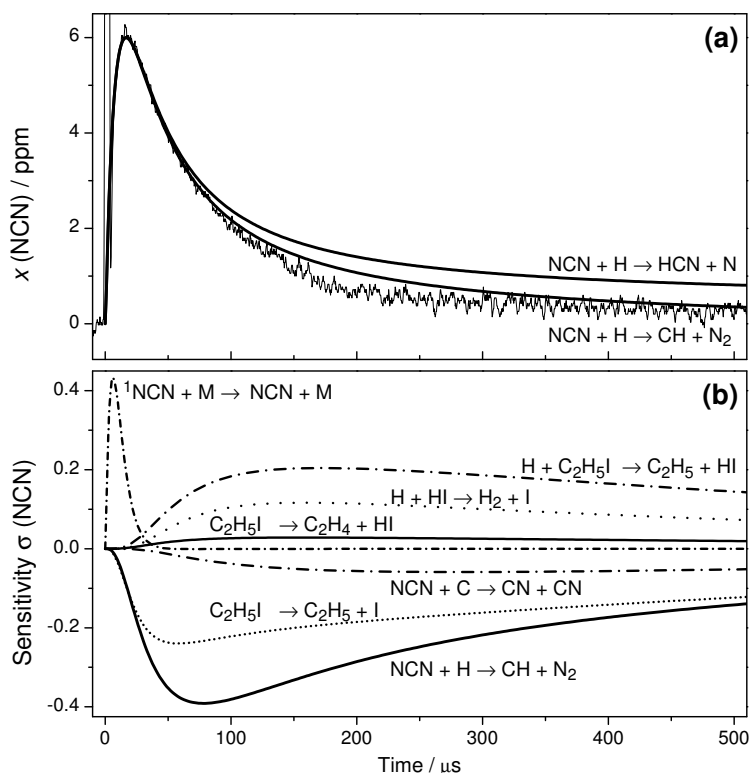
Figure 4.4: (a) Experimental NCN profile in comparison with numerical simulations. $T = 1150$ K, $\rho = 7.48 \times 10^{-6}$ mol/cm^3, $p = 720$ mbar, $x(NCN_3) = 6.5$ ppm, $x(C_2H_5I) = 138$ ppm, $k_2 = 4.8 \times 10^{13}$ cm^{3}mol^{-1}s^{-1}. (b) Sensitivity analysis.
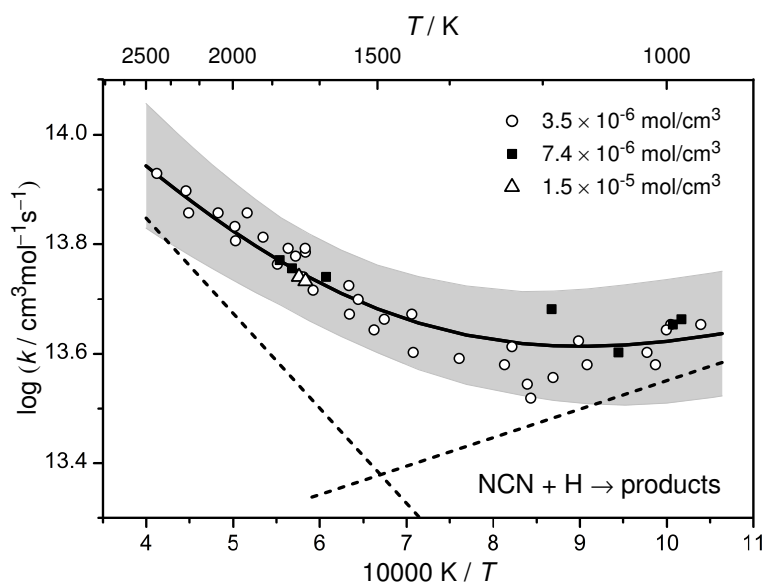
Figure 4.5: Arrhenius plot for k_2 measured at three different total densities. The solid curve corresponds to a fit of the data using a sum of two Arrhenius expressions (dashed lines). The gray area represents the uncertainty range based on a comprehensive error analysis.

50

Overall, the rate constants follow the same trend independent of total density (varied by a factor of 4) and mixture composition (varied within $1.7 < [C_2H_5I]_0/[NCN_3]_0 < 60$). The data reveal a shallow minimum at temperatures around 1050-1200 K indicating that at least two reaction channels are active, presumably channels (2a) and (2b) with (2b) becoming more important towards higher temperatures. Accordingly, in the temperature range $962\ \mathrm{K} < T < 2425\ \mathrm{K}$ the total rate constant can be best represented by the sum of two Arrhenius expressions,

$$k_2/(\mathrm{cm^3mol^{-1}s^{-1}}) =$$
$$3.49 \times 10^{14} \exp(-33.3\ \mathrm{kJ\ mol^{-1}}/RT) +$$
$$1.07 \times 10^{13} \exp(+10.0\ \mathrm{kJ\ mol^{-1}}/RT), \qquad \mathrm{(I)}$$

depicted as the solid curve in Fig. 4.5. The two single Arrhenius terms are also shown as dashed lines and can be roughly interpreted to represent the contributions of channel (2b) (first term) and channel (2a) (second term). A more refined analysis of the overall rate constant will be presented below.

An error analysis has to take into account uncertainties resulting from the scatter of the data ($\pm 6\%$), the mixture composition (in particular the initial ethyl iodide mole fraction, $\pm 3\%$), the channel branching ratio of the ethyl iodide decomposition (estimated from Fig. 4.2 to be $\pm 7\%$), the NCN absorption cross section ($\pm 25\%$, resulting in a 3% uncertainty in k_2), and the secondary chemistry. In the middle of the investigated temperature range ($T \approx 1600\ \mathrm{K}$), a direct pseudo first-order evaluation was possible and hence errors from secondary chemistry are minor. Nevertheless, we allow for a 10% error due to a possibly large uncertainty of the rate constant of the reaction (10), NCN + N, which has not been directly measured so far. Increasing its rate constant from $1 \times 10^{13}\ \mathrm{cm^3mol^{-1}\ s^{-1}}$ to 1×10^{14} $\mathrm{cm^3mol^{-1}\ s^{-1}}$ would make this reaction sensitive because N atoms are formed in reaction (2b) and hence slightly too high k_2 values would have been determined by our analysis. Taking into account partial error compensation, we estimate the overall uncertainty of k_2 to be $\pm 20\%$ at $T = 1600\ \mathrm{K}$, increasing to $\pm 30\%$ due to higher uncertainties resulting from secondary chemistry and the employed ethyl iodide branching ratio at the high and low temperature limit of the experiments. A corresponding uncertainty range is indicated by the gray shaded area in Fig. 4.5.

4.4 Discussion

The obtained total rate constant expression for k_2 is compared with selected literature values and further analyzed in order to derive a consistent set of rate constants for the two main high-temperature reaction channels (2a) and (2b) as well as the NCN enthalpy of formation $\Delta_f H^\circ_{298\ \mathrm{K}}$ (ΔH in the following) in Fig. 4.6. As it was shown by the high level *ab initio* calculations of Teng et al.,[4] from the four feasible reaction channels
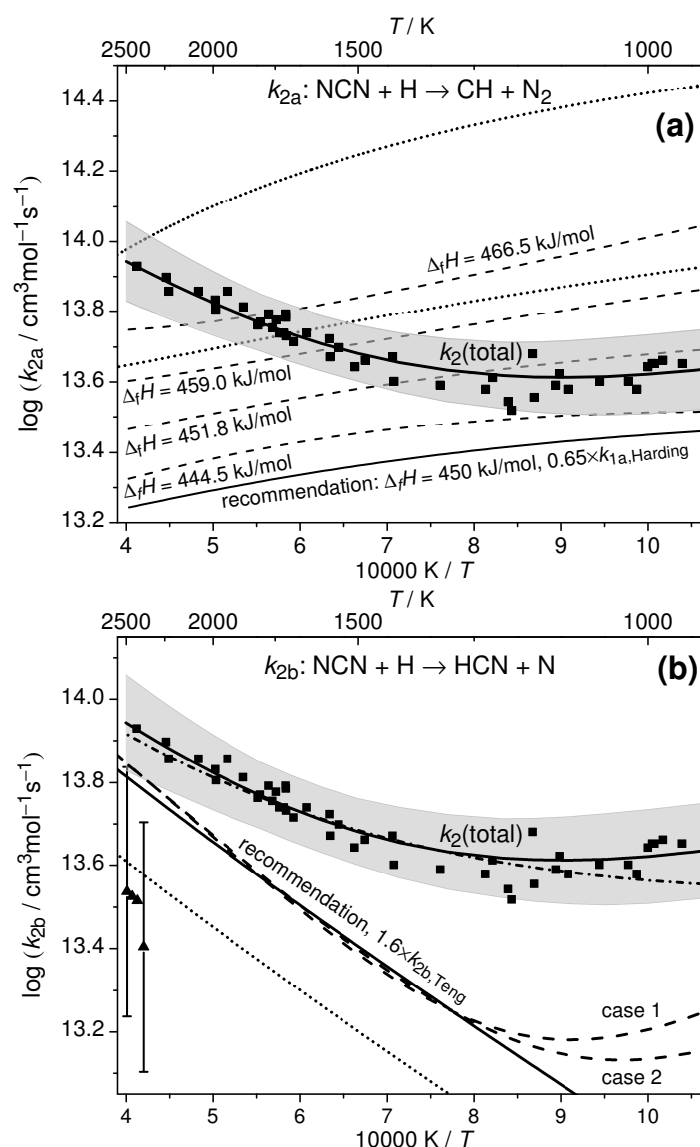
Figure 4.6: Analysis of total rate constant data in terms of $\Delta_f H^\circ_{298\ K}$(NCN) ($\Delta H$ in the following). The squares, the corresponding solid curves, and the shaded areas reflect the experimental data for k_2 of this work and their uncertainty limits. *Upper plot a*: Analysis with respect to channel (2a). The upper dotted curve depicts the original expression for k_{2a} adopted from Teng et al.,[4] the lower dotted curve a re-evaluation of their data using $\Delta H = 458$ kJ/mol. The dashed curves reflect $k_{2a} = k_{1a}/K$ with k_{1a} from Harding et al.[3] derived for different ΔH values using Eq. (II). For the lower solid curve, Eq. (II) was scaled by a factor of 0.65. *Lower plot b*: Analysis with respect to channel (2b). Triangles with error bars and the dotted line reflect the experimental and theoretical data reported by Vasudevan et al.[6] and Teng et al.,[4] respectively. The dashed curves depict $k_{2b} = k_2 - k_{2a}$ expressions obtained from the k_2 values of this work and k_{2a} derived from Harding et al.; case 1: $k_2 \times 1.0$, $k_{1a} \times 1.0$, $\Delta H = 440$ kJ/mol; case 2: $k_2 \times 1.0$, $k_{1a} \times 0.65$, $\Delta H = 450$ kJ/mol. The lower solid curve reflects the recommended k_{2b} expression, which is equal to the Teng et al.[4] expression scaled by a factor of 1.6. The dash-dotted curve corresponds to $k_2 = k_{2a} + k_{2b}$ using the two recommended rate expressions.

$$^3\text{NCN} + {}^2\text{H} \rightarrow {}^2\text{CH} + {}^1\text{N}_2, \tag{2a}$$

$$^1\text{HCN} + {}^4\text{N}, \tag{2b}$$

$$^1\text{HNC} + {}^4\text{N}, \tag{2c}$$

$$^2\text{HNCN}, \tag{2d}$$
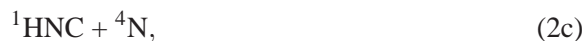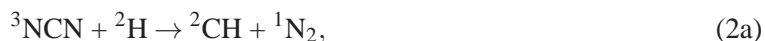
reaction channel (2c) yielding HNC + N exhibits high activation barriers and does not play a role. The recombination channel (2d), which dominates at room temperature and very high pressures, becomes less important with increasing temperature and can be expected to be of minor importance at combustion relevant temperatures $T > 1000$ K as well. At a typical total pressure of $p = 0.5$ bar used in this work, the theoretical predictions of Teng et al.[4] range channel (2d) to contribute about 1.2% at 1000 K and 3.8% at $T = 800$ K to the overall reaction. Due to the inconsistencies in that paper (vide infra) these number should be interpreted with caution, however, the order of magnitude reveals that this channel starts to play a role at the lowest experimental temperatures of this study. Nevertheless, as a good starting point, we limit our analysis of the k_2 data to channels (2a) and (2b) in the following. Regarding the potential energy surface for reaction (2) from Teng et al.,[4] channel (2a) proceeds on the doublet surface over the formation of an HNCN complex and is supposed to have a slightly negative temperature dependence. In contrast, channel (2b) exhibits a small activation barrier and predominantly proceeds on a quartet surface. The kinetic calculations also reveal that both reaction channels are important at combustion temperatures.

Analysis method a: In Fig. 4.6a, the upper dotted curve depicts the calculated rate expression for k_{2a} from Teng et al.[4] The very high rate constant values for k_{2a} as well as the very high total rate constants k_2 (dashed curve included in Fig. 4.1) are unreasonable. Compared to our experimentally determined *total* rate constant values, the expression yields up to 6 times higher rate constants for channel (2a) already. Moreover, there seems to be an inconsistency in the reported rate constants for the equilibrium $\text{CH} + \text{N}_2 \rightleftharpoons \text{NCN} + \text{H}$ in the paper of Teng et al. Using their values for the rate constant of the forward reaction (1a) and their preferred value for the enthalpy of formation, $\Delta H = 458$ kJ/mol, we calculate reverse rate constants k_{2b}. Thermodynamic data for CH, N_2, H, and NCN were taken from Burcat's database[47] with updated heat capacity data for NCN from Goos et al.,[22] where 7-term NASA polynomial parameter a_6 has been scaled to adjust $\Delta H(\text{NCN})$. Obtained k_{2b} values are 2-3 times lower than reported by Teng et al. (lower dotted curve in Fig. 4.6a). Another indication that the reported rate constants may be flawed comes from the reported total rate constant values; for example, the recommended room temperature value $k_2 \approx 7 \times 10^{14}$ cm^{3}mol^{-1}s^{-1} is higher than the Lennard-Jones collision limit of $k_{\text{LJ}} \approx (3.5 - 5.5) \times 10^{14}$ cm^{3}mol^{-1}s^{-1}, which can be estimated based on the Lennard-Jones parameters reported in the literature (parameters for H:[48,49,50] $\sigma = (2.00 - 3.26)$ Å and $\varepsilon/k_\text{B} = (2.7 - 145)$ K; parameters for NCN:[48] $\sigma = 3.83$ Å and $\varepsilon/k_\text{B} = 232$ K).

To the best of our knowledge, no other experimental or theoretical values for k_{2a} have been reported explicitly in the literature yet. Therefore, we continue our analysis by calculating k_{2a} values form the

reverse reaction k_{1a}, which has been thoroughly studied both experimentally and theoretically. For an overview of available literature data we refer to the work of Harding et al.[3] who performed high-level *ab initio* and transition state theory calculations on the reaction $CH + N_2$ using multi-reference electronic structure methods. Using their recommended value of the enthalpy of formation, $\Delta H = 459$ kJ/mol, the theoretical prediction was found to be in quantitative agreement with the most recent shock tube data of Vasudevan et al.[6] over the temperature range 2100 K $< T <$ 3350 K. At these high temperatures, the predicted rate constant is less dependent on the assumed value of ΔH. Towards lower temperatures and in the practically important temperature range of 1000 – 2000 K, however, an accurate enthalpy of formation is crucial. In an Arrhenius plot, Harding et al.[3] present their results of temperature dependent calculations of the rate constant of reaction (1a) assuming different values for the enthalpy of formation of NCN (Fig. 13 in their paper). For example, it was shown that changing ΔH by ± 8 kJ/mol yields a factor of 1.6 higher (-8 kJ/mol) or 1.9 lower ($+8$ kJ/mol) k_{1a} value at $T = 1000$ K. In order to take this pronounced thermodynamic effect into account in our analysis and to derive rate constant estimates for $k_{2a} = k_{1a}/K$ as function of the assumed NCN enthalpy of formation, we reparameterized the original data of Harding et al. and used the expression

$$k_{1a}/(\text{cm}^3\text{mol}^{-1}\text{s}^{-1}) = e^{(274.5-0.556x)} \times (T/\text{K})^{(-31.24+0.0706x)} \times e^{(-71.2 \text{ kJ mol}^{-1}/RT)} \quad \text{(II)}$$

with $x = \Delta_f H^{\circ}_{298 \text{ K}}(\text{NCN})$ in kJ/mol. Eq. (II) provides a stable fit of the rate constant data of Harding et al. and yields a reasonable extrapolation to somewhat higher and lower $\Delta_f H^{\circ}_{298 \text{ K}}(\text{NCN})$ values. Representative literature values of the enthalpy of formation span the range from 444.5 kJ/mol (single-reference computations)[16,23] to 459 kJ/mol (high-level basis set extrapolation or multi-reference computations)[3,4] for theoretical and from 451.8 kJ/mol (electron affinity of NCN)[51] to 466.5 kJ/mol (NCN photodissociation)[24] for experimental literature data. The resulting k_{2a} expressions are shown as dashed curves in Fig. 4.6a. They reveal a weak and negative temperature dependence of the reaction NCN + H $\rightarrow$ CH + N_2 with the absolute rate constant values basically offset by the assumed enthalpy of formation of NCN. Clearly, the higher enthalpies of formation yield unfeasible k_{2a} values that are up to a factor of 2.4 higher than the total rate constant measured in this work. Assuming that *(i)* the branching fraction $k_{2a}/k_2 = 1$ around $T = 1000$ K, *(ii)* k_{1a} from Harding et al. is correct, and *(iii)* k_2 is at the upper limit of the uncertainty range of our experimental data (+30%), an upper limit of $\Delta H < 454$ kJ/mol can be estimated from this analysis.

Analysis method b: A second analysis of our data focusing on the rate constant of channel (2b) is shown in Fig. 4.6b. The indirect experimental data of Vasudevan et al.[6] (triangles with error bars) and the most recent theoretical estimate of Teng et al.[4] (dotted curve) are shown as well. In the light of the negative temperature dependence of channel (2a) it becomes clear that the experimentally determined positive temperature dependence of k_2 towards higher temperatures arises from the increasingly dominant activation controlled channel (2b). Moreover, the high temperature activation energy $E_a = 33$ kJ/mol estimated from the two channel fit of our experimental data (see Fig. 4.5 and Eq. (I)) is in

very good agreement with the theoretically predicted activation energies of 35 kJ/mol and 28 kJ/mol reported by the M.C. Lin group[2,4] (see Figs. 4.1 and 4.6b). Hence, we consider the activation energy of reaction channel (2b) a well-constrained quantity with a preferred value of $E_a \approx 28$ kJ/mol adopted from the most recent *ab initio* study.[4] Having the temperature dependence of k_{2b} fixed, it is possible to arrive at a consistent value for the enthalpy of formation. Here, ΔH has been choosen in a way such that the rate constant expression for $k_{2b} = k_2 - k_{2a}$, with k_2 values taken from Eq. (I) of this work and k_{2a} values calculated via thermodynamic equilibrium from the k_{1a} expression Eq. (II), yields a temperature dependence that is consistent with 28 kJ/mol. A matrix of appropriate enthalpy of formations with k_2 and k_{1a} varied within their uncertainty limits is given in Table 4.3. Here, uncertainties of $k_2 \pm 30\%$ as obtained in this work and $k_{1a} \pm 35\%$ as reported for the experimental shock tube results of Vasudevan et al.[6] (which are in turn consistent with the k_{1a} expression of Harding et al.) have been assumed. Table 4.3 reveals a large range of possible enthalpy of formations, 423 kJ/mol $< \Delta H < 456$ kJ/mol. Nevertheless, two conclusions can be drawn from this analysis. First, increasing k_{1a} yields unfeasible enthalpy values that are even well below the results of the single-reference computations (about 444.5 kJ/mol), which can be regarded a reasonable lower limit for ΔH. Even with k_{1a} unchanged, the highest value of 445 kJ/mol would be close to this limit. Secondly, the upper limit of 456 kJ/mol, corresponding to a scenario with $k_2 + 30\%$ and $k_{1a} - 35\%$, is in agreement with the upper limit of 454 kJ/mol inferred from analysis method a. Therefore, the high experimental value of Bise et al.[24] (466.5 ± 2.9 kJ/mol), the results of the high-level basis set extrapolation and multi-reference computations (about 459 kJ/mol),[3,4] and the most recent recommendation of the Active Thermochemical Tables as cited in Goos et al.[22] (457.8 ± 2) are hardly compatible with this work.

Resulting k_{2b} expressions are illustrated in Fig. 4.6b for two selected cases. Case 1, assuming that both k_2 and k_{1a} exhibit values as given by Eqs. (I) and (II), yields $\Delta H = 440$ kJ/mol. Case 2, assuming k_2 from Eq. (I) and k_{1a} from Eq. (II) scaled by a factor of 0.65, yields $\Delta H = 450$ kJ/mol. For all other cases outlined in Table 4.3, similar k_{2b} curves have been obtained, of course somewhat offset for different assumed k_{1a} values (not shown). It is obvious from Fig. 4.6b that the calculated k_{2b} expressions deviate from linearity at temperatures below 1250 K. With decreasing temperatures and hence a decreasing contribution of k_{2b} the analysis procedure gets less reliable, hence, part of this deviation may be attributed to inaccuracies of the analysis method itself. However, it may also indicate the onset of the low temperature reaction channel (2d), which has been neglected in the analysis. In this sense, the increase of k_{2b} at low temperatures would simply arise from the neglected contributions of this channel.

Table 4.3: Feasible values of $\Delta_f H^\circ_{298\,K}(NCN)$ for different combinations of k_{1a} and k_2 values. The reported enthalpy values in kJ/mol yield activation energies $E_{a,2a} \approx 28$ kJ/mol for reaction channel (2a) that are consistent with the corresponding theoretical estimate of Teng et al.[4]

$\Delta_f H^\circ_{298\,K}(NCN)$	$k_2 + 30\%$	k_2	$k_2 - 30\%$
$k_{1a} + 35\%$	436	430	423
k_{1a}	445	440	432
$k_{1a} - 35\%$	456	450	443

Overall, relying on the direct k_2 determination of this work, an enthalpy value of 450 kJ/mol is most

consistent with both the enthalpy limits set by the single-reference computations and our analysis, $444.5 \, \text{kJ/mol} < \Delta_f H^\circ_{298 \, \text{K}}(\text{NCN}) < 454 \, \text{kJ/mol}$, the experimental and theoretical values for k_{1a} from Vasudevan et al.[6] and Harding et al.,[3] the activation energy of reaction channel (2b) reported by Teng et al.,[4] and the indirect shock tube measurements for k_{2b} from Vasudevan et al.[6] This enthalpy value is also in very good agreement with the experimental electron affinity measurements of Clifford et al.[51] ($451.8 \pm 16.7 \, \text{kJ/mol}$) that has been, for example, used in the GDFkin3.0_NCN flame modeling mechanism as well.[8]

Using $\Delta H = 450 \, \text{kJ/mol}$, the recommended rate constant expressions for k_{1a}, k_{2a}, and k_{2b} are as follows: Compatible with the lower experimental uncertainty limit of Vasudevan et al., k_{1a} is set to 0.65 times the values of Harding et al. (Eq. (II)):

$$k_{1a}/(\text{cm}^3\text{mol}^{-1}\text{s}^{-1}) = 2.3 \times 10^{10} \times (T/\text{K})^{0.53} \times \exp\left(-71.2 \, \text{kJ/mol}/RT\right)$$

Using the updated NASA polynomial parameters for NCN from Goos et al.[22] (scaled to $\Delta H = 450 \, \text{kJ/mol}$), this corresponds to a reverse reaction rate constant k_{2a} of

$$k_{2a}/(\text{cm}^3\text{mol}^{-1}\text{s}^{-1}) = 4.2 \times 10^{15} \times (T/\text{K})^{-0.69} \times \exp\left(-2.0 \, \text{kJ/mol}/RT\right)$$

Adopting the temperature dependence of Teng et al., their rate expression is recommended for k_{2b} adjusted by a factor of 1.6 to fit the case 2 data in Fig. 4.6b:

$$k_{2b}/(\text{cm}^3\text{mol}^{-1}\text{s}^{-1}) = 7.94 \times 10^{12} \times (T/\text{K})^{0.41} \times \exp\left(-22.8 \, \text{kJ/mol}/RT\right)$$

This expression is also compatible with the upper limit of the indirect shock tube measurements of Vasudevan et al.[6]

Finally, the sum of k_{2a} and k_{2b} is shown in Fig. 4.6b as dash-dotted curve. It is in close agreement with the k_2 rate expression given by Eq. (I), except at the lowest temperatures where channel k_{2d} presumably starts to play a role. The recommended rate expression for k_{2b} corresponds to a branching ratio $\phi = k_{2b}/k_2$ that increases from $\phi = 0.21$ at $T = 1000 \, \text{K}$ to $\phi = 0.74$ at $T = 2500 \, \text{K}$. Hence, in the temperature range relevant for flame modeling, channel switching between channel (2a) dominating at low temperatures and channel (2b) dominating at high temperatures takes place.

4.5 Concluding Remarks

The overall rate constant of the reaction NCN + H has been directly measured at temperatures between 962 K and 2425 K behind shock waves using the thermal decomposition of NCN_3 and $\text{C}_2\text{H}_5\text{I}$ as suitable precursors for NCN radicals and H atoms, respectively. A conservative error analysis revealed that comparatively narrow error limits of $\pm 20\%$ at $T = 1600 \, \text{K}$, increasing to $\pm 30\%$ at the upper and lower temperature limits of the measurements, could be achieved. A main error arises from the possibly large uncertainty of the potentially important secondary reaction (10), NCN + N, which has not been measured yet. If the theoretical estimate of Moskaleva and Lin[2] turns out to be right,

the influence of reaction (10) would be very small and the error estimate could be further reduced. The second most important uncertainty is related to the assumed overall H atom yield from C_2H_5I decomposition. However, relying on the very recently published global analysis data on the ethyl iodide composition by Varga et al.,[31] this error contribution could be safely assumed to be not more than 7% (an error estimate of 3.5% at $T = 1200$ K has been stated in the original paper).

The high reliability of the rate constant data enabled us to analyze the k_2 data in terms of branching ratio and the crucial value of the enthalpy of formation of NCN. Taking into account experimental and theoretical literature data for the rate constant of reaction (1a) and the temperature dependence of reaction channel (2b), $\Delta_f H^\circ_{298K} = 450$ kJ/mol was found to be most consistent. With a robust upper limit of $\Delta_f H^\circ_{298K} < 456$ kJ/mol derived from the k_2 values of this work, significantly higher literature values – about 459 kJ/mol from high-level *ab initio* calculations[3,4] and 466.5 kJ/mol from NCN photodissociation experiments[24] – are at odds with our analysis. Clearly, more work is needed to further constrain the uncertainty of the enthalpy of formation of NCN.

Modeling of NO_x formation in flames critically depends on the branching ratio of the reaction NCN + H. Whereas channel (2a) constitutes the reverse reaction of the main prompt-NO formation reaction (1a), CH + N_2, it is in particular reaction channel (2b) with the products HCN + N that brings the overall reaction forward on the prompt-NO pathway. The results of this study with branching fractions $\phi = k_{2b}/k_2$ increasing from $\phi(T = 1000$ K$) = 0.21$ to $\phi(T = 2500$ K$) = 0.74$ verifies the expected strong temperature dependence of this quantity. However, again the actual value of the derived branching ratio strongly depends on the assumed value of the enthalpy of formation of NCN. In fact, accurate measurements of the branching ratio would be very useful to constrain the enthalpy of formation of NCN. Moreover, in conjunction with the already compiled theoretical and experimental rate constant data, accurate branching fractions would help to draw final conclusions on this reaction system including the contributions of the recombination channel (2d), which may play a role even at temperatures as high as 1000 K.

Acknowledgments

References

[1] C. P. Fenimore. Formation of nitric oxide in premixed hydrocarbon flames. *Proc. Combust. Inst.*, 13:373–380, 1971.

[2] L. V. Moskaleva and M. C. Lin. The spin-conserved reaction CH + $N_2 \longrightarrow$ H + NCN: A major pathway to prompt NO studied by quantum/statistical theory calculations and kinetic modeling of rate constant. *Proc. Combust. Inst.*, 28:2393–2401, 2000.

[3] L. B. Harding, S. J. Klippenstein, and J. A. Miller. Kinetics of CH + N_2 Revisited with Multireference Methods. *J. Phys. Chem. A*, 112:522–532, 2008,.

[4] W.-S. Teng, L. V. Moskaleva, H.L. Chen, and M. C. Lin. Ab Initio Chemical Kinetics for H + NCN: Prediction of NCN Heat of Formation and Reaction Product Branching via Doublet and Quartet Surfaces. *J. Phys. Chem. A*, 117:5775–5784, 2013.

[5] G. P. Smith. Evidence of NCN as a flame intermediate for prompt NO. *Chem. Phys. Lett.*, 367:541–548, 2003.

[6] V. Vasudevan, R. K. Hanson, C. T. Bowman, D. M. Golden, and D. F. Davidson. Shock Tube Study of the Reaction of CH with N_2: Overall Rate and Branching Ratio. *J. Phys. Chem. A*, 111:11818–11830, 2007.

[7] A. A. Konnov. Implementation of the NCN pathway of prompt-NO formation in the detailed reaction mechanism. *Combust. Flame*, 156:2093–2105, 2009.

[8] N. Lamoureux, P. Desgroux, A. El Bakali, and J.F. Pauwels. Experimental and numerical study of the role of NCN in prompt-NO formation in low-pressure CH_4-O_2-N_2 and C_2H_2-O_2-N_2 flames. *Combust. Flame*, 157:1929–1941, 2010.

[9] R. S. Zhu and M. C. Lin. Ab Initio Study on the Oxidation of NCN by O (^{3}P): Prediction of the Total Rate Constant and Product Branching Ratios. *J. Phys. Chem. A*, 111:6766–6771, 2007.

[10] R. S. Zhu, Hue M. T. Nguyen, and M. C. Lin. Ab Initio Study on the Oxidation of NCN by OH: Prediction of the Individual and Total Rate Constants. *J. Phys. Chem. A*, 113:298–304, 2009.

[11] R. S. Zhu and M. C. Lin. Ab Initio Study of the Oxidation of NCN by O_2. *Int. J. Chem. Kinet.*, 37:593– 598, 2005.

[12] C.-L. Huang, S. Y. Tseng, T. Y. Wang, N. S. Wang, Z. F. Xu, and M. C. Lin. Reaction mechanism and kinetics of the NCN+NO reaction: Comparison of theory and experiment. *J. Chem. Phys.*, 122:184321, 2005.

[13] T.-J. Yang, N. S. Wang, L. C. Lee, Z. F. Xu, and M. C. Lin. Kinetics and Mechanism of the NCN + NO_2 Reaction Studied by Experiment and Theory. *J. Phys. Chem. A*, 112:10185–10192, 2008.

[14] A. Busch. *Stoßwellenuntersuchungen zum Zerfall stickstoffhaltiger Verbindungen mit spektroskopischen Methoden.* PhD thesis, Karlsruher Institut für Technologie KIT, 2010.

[15] A. Busch and M. Olzmann. Shock-Tube Study of the Thermal Decomposition of NCN. *Proc. Eur. Combust. Meeting*, Paper P810138, Vienna, Austria, 2009.

[16] J. Dammeier and G. Friedrichs. Thermal Decomposition of NCN_3 as a High-Temperature NCN Radical Source: Singlet-Triplet Relaxation and Absorption Cross Section of NCN($^3\Sigma$). *J. Phys. Chem. A*, 114:12963–12971, 2010.

[17] J. Dammeier, N. Faßheber, and G. Friedrichs. Direct measurements of the high temperature rate constants of the reactions NCN + O, NCN + NCN, and NCN + M. *Phys. Chem. Chem. Phys.*, 14:1030–1037, 2012.

[18] J. Dammeier and G. Friedrichs. Direct Measurements of the Rate Constants of the Reactions NCN + NO and NCN + NO_2 Behind Shock Waves. *J. Phys. Chem. A*, 115:14382–14390, 2011.

[19] J. F. Sutton, B. A. Williams, and J. W. Fleming. Investigation of NCN and prompt-NO formation in low-pressure C1-C4 alkane flames. *Combust. Flame*, 159:562–576, 2012.

[20] P. Glarborg, M. U. Alzueta, K. Dam-Johansen, and J. A. Miller. Kinetic Modeling of Hydrocarbon/Nitric Oxide Interactions in a Flow Reactor. *Combust. Flame*, 115:1–27, 1998.

[21] N. Lamoureux, C. M. Western, X. Mercier, and P. Desgroux. Reinvestigation of the spectroscopy of the $A^3\Pi_u$- $X^3\Sigma_g^-$ transition of the NCN radical at high temperature: Application to quantitative NCN measurement in flames. *Combust. Flame*, 160:755–765, 2013.

[22] E. Goos, C. Sickfeld, F. Mauß, L. Siedel, B. Ruscic, A. Burcat, and T. Zeuch. Prompt NO formation in flames: The influence of NCN thermochemistry. *Proc. Combust. Inst.*, 34:657–666, 2013.

[23] S. Canneaux, A. Wallet, M. Ribaucour, and F. Lousi. A theoretical study of the NCN ($^3\sigma^-$) biradical thermochemical properties: Implications for combustion chemistry. *Computational and Theoretical Chemistry*, 967:67–74, 2011.

[24] R. T. Bise, A. A. Hoops, and D. M. Neumark. Photodissociation and photoisomerisation pathways of the HNCN free radical. *J. Chem.Phys.*, 114:9000– 9011, 2001.

[25] M. Colberg and G. Friedrichs. Room Temperature and Shock Tube Study of the Reaction HCO + O_2 Using the Photolysis of Glyoxal as an Efficient HCO Source. *J. Phys. Chem. A*, 110:160–170, 2006.

[26] H. Bock and R. Dammel. The Pyrolysis of Azides in the Gas Phase. *Angew. Chem. Inter. Ed.*, 26:504–526, 1987.

[27] D. J. Benard, C. Linnen, A. Harker, H. H. Michels, J. B. Addison, and R. Ondercin. Dissociation of Cyanogen Azide: An Alternative Route to Synthesis of Carbon Nitride. *J. Phys. Chem. B*, 102:6010–6019, 1998.

[28] J. Dammeier, B. Oden, and G. Friedrichs. A consistent model for the thermal decomposition of NCN_3 and the singlet-triplet relaxation of NCN. *Int. J. Chem. Kinet.*, 45:30–40, 2013.

[29] D. E. Milligan, M. E. Jacox, and A. M. Bass. Matrix Isolation Study of the Photolysis of Cyanogen Azide. The Infrared and Ultraviolet Spectra of the Free Radical NCN. *J. Chem. Phys.*, 43:3149–3160, 1965.

[30] J. Dammeier. *A Shock Tube Study of NCN and HCO Radical Reactions Related to the NO_x Formation in Combustion Processes*. PhD thesis, Christian-Albrechts-Universität zu Kiel, 2011.

[31] T. Varga, I. G. Zsely, T. Turanyi, T. Bentz, and M. Olzmann. Kinetic Analysis of Ethyl Iodide Pyrolysis Based on Shock Tube Measurements. *Int. J. Chem. Kinet.*, 46:295–304, 2014.

[32] S. S. Kumaran, M.-C. Su, K. P. Lim, and J. V. Michael. The thermal decomposition of C_2H_5I. *Proc. Combust. Inst.*, 26:605–611, 1996.

[33] J. Herzler and P. Roth. Shock tube study of the reaction of H atoms with $SnCl_4$. *Phys.Chem. Chem. Phys.*, 4:5259–5264, 2002.

[34] Y. Yamamori, K. Takahashi, and T. Inomata. Shock- Tube Studies on the Reaktion of CF_2 (X^1A_1) with O (^3P) and H Atoms. *J. Phys. Chem. A*, 103:8803–8811, 1999.

[35] A. Miyoshi, N. Yamauchi, K. Kosaka, and M. Koshi. Two-channel thermal unimolecular decomposition of alkyl iodides. *J. Phys. Chem. A*, 103:46–53, 1999.

[36] B. R. Giri, T. Bentz, H. Hippler, and M. Olzmann. Shock-tube study on the reactions of hydrogen atoms with benzene and phenyl radicals. *Z. Phys. Chem.*, 223:539–549, 2009.

[37] K. H. Weber, J. M. Lemieux, and J. S. Zhang. Flash pyrolysis of ethyl, n-propyl, and isopropyl iodides as monitored by supersonic expansion vacuum ultraviolet photoionisation time-of-flight mass spectrometry. *J. Phys. Chem. A*, 113:583–591, 2009.

[38] X. Yang and R. S. Tranter. High-Temperature Dissociation of Ethyl Radicals and Ethyl Iodide. *Int. J. Chem. Kinet.*, 44:433–443, 2012.

[39] T. Bentz, M. Szõri, B. Viskolcz, and M. Olzmann. Pyrolysis of Ethyl Iodide as Hydrogen Atom Source: Kinetics and Mechanism in the Temperature Range 950-1200 K. *Z. Phys. Chem.*, 225:1117–1128, 2011.

[40] T. Turányi, T. Nagy, G. Zsély, M. Cserháti, T. Varga, B. T. Szabó, I. Sedyó, P. T. Kiss, and H. J. Curran A. Zempléni. Determination of rate parameters based on both direct and indirect measurements. *Int. J. Chem. Kinet.*, 44:284–302, 2012.

[41] G. Friedrichs, D. F. Davidson, and R. K. Hanson. Direct Measurements of the Reaction H + $CH_2O \longrightarrow H_2$ + HCO Behind Shock Waves by Means of Vis-UV Detection of Formaldehyde. *Int. J. Chem. Kinet.*, 34:374– 386, 2002.

[42] G. P. Smith, D. M. Golden, M. Frenklach, N. W. Moriarty, B. Eiteneer, M. Goldenberg, C. T. Bowman, R. Hanson, S. Song, W. C. Gardiner Jr., V. Lissianski, and Z. Qiu. *GRI-Mech Version 3.0*, 1999. http://www.me.berkeley.edu/gri_mech, last accessed: 15.04.2015.

[43] C. K. Westbrook. Inhibition of Hydrocarbon Oxidation in laminar Flames and Detonations by halogenated Compounds. *Proc. Combust. Inst.*, 19:127– 141, 1982.

[44] D. L. Baulch, C. T. Bowmann, C. J. Cobos, R. A. Cox, Th. Just, J. A. Kerr, M. J. Pilling, D. Stocker, J. Troe, W. Tsang, R. W. Walker, and J. Warnatz. Evaluated kinetic data for combusion modelling. Supplement II. *J. Phys. Chem. Ref. Data*, 34:757–1397, 2005.

[45] P. Camilleri, R. M. Marshall, and H. Purnell. Reaction of hydrogen atoms with ethane. *Journal of the Chemical Society*, 70:1434–1444, 1974.

[46] R. J. Kee, F. M. Ruply, and J. A. Miller. *Chemkin- II: A Fortran Chemical Kinetics Package for the Analysis of Gas-Phase Chemical Kinetics, Sandia Report SAND89-8009, Sandia National Laboratories, Livermore, California (Sept. 1989).*

[47] E. Goos, A. Burcat, and B. Ruscic. *Extended Third Millenium Ideal Gas and Condensed Phase Thermochemical Database for Combustion with Updates from Active Thermochemical Tables.* (2009) http://garfield.chem.elte.hu/Burcat/burcat.html, last accessed 10.01.2015.

[48] R. J. Kee, F. M. Rupley, J. A. Miller, M. E. Coltrin, J. F. Grcar, E. Meeks, H. K. Moffat, A. E. Lutz, G. Dixon-Lewis, M. D. Smooke, J. Warnatz, G. H. Evans, R. S. Larson, R. E. Mitchell, L. R. Petzold, W. C. Reynolds, M. Caracotsios, W. E. Stewart, P. Glarborg, C. Wang, and Ola Adigun. Chemkin collection (transport database). *Reaction Design, Inc.*, Release 3.6:San Diego, CA (2000).

[49] M. Freindorf, Y. Shao, T. R. Furlani, and J. Kong. Lennard-jones parameters for the combined QM/MM method using the B3LYP/6-31G*/AMBER potential. *J. Comput. Chem.*, 26:1270–1278, 2005.

[50] A. W. Jasper and J. A. Miller. Lennard-Jones parameters for combustion and chemical kinetics modeling from full-dimensional intermolecular potentials. *Combust. Flame*, 161:101–110, 2014.

[51] E. P. Clifford, P. G. Wenthold, W. C. Lineberger, G. A. Petersson, and G. B. Ellison. Photoelectron Spectroscopy of the NCN⁻ and HNCN⁻ Ions. *J. Phys. Chem. A*, 101:4338– 4345, 1997.

5 The rate constant of the reaction NCN + H$_2$ and its impact on NCN and NO concentrations in low pressure CH$_4$/O$_2$/N$_2$-flames

Nancy Faßheber,^{a} Nathalie Lamoureux^{b*} and Gernot Friedrichs^{a*}

^{a} *Institut für Physikalische Chemie, Christian-Albrechts-Universität zu Kiel, Max-Eyth-Str. 1, 24118 Kiel, Germany*
^{b} *Laboratoire PC2A, UMR8522 CNRS/Université Lille 1, 59655 Villeneuve d'Ascq, France*
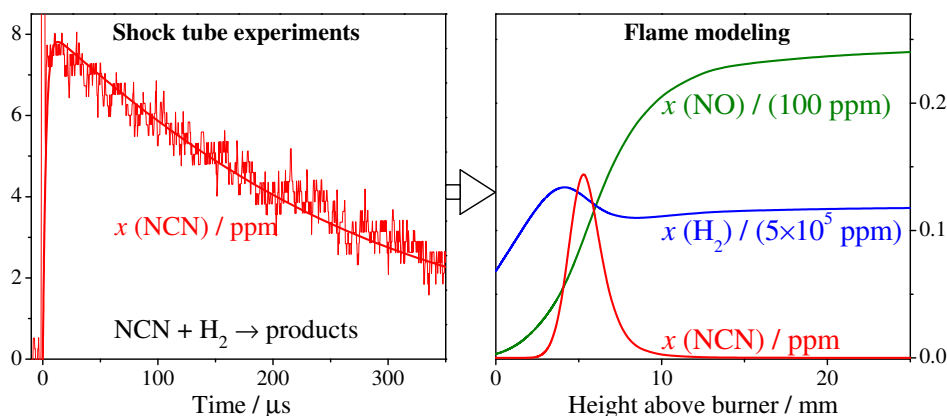
Own contributions:

Prior to dissertation:

- Shock tube experiments.

- Preliminary data analysis.

During the dissertation:

- Shock tube experiments at higher pressures to clarify the pressure dependence of the reaction.

- Discussion on the products considering the pressure independence of the reaction.

- Quantum chemical calculations for NCN + H$_2$ → HNCN + H.

- Collaboration with modeling group (N. Lamoureux, Université Lille 1) to implement the reaction NCN + H$_2$ into the GDFkin3.0_NCN mechanism.

- Writing of paper draft.

Abstract

Bimolecular reactions of the NCN radical play a key role for modeling prompt-NO formation in hydrocarbon flames. The rate constant of the so far neglected reaction NCN + H$_2$ has been experimentally determined behind shock waves under pseudo-first order conditions with H$_2$ as the excess component. NCN$_3$ thermal decomposition has been used as a quantitative high temperature source of NCN radicals, which have been sensitively detected by difference UV laser absorption spectroscopy at $\tilde{v} = 30383.11$ cm^{-1}. The experiments were performed at two different total densities of $\rho \approx 4.1 \times 10^{-6}$ mol/cm^3 and $\rho \approx 7.4 \times 10^{-6}$ mol/cm^3 (corresponding to pressures between $p = 324$ mbar and $p = 1665$ mbar) and revealed a pressure independent reaction. In the temperature range 1057 K $< T <$ 2475 K, the overall rate constant can be represented by the Arrhenius expression $k / \left(\text{cm}^3\text{mol}^{-1}\text{s}^{-1}\right) = 4.1 \times 10^{13}\exp\left(-101 \text{ kJ/mol}/RT\right)$ ($\Delta\log k = \pm 0.11$). The pressure independent reaction as well as the measured activation energy is consistent with a dominating H abstracting reaction channel yielding the products HNCN + H. The reaction NCN + H$_2$ has been implemented together with a set of reactions for subsequent HNCN and HNC chemistry into the detailed GDFkin3.0_NCN mechanism for NO$_x$ flame modeling. Two fuel-rich low-pressure CH$_4$/O$_2$/N$_2$-flames served as examples to quantify the impact of the additional chemical pathways. Although the overall NCN consumption by H$_2$ remains small, significant differences have been observed for NO yields with the updated mechanism. A detailed flux analysis revealed that HNC, mainly arising from HCN/HNC isomerization, plays a decisive role and enhances NO formation through a new HNC $\rightarrow$ HNCO $\rightarrow$ NH$_2$ $\rightarrow$ NH $\rightarrow$ NO pathway.

5.1 Introduction

Nitrogen oxides (NO$_x$) are atmospheric pollutants formed as byproducts in combustion processes. Especially under fuel rich conditions, NO is favorably formed over the so called prompt-NO pathway, which is initiated by the reaction of small hydrocarbon radicals with molecular nitrogen from the combustion air. According to the traditional Fenimore mechanism,[1] it has been assumed for a long time that prompt-NO formation is mainly initiated by the reaction

$$CH(^2\Pi) + N_2(^1\Sigma^+) \rightarrow N(^4S) + HCN(^1\Sigma^+). \tag{1a}$$

Even though the formation of the products N + HCN is spin-forbidden and despite of the fact that theoretical estimates[2,3] for the rate constant k_{1a} turned out to be inconsistent with the experimentally determined high temperature rate constants for the overall CH + N$_2$ reaction,[4,5] reaction (1a) is still used in some flame modeling studies. Already in the year 2000, based on quantum-chemical and RRKM calculations, Moskaleva et al.[6] suggested the alternative spin-conserved reaction channel

$$CH(^2\Pi) + N_2(^1\Sigma^+) \rightarrow H(^2S) + NCN(^3\Sigma_g^-) \tag{1b}$$

and predicted NCN + H to be the main product of the reaction. In the meantime it has been experimentally proven that NCN radicals are in fact formed in flames[7,8,9] and that NCN is the main product of the reaction CH + N$_2$.[10] Consequently, flame mechanisms for NO modeling have been updated with regard to NCN high temperature chemistry. Current versions of NCN submechanisms are the Konnov0.6[11] and the GDFkin3.0_NCN[12,13] mechanism. The performance of the latter has been extensively validated and improved over the last years by quantitative measurements and modeling of CH, NO and NCN concentration profiles in low-pressure CH$_4$/O$_2$/N$_2$ and C$_2$H$_2$/O$_2$/N$_2$ flames of various fuel/air equivalent ratios.[12,14] Recently, corresponding NCO, CN and HCN profiles have been measured as well.[13] Whereas early versions of NCN submechanisms relied on rate constant estimates of Glarborg et al.,[15] the more recent implementations are based on extensive rate constant data from the theoretical work performed in the M.C. Lin group. They reported RRKM and TST studies for the most important bimolecular NCN reactions NCN + O$_2$,[16] O,[17] OH[18] and H[19] as well as for the NCN forming reaction CH + N$_2$.[6,19] From the experimental point of view, most direct rate constant measurements of NCN reactions have been accomplished over the past few years in the shock tube laboratory of the authors (N.F. and G.F.). Beside our studies on NCN + O, H, M, NCN, NO, and NO$_2$,[20,21,22] only two other shock tube studies have been performed. Vasudevan et al.[10] measured NCN absorption profiles during the pyrolysis of ethane/N$_2$ mixtures and Busch et al.[23,24] investigated the unimolecular decomposition reaction NCN + M → C + N$_2$ + M by C atom resonance absorption spectroscopy (ARAS). Ongoing work of one of the authors (N.L.) is concerned with the implementation, testing, and validation of the expanding - even though not yet complete - experimental database on NCN chemistry for flame modeling. Here, in order to assess the potential influence of the reaction NCN + H$_2$ on NO$_x$ flame modeling, we rely on the GDFkin3.0_NCN submechanism as a well-validated starting point.

Surprisingly, despite of rather high H$_2$ concentrations in the flame front, the title reaction

$$NCN + H_2 \rightarrow products \tag{2}$$

has not yet been implemented into flame mechanisms. Seemingly it was considered to be rather slow and therefore dispensable. However, neither experimental nor theoretical studies have been performed so far to confirm or falsify this assumption. In contrast, the rather slow NCN + O$_2$ reaction is included both in the Konnov0.6 and the GDFkin3.0_NCN mechanisms. Starting from early and too high rate constant estimates,[15] this reaction was initially believed to be crucial for NCN modeling,[25] but later theoretical calculations of Zhu and Lin[16] clearly showed that the reaction is activation controlled, slow, and therefore plays a less important role for NO$_x$ formation in flames. As it turns out below, the rate constant of the reaction NCN + H$_2$ is about two orders of magnitude higher than for NCN + O$_2$. Therefore, an accurate rate constant determination and a thorough analysis of its impact for NO$_x$

modeling as reported in this work is overdue.

5.2 Experimental

The used shock tube apparatus has been described in more detail elsewhere.[26] Briefly, the experiments have been performed in an overall 8.3 m long stainless steel shock tube with a 4.4 m long electropolished test section that could be evacuated to pressures of $p \approx 10^{-7}$ mbar by a combination of an oil-free turbo-molecular drag and a diaphragm pump. The test section and the driver section were separated by aluminum membranes of 30, 80 or 100 μm thickness. Hydrogen or hydrogen/ nitrogen gas mixtures have been used as driver gas. The experimental conditions behind the incident and reflected shock waves were calculated from pre-shock conditions and the shock wave velocity, which was measured by four fast piezoelectronic sensors (PCB Piezotronics M113A21), by using a frozen-chemistry code.

Storage gas mixtures of 500 ppm to 1000 ppm NCN$_3$ in argon were prepared using the partial pressure method. The reaction mixtures were prepared using calibrated mass flow controllers (Aera, FC-7700CU; 10, 50, and 1000 sccm). Pure H$_2$ (Air Liquide, $\geq$ 99.999%) and the NCN$_3$ mixtures were further diluted with argon (Air Liquide, $\geq$ 99.999%) in a flow system and were passed into the test section of the shock tube. The section was flushed with the test gas mixture for about 5 min to minimize possible gas adsorption effects on the shock tube walls. High H$_2$ mole fractions up to 9.6% were necessary in the reaction gas mixtures to achieve a fast NCN consumption due to reaction (2). At such high mole fractions, vibrational relaxation effects may compromise a simple frozen-chemistry calculation of the experimental conditions. Equilibration of the Boltzman population of H$_2$ in its v = 0 and v = 1 vibrational states may cause a noticeable, gradual decrease of the temperature behind the shock wave. However, on the one hand the vibrational relaxation time of H$_2$ in argon is known to be rather short, about 9 μs at $p = 700$ bar and $T = 1750$ K,[27] and hence close to the time resolution of the experiments. On the other hand, due to the high vibrational quanta of H$_2$, the fraction of H$_2$ in the v = 1 state and with it the overall temperature effect remains small. At a typical experimental temperature of $T = 1750$ K, the ratio H$_2$(v = 1)/H$_2$(v = 0) = 0.03. Calculation of shock wave conditions assuming fully and non-relaxed H$_2$ showed that even at the highest experimental temperatures and H$_2$ concentrations used in this work, the maximum expected temperature effect was $\Delta T < 5$ K. This is within the 1% uncertainty of the temperature calculation from the shock wave velocity. Consequently, due to the fast relaxation and the overall small temperature effect, it could be safely assumed that H$_2$ relaxation did not interfere with the rate constant measurements.

5.2.1 NCN precursor

It has been shown by Dammeier et al.[28,29] that the thermal decomposition of cyanogen azide (NCN$_3$) serves as a quantitative source of NCN radicals. NCN$_3$ thermal decomposition yields NCN in its first electronically excited singlet state, which is rapidly converted to the triplet ground state by collision induced intersystem crossing (CIISC).

Table 5.1: Arrhenius parameters for the rate constants of all included NCN reactions as used for simulating the experimental NCN profiles behind shock waves. $k_i = AT^n \exp[-E_a/RT]$, given in units of cm^3, mol^{-1}, s^{-1} and kJ. Except for reactions (3) and (4), all reactions have been duplicated for ^1NCN to take ^1NCN chemistry approximately into account. In addition to the listed reactions, the GDFkin3.0 mechanism[12] was used as a background mechanism.

No.	Reaction	A	n	E_a	Ref.
2	NCN + H_2 → products	4.1×10^{13}		101	this work
3	NCN_3 → ^1NCN + N_2	4.9×10^9		71	$\rho = 3 \times 10^{-6}$ mol/cm^3, 29
		7.5×10^9		71	$\rho = 6 \times 10^{-6}$ mol/cm^3, 29
4	^1NCN → NCN	2.0×10^6		31	$\rho = 3.5 \times 10^{-6}$ mol/cm^3, 29
5a	NCN + H → HCN+N	7.94×10^{12}	0.41	22.8	22
5b	NCN + H → CH+N_2	4.2×10^{15}	−0.69	2.0	22
6	NCN + M ⇌ C + N_2+ M	8.9×10^{14}		260	21
7	NCN + NCN ⇌ CN + CN + N_2	3.7×10^{12}			21
8	NCN + C ⇌ CN + CN	1.0×10^{14}			21
9	NCN + N ⇌ N_2 + CN	1.0×10^{13}			6
10	NCN + CN ⇌ C_2N_2 + N	1.25×10^{14}		33.5	6
11	NCN + H ⇌ HNCN	2.98×10^{18}	−9.28	27	760 torr, 19

$$NCN_3 + M \rightarrow {}^1NCN + N_2 + M \qquad (3)$$

$$^1NCN + M \rightarrow {}^3NCN + M \qquad (4)$$

Rate constants for reaction (3) and (4) have been adopted from previous work and are listed in Table 5.1. As it is known that the CIISC process (4) strongly depends on the collision partner and hence reaction mixture composition, its rate constant was allowed to vary within the error limits reported in Ref. 29.

The extremely explosive and toxic precursor NCN_3 cannot be purified by freeze-pump cycles. It has therefore been synthesized directly in high purity in the gas phase, according to $BrCN(g) + NaN_3(s) \rightarrow NCN_3(g) + NaBr(s)$, using a method described in detail in Ref. 22. After an 8 h reaction time the remaining BrCN impurities were usually < 3% according to FTIR analysis. The pure NCN_3 was diluted in argon and was used within three days since NCN_3 tends to slowly form solid polymers. The actual initial NCN_3 concentrations in the reaction gas mixtures were determined from the NCN absorption signal plateaus behind the incident shock waves (for experiments behind the reflected shock wave) or by fitting the maximum of the NCN concentration profile (for experiments behind the incident shock wave). In all cases, the determined concentration was consistent with the concentration calculated from the expected NCN_3 mole fraction in the storage gas mixture.

5.2.2 NCN detection scheme

The narrow-bandwidth laser absorption setup for time-resolved radical detection behind shock waves has been described in detail elsewhere.[22] Briefly, about 1 mW of UV radiation was generated by

intra-cavity frequency doubling of a frequency-stabilized continuous-wave ring-dye laser (Coherent 899) operated with DCM-Special as dye and pumped using 8 W at $\lambda = 532$ nm from a Nd:YVO$_4$ solid state laser (Coherent Verdi V10). The UV laser beam was split into a detection and a reference beam by a 50:50 beam splitter plate. The detection beam was focused, passed the shock tube through two quartz windows, and was coupled into an optical fiber connected to a balance photo-detector and amplifier (Thorlabs PDB 150A-EC). The reference beam intensity could be precisely adjusted by a variable neutral density filter to match the intensity of the detection beam. The resulting difference signal (ΔI) and the monitor signal of the detection beam (I_0) were stored by an analog input board (Measurement Computing PCI-DAS4020/12, 12 bit, 20 MHz) for further data processing.

Triplet NCN has been detected at $\tilde{\nu} = 30381.11$ cm^{-1} ($\lambda = 329.1302$ nm) on the maximum of an absorption band stemming from the superposition of the $^3\Pi_1$ sub-band of the $\tilde{A}^3\Pi_u(000) - \tilde{X}^3\Sigma_g^-(000)$ transition with the Q_1 band head of the vibronic $^3\Sigma^+(010) - {}^3\Pi(010)$ transition.[30] NCN concentration-time profiles were calculated using the previously reported temperature-dependent absorption cross section, which has been measured with an accuracy of $\pm 25\%$ using the same apparatus at similar temperatures and pressures as used in this work.[28] As the (010) vibrational state becomes significantly populated at combustion temperatures, the absorption cross sections were comparatively high (e.g., $\sigma(1500\,\text{K}, \text{base e}) = 4.5 \times 10^7$ cm^{2}mol^{-1}). Hence, with a detection limit of 4×10^{-12} cm^3/mol (corresponding to 1.5×10^{-3} absorption at $T = 1500$ K, $p = 500$ mbar, and an electronic time-resolution of $\Delta t \approx 1\,\mu$s), NCN could be detected with high signal-to-noise ratios even at NCN mole fractions as low as a few ppm.

5.2.3 Numerical methods

Numerical simulations of NCN concentration-time profiles from the shock tube experiments were performed using the Chemkin-II program package[31] in combination with the GDFkin3.0_NCN as a detailed background mechanism. In order to be consistent with previous shock tube work, rate constants for NCN reactions have been replaced or added according to our directly measured rate constant data set.[20,21,22] The most important reactions for modeling the shock tube experiments are listed in Tab. 5.1. For sensitivity analysis, the sensitivity coefficient $\sigma(i,t)$ for reaction i at time t was normalized with respect to the maximum concentration [NCN]$_{\text{max}}$ over the time history, $\sigma(i,t) = 1/[\text{NCN}]_{\text{max}} \times (\partial[\text{NCN}]/\partial \ln k_i)$.

Flame modeling was performed with the Chemkin/Premix code[31,32] and the detailed mechanism GDFkin3.0_NCN.[12] As will be further outlined below, the mechanism has been modified to take into account reaction (2) and subsequent chemistry of HNCN and HNC. Rate-of-production (ROP) and the N-atom flux analyses have been accomplished at the NCN peak locations using a homemade post processor that relies mostly on the Chemkin subroutines.[31] Atom flux analysis has been performed with the program Kinalc, and the reaction fluxes were plotted with the included FluxViewer visualisation tool.[33] Thermodynamic data were adopted from GDFkin3.0[12] with updated NCN thermochemistry as described in Ref. 13. Hence, in agreement with recent experimental work,[22] the controversial value of the enthalpy of formation of NCN[34] was set to $\Delta_f H^\circ_{298\,\text{K}} = 450.2$ kJ/mol. For HNCN and
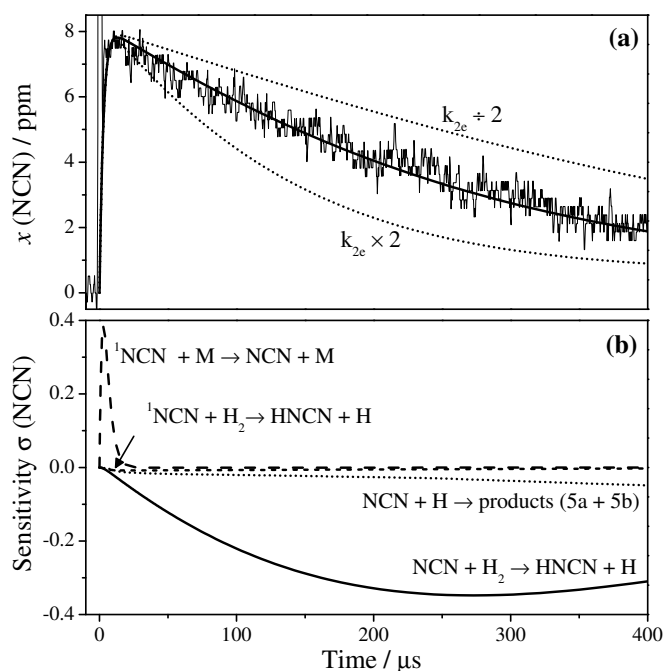
Figure 5.1: (a) Typical experimental NCN concentration-time profile in comparison with numerical simulations. $T = 1582$ K, $p = 544$ mbar, $\rho = 4.13 \times 10^{-6}$ mol/cm^3, [H$_2$] = 4.0%, [NCN$_3$] = 8.2 ppm, k_{2e}(NCN + H$_2$ → HNCN + H) = 1.8×10^{10} cm^{3}mol^{-1}s^{-1} (best fit, solid curve). (b) Corresponding sensitivity analysis for NCN.

HNC, thermodynamic data were extracted from the Goos/Ruscic database.[35]

Quantum chemical calculations were carried out using the Gaussian 09 suite of programs.[36] The transition state of the reaction NCN + H$_2$ → HNCN + H was located and verified by using a synchronous transit-guided quasi-Newton method (QST3 option) and intrinsic reaction coordinate following.

5.3 Results and discussion

5.3.1 Shock tube experiments

The rate constant of reaction (2), NCN + H$_2$, has been measured behind incident and reflected shock waves with reaction gas mixtures containing 3 - 27 ppm NCN$_3$ and 0.8 - 9.6 % H$_2$ in argon. k_2 values have been obtained in the temperature and pressure ranges 1057 K $\leq T \leq$ 2475 K and 324 mbar $\leq p \leq$ 1665 mbar, at two total densities of $\rho \approx 4.1 \times 10^{-6}$ and 7.4×10^{-6} mol/cm^3. Under these experimental conditions the reaction NCN + H$_2$ was always the most important reaction for NCN consumption. Experimental temperature limits were set by the thermal decomposition of NCN, which becomes the dominant reaction above 2500 K, and by the rate of reaction (2) itself, which becomes too slow at temperatures $T < 1000$ K to be measured with sufficient sensitivity.

Fig. 5.1a shows a typical NCN concentration-time profile behind the incident shock wave at $T =$

1582 K and a total density of $\rho = 4.13 \times 10^{-6}$ mol/cm^3. The NCN profile reveals a rather slow NCN consumption with a half-life of $t_{1/2} \approx 200$ μs. Since there are no studies on the possible reaction channels of the reaction NCN + H_2, numerical simulations of the experimental NCN profiles have been performed assuming different sets of reaction products. Potential reaction products of reaction (2) include:

$$\Delta_r H^\circ_{298\,K}/(\text{kJmol}^{-1})$$

(2a)	^{3}NCN + ^{1}H$_2$	$\rightarrow$ ^{1}H$_2$NCN	-317.2
(2b)		$\rightarrow$ ^{1}HNCNH	-304.2
(2c)		$\rightarrow$ ^{3}CH$_2$ + ^{1}N$_2$	-59.0
(2d)		$\rightarrow$ ^{1}HCN + ^{3}NH	38.4
(2e)		$\rightarrow$ ^{2}HNCN + ^{2}H	83.6
(2f)		$\rightarrow$ ^{1}HNC + ^{3}NH	100.5
(2g)		$\rightarrow$ ^{2}NH$_2$ + ^{2}CN	174.7

The formation of the thermodynamically most favorable products H$_2$NCN (2a) and HNCNH (2b) is spin-forbidden and hence their formation constitutes a presumably unimportant pathway. All other, increasingly endothermic channels are spin-allowed and may become accessible at combustion temperatures. Except for reaction (2e), the assumed product sets require the formation of an unlikely collision complex on the triplet surface followed by several rearrangement steps. This is in particular the case for reaction (2c), where a feasible reaction pathway can hardly be imagined. Actually, reactions (2a) and (2g) may become important for the corresponding ^{1}NCN reaction as singlet radicals are known to prefer insertion reactions. For the triplet radical, however, reaction (2e) constitutes the by far most probable reaction channel. Next to the decomposition of a ^{3}HNCNH intermediate, this reaction can take place as a direct activation controlled H abstraction reaction as well. It is known that H abstraction channels often become the dominating pathway at high temperatures even if complex-forming pathways are accessible.[26,37] Therefore, the most reasonable reaction products HNCN + H have been assumed for the target reaction NCN + H_2 in a first round of data evaluation. The effect of assuming different product sets will be further discussed below. The experimental NCN concentration-time profiles have been simulated based on a detailed mechanism assembled from our previous work (Table 5.1). Except for reactions (3) and (4), all reactions have been duplicated for ^{1}NCN to take ^{1}NCN chemistry approximately into account. Moreover, the reaction model was complemented by the extensive GDFkin3.0 mechanism.[12,13] Subsequent HNCN chemistry is only partly accounted for. Next to the reverse of reaction (2e), H + HNCN, only the thermal decomposition of HNCN has been included in the mechanism by the reverse of reaction (11). For the latter, the used rate expression for atmospheric pressure has been adopted from recent work of Teng et al.;[19] a formerly reported rate expression for the low pressure limit of the unimolecular decomposition reaction (-11) by Moskaleva and Lin,[6] which is implemented into the Konnov0.6 mechanism, turned out to yield unrealistic high rate constant values. Other rate constant data for bimolecular HNCN loss reactions such as HNCN + C/ CN/ N are not available in the literature, however, these reactions are not expected to play significant

roles for modeling the shock tube experiments.

In Fig. 5.1a, the solid curve represents the best numerical simulation of the NCN profile using $k_{2e} = 1.8 \times 10^{10}$ cm^{3}mol^{-1}s^{-1}. Variation of k_{2e} by a factor of two yields the two dotted curves that fail to reproduce the experiment. The sensitivity analysis in Fig. 5.1b reveals that reaction (2e) is by far the most important reaction for NCN consumption. Only at reaction times $t > 250$ μs, the reaction NCN + H gains some influence. Its high temperature rate constant and branching ratio, however, has been directly measured recently.[22] The sole other sensitive reaction, which is important to model the initial NCN formation at short reaction times, is the CIISC process (4). It has been studied in some detail by Dammeier et al.[29] and its rate constant value is dependent on the composition of the reaction gas mixture. Here, k_4 has been used as an adjustable parameter and was varied within the error limits reported in Ref. 29 in order to model the initial increase of the NCN signal. Finally, an alternative rate constant determination by fitting the NCN decay assuming a simple pseudo-first order exponential decay without applying any reaction mechanism has been performed as well. As expected for negligible secondary chemistry, very similar rate constant values are obtained. For example, for the experiment shown in Fig. 5.1 a rate constant of $k_2 = 1.9 \times 10^{10}$ cm^{3}mol^{-1}s^{-1} has been obtained over the interval 25 μs $\leq t \leq 250$ μs, which is very close to the $k_{2e} = 1.8 \times 10^{10}$ cm^{3}mol^{-1}s^{-1} value from the numerical simulation mentioned above.

In order to analyze a possible influence of the assumed products of reaction (2), the experimental NCN concentration-time profiles have been simulated using different product sets. Fig. 5.2a illustrates an experimental NCN profile at a reflected shock wave temperature of $T = 2123$ K. Assuming reaction channel (2e) with the radical products HNCN + H yields a rate constant of $k_{2e} = 1.3 \times 10^{11}$ cm^{3}mol^{-1}s^{-1} (red curve). The sensitivity analysis for the chosen high temperature experiment reveals that the influence of secondary chemistry is more pronounced than for the previously discussed $T = 1582$ K experiment (Fig. 5.1). For example, the thermal decomposition of NCN, NCN + M $\rightarrow$ C + N$_2$ + M, starts to play a significant role. Its rate constant has been measured in two independent studies and highly consistent values have been reported.[21,24] Hence, a sensitive determination of k_2 is still possible. Next, the same value for the rate constant k_2 but the alternative recombination product HNCNH of channel (2b) has been used instead of the products HNCN + H. The resulting simulated curve predicts a somewhat too slow NCN decay (black curve). As no additional HNCNH chemistry has been included into the mechanism and hence HNCNH has been treated as a stable species, the difference between the two simulations reflects the impact of the secondary reactions resulting from the radical products formed in case of the channel (2e) products. Similar results are obtained when assuming reaction channel (2a). In contrast, simulations with the other potential radical forming reaction channels (2c), (2d), (2f) or (2g) yielded more or less the same k_2 values as for channel (2e). In Fig. 5.2a, the blue curve represents the simulation using the products of channel (2f), HNC + NH, as an example. Within error limits it is identical to the simulation using channel (2e).

Total rate constant values for reaction (2) have been extracted from 36 shock tube experiments. The experimental conditions of all experiments are listed in Table 5.2, an Arrhenius plot of the obtained k_2 values is given in Fig. 5.3. The symbols correspond to the results assuming HNCN + H as the reaction products. Within the scatter, the obtained data for the two different total densities of $\rho \approx$

69
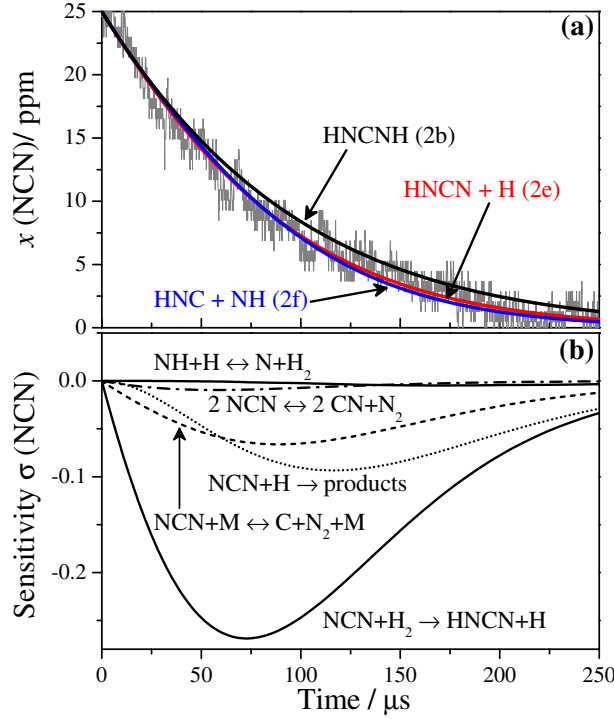
Figure 5.2: (a) Comparison of numerical simulations assuming HNCN + H (2e), HNC + NH (2f), or HNCNH (2b) as alternative products of the reaction NCN + H_2. $T = 2123$ K, $p = 719$ mbar, $\rho = 4.08 \times 10^{-6}$ mol/cm^3, $[H_2] = 1.5\%$, $[NCN_3] = 25$ ppm. $k_2 = 1.3 \times 10^{11}$ cm^{3}mol^{-1}s^{-1} has been used for all three simulations. (b) Corresponding sensitivity analysis assuming the products HNCN + H.

4.1×10^{-6} mol/cm^3 (open squares) and 7.4×10^{-6} mol/cm^3 (star symbols) agree, showing that the reaction is not significantly pressure dependent. The data points can be nicely represented by a two-parameter Arrhenius expression.

$$k_2 / \left(\text{cm}^3\text{mol}^{-1}\text{s}^{-1}\right) = 4.1 \times 10^{13}\exp\left(-\frac{101\,\text{kJ/ mol}}{RT}\right), \; \Delta\log k_2 = \pm 0.11.$$

The error bars in Fig. 5.3 exemplify the cumulative uncertainty of k_2 resulting from different error sources. Simulations show that a pessimistic $\pm 25\%$ error estimate for the initial NCN$_3$ concentration, which arises from the 25% error of the used NCN absorption cross section,[28] result in a $\pm 6\%$ uncertainty in k_2. Varying the most important background reactions within their error limits sum up to $\pm 8\%$. Finally, the uncertainty of the H_2 concentration was $\pm 2\%$ and the statistical error of the Arrhenius fit of the scattered data amounts to $\pm 8\%$ (2σ standard error of the mean). A reasonable total error estimate in the middle of our temperature range at $T \approx 1750$ K is therefore $\pm 24\%$, corresponding to $\Delta\log k_2 = \pm 0.11$. The dashed line in Fig. 5.3 corresponds to the Arrhenius expression $k_2/(\text{cm}^3\text{mol}^{-1}\text{s}^{-1}) = 6.5 \times 10^{13} \times \exp\left(-105\,\text{kJ/ mol}/RT\right)$ that has been obtained by assuming the unlikely formation of a stable reaction product (i.e., channel (2a) or (2b)). Such an evaluation yields data (not shown) that start to deviate from the evaluation assuming radical products (i.e., channels (2c)-(g))

Table 5.2: Experimental conditions and results for shock tube experiments with NCN$_3$/ H$_2$/ Ar reaction mixtures.

T/ K	p/ mbar	$\rho/10^{-6}$ mol/cm^3	H$_2$ %	NCN ppm	k_{2e}/ cm^{3}mol^{-1}s^{-1}	T/ K	p/ mbar	$\rho/10^{-6}$ mol/cm^3	H$_2$ %	NCN ppm	k_{2e}/ cm^{3}mol^{-1}s^{-1}
incident shock wave, $\rho \approx 4.06 \times 10^{-6}$ mol cm^{-3}						reflected shock wave, $\rho \approx 4.12 \times 10^{-6}$ mol cm^{-3}					
1057	324	3.69	2.81	13	5.0×10^8	1866	588	3.86	1.48	27	5.1×10^{10}
1171	371	3.81	2.81	10	1.3×10^9	1936	638	3.97	1.48	23	7.5×10^{10}
1402	466	4.00	2.81	10	7.0×10^9	2076	704	4.08	1.48	24	1.0×10^{11}
1433	489	4.10	6.34	4.5	8.5×10^9	2123	719	4.08	1.48	25	1.3×10^{11}
1449	498	4.13	7.48	5.3	9.0×10^9	2161	748	4.16	1.48	23	1.3×10^{11}
1503	510	4.08	9.63	3.2	1.2×10^{10}	2264	794	4.22	1.48	25	2.7×10^{11}
1520	518	4.10	3.38	6.8	1.2×10^{10}	2365	835	4.25	0.83	24	3.3×10^{11}
1525	520	4.10	3.64	7.6	1.3×10^{10}	2475	891	4.33	0.83	21	2.6×10^{11}
1533	526	4.13	5.06	6.0	1.7×10^{10}	incident shock wave, $\rho \approx 6.48 \times 10^{-6}$ mol cm^{-3}					
1534	523	4.10	3.15	5.6	1.3×10^{10}	1244	669	6.47	2.81	7	2.8×10^9
1534	525	4.11	3.17	4.2	1.4×10^{10}	1260	680.	6.49	2. 81	9	4.3×10^9
1535	527	4.13	4.31	8.6	1.8×10^{10}	reflected shock wave, $\rho \approx 7.67 \times 10^{-6}$ mol cm^{-3}					
1537	526	4.11	3.17	5.5	1.3×10^{10}	1247	652	6.29	2.93	10	5.0×10^9
1560	537	4.14	3.19	2.7	1.6×10^{10}	1543	916	7.14	2.93	12	2.0×10^{10}
1578	537	4.10	2.10	5.8	1.6×10^{10}	1705	1066	7.52	2. 93	13	2.2×10^{10}
1579	539	4.11	2.36	8.3	1.8×10^{10}	1824	1178	7.77	2. 93	10	4.9×10^{10}
1582	544	4.13	3.95	8.2	1.8×10^{10}	2044	1388	8.17	2. 93	9.3	9.0×10^{10}
1623	558	4.13	2.81	10	1.9×10^{10}	2062	1405	8.19	2.81	12	1.5×10^{11}
1626	529	3.91	2.93	5	2.7×10^{10}	2330	1665	8.59	2.81	9.0	3.0×10^{11}

at temperatures $T > 1700$ K with a maximum deviation of $+30\%$ at $T = 2480$ K.

A comparison with a similar reaction and quantum-chemical calculations show that the obtained activation energy is roughly consistent with a reaction that is dominated by an H abstraction pathway according to channel (2e). On the one hand, a comparable H abstraction reaction of the N-centered triplet species ^{3}NH, NH + H$_2$ → NH$_2$ + H, exhibits an activation energy, which is 33 kJ/mol higher than the corresponding reaction enthalpy of $\Delta_r H^\circ_{298\,K} = 32$ kJ/mol. [38] Accordingly, an activation energy of $E_A \approx 84$ kJ/mol $+ 33$kJ/mol $= 117$ kJ/mol would be expected for reaction (2e). On the other hand, an estimate of the activation enthalpy of channel (2e) based on quantum-chemical calculations using G4 level of theory yields a similar result. This method provides a reaction enthalpy for channel (2e) of $\Delta_r H^0_{298} = 86$ kJ/mol, which is close to the value of 84 kJ/mol from thermodynamic data taken from literature. The calculated energy of the H$_2 \cdots$ NCN transition state (H$_2$ is bonded to one of the N atoms and is oriented essentially perpendicular to the slightly bended NCN moiety) yields $\Delta H^\ddagger (T = 1750$ K$) = 101$ kJ/mol. Accordingly, taking into account the simple transition state theory expression $E_A \approx \Delta H^\ddagger + 2RT$, an activation energy of about 130 kJ/mol can be estimated for channel (2e) at $T = 1750$ K. However, a more detailed comparison with theory should be based on more advanced multi-reference quantum-chemical and kinetic calculations including tunneling corrections as well as a complete RRKM/master equation analysis of the possible role of additional complex-forming reaction pathways. Given that accurate energy calculation of NCN related species turned out to be very challenging, [34] such an analysis would have been beyond the scope of this paper.
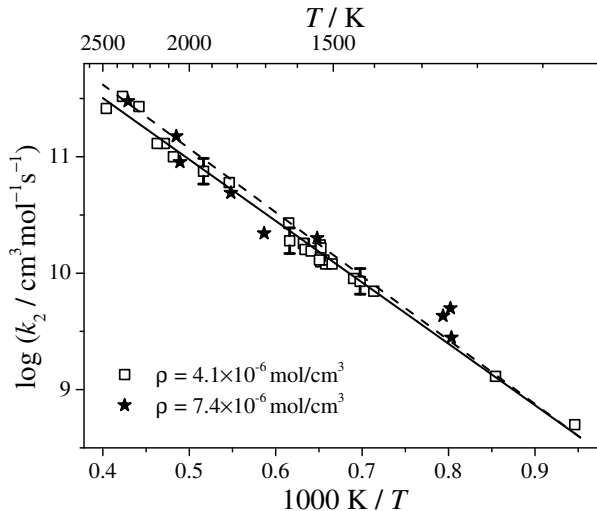
Figure 5.3: Arrhenius plot of the rate constant for the reaction NCN + H_2 $\rightarrow$ products. Experimental data at two different total densities $\rho \approx 4.1 \times 10^{-6}$ mol/cm^3 (open squares) and $\rho \approx 7.4 \times 10^{-6}$ mol/cm^3 (star symbols) and corresponding Arrhenius fit (solid line) for an evaluation assuming radical products (channel (2c)-(g)) are shown. The dashed line depicts an Arrhenius fit obtained for an alternative data evaluation (corresponding data points are not shown) assuming stable reaction products (channels (2a) and (2b)).

5.3.2 Flame modeling

The reaction NCN + H_2 turns out to be comparatively fast. With a rate constant of $k_2 = 3.2 \times 10^{10}$ cm^{3}mol^{-1}s^{-1} at a typical flame temperature of $T = 1700$ K, it is about a factor of 300 faster than the reaction NCN + O_2. Therefore, in order to assess the potential influence of reaction (2) for NO$_x$ formation in flames, reaction (2) as well as other NCN reactions have been implemented into the GDFkin3.0_NCN[12,13] flame mechanism. Arrhenius parameters of all reactions that have been added to the original mechanism are listed in Table 5.3. Simulations have been performed with HNCN + H, HCN + NH, and HNC + NH as the respective sole products of reaction (2).

Consideration of HNCN + H as main products implies an update of the mechanism with respect to HNCN reactions as well. HNCN species may rapidly react with O atoms (reactions (12)) generating HNC species. Consequently, two new blocks of reactions have been added to account for possible HNCN and HNC chemistry. In order to be coherent with the experimental rate constant determination, some additional NCN consumption reactions, (6) to (11), have also been considered in the detailed mechanism. In the following, this updated mechanism is named up-GDFkin3.0_NCN (up-GDF for short) in contrast to the original mechanism GDFkin3.0_NCN (GDF for short). Calculations were performed to simulate species profiles in selected low pressure premixed flames where the reaction NCN + H_2 may play an important role in the prompt-NO pathway. Two fuel rich flames of CH$_4$/ O$_2$/ N$_2$ have been considered numerically. Both flames were simulated at low pressure (5.0 kPa) with the same total volumetric flow rate (300 L/h, in the standard condition of temperature and pressure)

Table 5.3: Arrhenius parameters for rate constants of NCN, HNCN and HNC reactions added to the GDFkin3.0_NCN mechanism[13] for flame simulations. Rate constants are given as $k_i = AT^n \exp[-E_a/RT]$ in units of cm^3, mol^{-1}, s^{-1} and kJ.

No.	Reaction	A	n	E_a	Ref.
2	$NCN + H_2 \rightarrow$ (d) $HCN + NH$ / (e) $HNCN + H$ / (f) $HNC + NH$	4.1×10^{13}		101	This work
6	$NCN + M \rightleftharpoons C + N_2 + M$	8.9×10^{14}		260	21
7	$NCN + NCN \rightleftharpoons CN + CN + N_2$	3.7×10^{12}			29
8	$NCN + C \rightleftharpoons CN + CN$	1.0×10^{14}			29
9	$NCN + N \rightleftharpoons N_2 + CN$	1.0×10^{13}			6
10	$NCN + CN \rightleftharpoons C_2N_2 + N$	1.25×10^{14}		33.5	6
11	$NCN + H \rightleftharpoons HNCN$	1.78×10^{41}	-9.58	21.9	100 torr, 19
12a	$HNCN + O \rightarrow NO + HNC$	1.22×10^{14}	-0.05	0.3	39
12b	$HNCN + O \rightarrow NH + NCO$	5.60×10^{13}	-0.05	0.3	39
12c	$HNCN + O \rightarrow CN + HNO$	9.36×10^{12}	-0.05	0.3	39
13	$HNCN + O_2 \rightarrow HO_2 + NCN$	1.26×10^8	1.28	101.3	39
14	$HNCN + OH \rightarrow H_2O + NCN$	1.04×10^5	2.48	-7.9	40
15	$HCN (+ M) \rightarrow HNC (+ M)$	3.5×10^{13}		197.5	k_∞, 41
		1.60×10^{26}	-3.23	207.5	k_0, 41
16	$HNC + H \rightarrow HCN + H$	7.8×10^{13}		15	42
17	$HNC + O \rightarrow NH + CO$	4.6×10^{12}		9.2	41
18	$HNC + OH \rightarrow HNCO + H$	2.8×10^{13}		15.5	41
19	$HNC + CN \rightarrow C_2N_2 + H$	1.0×10^{13}			43

and nitrogen dilution ratio (60%), but a different richness equal to $\phi = 1.3$ and $\phi = 1.5$, respectively. Imposed temperature profiles were identical for each flame. The temperature in the burned gas was limited to remain lower than 1850 K, hence thermal-NO contribution was reduced and prompt-NO formation was promoted.

Considering the original GDF mechanism, simulated temperature and species profiles of NO, NCN and H_2 are reported in Fig. 5.4. In the burned gases, NO mole fractions are equal to 24.5 and 38.3 ppm for $\phi = 1.3$ and $\phi = 1.5$, respectively. As shown in Fig. 5.4a, the NO mole fraction in the burned gases is hardly affected at $\phi = 1.3$, but is increased by 8% at $\phi = 1.5$ when the calculations are performed with the up-GDF mechanism instead. H_2 and NCN profiles are reported in Fig. 5.4b using the up-GDF mechanism. The profiles show that at the NCN peak location (height above burner, HAB ($\phi = 1.3$) = 5.3 mm and HAB ($\phi = 1.5$) = 6.8 mm) the mole fractions of H_2 with $x(\phi = 1.3) = 0.064$ and $x(\phi = 1.5) = 0.091$ are high. NCN peak mole fractions are quite similar in the two flames with peak values close to 145 ppb, but the shape of the NCN profile is much thinner at $\phi = 1.3$.

N-atom flux analysis was performed after all the reactions have been declared in a non reversible format. In this way the atom flux reveals the flux in both directions of reversible reactions (forward and backward) separately. Some results at the NCN peak locations for both flames are presented in Table 5.4. Only NCN losses in the direction of the prompt-NO formation pathway (forward flux) are included. As expected, the reaction $NCN + H \rightarrow HCN + N$ is the most important NCN loss reaction that dominates the NCN forward flux, followed by the reaction with O atoms (yielding $CN + NO$). Nevertheless, about 1.8% of the NCN radicals are consumed through reaction (2) at $\phi = 1.3$ and 3.5% at $\phi = 1.5$. The so far neglected reaction with H_2 ranks third place and its contribution is even three
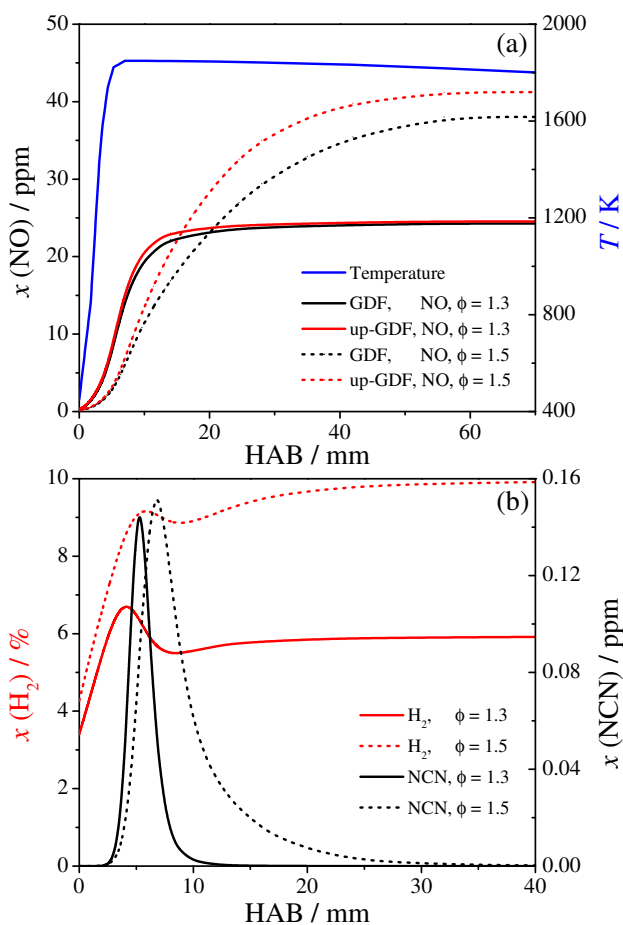
Figure 5.4: a) NO profiles simulated for the low pressure flames (see text) at a richness of $\phi = 1.3$ and $\phi = 1.5$. Results are shown for both the GDF and up-GDF mechanisms. b) Corresponding H$_2$ and NCN profiles simulated with the up-GDF mechanism.

orders of magnitude higher than for the reaction NCN + O$_2$. Note that the N-flux analysis reveals that next to reaction (2) also reaction (8), NCN + C, which was omitted in the original mechanism as well, becomes more important than other, already implemented bimolecular reactions such as NCN + OH/ HO$_2$/ NO/ M that are negligible under the assumed flame conditions.

Although it turned out that the implementation of reaction (2) is important, its rather low contribution to the forward flux is in seemingly contrast to the mentioned significant change of the overall NO yield. Obviously, other reactions added to the updated mechanism must be responsible for this prominent effect. A complete reaction pathway diagram for the $\phi = 1.5$ flame using the up-GDF mechanism is shown in Fig. 5.5. New reaction pathways that are absent in the corresponding diagram using the original GDF mechanism (not shown) are highlighted in red color. These pathways include the formation and loss reactions of the newly included species HNCN and HNC. Once formed, HNCN reacts quickly with O-atoms through reaction (12). According to theoretical calculations, the products

Table 5.4: N-atom flux analysis for the two CH$_4$/O$_2$/N$_2$ model flames. The Table lists the forward
fluxes associated with several NCN + X reactions on the prompt-NO formation pathway.

Forward flux %	H[a]	O	H$_2$	C	H$_2$O	OH	HO$_2$	O$_2$	NO	M
$\phi = 1.3$	69.21	25.68	1.76	1.36	1.33	0.44	0.21	< 0.01	< 0.01	< 0.01
$\phi = 1.5$	79.33	12.54	3.52	2.17	1.96	0.33	0.13	< 0.01	< 0.01	0.03

[a] for NCN + H (yielding either CH + N$_2$ or HCN + N, with a relative ratio of 77/23) only the HCN + N forming channel
contributes to the forward flux along the prompt-NO formation pathway
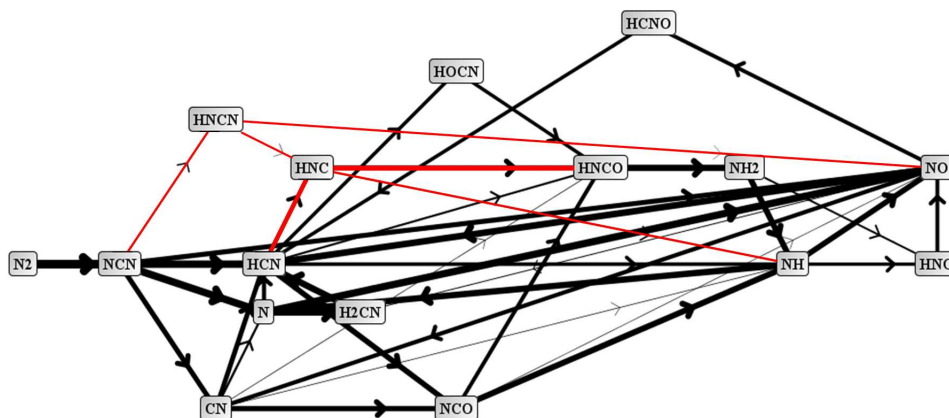
Figure 5.5: N-atom flux analysis at the NCN peak location in the $\phi = 1.5$ CH$_4$/O$_2$/N$_2$ flame using the
up-GDF mechanism. The pathways highlighted in red color are absent in a corresponding
flux analysis using the original GDF mechanism.[13]

of the reaction HNCN + O are mostly HNC + NO.[39] HNC then reacts with OH radicals yielding
HNCO + H, and HNCO reacts with H atoms yielding NH$_2$ + CO. However, it becomes clear from the
flux diagram that HNC radicals are formed primarily from HCN and only secondly from HNCN. In
fact, the HCN/ HNC isomerization according to reactions (15), which is close to its low-pressure limit,
and the H atom initiated isomerization reaction (-16), HNC + H $\rightarrow$ HCN + H, represent 12% and 20%
of the HCN consumption at $\phi = 1.3$ and $\phi = 1.5$, respectively. This finding is also reflected in the
HCN profiles shown in Fig. 5.6 for the $\phi = 1.5$ flame. HCN mole fraction peak values obtained with
the updated mechanism decrease by 20%. According to the ROP, HCN is mainly consumed through
the reaction HCN + O $\rightleftharpoons$ NCO + H and the reaction (-16), both being three times more important than
the reactions HCN + OH $\rightleftharpoons$ HOCN + H and HNC (+M) $\rightleftharpoons$ HCN (+M). The combined effect of HNC
formation from the reactions (-16) and (12a) results in a substantial increase of HNCO by a factor of
two (Fig. 5.6). This increase is followed by a comparable increase of the peak values of NH$_2$ as well.

To sum up, although the implementation of the reaction (2) has indeed a significant impact on NO
formation through a new HNC $\rightarrow$ HNCO $\rightarrow$ NH$_2$ $\rightarrow$ NH $\rightarrow$ NO pathway, it is in fact the HCN/
HNC isomerization and not the reaction NCN + H$_2$ that is mainly responsible for the distinct changes
obtained with the up-GDF mechanism. Note that the rate constant of the H initiated isomerization
reaction (16), H + HNC $\rightarrow$ HCN + H, is based on a theoretical QRRK estimate[42] and, to the best
of our knowledge, has not been experimentally confirmed yet. Therefore, our interesting preliminary
finding calls for a more detailed analysis to better constrain and verify the role of the HNC initiated
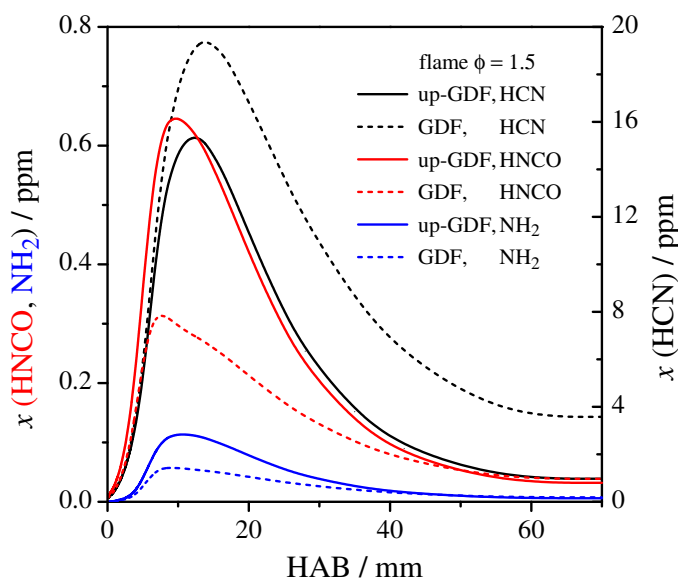
Figure 5.6: Comparison of HCN, HNCO, and NH_2 profiles of the $\phi = 1.5$ flame calculated with the original GDF (dashed curves) and the up-GDF (solid curves) mechanisms.

pathway for NO formation in flames.

The possible influence of the assumed products of the reaction (2) for the NO formation in flames has also been analyzed. Whatever channel (d, e, f) of reaction (2) was assumed, simulated NO profiles are identical to each other. However, considering the channel (2d), implementation of the reactions (12-19) could be removed since HCN and NH species are already declared in GDF.[13] In that case, simulated NO profiles would be identical to those obtained with the original GDF mechanism. Again, this clearly highlights the potential importance of the HCN/ HNC isomerization pathway through reactions (15) and (-16).

5.4 Conclusion

The rate constant of the reaction (2), NCN + $H_2 \rightarrow$ products, has been measured for the first time. Shock wave experiments with time-resolved NCN radical detection by narrow-bandwidth laser UV absorption were carried out under nearly pseudo-first order reaction conditions with H_2 as the excess component. The total rate constant has been measured at temperatures $1057\,\mathrm{K} \leq T \leq 2475\,\mathrm{K}$ and can be represented by the Arrhenius expression

$$k_2 / \left(\mathrm{cm^3 mol^{-1} s^{-1}}\right) = 4.1 \times 10^{13} \exp\left(-\frac{101\,\mathrm{kJ/\,mol}}{RT}\right), \ \Delta \log k_2 = \pm 0.11.$$

No pressure dependence could be observed between $p = 324$ mbar and $p = 1665$ mbar. Quantum-chemical calculations show that the activation energy is roughly consistent with the formation of the products HNCN + H, hence the most likely direct abstraction pathway. Still, detailed quantum-

chemical calculations in combination with RRKM/TST/ME modeling are desirable to further assess the role of complex-forming reaction pathways.

The detailed reaction mechanism GDFkin3.0_NCN has been updated to assess the potential influence of the so far neglected reaction (2) on prompt-NO formation in flames. Next to reaction (2), HNC and HNCN submechanisms have been implemented as well to describe the subsequent chemistry of the reaction products. Two fuel-rich low-pressure methane flames served as a model case and it was shown that the contribution of reaction (2) on the overall NCN loss in the direction of prompt-NO is on the order of a few percent. Of course, the reaction may become even more important for other flame conditions and, therefore, needs to be included in detailed flame mechanisms. The flame simulation also highlights the fact that the reaction NCN + C $\rightleftharpoons$ CN + CN, which was also omitted in the original GDFkin3.0_NCN mechanism should be considered in the future as well. As yet the rate constant for NCN + C has only been roughly determined experimentally, improved direct measurements are required. Moreover, as a pronounced impact of HCN/ HNC isomerization on NO formation has been found in this study, a critically assessment and experimental verification of the role of this new HNC $\rightarrow$ HNCO $\rightarrow$ NH$_2$ $\rightarrow$ NH $\rightarrow$ NO prompt-NO formation pathway is important. A thorough validation of the updated mechanism going along with the implementation of other new experimental rate constant data that recently have become available for several bimolecular reactions of NCN is currently underway.

Acknowledgment

References

[1] C. P. Fenimore. Formation of nitric oxide in premixed hydrocarbon flames. *Proc. Combust. Inst.*, 13:373–380, 1971.

[2] Q. Cui and K. Morokuma. The spin-forbidden reaction CH($^2\Pi$) + N$_2$ $\longrightarrow$ HCN + N(^{4}S) revisited. I. Ab initio study of the potential energy surfaces. *Theoretical Chemistry Accounts*, 102:127–133, 1999.

[3] Q. Cui, K. Morokuma, J. M. Bowman, and S. J. Klippenstein. The spin-forbidden reaction CH($^2\Pi$) + N$_2$ $\longrightarrow$ HCN + N(^{4}S) revisited. II. Nonadiabatic transition state theory and application. *J. Chem. Phys.*, 110:9469–9482, 1999.

[4] D. Lindackers, M. Burmeister, and P. Roth. Perturbation studies of high temperature carbon and CH reactions with nitrogen and nitrogen oxide (NO). *Proc. Combust. Inst.*, 23:251–257, 1991.

[5] A. J. Dean, R. K. Hanson, and C. T. Bowman. High temperature shock tube study of reactions of CH and carbon-atoms with nitrogen. *Proc. Combust. Inst.*, 23:259–265, 1991.

[6] L. V. Moskaleva and M. C. Lin. The spin-conserved reaction CH + N$_2$ $\longrightarrow$ H + NCN: A major pathway to prompt NO studied by quantum/statistical theory calculations and kinetic modeling of rate constant. *Proc. Combust. Inst.*, 28:2393–2401, 2000.

[7] G. P. Smith. Evidence of NCN as a flame intermediate for prompt NO. *Chem. Phys. Lett.*, 367:541–548, 2003.

[8] J. A. Sutton, B. A. Williams, and J. W. Fleming. Laser-induced fluorescence measurements of NCN in low-pressure CH$_4$/O$_2$/N$_2$ flames and its role in prompt NO formation. *Combust. Flame*, 153:465–478, 2008.

[9] N. Lamoureux, X. Mercier, C. Western, J. F. Pauwels, and P. Desgroux. NCN quantitative measurement in a laminar low pressure flame. *Proc. Combust. Inst.*, 32:937–944, 2009.

[10] V. Vasudevan, R. K. Hanson, C. T. Bowman, D. M. Golden, and D. F. Davidson. Shock Tube Study of the Reaction of CH with N$_2$: Overall Rate and Branching Ratio. *J. Phys. Chem. A*, 111:11818–11830, 2007.

[11] A. A. Konnov. Implementation of the NCN pathway of prompt-NO formation in the detailed reaction mechanism. *Combust. Flame*, 156:2093–2105, 2009.

[12] N. Lamoureux, P. Desgroux, A. El Bakali, and J.F. Pauwels. Experimental and numerical study of the role of NCN in prompt-NO formation in low-pressure CH$_4$-O$_2$-N$_2$ and C$_2$H$_2$-O$_2$-N$_2$ flames. *Combust. Flame*, 157:1929–1941, 2010.

[13] N. Lamoureux, H. El Merhubi, L. Gasnot, C. Schoemaecker, and P. Desgroux. Measurements and modelling of HCN and CN species profiles in laminar CH$_4$/O$_2$/N$_2$ low pressure flames using LIF/CRDS techniques. *Proc. Combust. Inst.*, 35:745–752, 2015.

[14] N. Lamoureux, X. Mercier, J. F. Pauwels, and P. Desgroux. NCO quantitative measurement in premixed low pressure flames by combining LIF and CRDS techniques. *J. Phys. Chem. A*, 115:5346–5353, 2011.

[15] P. Glarborg, M. U. Alzueta, K. Dam-Johansen, and J. A. Miller. Kinetic Modeling of Hydrocarbon/Nitric Oxide Interactions in a Flow Reactor. *Combust. Flame*, 115:1–27, 1998.

[16] R. S. Zhu and M. C. Lin. Ab Initio Study of the Oxidation of NCN by O$_2$. *Int. J. Chem. Kinet.*, 37:593–598, 2005.

[17] R. S. Zhu and M. C. Lin. Ab Initio Study on the Oxidation of NCN by O (^{3}P): Prediction of the Total Rate Constant and Product Branching Ratios. *J. Phys. Chem. A*, 111:6766–6771, 2007.

[18] R. S. Zhu, Hue M. T. Nguyen, and M. C. Lin. Ab Initio Study on the Oxidation of NCN by OH: Prediction of the Individual and Total Rate Constants. *J. Phys. Chem. A*, 113:298–304, 2009.

[19] W.-S. Teng, L. V. Moskaleva, H.L. Chen, and M. C. Lin. Ab Initio Chemical Kinetics for H + NCN: Prediction of NCN Heat of Formation and Reaction Product Branching via Doublet and Quartet Surfaces. *J. Phys. Chem. A*, 117:5775–5784, 2013.

[20] J. Dammeier and G. Friedrichs. Direct Measurements of the Rate Constants of the Reactions NCN + NO and NCN + NO$_2$ Behind Shock Waves. *J. Phys. Chem. A*, 115:14382–14390, 2011.

[21] J. Dammeier, N. Faßheber, and G. Friedrichs. Direct measurements of the high temperature rate constants of the reactions NCN + O, NCN + NCN, and NCN + M. *Phys. Chem. Chem. Phys.*, 14:1030–1037, 2012.

[22] N. Faßheber, J. Dammeier, and G. Friedrichs. Direct measurements of the total rate constant of the reaction NCN + H and implications for the product branching ratio and the enthalpy of formation of NCN. *Phys.Chem. Chem. Phys.*, 16:11647–11657, 2014.

[23] A. Busch and M. Olzmann. Shock-Tube Study of the Thermal Decomposition of NCN. *Proc. Eur. Combust. Meeting*, Paper P810138, Vienna, Austria, 2009.

[24] A. Busch, N. González-García, G. Lendvay, and M. Olzmann. Thermal Decomposition of NCN: Shock-Tube Study, Quantum Chemical Calculations, and Master-Equation Modeling. *J. Phys. Chem. A*, 2015, DOI: 10.1021/acs.jpca.5b01347.

[25] A. El Bakali, L. Pillier, P. Desgroux, B. Lefort, L. Gasnot, J. F. Pauwels, and I. da Costa. NO prediction in natural gas flames using GDF-Kin 3.0 mechanism. NCN and HCN contribution to prompt-NO formation. *Fuel*, 85:896–909, 2006.

[26] M. Colberg and G. Friedrichs. Room Temperature and Shock Tube Study of the Reaction HCO + O$_2$ Using the Photolysis of Glyoxal as an Efficient HCO Source. *J. Phys. Chem. A*, 110:160–170, 2006.

[27] J. E. Dove and H. Teitelbaum. The vibrational relaxation of H$_2$. I. Experimental measurements of the rate of relaxation by H$_2$, He, Ne, Ar, and Kr. *Chem. Phys.*, 6:431–444, 1974.

[28] J. Dammeier and G. Friedrichs. Thermal Decomposition of NCN$_3$ as a High-Temperature NCN Radical Source: Singlet-Triplet Relaxation and Absorption Cross Section of NCN($^3\Sigma$). *J. Phys. Chem. A*, 114:12963–12971, 2010.

[29] J. Dammeier, B. Oden, and G. Friedrichs. A consistent model for the thermal decomposition of NCN$_3$ and the singlet-triplet relaxation of NCN. *Int. J. Chem. Kinet.*, 45:30–40, 2013.

[30] N. Lamoureux, C. M. Western, X. Mercier, and P. Desgroux. Reinvestigation of the spectroscopy of the A$^3\Pi_u$- X$^3\Sigma_g^-$ transition of the NCN radical at high temperature: Application to quantitative NCN measurement in flames. *Combust. Flame*, 160:755–765, 2013.

[31] R. J. Kee, F. M. Ruply, and J. A. Miller. *Chemkin- II: A Fortran Chemical Kinetics Package for the Analysis of Gas-Phase Chemical Kinetics, Sandia Report SAND89-8009, Sandia National Laboratories, Livermore, California (Sept. 1989).*

[32] R.J. Kee, J.F. Grcar, M.D. Smooke, and J.A. Miller. A fortran program for modelling steady laminar one-dimensional premixed flames, Sandia report SAND85-8240, 1985.

[33] Kinalc: program for the kinetic analysis of combustion mechanisms, http://garfield.chem.elte.hu/combustion/kinalc.htm, last accessed 24.04.2015.

[34] E. Goos, C. Sickfeld, F. Mauß, L. Siedel, B. Ruscic, A. Burcat, and T. Zeuch. Prompt NO formation in flames: The influence of NCN thermochemistry. *Proc. Combust. Inst.*, 34:657–666, 2013.

[35] E. Goos, A. Burcat, and B. Ruscic. *Extended Third Millenium Ideal Gas and Condensed Phase Thermochemical Database for Combustion with Updates from Active Thermochemical Tables.* (2009) http://garfield.chem.elte.hu/Burcat/burcat.html, last accessed 10.01.2015.

[36] M. J. Frisch, G. W. Trucks, H. B. Schlegel, G. E. Scuseria, M. A. Robb, J. R. Cheeseman, G. Scalmani, V. Barone, B. Mennucci, G. A. Petersson, H. Nakatsuji, M. Caricato, X. Li, H. P. Hratchian, A. F. Izmaylov, J. Bloino, G. Zheng, J. L. Sonnenberg, M. Hada, M. Ehara, K. Toyota, R. Fukuda, J. Hasegawa, M. Ishida, T. Nakajima, Y. Honda, O. Kitao, H. Nakai, T. Vreven, J. A. Montgomery, Jr., J. E. Peralta, F. Ogliaro, M. Bearpark, J. J. Heyd, E. Brothers, K. N. Kudin, V. N. Staroverov, R. Kobayashi, J. Normand, K. Raghavachari, A. Rendell, J. C. Burant, S. S. Iyengar, J. Tomasi, M. Cossi, N. Rega, J. M. Millam, M. Klene, J. E. Knox, J. B. Cross, V. Bakken, C. Adamo, J. Jaramillo, R. Gomperts, R. E. Stratmann, O. Yazyev, A. J. Austin, R. Cammi, C. Pomelli, J. W. Ochterski, R. L. Martin, K. Morokuma, V. G. Zakrzewski, G. A. Voth, P. Salvador, J. J. Dannenberg, S. Dapprich, A. D. Daniels, Ö. Farkas, J. B. Foresman, J. V. Ortiz, J. Cioslowski, and D. J. Fox. Gaussian 09 Revision D.01. Gaussian Inc. Wallingford CT 2009.

[37] J. Dammeier, Colberg, and G. Friedrichs. Wide temperature range (T = 295 K and 770 - 1305 K) study of the kinetics of the reactions HCO + NO and HCO + NO$_2$ using frequency modulation spectroscopy. *Phys.Chem. Chem. Phys.*, 9:4177–4188, 2007.

[38] A. Fontijn, S. M. Shamsuddin, D. Crammond, P. Marshall, and W. R. Anderson. Kinetics of the NH reaction with H$_2$ and reassessment of HNO formation from NH + CO$_2$, H$_2$O. *Combust. Flame*, 145:543–551, 2006.

[39] S. Xu and M. C. Lin. Ab initio chemical kinetics for the reactions of HNCN with O(^{3}P) and O$_2$. *Proc. Combust. Inst.*, 32:99–106, 2009.

[40] S. Xu and M. C. Lin. Ab Initio Chemical Kinetics for the OH + HNCN Reaction. *J. Phys. Chem. A*, 111:6730–6740, 2007.

[41] A. M. Dean and J. W. Bozzelli. *Combustion chemistry of nitrogen*. In: Gardiner WC (ed) Gasphase Combustion Chemistry. Springer, New York, 2000.

[42] R. Sumathi and M. T. Nguyen. A theoretical study of the CH$_2$N system: reactions in both lowest lying doublet and quartet states. *J. Phys. Chem. A*, 102:8013–8020, 1998.

[43] S. Petrie and Y. Osamura. NCCN and NCCCCN Formation in Titan's Atmosphere: 2. HNC as a Viable Precursor. *J. Phys. Chem. A*, 108:3623–3631, 2004.

6 Shock tube measurements of the rate constant of the reaction NCN + O$_2$

Nancy Faßheber and Gernot Friedrichs[*]

Institute für Physikalische Chemie, Christian-Albrechts-Universität zu Kiel

Own contributions:

- Shock tube experiments.

- Analysis of the experimental data including temperature correction procedure.

- Writing of paper draft.

Abstract

The rate constant of the comparably slow bimolecular NCN radical reaction $NCN + O_2$ has been measured for the first time under combustion relevant conditions using the shock tube method. The thermal decomposition of cyanogen azide (NCN_3) served as a clean high-temperature source of NCN radicals. NCN concentration-time profiles have been detected by narrow-bandwidth laser absorption at $\tilde{\nu} = 30383.11$ cm^{-1}. The experiments behind incident shock waves have been performed with up to 17% O_2 in the reaction gas mixture. At such high O_2 mole fractions it was necessary to take O_2 relaxation into account that caused a gradual decrease of the temperature during the experiment. Moreover, following fast decomposition of NCN_3 and collision-induced intersystem crossing of the initially formed singlet NCN to its triplet ground state, an unexpected and slow additional formation of triplet NCN has been observed on a 100 μs timescale. This delayed NCN formation was attributed to a fast recombination of ^{1}NCN with O_2 forming a ^{3}NCNOO adduct acting as a reservoir species for NCN. Rate constant data for the reaction $NCN + O_2$ have been measured at temperatures between 1674 K and 2308 K. They are best represented by the Arrhenius expression $k_2 / \left(\mathrm{cm^3 mol^{-1} s^{-1}}\right) = 1.3 \times 10^{12} \exp\left(-\frac{97\,\mathrm{kJ/\,mol}}{RT}\right), (\pm 57\%)$. No pressure dependence has been observed at pressures between 216 mbar and 706 mbar.

6.1 Introduction

Nitrogen oxides, such as NO and NO_2 (NO_x), are harmful atmospheric pollutants from fossil fuel combustion. Under fuel rich combustion conditions NO_x is mainly formed over the so-called prompt-NO pathway, which is initiated by the reactions of small hydrocarbon radicals with molecular nitrogen stemming from the combustion air according to the Fenimore mechanism.[1] Based on quantum chemical calculations[2] and verified by shock tube measurement[3] it has been shown that the initiation reaction $CH + N_2$ yields the spin-allowed products H + NCN.

$$CH\left(^2\Pi\right) + N_2\left(^1\Sigma^+\right) \rightarrow H\left(^2S\right) + NCN\left(^3\Sigma^-\right) \tag{1}$$

In recent years, using NCN_3 thermal decomposition as a quantitative source of NCN radicals and sensitive time-resolved UV absorption spectroscopy to detect NCN concentration-time profiles, we have performed several direct shock tube measurements of bimolecular NCN rate constants at high temperatures. These studies include the reactions NCN + NO, NO_2,[4] NCN + NCN, O, and M[5] as well as NCN + H[6] and NCN + H_2.[7] The only other direct study reported in the literature, which is in excellent agreement with our work, was concerned with the unimolecular decomposition of NCN using the C-ARAS technique.[8,9] So far, no experimental high temperature rate constant measurements have been performed for the reaction with molecular oxygen,

$$NCN + O_2 \rightarrow products. \tag{2}$$

This reaction has been discussed to play an important role for NO_x formation in flames.[11,12] Baren
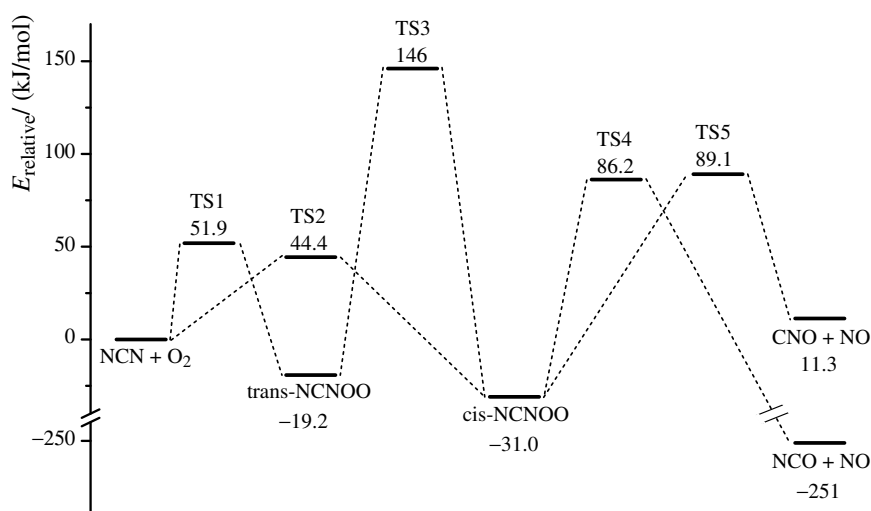
Figure 6.1: Simplified potential energy diagram (G2M(CC1) level of theory) for the reaction NCN + O_2, according to Zhu and Lin.[10]

and Hershberger performed kinetic measurements of NCN radical reactions at low temperatures and pressures by detecting NCN concentration-time profiles following 193 nm photolysis of CH_2N_2/C_2N_2 mixtures using laser-induced fluorescence. They could not observe significant changes in the NCN profiles by adding O_2 to their reaction mixtures and therefore estimated an upper limit of $k_2 < 6.0 \times 10^9$ $cm^3mol^{-1}s^{-1}$ for temperatures between 298 K and 573 K.[13] In a first attempt to compile a high temperature NCN mechanism for NO_x formation, Glarborg et al. estimated a value of $k_2 = 1.0 \times 10^{13}$ $cm^3mol^{-1}s^{-1}$.[14] Such a high value, which has been adopted by El Bakali et al.[11] in their NCN submechanism for flame modeling, would make the reaction NCN + O_2, together with NCN + H, one of the most important reactions for modeling the fate of NCN in flames. According to ab initio and transition state theory calculations by Zhu and Lin,[10] the following two main reaction channels are accessible at high temperatures:

$$NCN + O_2 \rightarrow cis\text{-}NCNOO \quad \rightarrow \quad NCO + NO \qquad (2a)$$
$$\rightarrow \quad CNO + NO \qquad (2b).$$

In Fig. 6.1 these two energetically most favorable reaction pathways are illustrated in a potential energy diagram. As discussed by Zhu and Lin, the possible formation of NCNO + O(^{3}P) and NCNO + O(^{1}D) is not important under combustion conditions and, for the sake of clarity, is omitted in Fig. 6.1. The cis- and trans-NCNOO intermediates refer to the two possible NC-NO-O isomers of the initially formed NCN-O_2 adduct. Relying on the G2M (CC1) level of theory results,[10] both product sets are formed from the cis-isomer with high transition state barriers of 117 kJ/mol (86 kJ/mol) for channel (2a) and 120 kJ/mol (89 kJ/mol) for channel (2b) relative to the energy of the cis-intermediate (of the educts). cis-trans isomerisation, with a calculated barrier height of 165 kJ/mol, does not take place. Reaction channel (2a), the formation of NCO and NO, turned out to be the most important channel with a branching ratio of about 85% in the temperature range 1000 K to 3000 K. The calculations for the total rate constant resulted in the rate expression

$k_2 / \left(\mathrm{cm^3 mol^{-1} s^{-1}}\right) = 4.4 \times 10^9 \times (T/\mathrm{K})^{0.51} \exp\left(-\frac{103\,\mathrm{kJ/mol}}{RT}\right)$.[10] At $T = 1500$ K, this rate constant is five orders of magnitude lower than the estimated rate constant value of Glarborg et al.[14] Of course, such a low value implies a reduced influence of the reaction NCN + O_2 on the modeled NCN concentrations in flames than initially anticipated. For sure, the outcome of the theoretical study of Zhu and Lin supports an overall slow reaction. However, taking into account the difficulties in calculating reliable NCN energies and transition state barrier heights,[15,16,17] and facing the lack of experimental studies, the absolute value of the rate constant awaits experimental validation. This paper now reports the first direct measurements of the rate constant of the reaction NCN + O_2. Compared to our previous NCN studies, the data analysis was less straightforward. Vibrational relaxation of O_2 as well as the apparent intermediate formation of an NCN reservoir species had to be properly taken into account. Nevertheless, it was possible to extract reliable rate constant values, which turned out to be about a factor of five higher than the transition state theory estimate.

6.2 Experimental

6.2.1 Shock tube setup

Similar to our previous NCN measurements the experiments have been performed in an about 8 m long stainless steel shock tube with an electro-polished test section with an inner diameter of 81 mm. The whole apparatus is described in more detail elsewhere.[18] Experimental temperatures and pressures behind the shock waves were calculated from the shock wave velocity, taking into account shock wave damping of $\sim 1\%$ per meter, and the pre-shock conditions using a one dimensional frozen-chemistry code with real gas correction. Reported times behind the incident shock wave correspond to the actual reaction times taking into account the gas flow, $t_{\mathrm{reaction}} = t_{\mathrm{laboratory}} \times \rho_2/\rho_1$. Reaction gas mixtures of 14 - 56 ppm NCN_3 in Ar were prepared in a stainless steel gas mixing system equipped with several glass flasks and storage tanks. NCN_3 synthesis as well as the procedures for gas mixture preparation have been described elsewhere.[4,19] Very high O_2 mole fractions of 5.5 to 17% had to be used to achieve a measurable effect of the reaction NCN + O_2 on the NCN profiles. At such high O_2 concentrations, due to the relatively slow vibrational relaxation of O_2, the temperature (and density) behind shock waves cannot be assumed as constant. While the translational and rotational degrees of freedom are heated within 1 μs, the vibrational relaxation of oxygen is much slower, about 166 μs at $T = 1500$ K and $p = 1$ bar for 2.5% O_2 in Ar.[20] Due to this slow equilibration, the actual temperatures decrease during the experiments. In fact, the initial temperatures are higher than the calculated temperatures using the standard shock tube code, which assumes instantaneous and complete relaxation of O_2. Therefore, starting temperatures have been calculated using a modified NASA polynomial for oxygen taking only translational and rotational degrees of freedom into account. This oxygen species will be referred to as O_2(cold) in the following. In this way, the change of the temperature (and density) behind the incident shock wave could be taken into account in a straightforward manner by implementing the relaxation process O_2(cold) $\rightarrow O_2$ into the reaction mechanism and by performing numerical simulations assuming isobaric reaction conditions. As outlined by Oertel,[21] assuming that the specific enthalpy of the heated gas mixture as well as the vibrational relaxation time τ is approximately constant over the

whole relaxation process, the temperature change can be described by a mono-exponential law:

$$\frac{T(t) - T_\infty}{T_2 - T_\infty} = \exp\left(-\frac{c_p}{c_{p,2}} \times \frac{t}{\tau}\right)$$

Here, $T(t)$ is the actual temperature, T_2 the initial temperature behind the incident shock wave, and T_∞ the equilibrated temperature after relaxation. c_p and $c_{p,2}$ are the specific heat capacities of the reaction mixture with and without vibrational excitation of O_2, respectively. The ratio $c_p/c_{p,2}$ is very close to one. Under these assumptions, the experimental pressure behind the incident shock wave remains constant and $T \times \rho = const.$ holds as well.

6.2.2 NCN source

As shown by Dammeier et al.,[19,22] the thermal decomposition of NCN_3

$$NCN_3 + M \ \rightarrow \ ^1NCN + N_2 + M \tag{4}$$

$$^1NCN + M \ \rightarrow \ ^3NCN + M, \tag{5}$$

serves as a clean and quantitative source for NCN with a yield of unity. The fast unimolecular decomposition of NCN_3 generates NCN in its singlet excited electronic state, which undergoes a collision induced intersystem crossing (CIISC) process to the triplet ground state (^3NCN stated in the following as NCN). Our previous work showed that the CIISC process is the rate-limiting process for NCN formation at temperatures above 700 K, but is still fast compared to the reaction $NCN + O_2$ measured here.[22]

6.2.3 NCN detection

NCN has been detected by time-resolved narrow-bandwidth laser absorption spectroscopy at a wavelength of $\lambda = 329.1302$ nm ($\tilde{v} = 30383.11$ cm^{-1}). Details on the employed difference UV absorption setup, which was operated with about 1 mW output power of a frequency-doubled continuous-wave ring dye laser, have been described elsewhere.[19] The observed absorption band of the triplet NCN ground state is a superposition of the $^3\Pi_1$ sub-band of the $\tilde{A}^3\Pi_u(000) - \tilde{X}^3\Sigma_g(000)$ transition and the Q_1 band head of the vibrationally excited Renner-Teller split $^3\Sigma^+(010)$-$^3\Pi(010)$ transition.[23] The corresponding strongly temperature dependent but nearly pressure independent absorption cross section, $\log\left(\sigma(\text{base e})/(\text{cm}^2\text{mol}^{-1})\right) = 8.9 - 8.3 \times 10^{-4} \times T/\text{K}$, has been adopted from previous work.[19] Note that this value was recently put into question by Lamoureux et al.[24] who reported a 2.6 higher value based on elaborated theoretical spectroscopic calculations referenced to the electronic transition moment obtained from zero pressure fluorescence lifetime measurements by Smith et al.[25] A possible explanation for this discrepancy could be that the ^1NCN yield from NCN_3 thermal decomposition is well below unity. However, no indication was found in this and in our previous studies that the assumption of a quantitative ^1NCN formation is invalid. Moreover, in a very recent study of Busch et al.,[9] who also used NCN_3 as a source of NCN radicals, a C atom yield

from NCN thermal decomposition, NCN $\rightarrow$ N_2 + C, was reported that is consistent with a quantitative NCN formation from NCN_3 as well. We therefore rely on our previously reported absorption cross section value, which has been measured with an accuracy of $\pm 25\%$ [19] using the same apparatus at similar temperatures and pressures as used in this work. Numerical simulations of concentration-time profiles were performed by the Chemkin-II program package, using the Senkin routine for sensitivity analyses.[26] An NCN mechanism for the simulations was assembled from our previous work[4,5,19] and available literature data. The most important reactions are listed in Tab. 6.1. Additionally, the GRI-Mech 3.0[27] has been used as a background mechanism to make sure that potentially important secondary reactions are considered in the simulations as well. Thermodynamic data were taken from Goos' and Burcat's thermodynamic database[28] with updated NASA polynomial parameters for NCN from Goos et al.[16] In agreement with previous work,[6] the enthalpy of formation of NCN was set to 450 kJ/mol.

6.3 Results

6.3.1 O_2 relaxation and NCNOO formation

Experiments have been performed behind incident shock waves at temperatures between 918 K and 2308 K and pressures of 164 mbar$< p <$ 706 mbar, corresponding to total densities of about $\rho = 2.2 \times 10^{-6}$ mol/cm^3 and $\rho = 3.6 \times 10^{-6}$ mol/cm^3. The reaction mixtures contained 14 - 56 ppm of NCN_3 and 5.5 - 17% of O_2.

Fig. 6.2 shows a typical experiment at a temperature of 1573 K. The two large Schlieren signals at $t = 0\,\mu$s and $t = 570\,\mu$s indicate the arrival of the incident and reflected shock wave at the observation point, respectively. Simulations using the compiled NCN mechanism revealed that, following a fast formation of NCN within a few μs, a slow decrease of the NCN concentration at longer reaction times would be expected mainly due to the reaction NCN + NCN. Additional loss due to the reaction NCN + O_2 should further enhance the decay rate. Surprisingly, the measured NCN profile (red noisy curve) did not show the expected shape (dotted curve) but a pronounced increase during the first 300 μs. Only at longer reaction times, the observed decay was similar to the one expected from the reaction NCN + NCN alone. A first explanation for this increase could be the slow O_2 relaxation resulting in a temperature decrease during the experiment. With decreasing temperature, the NCN absorption cross section strongly increases such that the observed (apparent) NCN increase would simply reflect the temperature change due to the vibrational relaxation process. Therefore, the temperature (and density) change during the experiment has been explicitly taken into account as described in Section 6.2. The rate constants $1/\tau$ for the relaxation process have been calculated for each reaction mixture using the relaxation times measured for Ar and O_2 by White and Millikan[29] and Rao and Skinner[20] assuming a linear mixture rule. For the experiment shown in Fig. 6.2, the calculated temperature profile (blue curve) and an accordingly corrected NCN profile (black noisy curve) have been included. Two conclusions can be drawn: i) The black and red colored NCN profiles nearly overlap, hence the overall temperature (and density) effect, $\Delta T = -9$ K and $\Delta \rho = +1 \times 10^{-8}$ mol/cm^3, is way to low to be responsible for the observed NCN increase. In fact an unfeasible temperature change of $\Delta T = -90$ K

Table 6.1: Selected reaction rate constant data for the numerical simulations of the experiments. Rate constants are given as $k_i = A \times \exp[-E_a/RT]$ in units of cm^3, mol^{-1}, s^{-1} and kJ. The listed rate constants for NCN reactions have been duplicated for triplet and singlet NCN to take ^{1}NCN chemistry approximately into account. Similarly, all reactions containing O_2 have been duplicated to account for both O_2 and O_2(cold) reactivity. In addition to the reactions shown in the Table, the GRI-Mech 3.0 was used as background mechanism.

No.	Reaction	A	E_a		Ref.
2	$NCN + O_2 \rightarrow$ products	1.3×10^{12}	97		this work
3	$O_2(\text{cold}) \rightarrow O_2$	see text			this work
4	$NCN_3 \rightarrow {}^1NCN + N_2$	4.9×10^9	71	$\rho = 3 \times 10^{-6}$ mol/cm^3	22
5	$^1NCN \rightarrow NCN$	$> 1.5 \times 10^6$			see text
6	$^1NCN + O_2 \rightarrow NCNOO$	see text			this work
7	$NCNOO \rightarrow NCN + O_2$	6.9×10^3	2.6		this work
8	$NCN + NCN \rightleftharpoons CN + CN + N_2$	1.0×10^{12}	0		5, see text
9	$NCN + O \rightleftharpoons CN + NO$	9.6×10^{13}	5.8		5
10	$NCN + M \rightleftharpoons C + N_2 + M$	8.9×10^{14}	260		5
11	$NCN + NO \rightleftharpoons CN + N_2O$	1.9×10^{12}	26		4
12	$NCN + NO_2 \rightleftharpoons NCNO + NO$	4.7×10^{12}	38		4
13	$NCN + C \rightleftharpoons CN + CN$	1.0×10^{14}	0		22
14	$NCN + N \rightleftharpoons N_2 + CN$	1.0×10^{13}	0		2
15	$NCN + CN \rightleftharpoons C_2N_2 + N$	1.3×10^{14}	33.5		2

would have been needed to fully account for the experimentally observed NCN signal increase. ii) The timescale of the vibrational relaxation process (which is not yet complete after 570 μs in Fig. 6.2) is significantly longer than the observed characteristic timescale of the NCN increase, hence vibrational relaxation of O_2 cannot be responsible for the observed signal shape. To confirm this conclusion, additional experiments with He added to the reaction gas mixtures have been performed. Helium is known to promote O_2 relaxation, however, He addition did not have any effect on the initial slope of the NCN signals.

Having shown that the effect of O_2 relaxation is minor, the increase of the NCN profile must be assigned to an actual concentration increase. As it is not conceivable that O_2 triggers an additional NCN formation reaction sequence that may account for the extra NCN at longer reaction times, we rather assume that the slow NCN formation indicates the formation of an NCN reservoir species that must have been formed right at the beginning of the reaction. In accordance with the initial NCN-OO adduct found by Zhu and Lin on the singlet potential energy surface,[10] it is likely that a similar adduct exists on the triplet surface as well. To serve as an explanation, the formation of this adduct must be fast in order to be able to compete against the likewise fast CIISC process (5), $^1NCN \rightarrow NCN$. To test the reasonability of the postulated formation of a reservoir species, the reactions

$$^1NCN + O_2 \rightarrow NCNOO \text{ and} \tag{6}$$

$$NCNOO \rightarrow NCN + O_2 \tag{7}$$
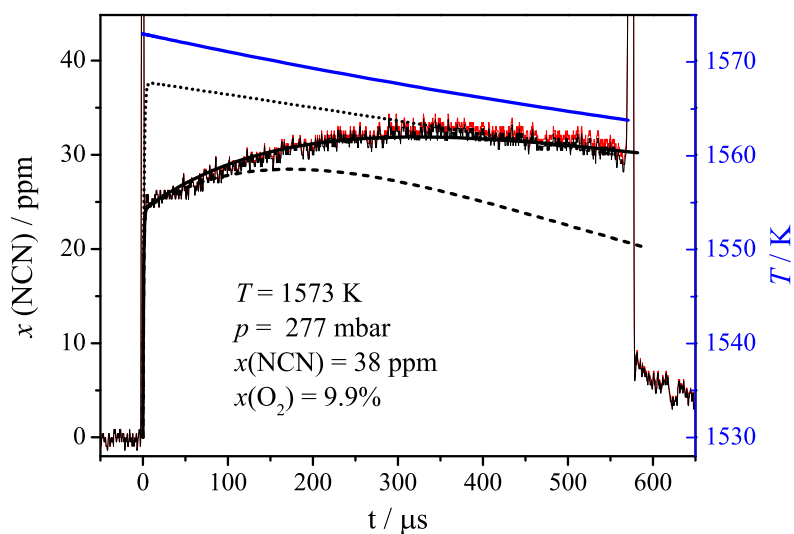
Figure 6.2: Shock tube experiment behind an incident shock wave. Red noisy curve: Experimental NCN profile assuming constant temperature and density. Black noisy curve: Calculated NCN profile allowing for temperature and density change caused by O_2 vibrational relaxation. Dotted curve: Simulated NCN profile with constant temperature and without the formation of an NCN reservoir species. Solid curve: Best fit obtained with k_7 and $\phi = k_6/(k_6 + k_5)$ as adjustable parameters and $k_8 = 1.0 \times 10^{12}$ cm³mol⁻¹s⁻¹. Dashed curve: Simulated NCN profile using the same k_7 and ϕ value but with k_8 set to a high value of 3.7×10^{12} cm³mol⁻¹s⁻¹. Blue curve: Simulated temperature profile.

have been implemented into the reaction mechanism.

Actually, by adjusting the rate constants k_6 and k_7, the experimental NCN profiles could be well captured in all cases; the simulated solid thick curve in Fig. 6.2 serves as an example. Reaction (7) determines the slope of the delayed NCN formation, whereas the ratio $\phi = k_6/(k_6 + k_5)$ determines the amount of ¹NCN captured by O_2 and hence the overall NCN plateau. By fitting the measured NCN profiles, k_7 and ϕ could be reliably determined at temperatures between 918 K $\leq T \leq$ 1595 K. At these temperatures, the reaction NCN + O_2 was too slow to contribute significantly to the overall NCN profiles and the gradual decrease of NCN at longer reaction times could be fully attributed to the reaction NCN + NCN (8). Its rate constant was inferred from Ref. 5, however, instead of adopting the recommended value of 3.7×10^{12} cm³mol⁻¹s⁻¹ that was obtained for higher total densities, we used the reported lower limit for k_8 with a value of 1.0×10^{12} cm³mol⁻¹s⁻¹. According to Fig. 2 in Ref. 5, this value corresponds better to the densities used in this work. Note that the dashed curve in Fig. 6.2, which represents a simulation with k_8 set to 3.7×10^{12} cm³mol⁻¹s⁻¹, clearly shows that such a high rate constant value overestimates the observed NCN loss at longer reaction times.

The rate constant k_5 of the ¹NCN CIISC process has been determined by Dammeier et al. for NCN₃/argon mixtures.[22] Compared to their work, our experiments showed a much faster rise time of the ³NCN profiles revealing that oxygen is a more efficient collision partner than argon and that the CIISC process is dominated by collisions with O_2. Even for the experiment at the lowest temperature of this work, the initial increase of the NCN profile was already close to the time resolution of the experimental setup (about 3 μs). Therefore, it was not possible to accurately determine k_5 values and
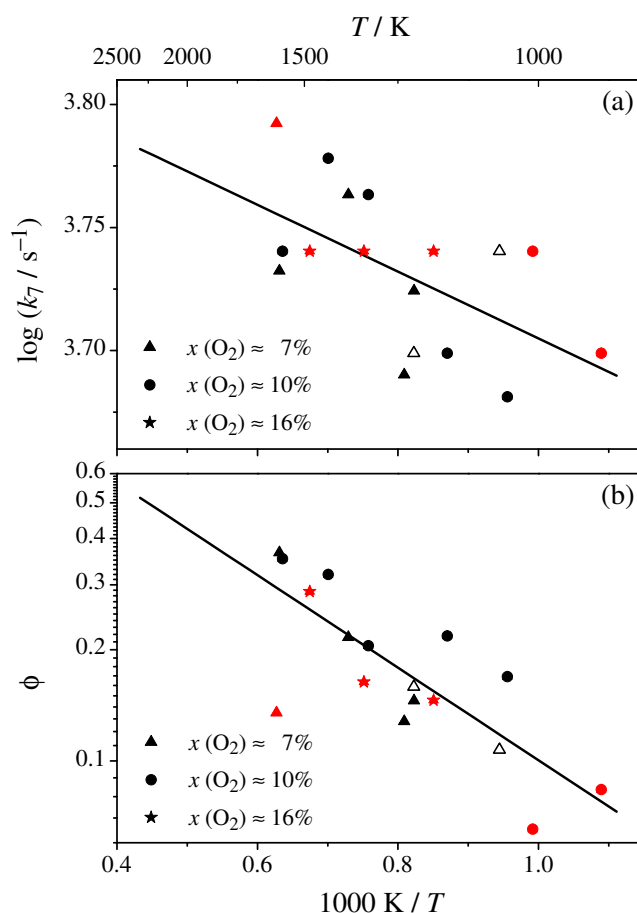
Figure 6.3: a) Determined rate constants k_7 for the NCNOO decomposition and b) semilogarithmic plot of the branching ratio $\phi = k_6/(k_6 + k_5)$. Red symbols: experiments with about 3% He in the reaction mixture; black symbols: experiments without He; filled symbols: $\rho \approx 2.0 \times 10^{-6}$ mol/cm^3; open symbols: $\rho \approx 3.8 \times 10^{-6}$ mol/cm^3.

hence, k_5 was simply increased to a lower limit of 1.6×10^6 s^{-1} to make sure that the CIISC process was modeled fast enough. Consequently, also the absolute value of k_6 could not be determined but only its value relative to k_5. Experimental conditions and fitting results for k_7 and $\phi = k_6/(k_6 + k_5)$ are listed in Tab. 6.2 and plotted in Fig. 6.3a and b.

ϕ increases from a value of 0.08 at $T = 920$ K to 0.29 at $T = 1600$ K. By attributing this temperature dependence to reaction (6) alone, a lower limit of the activation energy $E_a > 32$ kJ/mol for the formation of the NCNOO adduct can be inferred. In contrast to the branching ratio ϕ, the rate constant k_7 of the NCNOO decomposition was found to be almost temperature independent. It can be represented by the Arrhenius expression

$$k_7/\left(\text{cm}^3\text{mol}^{-1}\text{s}^{-1}\right) = 6.9 \times 10^3 \exp\left(-\frac{2.6\,\text{kJ/ mol}}{RT}\right)$$

with $E_a = (2.6 \pm 1.9)$ kJ/mol (2 σ error). Within the scatter of the data, no dependence neither from the used O_2 mole fractions (different symbols in Fig. 6.3a and b) nor from the density ($\rho \approx 2.0 \times 10^{-6}$ mol/cm^3 for the filled and $\rho \approx 3.8 \times 10^{-6}$ mol/cm^3 for the open symbols in Fig. 6.3) was found.

Table 6.2: Experimental conditions for the measurements of the rate constant of the NCNOO decomposition (7) and the $k_6/(k_6 + k_5)$ branching ratio ϕ.

T / K	p / mbar	NCN_3 / ppm	O_2 / %	k_7 / 10^3 s^{-1}	ϕ
1046	164	28	9.9	4.8	0.17
1059	329	24	7.3	5.5	0.11
1149	186	28	10	5.8	0.22
1215	197	26	7.3	5.3	0.15
1216	394	26	7.3	5.0	0.16
1236	201	29	6.6	4.9	0.13
1320	218	27	10	5.8	0.21
1356	230	27	7.3	5.8	0.22
1427	245	32	10	6.0	0.32
1573	277	38	9.9	5.5	0.35
1584	276	33	7.3	5.4	0.37
experiments with about 3% He					
918	140	14	13	5.0	0.08
1008	156	14	11	5.5	0.07
1176	196	21	17	5.5	0.15
1331	230	22	17	5.5	0.16
1483	263	24	17	5.5	0.29
1595	276	15	6.3	6.2	0.14

Also the addition of He (red symbols in Fig. 6.3) had no influence on the extracted data for k_7 and ϕ.

6.3.2 NCN + O$_2$

The rate constant of the reaction $NCN + O_2$ has been determined at temperatures $1674\,K \leq T \leq 2308\,K$ and pressures between 216 and 634 mbar, corresponding to total densities of $\rho = 1.48 \times 10^{-6}$ and $\rho = 3.76 \times 10^{-6}$ mol/cm^3. The upper accessible temperature limit was determined by the onset of NCN thermal decomposition, $NCN + M$; the lower temperature limit was set by the reaction $NCN + NCN$, which becomes dominant at temperatures below 1700 K. For modeling purposes, $NCO + NO$ have been assumed as the sole products of reaction (2), hence small contributions from the minor $CNO + NO$ channel are included in k_7

An example for a typical NCN concentration-time profile at initial reaction conditions of $T = 2036$ K and $p = 264$ mbar ($\rho = 1.62 \times 10^{-6}$ mol/cm^3) is presented in Fig. 6.4a. Again, the experimental NCN profile calculated with constant reaction conditions (red noisy curve) is shown in comparison with the NCN profile (black noisy curve) accounting for an O_2 relaxation induced temperature ($\Delta T = -38$ K) and density change ($\Delta \rho = +6.6 \times 10^{-8}$ mol/cm^3). The correction is more distinct than for the profile shown in Fig. 6.2 because with 17% O_2 in the reaction mixture the overall effect was stronger and at higher temperatures the O_2 relaxation is faster. As can be seen from the resulting temperature profile (blue curve) the timescale of the O_2 relaxation was about 50 μs. The solid black curve represents
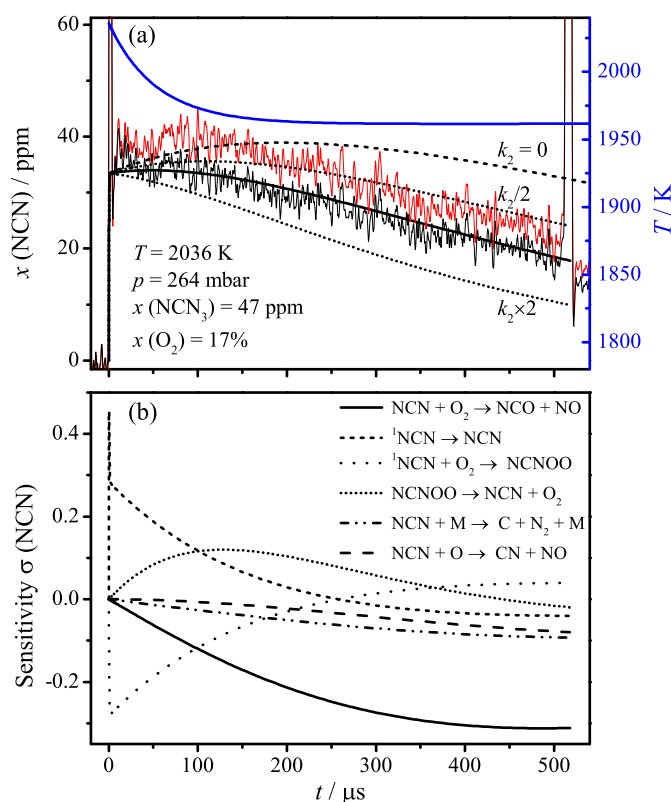
Figure 6.4: Determination of the rate constant k_2 (NCN + O$_2$). a) Experimental NCN concentration-time profiles assuming constant temperature (red noisy curve) and changing temperature (black noisy curve) resulting from O$_2$ relaxation. The blue curve corresponds to the assumed temperature profile. The thick black curve represents the best fit using $k_2 = 5.0 \times 10^9 \mathrm{cm^3 mol^{-1} s^{-1}}$, the other curves correspond to simulations using varied k_2 values. b) Corresponding sensitivity analysis of the best fit simulation.

the best simulation using $k_2 = 5.0 \times 10^9$ cm^{3}mol^{-1}s^{-1}. The two dotted curves and the dashed curve, which do not fit the measured signal, correspond to simulations using a two times higher or lower k_2 value and a simulation with k_2 set to zero. The strong influence of the reaction NCN + O$_2$ on the observed NCN profile is further outlined by the sensitivity analysis shown in Fig. 6.4b. At $t >$ 100 μs the target reaction becomes the most sensitive reaction and hence dominates the experimentally observed NCN decay. During the first 100 μs, however, the assumed branching ratio ϕ as well as the NCNOO decomposition are most important. In order to improve the quality of the fit, these values have been allowed to vary within their error limits but were found to be essentially consistent with the high-temperature extrapolations of the data in Fig. 6.3a and b. The used values of ϕ and k_7 were important to reproduce the overall shape of the NCN profile at the beginning of the experiment but have only a minor influence on the NCN consumption at longer reaction times and the extracted k_2 values. Interestingly, the reaction NCN + O (9) gains some importance towards the end of the observation time because O atoms are formed through the secondary reactions CN + O$_2$ and C + O$_2$. The rate constant k_9 has been precisely measured in previous work.[5] Since the rate constant k_2 is now much faster, in contrast to the experiment in Fig. 6.2, the experiment at $T = 2036$ K in Fig. 6.4 does not show a distinct influence of the reaction NCN + NCN.

As becomes clear from the discussion above, despite the interfering O_2 relaxation and NCN re-formation, the rate constant of the reaction $NCN + O_2$ could be reliably extracted. Experimental conditions for 18 experiments are given in Tab. 6.3 and the extracted k_2 values are plotted in Arrhenius form in Fig. 6.5. Open symbols correspond to measurements at higher total densities of $\rho \approx 3.52 \times 10^{-6}$ mol/cm^3, filled symbols to measurements at $\rho \approx 1.75 \times 10^{-6}$ mol/cm^3. Furthermore, the square symbols indicate experiments with 1% He added to the reaction mixture, circles are experiments without He. Within the scatter of the data neither the total density nor the addition of He influenced the outcome for k_2. Also experiments with varied O_2 mole fractions yielded consistent results. Overall, the data points reveal a strong temperature dependence, $E_a = (97 \pm 11)$ kJ/mol, and are best represented by the Arrhenius expression (solid line)

Table 6.3: Experimental conditions for the measurements of the rate constant k_2 for $NCN + O_2$.

T / K	p / mbar	NCN_3/ ppm	O_2 / %	He / %	k_2 / $(cm^3 mol^{-1} s^{-1})$
1674	408	41	17	1.2	1.4×10^9
1756	216	35	17	1.2	2.6×10^9
1777	522	18	5.5	0	1.8×10^9
1841	343	49	17	1.2	2.0×10^9
1849	344	40	10	1.2	3.0×10^9
1856	336	36	9.9	0	1.6×10^9
1926	587	25	11	0	2.4×10^9
1984	249	51	17	1.2	4.5×10^9
2020	255	47	17	1.2	5.2×10^9
2036	264	47	17	1.2	5.0×10^9
2059	634	20	11	0	3.5×10^9
2086	264	55	17	1.2	5.3×10^9
2107	267	45	17	1.2	4.2×10^9
2117	269	56	17	1.2	4.2×10^9
2232	286	55	17	1.2	1.0×10^{10}
2257	706	18	11	0	1.1×10^{10}
2263	290	43	17	1.2	6.0×10^9
2308	445	54	17	1.2	9.0×10^9

$$k_2 / \left(cm^3 mol^{-1} s^{-1}\right) = 1.3 \times 10^{12} \exp\left(-\frac{97 \, kJ/\, mol}{RT}\right), (\pm 57\%).$$

Allowing for partial error compensation, the error of the stated rate expression has been estimated to be $\pm 57\%$. Corresponding error bars for selected data points are shown in Fig. 6.5. The error arises from the statistical fit ($\pm 25\%$), the uncertainties of the absolute NCN_3 and O_2 concentrations ($\pm 5\%$) and of the rate constants assumed for the background mechanism. The two most important reactions for NCN consumption are NCN + NCN (8) and NCN + O (9). Varying k_8 in the range of $0 \leq k_8 \leq 2 \times 10^{12}$ cm^{3}mol^{-1}s^{-1} and k_9 within error limits ($k_9 \pm 40\%$) add a $\pm 25\%$ uncertainty. For the less important secondary chemistry, the cumulated overall uncertainty for k_2 was found to be $\pm 7\%$. Note that the uncertainties arising from the formation (represented by ϕ) and slow decomposition
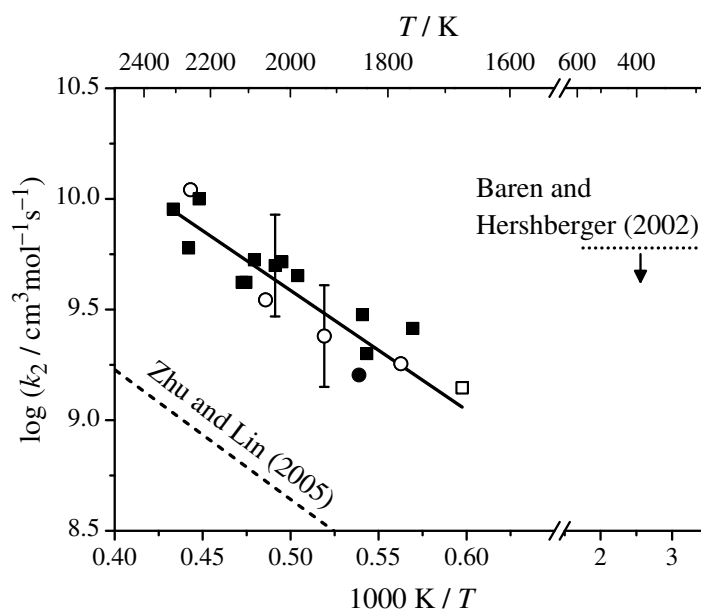
Figure 6.5: Arrhenius plot of k_2 (NCN + O$_2$) data obtained in this work (symbols) in comparison with the theoretical prediction of Zhu and Lin[10] (dashed curve) and the low temperature upper estimate of Baren and Hershberger (dotted curve).[13] Open symbols: $\rho \approx 3.52 \times 10^{-6}$ mol/cm^3; filled symbols: $\rho \approx 1.75 \times 10^{-6}$ mol/cm^3; squares: experiments with 1.2% He added; circles: experiments without helium; solid line: Arrhenius fit.

(k_7) of the NCNOO complex are comparably minor because these processes do not have a strong influence on the NCN decay at longer reaction times. However, as already mentioned above, k_7 and ϕ are important to reproduce the overall shape of the NCN profile, hence we allow for an additional uncertainty of k_2 on the order of $\pm 5\%$.

6.4 Discussion

Fig. 6.5 compares k_2 (NCN + O$_2$) data of this work with the transition state theory prediction of Zhu and Lin (dashed curve).[10] The outdated, several orders of magnitude higher rate constant estimate from Glarborg et al.[14] is not shown. The reported upper limit by Baren and Hershberger (dotted curve),[13] which was based on low temperature (298 K to 573 K) and low pressure ($\sim$ 3 Torr) experiments is not directly comparable with our data but does not contradict our results. The overall agreement with the transition state calculations is rather satisfying. The measured Arrhenius activation energy of $E_A = 97$ kJ/mol is in very good agreement with the theoretical estimate, but the absolute experimental values are about a factor of five higher. As the overall temperature dependence is dominated by the transition state barrier connecting the *cis*-NCN-OO isomer with the products (see Fig. 6.1), we tentatively assume that the remaining discrepancy stems from uncertainties of the relative heights of the entratnce barriers either forming the *cis*- or *trans*-isomer, respectively. Already Zhu and Lin noted in their paper that, due to the lack of experimental data, it would be hard to quantitatively assess the reliability of their calculated energies, which were obtained by the G2M(CC1) level of theory.

93

The alternative CNO forming channel of reaction (2) has been neglected for the simulations of the NCN profiles. Not only that this channel has been published to be minor ($< 15\%$, according to Ref. 10), also the assumed products of the reaction turned out to be unimportant. Subsequent chemistry of NCO, which is included in the background mechanism (GRI-Mech 3.0), did not play any discernible role. Hence, no information on the product branching ratio of reaction (2) could be inferred from the experiments presented in this work.

Although the actual kinetic treatment of the NCN re-formation process turns out to be less important for the rate constant determination of k_2, it deserves a closer look. In fact ^{1}NCN relaxation by CIISC, which is dominated by collisions with O_2, and the formation of the NCNOO adduct according to ^{1}NCN + $^3O_2 \rightarrow ^3$NCNOO represent two directly competing processes. Therefore, in agreement with the experimental findings (see Fig. 6.3b), the branching ratio $\phi = k_6/(k_6 + k_5)$ is not expected to change significantly with the amount of oxygen present in the reaction mixture. Interestingly, the pronounced increase of the branching ratio with temperature reveals that NCNOO formation is an activation controlled process. As already mentioned above, a rough estimation of the corresponding activation energy yields a lower limit of $E_a = 32$ kJ/mol. Here, the CIISC process (5) was assumed to be temperature independent; allowing for a positive temperature dependence would yield an even higher E_a value for k_6. Apparently, the formation of the ^{3}NCNOO adduct exhibits a pronounced entrance barrier, hence similar to the ^{3}NCN + $^3O_2 \rightarrow ^1$NCNOO reaction. In contrast to ϕ, the rate constant k_7 for the assumed re-formation of NCN has been found to be nearly temperature independent. It is therefore unfeasible that NCN is formed through the simple reverse of reaction (6), which should be temperature dependent as well. Hence, it can be speculated that NCN re-formation takes actually place through a reaction sequence according to ^{3}NCNOO $\rightarrow ^1$NCNOO $\rightarrow ^3$NCN + O_2 involving an intersystem crossing (ISC) process. To confirm this hypothesis, ab initio calculations of the triplet potential energy surface including accurate ISC probabilities to the singlet surface are needed. Such calculations would have been beyond the scope of this paper.

6.5 Conclusion

Using NCN_3 pyrolysis behind shock waves as a quantitative NCN radical source, the total rate constant of the reaction NCN + O_2 has been directly measured for the first time. Between $1674 \,\text{K} \leq T \leq 2308 \,\text{K}$, the experimental data are best represented by the Arrhenius expression $k_2 / (\text{cm}^3\text{mol}^{-1}\text{s}^{-1}) = 1.3 \times 10^{12} \exp\left(-\frac{97 \,\text{kJ/ mol}}{RT}\right)$, no pressure dependence was observed. The high activation energy of 97 kJ/mol is in very good agreement with the transition state theory prediction of Zhu and Lin,[10] but the absolute experimental rate constant values are about a factor of 5 above the theoretical estimate. Compared to other bimolecular NCN reactions, such as NCN + H/O/OH/H_2, the reaction is still slow. Hence the results of this work confirm recent findings that the reaction NCN + O_2 is less important for NCN modeling in hydrocarbon flames.

The determination of k_2 turned out to be difficult, which is reflected in the rather high stated uncertainty for k_2 of about $\pm 57\%$. High O_2 mole fractions up to 17% had to be used for sensitive rate constant extraction. At such high O_2 concentrations, the O_2 vibrational relaxation and the resulting temperature

change during the experiments had to be included for the evaluation of the NCN concentration-time profiles. Unexpectedly, the shape of the NCN profiles indicated the fast formation of an NCN reservoir species, presumably NCNOO from the reaction of ^{1}NCN with O$_2$. The slow decomposition of this complex results in a re-formation of NCN at longer reaction times. While the formation of the NCNOO complex seems to be an activation controlled process, the delayed NCN formation was found to be temperature independent. This can be taken as an indication that a ^{3}NCNOO $\rightarrow$ ^{1}NCNOO intersystem crossing process is involved.

Acknowledgments

References

[1] C. P. Fenimore. Formation of nitric oxide in premixed hydrocarbon flames. *Proc. Combust. Inst.*, 13:373–380, 1971.

[2] L. V. Moskaleva and M. C. Lin. The spin-conserved reaction CH + N$_2$ $\longrightarrow$ H + NCN: A major pathway to prompt NO studied by quantum/statistical theory calculations and kinetic modeling of rate constant. *Proc. Combust. Inst.*, 28:2393–2401, 2000.

[3] V. Vasudevan, R. K. Hanson, C. T. Bowman, D. M. Golden, and D. F. Davidson. Shock Tube Study of the Reaction of CH with N$_2$: Overall Rate and Branching Ratio. *J. Phys. Chem. A*, 111:11818–11830, 2007.

[4] J. Dammeier and G. Friedrichs. Direct Measurements of the Rate Constants of the Reactions NCN + NO and NCN + NO$_2$ Behind Shock Waves. *J. Phys. Chem. A*, 115:14382–14390, 2011.

[5] J. Dammeier, N. Faßheber, and G. Friedrichs. Direct measurements of the high temperature rate constants of the reactions NCN + O, NCN + NCN, and NCN + M. *Phys. Chem. Chem. Phys.*, 14:1030–1037, 2012.

[6] N. Faßheber, J. Dammeier, and G. Friedrichs. Direct measurements of the total rate constant of the reaction NCN + H and implications for the product branching ratio and the enthalpy of formation of NCN. *Phys.Chem. Chem. Phys.*, 16:11647–11657, 2014.

[7] N. Faßheber, N. Lamoureux, and G. Friedrichs. Rate constant of the reaction NCN + H$_2$ and its impact on NCN and NO concentrations in low pressure CH$_4$/O$_2$/N$_2$-flames. *Phys. Chem. Chem. Phys.*, 17:15876–15886, 2015.

[8] A. Busch and M. Olzmann. Shock-Tube Study of the Thermal Decomposition of NCN. *Proc. Eur. Combust. Meeting*, Paper P810138, Vienna, Austria, 2009.

[9] A. Busch, N. González-García, G. Lendvay, and M. Olzmann. Thermal Decomposition of NCN: Shock-Tube Study, Quantum Chemical Calculations, and Master-Equation Modeling. *J. Phys. Chem. A*, 2015, DOI: 10.1021/acs.jpca.5b01347.

[10] R. S. Zhu and M. C. Lin. Ab Initio Study of the Oxidation of NCN by O$_2$. *Int. J. Chem. Kinet.*, 37:593– 598, 2005.

[11] A. El Bakali, L. Pillier, P. Desgroux, B. Lefort, L. Gasnot, J. F. Pauwels, and I. da Costa. NO prediction in natural gas flames using GDF-Kin 3.0 mechanism. NCN and HCN contribution to prompt-NO formation. *Fuel*, 85:896–909, 2006.

[12] I. Gy. Zsely, J. Zador, and T. Turany. Uncertainty analysis of no production during methane combustion. *Int. J. Chem. Kinet.*, 40:754–768, 2008.

[13] R. E. Baren and J. F. Hershberger. Kinetics of the NCN Radical. *J. Phys. Chem. A*, 106:11093– 11097, 2002.

[14] P. Glarborg, M. U. Alzueta, K. Dam-Johansen, and J. A. Miller. Kinetic Modeling of Hydrocarbon/Nitric Oxide Interactions in a Flow Reactor. *Combust. Flame*, 115:1–27, 1998.

[15] L. B. Harding, S. J. Klippenstein, and J. A. Miller. Kinetics of CH + N$_2$ Revisited with Multireference Methods. *J. Phys. Chem. A*, 112:522–532, 2008,.

[16] E. Goos, C. Sickfeld, F. Mauß, L. Siedel, B. Ruscic, A. Burcat, and T. Zeuch. Prompt NO formation in flames: The influence of NCN thermochemistry. *Proc. Combust. Inst.*, 34:657–666, 2013.

[17] H.-L. Chen W.-S. Teng, L. V. Moskaleva and M. C. Lin. Ab Initio Chemical Kinetics for H + NCN: Prediction of NCN Heat of Formation and Reaction Product Branching via Doublet and Quartet Surfaces. *J. Phys. Chem. A*, 117:5775–5784, 2013.

[18] M. Colberg and G. Friedrichs. Room Temperature and Shock Tube Study of the Reaction HCO + O$_2$ Using the Photolysis of Glyoxal as an Efficient HCO Source. *J. Phys. Chem. A*, 110:160–170, 2006.

[19] J. Dammeier and G. Friedrichs. Thermal Decomposition of NCN$_3$ as a High-Temperature NCN Radical Source: Singlet-Triplet Relaxation and Absorption Cross Section of NCN($^3\Sigma$). *J. Phys. Chem. A*, 114:12963–12971, 2010.

[20] V. S. Rao and G. B. Skinner. A shock tube study of vibrational relaxation of O$_2$ in argon by small amounts of H$_2$ (860-1290 K), D$_2$ (890-1070 K), and He (1000-1500 K). *J. Chem. Phys.*, 81:775–778, 1984.

[21] H. Oertel. *Stoßrohre / Shock Tubes / Tubes á choc*, volume section B. 7.4.2. Schwingungsrelaxation. Springer-Verlag, Wien, 1966, ISBN: 3211807748.

[22] J. Dammeier, B. Oden, and G. Friedrichs. A consistent model for the thermal decomposition of NCN$_3$ and the singlet-triplet relaxation of NCN. *Int. J. Chem. Kinet.*, 45:30–40, 2013.

[23] S. A. Beaton and J. M. Brown. Laser Excitation Spectroscopy of the A$^3\Pi_u$- X$^3\Sigma_g^-$ Transition of the NCN Radical. 2. The ν_2 Hot Band. *J. Mol. Spectrosc.*, 183:347–359, 1997.

[24] N. Lamoureux, C. M. Western, X. Mercier, and P. Desgroux. Reinvestigation of the spectroscopy of the A$^3\Pi_u$- X$^3\Sigma_g^-$ transition of the NCN radical at high temperature: Application to quantitative NCN measurement in flames. *Combust. Flame*, 160:755–765, 2013.

[25] G. P. Smith, R. A. Copeland, and D. R. Crosley. Electronic quenching, fluorescence lifetime, and spectroscopy of the A$^3\pi_u$ state of NCN. *J. Chem. Phys.*, 91:1987–1993, 1989.

[26] R. J. Kee, F. M. Ruply, and J. A. Miller. *Chemkin- II: A Fortran Chemical Kinetics Package for the Analysis of Gas-Phase Chemical Kinetics, Sandia Report SAND89-8009, Sandia National Laboratories, Livermore, California (Sept. 1989).*

[27] G. P. Smith, D. M. Golden, M. Frenklach, N. W. Moriarty, B. Eiteneer, M. Goldenberg, C. T. Bowman, R. Hanson, S. Song, W. C. Gardiner Jr., V. Lissianski, and Z. Qiu. *GRI-Mech Version 3.0*, 1999. http://www.me.berkeley.edu/gri_mech, last accessed: 15.04.2015.

[28] E. Goos, A. Burcat, and B. Ruscic. *Extended Third Millenium Ideal Gas and Condensed Phase Thermochemical Database for Combustion with Updates from Active Thermochemical Tables.* (2009) http://garfield.chem.elte.hu/Burcat/burcat.html, last accessed 10.01.2015.

[29] D. R. White and R. C. Milikan. Oxygen Vibrational Relaxation in O$_2$-H$_2$ Mixtures. *J. Chem. Phys.*, 39:2107–2108, 1963.

7 Characterization of a high temperature HNO source, first measurements of HNO profiles behind shock waves and determination of the rate constant for the reaction HNO + O$_2$

Nancy Faßheber, and Gernot Friedrichs[*]

Institute für Physikalische Chemie, Christian-Albrechts-Universität zu Kiel

to be submitted

Own contributions:

- FM setup.

- Shock tube experiments.

- Room temperature measurements.

- Analysis of the experimental data.

- Writing of manuscript draft.

Abstract

Using the very sensitive absorption based frequency modulation (FM) spectroscopy, concentration-time profiles of HNO have been measured behind shock waves for the first time. The UV photolysis of glyoxal/NO mixtures at $\lambda = 193$ nm served as a HNO source via the fast initial formation of HCO followed by the reaction HCO + NO $\rightarrow$ CO + HNO. High temperature and room temperature FM spectra of three selected lines of the $\tilde{A}^1A''$ - $\tilde{X}^1A'$ transition of HNO have been recorded at wavelengths around 618 and 625 nm. By analyzing HNO and HCO concentration-time profiles under similar reaction conditions it was possible to determine the HNO absorption cross section. A temperature dependent value of $\log\frac{\sigma_{HNO}}{cm^2mol^{-1}} = 5.14 - 6.0 \times 10^{-4} \times (T/K)$ was determined at temperatures between 700 K and 1150 K. Experiments with 0.4% - 1% O$_2$ in the reaction gas mixture were performed to measure the rate constant of the reaction HNO + O$_2$ $\rightarrow$ NO + HO$_2$. Between 750 K and 1275 K the experimental data are best represented by the Arrhenius expression $k_1 / (cm^3mol^{-1}s^{-1}) = 6.1 \times 10^{12}\exp\left(-\frac{21\,kJ/\,mol}{RT}\right)$. The experiments have been performed at total densities of 7.3×10^{-6} mol/cm^3 $\leq \rho \leq 16.6 \times 10^{-6}$ mol/cm^3. No pressure dependence was discernible. The determined rate constant data are up to four orders of magnitude higher than frequently used literature data.

7.1 Introduction

Nitrogen oxides (NO$_x$) are atmospheric pollutants formed during combustion processes. Nitroxyl (HNO) is an important flame intermediate closely linked to NO$_x$. Most HNO reactions with other flame intermediates like H, OH, O and O$_2$ and the HNO thermal decomposition directly form NO. Depending on the combustion conditions, most of these reactions can also proceed in the opposite direction and in this case decrease the amount of NO formed in flames. For example the Reaction H + NO + M $\rightleftharpoons$ HNO + M contributes significantly to NO reduction using CO/H$_2$ mixtures as reducing agents during combustion (NO reburning).[1,2] To model the most favorable reaction conditions for overall NO reduction detailed mechanisms including accurate high temperature rate constant data for HNO are necessary. Yet most HNO reactions are poorly investigated experimentally, because intermediate concentrations of HNO in flames are low and the high temperature cross section is presumably small. HNO measurements at high temperatures are only reported by Lozovsky et al.[3,4]. They used the sensitive intracavity laser absorption spectroscopy (ICLAS) to monitor HNO spectra in low-pressure CH$_4$ flames. So far, rate expressions for most HNO reactions implemented into combustion mechanisms rely on experiments at low temperatures or theoretical studies.

Also the title reaction

$$HNO + O_2 \rightarrow HO_2 + NO \qquad (1)$$
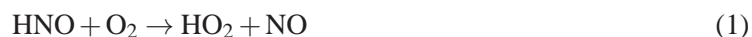
has only been measured between 296 K and 421 K by Bryokov et al.[5,6] In the only high temperature study, Miller and Bowman indirectly determined the k value for this reaction by adjusting its rate constant as part of a high temperature mechanism assembled for the reaction of isocyanic acid with nitric oxide.[7] They recommended a fairly low rate constant expression $k_1/(cm^3mol^{-1}s^{-1}) = 1.0 \times 10^{13}\exp[-105$ kJ/mol/(RT)]. In the widely used mechanism GRI-Mech 3.0[8] for methane

combustion the Arrhenius activation energy of this expression has been reduced to 54 kJ/mol by comparison with the analogous reaction $RH + O_2$, which is not supposed to have a large barrier height. At temperatures around 1500 K, this provides about three orders of magnitude higher k_1 values than reported by Miller and Bowman. An even higher overall rate expression has been assumed by Klaus and Warnatz as part of an NO_x formation/reduction mechanism.[9,10] However, the basis of their expression has not been explicated in these studies. The influence of the reaction $HNO + O_2$ on the NO formation is strongly dependent on the reaction conditions. In a study by Wang et al. on the combustion of pyridine, reaction (1) turned out to be the main source for NO under reducing atmosphere.[11] The strong discrepancy of the few available literature data and their implementation in detailed combustion mechanisms clearly points out the need for a reliable experimental high temperature rate constant value for the reaction $HNO + O_2$.

7.2 Experimental

7.2.1 Shock tube and slow flow cell

All high temperature measurements were carried out in an overall 8 m long electropolished, stainless steel shock tube, which has been described in detail elsewhere.[12] Briefly, the 4.5 m long test section with an inner diameter of 81 mm could be pumped down to pressures of $p = 10^{-7}$ mbar by a combination of turbomolecular and diaphragm pumps. The shock tube was operated with hydrogen or mixtures of hydrogen and nitrogen as driver gas, 30 μm thick aluminum foils have been used as diaphragms. The experimental conditions were calculated from the pre-shock conditions together with the shock wave velocity, measured by four fast piezo-electric sensors mounted flush in the shock tube wall. A frozen-chemistry code taking into account real gas effects and shock wave damping has been applied. In principle the slow O_2 vibrational relaxation process may compromise a simple frozen-chemistry calculation of the experimental conditions. However, the used O_2 mole fractions were always below 1%, which results in a very small effect on the experimental conditions that turned out to be negligible for our analyses.

Room temperature experiments were performed in a 45 cm long slow flow cell equipped with quartz windows. The detection and the photolysis laser beams were overlapped in the cell and propagated in opposite directions.

An ArF excimer laser (Radiant Dyes Exc 200) was used for the UV photolysis of glyoxal at $\lambda = 193$ nm. Two dichroic mirrors in front and behind the shock tube or the flow cell were used to collinearly overlap the detection and the UV laser beams. Additionally, a UV filter was placed in front of the detector to block residual intensity of the photolysis laser. For the shock tube experiments, the photolysis beam was slightly focused by a 1000 mm lens (effective diameter was about 4 mm in the shock tube), for the room temperature measurements the area of the UV beam was reduced by a telescope to about 1 cm^2. In both cases the excimer laser beam diameter was larger than the diameter of the detection laser to minimize the effects of diffusional processes on the measured HNO concentration-time profiles.

7.2.2 Gas mixture preparation

Storage gas mixtures of about 2% glyoxal and 3% NO in Ar were prepared in a gas mixing system using the partial pressure method. The mixing system could be evacuated to pressures of $p < 1 \times 10^{-5}$ mbar and was equipped with several 5 - 20 L glass flasks. A flask with a cooling finger was used for purification of NO by several freeze-pump-thaw cycles. The storage gas mixtures were mixed and further diluted by a flow system with mass flow controllers. The freshly prepared reaction gas mixtures slowly flushed the test section for a few minutes prior to the actual shock tube experiments to prevent possible effects from the adsorption of the reactants at the shock tube walls. Storage mixtures were used within three to four days.

Glyoxal was prepared by dehydration of the trimer dehydrate $((CHO)_2)_3 \times 2H_2O$ by 3 eq. of phosphoric anhydride (P_2O_5). The solid reaction mixture was slowly heated up to $155°C$ i. vac. $(1 \times 10^{-2}$ mbar). The gaseous product was passed through an ice water cooling trap to remove impurities. The purity of glyoxal was checked by FT-IR measurements and it was stored in a liquid nitrogen trap.

7.2.3 FM-spectroscopy

HNO and HCO were detected by means of frequency modulation (FM) spectroscopy which is a sensitive, absorption based detection method.[13,14,15] The used setup was similar to the one described by Friedrichs et al.[14,16] Briefly, wavelengths between 600 nm and 650 nm were generated by a cw ring dye-laser (Coherent 899 series) operated with Kiton Red as laser dye and pumped by a solid state Nd:YVO$_4$ laser (Coherent Verdi V 10). The wavelength was measured interferometrically by a wavemeter (MetroLux WL200). The laser beam was modulated at a frequency of 1 GHz by a resonant electro-optic modulator (New Focus 4421), the resulting frequency modulated spectrum was analyzed by a scanning etalon. The modulation depth was set to a modulation index of $M \approx 1.4$. The laser beam was focused through the shock tube windows by a 300 mm lens, coupled into an optical fiber and detected by a fast silicon photodiode (Hamamatsu, S5973). The signal was split into the AC and the DC part by a Bias Tee (Mini Circuits, ZFBT-4R2G). The DC component corresponds to I_0 and was directly monitored by a digital oscilloscope, the AC component represents the FM signal. It was bandpass filtered at 1 GHz (Trilithic), demodulated by a frequency mixer (Mini Circuits, 5542-ZFM-2000), amplified and low pass filtered at 2.5 MHz resulting in the signal intensity I_{FM}. A two-polarizer setup was used to adjust a voltage controlled phase shifter (Knick, J45) to set the phase angle of demodulation to zero, resulting in pure absorption induced signal. The demodulated FM-signal is proportional to the concentration c of the absorbing species according to

$$I_{FM} = \frac{I_0}{2} \times \Delta f \times \sigma \times [c] \times l_{eff} \times G.$$

σ is the narrow-bandwidth line center absorption cross section and l the absorption path length. The electronic gain factor $G = 184$ of the used FM setup was determined experimentally and was in agreement with previous determinations.[12] The FM factor Δf was calculated from line shape data and

was about $\Delta f = 0.8$ for HNO and $\Delta f = 0.3$ for HCO under the experimental conditions of this work. If the absorption cross section and line shape data for one species are known, it is therefore possible to perform quantitative FM measurements. Whereas for HCO the data are well known for the Q(6)P(1) absorption line of the $\tilde{A}^2 A'' - \tilde{X}^2 A' (09^0 0 \leftarrow 00^1 0)$ transition at $\lambda = 614.752$ nm[12], they were determined for HNO for three selected absorption lines of the $\tilde{A}^1 A''(100) - \tilde{X}^1 A'(000)$ transition in this work. To determine the initial HCO concentrations generated by glyoxal UV photolysis, HCO concentration-time profiles have been measured as a reference (see below) at similar reaction conditions and comparable photolysis energies.

7.2.4 HNO source

HNO molecules were generated by $\lambda = 193$ nm photolysis of glyoxal/NO mixtures in argon. The HNO formation proceeds according to the reaction sequence

$$(CHO)_2 + h\nu \rightarrow (H, HCO, CO, H_2, CH_2O), \tag{2}$$

$$H + (CHO)_2 \rightarrow HCO + CO + H_2, \tag{3}$$

$$HCO + NO \rightarrow HNO + CO. \tag{4}$$
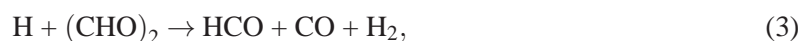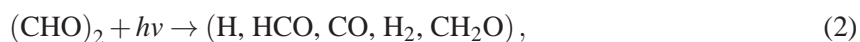
To model HNO formation, additional glyoxal and HCO reactions have been adopted from our previous work[12,14,16,17,18] and the GRI-Mech 3.0[8] has been assumed as a background mechanism in order to take possible secondary chemistry into account. The initial $[H]_0/[HCO]_0$ ratio from the glyoxal photolysis has been adopted from a previous study of Colberg and Friedrichs.[12] They showed that H atoms are formed in excess, typically ratios of about 3 at high temperatures and about 2 at room temperature were used. Over the fast reaction HCO + NO (4), which has been investigated experimentally behind shock waves by Dammeier et al.,[17] the HCO concentration is directly linked to HNO formation. Hence, both the assumed HCO mechanism as well as the overall HNO yield could be confirmed by quantitative measurements of HCO concentration-time profiles resulting from the photolysis of glyoxal and glyoxal/NO mixtures. It turned out that the HCO concentration profiles could be nicely modeled without adjusting the mechanism.

Note that the reaction

$$H + NO + M \rightleftharpoons HNO + M \tag{5}$$

was also included in the mechanism but was found to be too slow to contribute notably to the overall HNO concentrations. Just as well, the reverse reaction HNO + M is slow and only had a minor influence on HNO removal at longer reaction times.

7.3 Results and Discussion

Shock tube and room temperature measurements of HNO and HCO concentration-time profiles at similar reaction conditions (temperature, pressure, mixture composition, and photolysis energy) have

Table 7.1: Important reactions for HNO formation and consumption from the photolysis of gly-
oxal/NO mixtures in shock tube experiments. Parameters for modified Arrhenius expres-
sion $k = AT^n \exp(-E_a/(RT))$ are given in units of mol, cm, s and kJ.

no.	reaction	A	n	E_a	ref.	T-range
1	HNO + O$_2$ → HO$_2$ + NO	6.1×10^{12}		21	this work	750-1275 K
3	(CHO)$_2$ + H → H$_2$ + CO + HCO	5.4×10^{13}		18	12	295-1107 K
4	HCO + NO → HNO + CO	8.1×10^{12}			17	295 K
		7.1×10^{12}			17	770-1300 K
6	HNO + H → H$_2$ + NO	9.7×10^{11}	0.62	1.49	19	200-2500 K
8	HCO + H → H$_2$ + CO	1.1×10^{14}			16	195-2100 K
9	HCO + M → H + CO + M	4.0×10^{13}		65	14	835-1230 K
11	NO$_2$ + H → NO + OH	9×10^{13}			20	195-2000 K
12	(CHO)$_2$ + OH → H$_2$O + CO + HCO	1.3×10^{13}			12	700-1150 K
		6.4×10^{12}			21	298 K
13	HCO + O$_2$ → HO$_2$ + CO	6.9×10^6	1.9	−5.7	22	295-1705 K
14	HNO diffusion	1×10^3			this work	750-1275 K
		3×10^3			this work	298 K

been performed. Different reaction mixtures with initial [NO]/[glyoxal] ratios from zero to 0.87 were used. From repeated, iterative analysis aiming on the consistent modeling of all measured HNO and HCO profiles at different experimental conditions, the HNO formation mechanism, the HNO absorption cross section, and the rate constant of the reaction HNO + O$_2$ could be determined.

7.3.1 HNO detection

For quantitative HNO detection and to determine the position of the maximum of the FM signal, the Doppler and pressure broadened FM spectra of three selected absorption lines of the $\tilde{A}^1A''(100) - \tilde{X}^1A'(000)$ band at wavenumbers of 16171.99, 16173.86 and 16002.36 cm^{-1} were investigated at different experimental conditions summarized in Tab. 7.2. The HNO absorption spectra measured by Bancroft et al.[23] and Pearson et al.[24] were used as a starting point to determine the exact positions of the HNO FM-signals. Fig. 7.1 illustrates the measured (red symbols), normalized FM spectra of the three absorption bands in comparison with the simulated absorption (dashed curves) and FM spectra (red curve).

Table 7.2: Summary of the measured pressure broadening parameters for three selected HNO absorp-
tion lines.

line	center wavelength/ cm^{-1}	max FM signal/ cm^{-1}	average T/ K	average p / mbar	$\Delta\tilde{v}_p$/ (GHz/bar)
1	16173.86	16173.82	770	570	2.0
2	16171.99	16171.93	970	880	1.8
2	16171.99	16171.93	298	100	3.5
3	16002.36	16002.32	1250	1140	1.4

The HNO absorption spectrum has been simulated with the PGOPHER program[25] based on the spectroscopic constants taken from Pearson et al. The simulated line positions and relative intensities

have been adopted from the PGOPHER output to calculate the corresponding FM spectra with a program developed in our working group. The simulations are in good agreement with the measured data, only small line shifts on the order of 0.02 cm^{-1} were necessary. The three absorption bands have been measured at different temperatures of about 298, 970, 770 and 1250 K, respectively, and therefore yielded a set of pressure broadening parameters (see Tab. 7.2). From these data the pressure broadening coefficient was determined to be $\Delta\nu_p \approx 3.5(T/298\ \text{K})^{-0.6}$ GHz/bar. In agreement with our experiments the PGOPHER simulations predict similar intensities for the two $R_3(J'')$ lines and a two times higher intensity for the $Q_0(16)$ line at temperatures around 1000 K. Therefore, the $Q_0(16)$ line provides better signal-to-noise ratios and was selected for all kinetic shock tube measurements of this work.
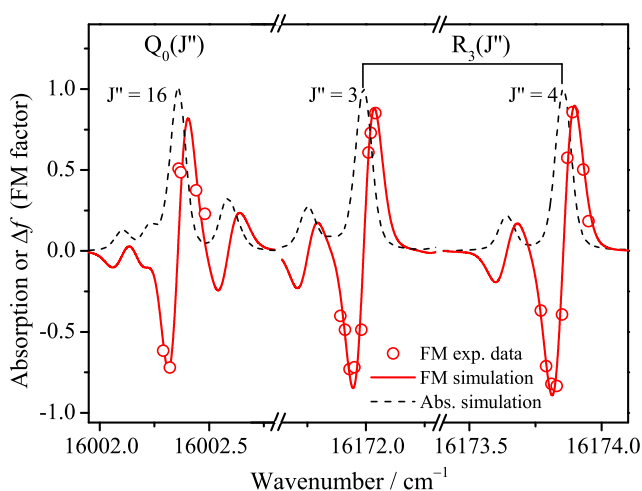
Figure 7.1: Normalized experimental FM-spectrum of HNO (red symbols) in comparison with simulated FM (red curve) and absorption spectra (dashed curve) for three lines of the (100)-(000) band of the $\tilde{A}^1A'' - \tilde{X}^1A'$ HNO transition. The experimental conditions are listed in Tab. 7.2.

7.3.2 HNO formation mechanism and absorption cross section

For quantitative HNO measurements it is important to know the initial [HCO]$_0$ concentrations from glyoxal photolysis. Ideally, simultaneous measurements of HCO and HNO profiles would have to be performed. However, as either HCO or HNO could be detected with our setup, all experiments have been performed at least twice under very similar reaction conditions (T, p, mixture composition, photolysis energy) either detecting HCO or HNO. In Fig. 7.2a and 7.2b experimental and numerically modeled HNO and their corresponding HCO concentration-time profiles are displayed. As already outlined above, the HCO profile could be well simulated without any adjustment of the mechanism adopted from the literature. Only the initial [HCO]$_0$ concentrations were varied to fit the maximum of the measured HCO profile.

HNO reactions were initially taken from GRI-Mech 3.0[8] and were varied by a factor of up to 100

to identify reactions with potentially strong impact on the simulated HNO profile. From the reactions (HNO + H, HNO + H$_2$, HNO + CO, HNO + NO, and HNO + M) only the reaction

$$HNO + H \rightleftharpoons H_2 + NO \tag{6}$$

turned out to be actually important for the overall HNO concentration. Available literature data for k_6 at high temperatures differ by two orders of magnitude.[19,26,27] Simulations of the measured HNO concentration-time profiles both behind shock waves and at room temperature were most consistent using the most recent theoretical expression by Nguyen et al. which is valid for the entire temperature range of this work and is on the upper limit of the reported literature values.[19] Using lower rate constant values for HNO + H would result in higher simulated overall HNO concentrations and to a little to steep HNO increase at the beginning of the experiment.
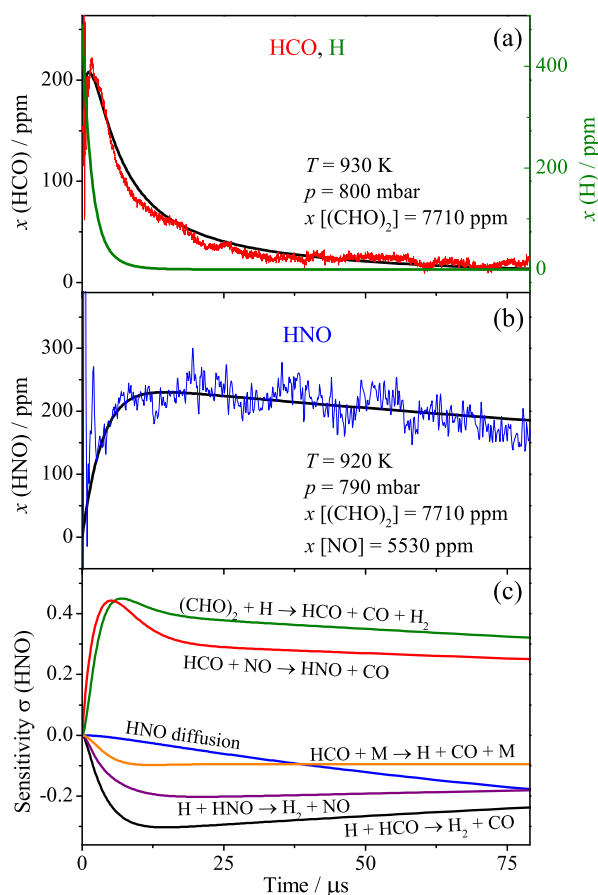
Figure 7.2: a) HCO concentration-time profile measured after the photolysis of 7720 ppm glyoxal in argon in comparison with the simulation for HCO and H. b) Experimental and simulated HNO concentration-time profile at similar reaction conditions. c) Corresponding HNO sensitivity analysis.

A sensitivity analysis for an HNO profile measured behind the reflected shock wave is illustrated in Fig 7.2c and reveals the six most important reactions for HNO formation and consumption. The rate constants of the reactions (3), (4), (8) and (9) are important for HCO as well and have been validated

by the HCO experiments. The reaction HNO + H is important because, next to HCO, H atoms are formed in high yields from the glyoxal photolysis as well. As already outlined above, its rate constant k_6 is not accurately known, however its influence remains comparably small. All simulations (for reaction mixtures without O_2) predict stable HNO concentration plateaus towards longer reaction times showing that HNO is a stable species under the reaction conditions applied in this work. In contrast, we observe a slow loss of HNO that can be attributed to diffusional loss of HNO out of the photolysis volume. HCO reacts on a much faster timescale than HNO such that no diffusion correction is needed for HCO.

Table 7.3: Experimental conditions and results for HNO absorption cross section of the $^R R_3(4)$ transition at room temperature (295 K) and behind shock waves.

p / mbar	glyoxal/ ppm	NO/ ppm	O_2 / ppm	HCO_0 / ppm	$\sigma \times 10^{-5}$ / $cm^2 mol^{-1}$
		room temperature			
50	9990	4710	1500	20	1.8
95	10400	6560	6095	19	1.7
100	9850	8380	2000	19	1.9
101	10075	4180	640	12	2.0
101	10040	4180	1565	11	1.8
102	9970	4150	2790	13	2.0
104	15400	6675	3400	22	1.9

T / K	p / mbar	glyoxal/ ppm	NO/ ppm	HCO_0 / ppm	$\sigma \times 10^{-4}$ / $cm^2 mol^{-1}$
		reflected shock wave			
721	495	8915	7780	100	5.8
765	554	7995	4370	125	5.1
771	570	9990	8670	120	5.1
785	591	9990	8670	120	5.7
808	625	7735	4425	150	4.0
837	660	9990	8670	130	3.5
863	596	10645	6750	120	3.5
864	600	12150	6495	130	4.0
898	755	7880	4600	120	3.8
908	770	7735	4425	150	3.0
916	781	8080	1454	130	3.5
920	790	7710	5525	160	2.9
938	819	7690	6620	160	3.2
948	835	7975	5090	130	2.9
983	891	7880	4600	120	3.5
1042	1360	11505	7180	90	3.4
1046	1373	11640	7260	90	3.0
1049	1371	11505	7180	90	3.0
1055	1032	10810	5825	100	3.0
1065	1049	10270	8050	110	3.7
1117	942	9040	6990	150	3.0
1118	1542	11500	7175	90	2.5
1133	1170	10270	8050	110	3.3

The HNO absorption cross section for a single transition at the line center can be determined by the equation:

$$\sigma = \frac{2 \times I_{FM}}{I_0 \times \Delta f \times [\text{HNO}] \times l_{\text{eff}} \times 184}$$

The maximum [HNO] concentrations were simulated based on the mechanism in Tab. 7.1 together with the initial $[\text{HCO}]_0$ concentrations, which were taken from the direct HCO measurements. The

Δf values were determined using the line shape data from the measured HNO FM spectra together with the calculated experimental conditions and modulation indices M. The experimental conditions and the determined absorption cross section values for the $^RR_3(4)$ line are listed in Tab. 7.3 and plotted in Fig. 7.3. Between 720 K $< T <$ 1133 K the logarithm of the cross section can be approximated by the linearized expression:

$$\log\left(\frac{\sigma_{HNO}}{cm^2 mol^{-1}}\right) = 5.14 - 6.0 \times 10^{-4} \times \left(\frac{T}{K}\right).$$
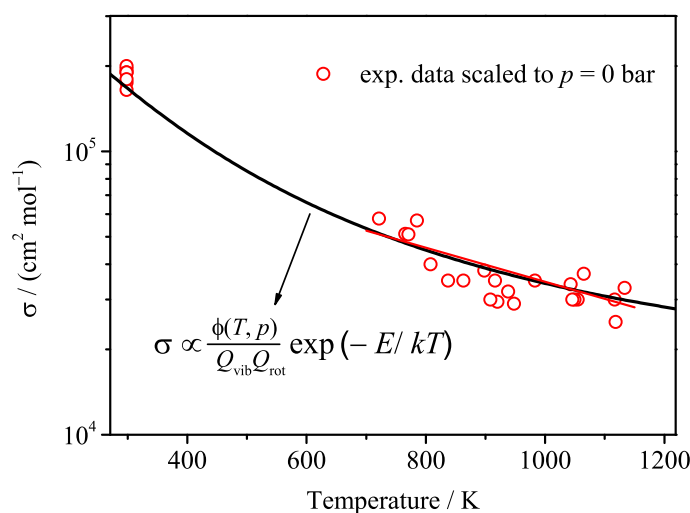
Figure 7.3: Temperature dependence of the experimentally determined HNO absorption cross section of the $^RR_3(4)$ transition between 298 and 1133 K.

7.3.3 Room temperature measurements

FM measurements of HNO at room temperature have been performed to verify the absolute value and the temperature dependence of the HNO absorption cross section determined from the shock tube experiments. The experimental conditions of seven room temperature experiments are summarized in Tab. 7.3. Mixtures of about 1% glyoxal and 4180 to 8380 ppm NO were studied at pressures of 50 and 100 mbar. Additional O_2 has been added to the reaction mixtures to capture the large amounts of H atoms, formed from the glyoxal photolysis, that would cause a low HNO yield due to the fast reaction $HNO + H \rightarrow H_2 + NO$. Actually, over the equilibrium

$$2\,NO + O_2 \rightleftharpoons NO_2 \tag{7}$$

certain amounts of NO_2 are formed during the mixing of the reactants that rapidly react with H atoms as well. Sensitivity analyses reveal that the formed H atoms mainly react through this reaction. In Fig. 7.4a and Fig. 7.4b, a typical HNO (blue curve) and the corresponding HCO (red curve)

concentration-time profiles at room temperature and $p = 50$ mbar are shown together with the best numerical fits. Also the simulated profiles without O$_2$ in the reaction mixtures are shown (dashed black curves). Both HNO yield and HCO concentrations at longer reaction times would be significantly lower without the addition of O$_2$ due to fast reaction with H atoms. This effect is more pronounced for HNO and would result in about a factor of two lower HNO concentrations at 50 μs reaction time.
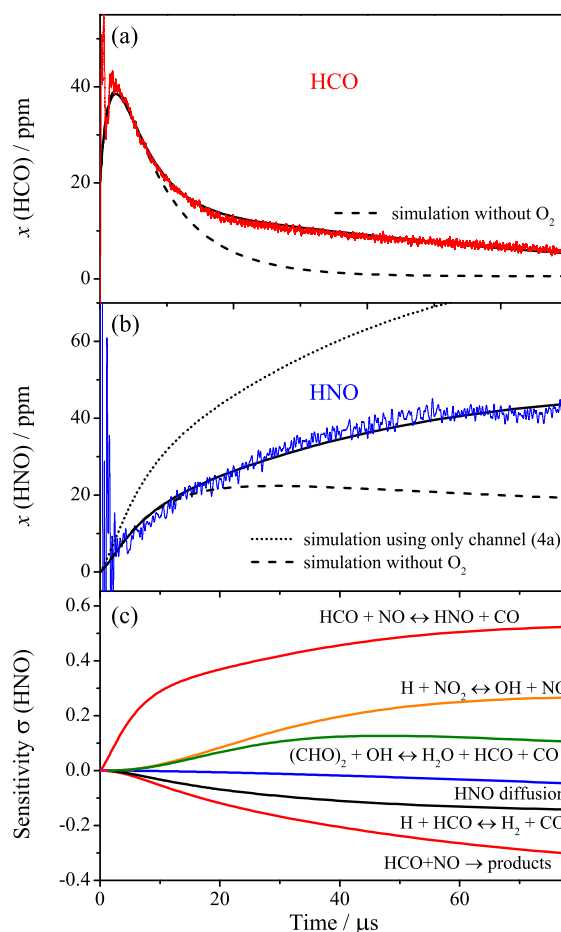
Figure 7.4: a) Experimental concentration-time profiles of HCO (red curve) and b) HNO (blue curve) under the same reaction conditions at room temperature and $p = 50$ mbar together with the respective simulated profiles (black curves) using 1% glyoxal, 4700 ppm NO and 1500 ppm O$_2$. Dotted and dashed curves represent simulations using different assumptions (see text). c) Corresponding HNO sensitivity analysis.

It is known from theoretical work of Xu et al.[28] that at room temperature a second reaction channel for the HNO forming reaction HCO + NO needs to be considered.

$$HCO + NO \;\rightarrow\; HNO + CO \qquad \sim 70\% \tag{4a}$$

$$HCO + NO \;\rightarrow\; HC(O)NO \;(\rightarrow \; products) \qquad \sim 30\% \tag{4b}$$

For reaction channel (4b), the formation of a stable complex was assumed, which did not contribute further to the overall HNO formation. The actually assumed branching ratio has been fine-tuned by carefully fitting the HNO concentration rise at the beginning of the experiment. For comparison, an HNO concentration-time profile simulation only considering the HNO forming channel (4a) is also shown in Fig. 7.4b (dotted curve). This simulation does not fit the experimental profile. Also the corresponding HNO sensitivity analysis in Fig. 7.4c illustrates that the branching ratio for the two channels of reaction (4) is crucial for the overall HNO concentration Overall, the branching ratio for the HNO forming channel (4a) was found to be about 0.70 in our experiments, which is consistent with the theoretical value of about 0.75 estimated by Xu et al. Four other reactions also appear in the HNO sensitivity analysis. The reactions H + HCO (8), H + NO$_2$ (11), and glyoxal + OH (12) are again validated by consistent modeling of HCO and HNO measurements. Also the HNO diffusion is included but its contribution is only minor due to large beam diameter of the photolysis laser (compared to the detection beam) in case of the room temperature experiments.

By analyzing experiments at different pressures and glyoxal/NO ratios an HNO absorption cross section of

$$\sigma = (1.8 \pm 0.2) \times 10^5 \ \text{cm}^2/\text{mol}$$

has been found which is in very good agreement with the shock tube data. In Fig. 7.3 all experimental σ values (red dots) are shown together with the theoretically expected (black curve) temperature dependence of the absorption cross section. The prediction is based on the line shape parameter $\phi(T, p)$, the term value of the lower energy state E as well as the vibrational (Q_{vib}) and rotational (Q_{rot}) partition function of HNO. Overall, the experimental data points are well described by the prediction, showing that the room temperature and high temperature experiments are consistent.

7.3.4   Rate constant of the reaction HNO + O$_2$

The rate constant of the reaction

$$HNO + O_2 \rightarrow HO_2 + NO \tag{1}$$

has been measured behind reflected shock waves by adding between 0.43% and 1% O$_2$ to the glyoxal/NO reaction mixtures. The experimental conditions are summarized in Tab. 7.4. The HNO absorption cross section as well as the background mechanism for HNO have been adopted from the experiments without O$_2$.

A typical HNO concentration-time profile obtained at $T = 945$ K and $p = 700$ mbar can be seen in Fig. 7.5a. 6900 ppm O$_2$ were added to a typical reaction mixture of 1 % glyoxal and 7600 ppm NO in argon. The two black curves in the Figure represent HNO simulations with and without oxygen present in the reaction mixture. While the rapid HNO formation directly after the photolysis is not affected by the addition of O$_2$, the HNO concentration decreases faster in the experiment with O$_2$. The direct comparison between the two simulations reveals that the rate constant for reaction (1) could be derived from this experiments. The corresponding sensitivity analysis is shown in Fig. 7.5b. Only the five most sensitive reactions are included in the diagram. The reaction HNO + O$_2$ is the most important reaction

to model the HNO decrease at longer reaction times, but the reactions of HCO, HNO and (CHO)$_2$ with H atoms do also contribute to the overall HNO concentration profile. However, as the mechanism has been validated by the experiments without O$_2$ added, the perturbation of the HNO concentration-time profile can be attributed mostly to the reaction HNO + O$_2$.
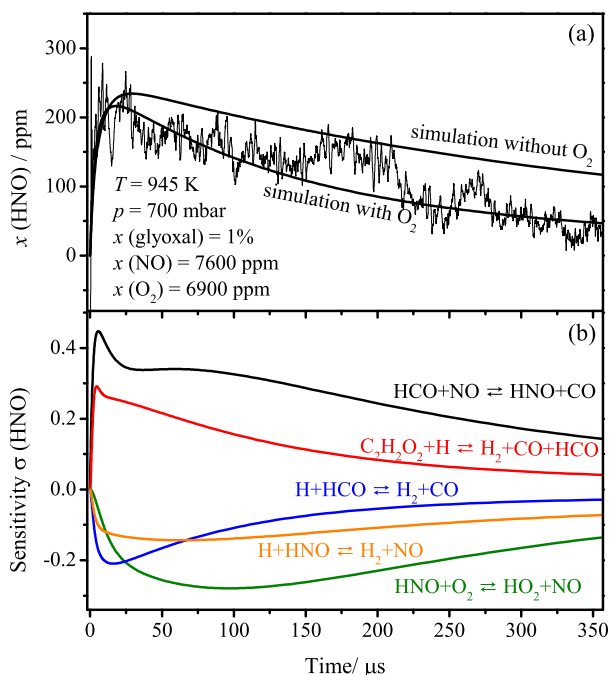
Figure 7.5: a) Typical HNO concentration-time profile with O$_2$ present in the reaction mixture. b) Corresponding HNO sensitivity analysis.

All experimental conditions and results for 21 experiments for the determination of k_1 are summarized in Tab. 7.4 and are plotted in the Arrhenius diagram in Fig. 7.6. The data are best represented by the Arrhenius expression (solid line in Fig. 7.6):

$$k_1 / \left(\mathrm{cm^3 mol^{-1} s^{-1}}\right) = 6.1 \times 10^{12} \exp\left(-\frac{21\,\mathrm{kJ/\,mol}}{RT}\right),\ \Delta(\log k_1) = \pm 0.17$$

with a weak temperature dependence of 21 ± 3 kJ/mol. At densities of $\rho = 7.26 \times 10^{-6}$ mol/cm^3 to $\rho = 1.66 \times 10^{-5}$ mol/cm^3 (corresponding to pressures of 452 - 1542 mbar) no pressure dependence was discernible. The error stated for the total rate constant expression includes several sources of uncertainty. Main errors may result from the uncertainties of the initial HCO concentrations, the HNO absorption cross section, and the secondary chemistry of HNO, HCO and glyoxal. However, both the absorption cross section and the HNO formation mechanism have been adopted from experiments without O$_2$ and therefore it can be safely assumed that the uncertainties compensate. Overall, the associating uncertainty is about 25%. The statistical error from the fitting procedure of the experiments results in an additional $\pm 23\%$ error (2σ standard error of the mean). An overall error of about $\pm 48\%$

($\Delta (\log k_1) = \pm 0.17$) is obtained.

Table 7.4: Experimental conditions and results for the experiments on the reaction HNO + O$_2$ behind reflected shock waves.

T / K	p / mbar	ρ / 10^{-6} mol/cm^3	x (glyoxal) / %	x (NO) /ppm	x (O$_2$) / ppm	x_0 (HCO) / ppm	k_1 / 10^{11} cm^3/ (mol s)
749	452	7.26	1.10	5823	7485	160	2.1
822	546	7.99	1.16	7257	8290	85	3.0
863	596	8.30	1.06	6747	4884	165	3.0
882	619	8.44	0.93	9603	6309	150	3.7
945	707	9.01	1.02	7574	9640	140	4.5
971	750	9.29	1.15	7216	7475	110	5.2
1033	843	9.82	1.28	5887	4402	130	5.0
1041	844	9.74	0.97	7259	7991	70	5.0
1046	1372	15.8	1.16	7257	8290	90	4.8
1047	1375	15.8	1.14	7175	6732	90	6.7
1102	1505	16.4	1.16	7214	7754	90	6.5
1110	958	10.4	1.17	7325	8779	85	5.7
1118	1542	16.6	1.15	7174	6983	90	7.0
1145	997	10.5	1.06	6747	4884	160	7.0
1166	1035	10.7	1.06	6712	10016	130	8.0
1181	1055	10.8	1.02	7564	8223	140	6.5
1200	1090	11.0	1.06	6712	10016	130	7.3
1205	1090	10.9	1.00	6482	8737	120	7.4
1259	1178	11.3	1.06	6730	7457	130	8.5
1273	1191	11.2	1.01	6496	6502	120	9.0
1274	1190	11.2	1.01	6511	4257	120	8.0

7.3.5 Discussion

Selected literature data on the rate of the reaction HNO + O$_2$ are shown in comparison with the experimental data of this work in Fig. 7.6. A simple high temperature extrapolation of the low temperature intracavity laser absorption spectroscopic (ICLAS) measurements by Bryukov et al.[6], which have been performed between 296 and 421 K, would yield about three order of magnitude lower rate constants at a temperature of 1000 K. However, allowing for the often found positive curvature in the Arrhenius plot, this discrepancy would be somewhat smaller. As no transition state calculations have been performed yet, a reliable extrapolation of the low temperature data is not possible. Miller and Bowman indirectly determined the rate constant of reaction (1) as part of an extensive mechanism for the gas phase reaction of isocyanic acid with nitric oxide in the presence of O$_2$, H$_2$O and CO.[7] They compared their calculated mole fractions of species like NO, HNCO, and O$_2$ to measured mole fractions from different experimental investigations[29]. Their estimated rate expression $k_1/(\text{cm}^3\text{mol}^{-1}\text{s}^{-1}) = 1 \times 10^{13} \times \exp(-105 \text{ kJ/mol/RT})$ yields a four orders of magnitude lower rate constant at $T = 1000$ K and suggests a very strong temperature dependence of reaction (1) that is not consistent with our data. Already for the development of the combustion mechanism GRI Mech 3.0,[8] this unfeasible rate constant expression has been adjusted. Without further justification, by comparison with the analogous RH + O$_2$ reaction, in the GRI Mech 3.0 the pre-exponential factor has been adopted from Miller and Bowman but the Arrhenius activation energy has been decreased to 54 kJ/mol. This change increases the rate constant by a factor of 400 at $T = 1000$ K, hence still a factor of 30

lower than the experimental data of this work. Finally, the expression from Klaus and Warnatz[9] $k_1/(\text{cm}^3\text{mol}^{-1}\text{s}^{-1}) = 3.2 \times 10^{12} \times \exp(-12.5\ (\text{kJ/mol})/RT)$, provides the best agreement with our data. This expression stems from a detailed mechanism for NO$_x$ formation/reduction. Unfortunately, no information about the derivation of this comparably high value has been given.

Compared to the rather uncertain and inconsistent literature data, the measurements performed in this work constitute by far the most reliable high temperature determination. Although the overall effect of O$_2$ addition on the detected HNO profiles remained small, thanks to the perturbation approach (i.e., measurements with and without oxygen present), the rate constant could be determined with good accuracy. Note that the low rate constant estimate according to the GRI Mech 3.0 and the Miller and Bowman expressions would not have resulted in any noticeable change in the HNO profiles for experiments with and without O$_2$. This is in obvious disagreement with the experiments reported here.
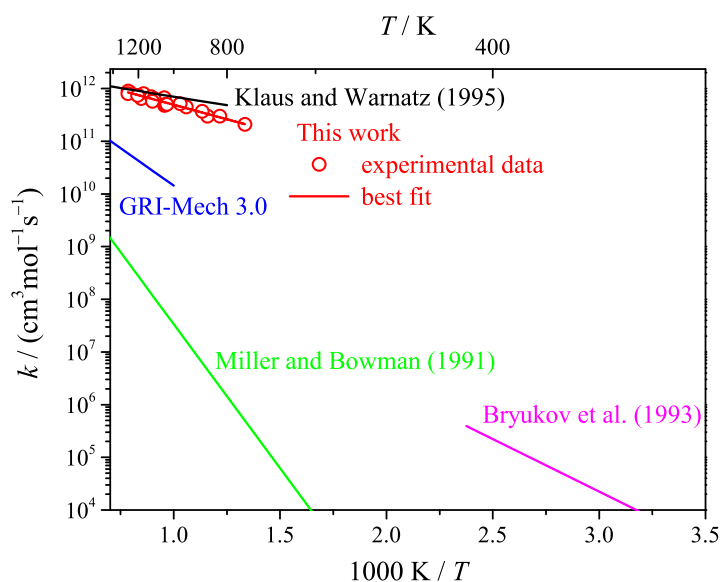
Figure 7.6: Arrhenius plot of measured rate constants for the reaction HNO + O$_2$ in comparison with available literature data.[6,7,8,9]

7.4   Conclusion

HNO has been detected behind shock waves for the first time by means of the very sensitive FM spectroscopy approach. FM spectra of three selected transitions have been recorded to determine accurate FM factors Δf and pressure broadening coefficients. The photolysis of glyoxal/NO mixtures was used as a source for HNO. Corresponding experiments with either HNO or HCO detection have been performed behind reflected shock waves and at room temperature to determine the HNO absorption cross section. Between 700 and 1150 K the absorption cross section of the ^{R}R$_3$(4) transition at

16173.86 cm^{-1} can be expressed by

$$\log\left(\frac{\sigma_{\text{HNO}}}{\text{cm}^2\text{mol}^{-1}}\right) = 5.14 - 6.0 \times 10^{-4} \times \left(\frac{T}{\text{K}}\right).$$

An HNO mechanism including the HNO formation from the reaction HCO + NO following the glyoxal photolysis as well as HNO secondary chemistry was developed and tested for various experimental conditions. Based on the determined HNO absorption cross section and this submechanism for HNO formation, which reliably describes the measured HNO profiles without O$_2$ in the reaction mixture, it was possible to measure rate constant data for the reaction HNO + O$_2$ $\rightarrow$ NO + HO$_2$. Up to 1% O$_2$ were added to the glyoxal/NO reaction mixtures. At temperatures of 749 K $\leq T \leq$ 1274 K the experimental data can be summarized by the Arrhenius expression:

$$k_1 / \left(\text{cm}^3\text{mol}^{-1}\text{s}^{-1}\right) = 6.1 \times 10^{12}\exp\left(-\frac{21\,\text{kJ/ mol}}{RT}\right), \Delta(\log k_1) = \pm 0.17$$

The comparison with existing literature data reveals that the most frequently used rate constant expression of Miller and Bowman[7] and from the GRI Mech 3.0[8] yield at least one order of magnitude too low rate constant data. Clearly, future work on a detailed theoretical treatment of the reaction based on high-level quantum-chemical calculations is needed to confirm both the high temperature rate constant expression as well as the reported temperature dependence obtained in this work. Furthermore, modeling work is required to range the importance of the reaction HNO + O$_2$ for NO$_x$ formation in flames. Finally, with the experimental setup presented in this work measurements of further bimolecular HNO reactions should be possible. Such data would hold the potential to contribute to a much better and quantitative understanding of HNO for NO$_x$ modeling in flames.

Acknowledgment

References

[1] P. Glarborg, P.G. Kristensen, K. Dam-Johansen, M.U. Alzueta, A. Millera, and R. Bilbao. Nitric oxide reduction by non-hydrocarbon fuels. Implications for reburning with gasification gases. *Energy & Fuels*, 14:828–838, 2000.

[2] P. Dagaut and F. Lecomte. Experiments and Kinetic Modeling Study of NO-Reburning by Gases from Biomass Pyrolysis in a JSR. *Energy & Fuels*, 17:608–613, 2003.

[3] V. A. Lozovsky and S. Cheskis. Intracavity laser absorption spectroscopy study of HNO in hydrocarbon flames dopted with N$_2$O. *Chem. Phys. Lett.*, 332:508–514, 2000.

[4] V. A. Lozovsky, I. Rahinov, N. Ditzian, and S. Cheskis. Laser absorption spectroscopy diagnostics of nitrogen-containing radicals in low-pressure hydrocarbon flames doped with nitrogen oxides. *Faraday Discuss.*, 119:321–335, 2002.

[5] M. G. Bryukov, A. A. Kachanov, S. I. Panov, V. P. Balakhnin, J. Vandoren, and O. M. Sarkisov. Study of the reaction of nitrosyl hydride with oxygen by intracavity laser spectroscopy. *Khim. Fiz*, 11:43–49, 1992.

[6] M. G. Bryukov, A. A. Kachanov, R. Timonnen, J. Seetula, J. Vandoren, and O. M. Sarkisov. Kinetics of HNO reactions with O$_2$ and HNO. *Chem. Phys. Lett.*, 208:392–398, 1993.

[7] J. A. Miller and C. T. Bowman. Kinetic Modeling of the Reduction of Nitric Oxide in Combustion Products by Isocyanic Acid. *Int. J. Chem. Kinet.*, 23:289–313, 1991.

[8] G. P. Smith, D. M. Golden, M. Frenklach, N. W. Moriarty, B. Eiteneer, M. Goldenberg, C. T. Bowman, R. Hanson, S. Song, W. C. Gardiner Jr., V. Lissianski, and Z. Qiu. *GRI-Mech Version 3.0*, 1999. http://www.me.berkeley.edu/gri_mech, last accessed: 15.04.2015.

[9] P. Klaus and J. Warnatz. A contribution towards a complete mechanism for the formation of NO in flames. *Joint meeting of the French and German Sections of the Combustion Institute*, Mulhouse, 1995.

[10] J. Warnatz, R. W. Dibble, and U. Maas. *Combustion: Physical and Chemical Fundamentals, Modeling and Simulation, Experiments, Pollutant Formation*. Springer, 2006.

[11] B. Wang, L.S. Sun, S. Su, J. Xiang, S. Hu, and H. Fei. A kinetic study of NO formation during oxy-fuel combustion of pyridine. *Applied Energy*, 92:361–368, 2012.

[12] M. Colberg and G. Friedrichs. Room Temperature and Shock Tube Study of the Reaction HCO + O$_2$ Using the Photolysis of Glyoxal as an Efficient HCO Source. *J. Phys. Chem. A*, 110:160–170, 2006.

[13] G. Friedrichs and H. Gg. Wagner. Quantitative FM Spectroscopy at High Temperatures: The Detection of ^{1}CH$_2$ behind Shock Waves. *Zeitschrift für Physikalische Chemie*, 12:1723–1746, 2000.

[14] G. Friedrichs, J. T. Herbon, D. F. Davidson, and R. K. Hanson. Quantitative detection of HCO behind shock waves: The thermal decomposition of HCO. *Phys.Chem. Chem. Phys.*, 4:5778–5788, 2002.

[15] G. Friedrichs. Sensitive Absorption Methods for Quantitative Gas Phase Kinetic Measurements. Part 1: Frequency Modulation Spectroscopy. *Zeitschrift für Physikalische Chemie*, 222:1–30, 2008.

[16] G. Friedrichs, D. F. Davidson, and R. K. Hanson. Validation of a Thermal Decomposition Mechanism of Formaldehyde by Detection of CH$_2$O and HCO Behind Shock Waves. *Int. J. Chem. Kinet.*, 36:157–169, 2004.

[17] J. Dammeier, Colberg, and G. Friedrichs. Wide temperature range (T = 295 K and 770 - 1305 K) study of the kinetics of the reactions HCO + NO and HCO + NO$_2$ using frequency modulation spectroscopy. *Phys.Chem. Chem. Phys.*, 9:4177–4188, 2007.

[18] G. Friedrichs, M. Colberg, J. Dammeier, T. Bentz, and M. Olzmann. HCO Formation in the Thermal Unimolecular Decomposition of Glyoxal: Rotational and Weak Collision Effects. *Phys.Chem. Chem. Phys.*, 10:6520–6533, 2008.

[19] H. M. T. Nguyen, S. Zhang, J. Peeters, T. N. Truong, and M. T. Nguyen. Direct ab initio dynamics studies of the reactions of HNO with H and OH radicals. *Chem. Phys. Lett.*, 388:94–99, 2004.

[20] M.-C. Su, S. S. Kumaran, J. V. Michael K. P. Lim, A. F. Wagner, L. B. Harding, and D.-C. Fang. Rate constants, 1100 $\leq T \leq$ 2000 K, for H + NO$_2$ $\longrightarrow$ OH + NO Using Two Shock Tube Techniques: Comparison of Theory to Experiment. *J. Phys. Chem. A*, 106:8261–8270, 2002.

[21] C. N. Plum, E. Sanhueza, R. Atkinson, W. P. L. Carter, and J. N. Pitts. Hydroxyl radical rate constants and photolysis rates of α-dicarbonyls. *Environ. Sci. Technol.*, 17:479–484, 1983.

[22] N. Faßheber, G. Friedrichs, P. Marshall, and P. Glarborg. Glyoxal oxidation: Implications for the reactions HCO + O$_2$ and OCHCHO + HO$_2$. *J. Phys. Chem. A*, 119:7305–7315, 2015.

[23] J. L. Bancroft, J. M. Hollas, and D. A. Ramsay. The absorption spectra of the HNO and DNO. *Can. J. Phys.*, 40:322–347, 1962.

[24] J. Pearson, A. J. Orr-Ewing, M. N. R. Ashfold, and R. N. Dixon. Spectroscopy and predissociation dynamics of the $\tilde{A}^1A$" state of HNO. *J. Chem. Phys.*, 106:5850–5873, 1997.

[25] C. M. Western. PGOPHER. *A Program for Simulating Rotational Structure, University of Bristol*, available at http://pgopher.chm.bris.ac.uk. last accessed: 10.04.2015.

[26] C. J. Halstead and D. R. Jenkins. Catalysis of recombination reactions in flames by nitric oxide. *Chem. Phys. Lett.*, 2:281–282, 1968.

[27] W. Tsang and J. T. Herron. Chemical kinetic data base for propellant combustion. I. Reactions involving NO, NO$_2$, HNO, HNO$_2$, HCN and N$_2$O. *J. Phys. Chem. R*, 20:609–663, 1991.

[28] Z. F. Xu, C.-H. Hsu, and M. C. Lin. Ab initio kinetics of the reaction of HCO with NO: Abstraction versus association/elimination mechanism. *J. Chem. Phys.*, 133:234308(1–11), 2005.

[29] D. L. Siebers and J. A. Caton. Removal of nitric oxide from exhaust gas with cyanuric acid. *Combust. Flame*, 79:31–46, 1990.

8 Glyoxal Oxidation Mechanism: Implications for the reactions HCO + O$_2$ and OCHCHO + HO$_2$

N. Faßheber[1], G. Friedrichs[*,1], Paul Marshall[2], and Peter Glarborg[3]

[1]*Institute für Physikalische Chemie, Christian-Albrechts-Universität zu Kiel*

[2]*Department of Chemistry and Center for Advanced Scientific Computing and Modeling (CASCaM), University of North Texas, Denton, 1155 Union Circle #305070, Texas 76203–5017*

[3]*Department of Chemical and Biochemical Engineering, Technical University of Denmark, DK-2800 Kgs. Lyngby, Denmark*
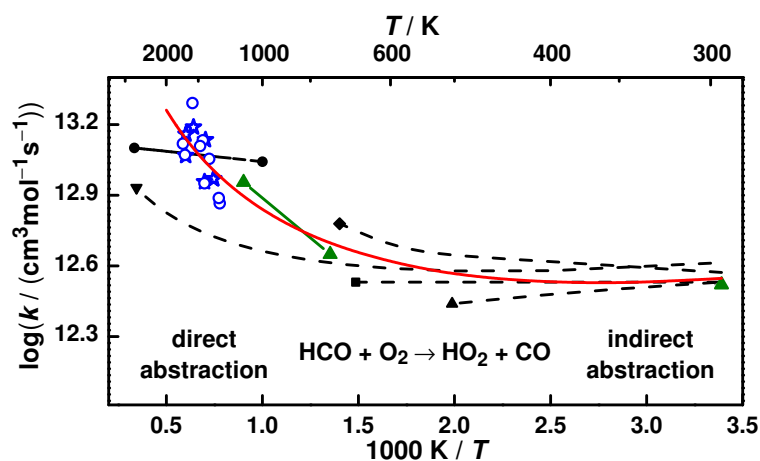
New measurements and a detailed analysis of the glyoxal oxidation mechanism revealed rate constant data for the reaction HCO + O$_2$ up to combustion-relevant high temperatures.

Own contributions:

- Shock tube experiments.

- Analysis of the experimental data.

- Interpretation and comparison of experimental data.

- Collaboration with P. Glarborg (Technical University of Denmark) and P. Marshall (University of North Texas) to assemble the glyoxal oxidation mechanism.

- Writing of manuscript draft (Experimental, Results and Discussion section and Conclusion).

Abstract

A detailed mechanism for the thermal decomposition and oxidation of the flame intermediate glyoxal (OCHCHO) has been assembled from available theoretical and experimental literature data. The modeling capabilities of this extensive mechanism have been tested by simulating experimental HCO profiles measured at intermediate and high temperatures in previous glyoxal photolysis and pyrolysis studies. Additionally, new experiments on glyoxal pyrolysis and oxidation have been performed with glyoxal and glyoxal/oxygen mixtures in Ar behind shock waves at temperatures of 1285 K − 1760 K at two different total density ranges. HCO concentration-time profiles have been detected by frequency modulation spectroscopy at a wavelength of $\lambda = 614.752$ nm. The temperature range of available direct rate constant data of the high temperature key reaction HCO + O$_2$ → CO + HO$_2$ has been extended up to 1705 K and confirms a temperature dependence consistent with a dominating direct abstraction channel. Taking into account available literature data obtained at lower temperatures, the following rate constant expression is recommended over the temperature range 295 K $< T <$ 1705 K:

$$k_1/(\mathrm{cm^3mol^{-1}s^{-1}}) = 6.92 \times 10^6 \times T^{1.90} \times \exp\left(+5.73 \text{ kJ/mol}/RT\right)$$

At intermediate temperatures, the reaction OCHCHO + HO$_2$ becomes more important. A detailed reanalysis of previous experimental data as well as more recent theoretical predictions favor the formation of a recombination product in contrast to the formerly assumed dominating and fast OH forming channel. Modeling results of the present study support the formation of HOCH(OO)CHO and provide a two orders of magnitude lower rate constant estimate for the OH channel. Hence, low-temperature generation of chain carriers has to be attributed to secondary reactions of HOCH(OO)CHO.

8.1 Introduction

The oxidation chemistry of glyoxal (OCHCHO) is of interest, partly because it is recognized as an intermediate in combustion of hydrocarbons and partly because glyoxal has been identified as a promising HCO high-temperature source for shock tube measurements.[1,2] Moreover, glyoxal is discussed as an important component in tropospheric chemistry.[3,4] Glyoxal can be formed from oxidation of C$_2$H$_2$ at low to medium temperatures,[5,6,7,8,9] as well as in the atmosphere,[10,11,12,13,14,15,16] mostly through the chain-propagating sequence

$$C_2H_2 \xrightarrow{+OH} C_2H_2OH \xrightarrow{+O_2} OCHCHO + OH$$
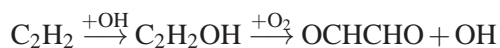
Previous studies of OCHCHO chemistry include thermal decomposition in static reactors[17] and shock tubes[18,19] as well as low-temperature oxidation[20,21,22] and determination of explosion limits in static reactors.[23] Also data on the low temperature oxidation of glyoxal by H$_2$O$_2$[24] and NO$_2$[25] have been reported. More recently, Colberg and Friedrichs,[2] in a combined shock tube/photolysis study of OCHCHO/O$_2$ mixtures, obtained rate coefficients for the reaction HCO + O$_2$ at 750-1110 K. To our knowledge, no detailed chemical kinetic modeling studies of glyoxal oxidation have previously been reported.

The objective of the present study is two-fold. We aim to develop a detailed chemical kinetic model for oxidation of OCHCHO in the intermediate to high temperature range for use in combustion studies. Furthermore, we wish to extend the measurement range for the rate constant of HCO + O$_2$ to higher temperatures. Novel shock tube experiments are conducted for OCHCHO and OCHCHO/O$_2$ mixtures in argon at temperatures from 1285 to 1760 K. The results from these experiments are combined with the previous data from Colberg and Friedrichs and implications for our understanding of glyoxal oxidation and for the overall rate constant of the reaction HCO + O$_2$ are discussed.

8.2 Detailed Kinetic Model

A mechanism has been assembled from recent work on the chemistry of glyoxal,[2,19] formic acid,[26] formaldehyde,[27] carbon monoxide[28] and hydrogen.[29] In the present work the OCHCHO oxidation subset of the mechanism was updated. The thermodynamic properties for OCHCHO and OCHCO are shown in Table 8.1,[30,31] while Table 8.2 lists key reactions in the OCHCHO oxidation scheme.[2,19,32,34,35] The full mechanism, including pressure dependent rate coefficients for many decomposition and recombination reactions, is available as Supporting Information.

In addition to the OCHCHO subset discussed below, particular attention was paid to the reaction of HCO with O$_2$,

$$HCO + O_2 \rightleftharpoons CO + HO_2 \qquad (1)$$

High temperature oxidation of hydrocarbons as well as of glyoxal is very sensitive to this step. Starting from the experimentally determined rate coefficients by Colberg and Friedrichs[2] and the new experimental data presented below, we derived a rate constant expression valid over a wide range of temperatures. Hsu et al.[36] reported a theoretical study of this reaction, based on RRKM calculations for the indirect abstraction channel and VTST calculations for the direct abstraction channel. Both channels yield the products CO + HO$_2$. According to these calculations, at low temperatures the more or less temperature independent indirect channel dominates and the increase of the total rate constant, which is due to the direct abstraction channel, takes place not before temperatures of $T > 1250$ K. In contrast, the Colberg and Friedrichs determination implies a distinct increase of the rate constant already at temperatures above $T > 700$ K. For the temperature range of the present shock tube study

Table 8.1: Thermodynamic properties of selected species in the reaction mechanism. Units are kJ mol^{-1} for ΔH, J mol^{-1} K^{-1} for S and $c_{p,T}$, and K for temperature T.

Species	ΔH°_{298}	S°_{298}	$c_{p,300}$	$c_{p,400}$	$c_{p,500}$	$c_{p,600}$	$c_{p,800}$	$c_{p,1000}$	$c_{p,1500}$	Ref.
OCHCHO	−212.07	272.45	60.60	71.38	81.42	89.93	101.43	108.64	117.36	30
OCHCO	−63.80	281.28	57.81	65.15	71.39	76.64	84.65	90.17	98.25	this work, a

a: The C-H bond dissociation enthalpy at 298 K in OCHCHO was obtained via computed CBS-QB3 energies[31] and the reaction OCHCHO → OCHCO + H. There are isomers of OCHCO with bent C-C-O structures but the most stable isomer has an almost linear C-C-O group. The corresponding bond dissociation enthalpy is 366.2 kJ/mol, which corresponds to $\Delta_f H^\circ_{298}$(OCHCO) = −63.8 kJ/mol. Entropies and heat capacities of OCHCO were derived using the harmonic oscillator/rigid rotor model.

Table 8.2: The OCHCHO subset of the reaction mechanism. Parameters for use in the modified Arrhenius expression $k = AT^n \exp(-E_a/(RT))$. Units are mol, cm, s, kJ. The full mechanism, including pressure dependent expressions, are given in the Supporting Information.

No.		A [cm,mol,s]	n	E_a [kJ/mol]	Ref.
1	HCO + O$_2$ $\rightleftharpoons$ CO + HO$_2$	6.92E06	1.900	−5.73	this work, a
2a	OCHCHO $\rightleftharpoons$ CH$_2$O + CO	8.04E55	-12.600	321.00	19, b
2b	OCHCHO $\rightleftharpoons$ CO + CO + H$_2$	6.12E57	-13.100	335.34	19, b
2c	OCHCHO $\rightleftharpoons$ HCOH + CO	2.62E57	-13.200	333.69	19, b, c
2d	OCHCHO $\rightleftharpoons$ HCO + HCO	1.89E57	-12.800	352.80	19, b
3	OCHCHO + H $\rightleftharpoons$ OCHCO + H$_2$	5.4E13	0	18.00	2
4	OCHCHO + O $\rightleftharpoons$ OCHCO + OH	8.4E11	0.570	11.55	est., $2 \times k_{CH2O+O}$
5	OCHCHO + OH $\rightleftharpoons$ OCHCO + H$_2$O	4.0E06	2.000	−6.82	32
6	OCHCHO + HO$_2$ $\rightarrow$ HOCH(OO)CHO	1.3E31	-7.532	6.03	34, d
-6	HOCH(OO)CHO $\rightarrow$ OCHCHO + HO$_2$	1.9E29	-5.781	66.07	34, d
7	OCHCHO + HO$_2$ $\rightleftharpoons$ HOCHO + CO + OH	3.3E-4	3.995	1.26	34, d
8	OCHCHO + HO$_2$ $\rightleftharpoons$ OCHCO + H$_2$O$_2$	8.2E04	2.500	42.70	est., $2 \times k_{CH2O+HO2}$
9	OCHCHO + O$_2$ $\rightleftharpoons$ OCHCO + HO$_2$	4.8E05	2.500	152.55	est., $2 \times k_{CH2O+O2}$
10	OCHCO $\rightleftharpoons$ HCO + CO	4.1E14	0	36.67	35, d
11a	OCHCO + O$_2$ $\rightleftharpoons$ CO + CO$_2$ + OH	3.3E14	0	8.68	35, d
12	HOCH(OO)CHO $\rightarrow$ HOCHO + CO + OH	1.6E10	0.051	63.56	34
13	HOCH(OO)CHO + HO$_2$ $\rightarrow$ HOCH(O)CHO + O$_2$ + OH	3.0E12	0	0	est., e, f
14	HOCH(OO)CHO + HO$_2$ $\rightarrow$ HOCH(OOH)CHO + O$_2$	3.0E12	0	0	est., f

a: 295 K $< T <$ 1705 K,
b: 1.0 bar, 800 K $< T <$ 2500 K,
c: Treated as a duplicate of reaction (2a), see text,
d: 1.0 atm,
e: HOCH(O)CHO immediately dissociates to HOCHO and HCO,
f: 298 K.

(1285 - 1705 K), the extrapolated Arrhenius expression of Colberg and Friedrichs yields 2.1 - 2.5 times higher values than the theoretical prediction of Hsu et al. Hence, the new glyoxal oxidation experiments served as a critical test of both the absolute value of the rate constant and the overall temperature dependence of the reaction HCO + O$_2$.

Thermal dissociation of OCHCHO has been characterized experimentally behind shock waves[18,19] and theoretically.[19,37] It is a highly temperature and pressure dependent multi-channel reaction that may yield a range of products:

$$OCHCHO \rightleftharpoons CH_2O + CO \tag{2a}$$

$$OCHCHO \rightleftharpoons CO + CO + H_2 \tag{2b}$$

$$OCHCHO \rightleftharpoons HCOH + CO \tag{2c}$$

$$OCHCHO \rightleftharpoons HCO + HCO \tag{2d}$$

We have adopted the results by Friedrichs et al.[19] who detected species profiles of OCHCHO, HCO, and H behind shock waves at temperatures of 1032–2320 K. In their work, the obtained branching ratios of the thermal glyoxal decomposition were interpreted by means of RRKM/SACM/ME calculations and rate coefficients over a wide range of temperature (800 – 2500 K) and pressure (1 mbar – 100 bar) have been reported. Original data have been represented in terms of Chebyshev polynomial coefficients. We reparametrized their data and report extended Arrhenius expressions at $p = 1$ bar in

Table 8.2 and at other total pressures in the Supporting Information. A key finding of Friedrichs et al. was that the previously neglected, energetically most unfavorable HCO channel (2d), due to its loose transition state character, becomes the dominant product channel at high temperatures and pressures. For example, at $T = 2300$ K and $p = 3$ bar the branching fraction of channel (2d) accounts for 48% of the total reaction rate. In contrast, the hydroxymethylene forming HCOH channel (2c), in agreement with a photochemical study of Hepburn et al.,[38] with branching fractions $< 7\%$ at all temperatures and pressures turned out to be minor. Arguments have been put forward in ref 19 that subsequent chemistry of HCOH is not expected to serve as a significant source of additional atoms or radicals such that the overall influence of this minor channel on glyoxal chemistry remains small. With regard to a simplified description of the thermal decomposition of glyoxal, channel (2c) has therefore not been treated as a separate channel but its reported rate constant expression has been merged with reaction channel (2a), which is the main channel under the experimental conditions of this work.

Other reactions of OCHCHO include abstraction of H by radicals or O$_2$. Only a few of these steps have been characterized experimentally. The reaction with atomic hydrogen,

$$OCHCHO + H \rightleftharpoons OCHCO + H_2 \tag{3}$$
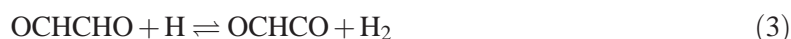
has been measured at elevated temperatures (769–1107 K) by Colberg and Friedrichs[2] and their value is used in the reaction mechanism. The reaction with OH (5),

$$OCHCHO + OH \rightleftharpoons OCHCO + H_2O \tag{5}$$

has been studied both experimentally[32,33,39] and theoretically,[40] though only at low temperatures. The experimental results are in good agreement. We have adopted the rate constant measured by Feierabend et al.[32] in the 210-390 K range.

For the reactions of OCHCHO with O (4) and O$_2$ (9),

$$OCHCHO + O \rightleftharpoons OCHCO + OH \tag{4}$$
$$OCHCHO + O_2 \rightleftharpoons OCHCO + HO_2 \tag{9}$$

we estimate the rate constants to be similar to the analogue reactions of CH$_2$O.

The reaction of OCHCHO with HO$_2$ is of particular importance, since HO$_2$ is formed in significant quantities compared to the other radicals in the O/H pool at low to medium temperature conditions. The H-abstraction channel,

$$OCHCHO + HO_2 \rightleftharpoons OCHCO + H_2O_2 \tag{8}$$
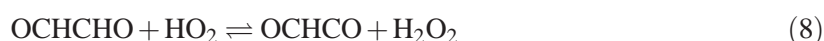
has not been characterized experimentally, but we assume that it has a rate constant similar to that of CH$_2$O + HO$_2$. The reaction would be expected to be too slow to compete at low temperatures, but may become dominating at elevated temperatures. According to the recent theoretical study of da Silva,[34]

the main product of OCHCHO + HO$_2$ at low temperature is HOCH(OO)CHO,

$$OCHCHO + HO_2 \rightleftharpoons HOCH(OO)CHO \tag{6}$$

However, even at low temperatures the HOCH(OO)CHO radical predominantly dissociates to reform the reactants.[34] In analogy with a corresponding formaldehyde reaction,

$$CH_2O + HO_2 \rightleftharpoons HOCHO + OH,$$

a secondary product channel yielding OH radicals has been proposed for glyoxal oxidation by Hay and Norrish,[21]

$$OCHCHO + HO_2 \rightleftharpoons OCHC(O)OH + OH.$$
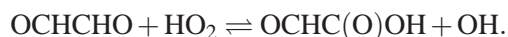
OCHC(O)OH would be expected to decompose rapidly to formic acid (HOCHO) + CO. Indeed, the existence of the OH producing channel for glyoxal + HO$_2$ seems to be supported by the detection of formic acid[41] in glyoxal oxidation and appears to be required to explain the generation of chain carriers in glyoxal oxidation at 563-643 K.[21] From a photolysis study at 298 K, Niki et al.[41] derived a room temperature value for the OH channel of 3×10^8 cm^3 mol^{-1} s^{-1}. Support for an OH-producing channel of the OCHCHO + HO$_2$ reaction is also provided theoretically. According to da Silva,[34] the reaction forms a hydroxyperoxy radical, which decomposes to HOCHO + CO + OH,

$$OCHCHO + HO_2 \rightarrow HOCHO + CO + OH \tag{7}$$

However, the rate constant calculated by da Silva is two orders of magnitude smaller than the value reported by Niki et al. In order to resolve this discrepancy, we have thoroughly re-interpreted the experimental results of Niki et al. (see Appendix). Our analysis indicates that the data of Niki et al. are compatible with the rate constant for (7) from da Silva,[34] provided that the association reaction (6) and the subsequent reactions of HOCH(OO)CHO are taken into account. Consequently, we have adopted the rate coefficients for (6) and (7) from da Silva.

Only a few studies of the chemistry of the OCHCO radical have been reported.[33,41,42] It is expected to decompose thermally or react with O$_2$. The thermal dissociation,

$$OCHCO \rightleftharpoons HCO + CO \tag{10}$$

was studied theoretically by da Silva,[35] who determined a high-pressure limit of $k_{10,\infty} = 1.1 \times 10^{14} \times T^{0.133} \exp(-5102/T)$ between 200 and 2000 K. At the conditions of interest in the present study, this reaction is in the fall-off regime, and consequently we used extrapolations of rate constants provided by da Silva for the 150-400 K range for pressures of 0.01, 0.1, and 1 atm. The rate constant calculated by da Silva is considerably lower than the experimental value reported by Orlando and Tyndall[42] for 0.92 atm and 224-370 K. However, the latter determination was affected by the use of a too large rate constant value for OCHCO + O$_2$, as pointed out by da Silva.[35]

The reaction of OCHCO with O_2 could involve a number of product channels, i.e.,

$$OCHCO + O_2 \rightleftharpoons CO + CO_2 + OH \tag{11a}$$

$$OCHCO + O_2 \rightleftharpoons CO + CO + HO_2 \tag{11b}$$

$$OCHCO + O_2(+M) \rightleftharpoons OCHC(O)OO(+M) \tag{11c}$$

Da Silva[35] predicts the $CO + CO_2 + OH$ channel (11a) to be dominating above room temperature. In fact, in a recent kinetic study on OH formation in the $Cl/OCHCHO/O_2$ reaction system, Lockhart et al.[33] found strong evidence that the reaction (11) directly yields OH radicals with a rate constant consistent with the Da Silva estimate. The OCHCO + O_2 addition reaction is strongly exothermal and isomerization/decomposition of the excited peroxy radical adduct is competitive with collisional deactivation even at low temperature, leading directly to the dissociated products $CO_2 + CO + OH$. Similar to reaction (10), da Silva uses RRKM/ME theory to calculate values of k_{11a} for temperatures between 150 and 400 K and pressures of 0.01–1 bar; we extrapolate these data to the conditions of the present work. The work of da Silva indicates a small, positive activation energy (4–8 kJ mol^{-1}). The finding that (11a) is the main product channel for OCHCO + O_2 is in agreement with experimental observations by Orlando and Tyndall.[42] However, they assumed the reaction to be barrierless and estimated a somewhat larger rate constant.

Addition of O_2 (11c) yields a ketoperoxy radical, OCHC(O)OO. This radical isomerizes with a computed barrier of 63 kJ mol^{-1} to make OCC(O)OOH through a 1 - 4 hydrogen shift. With a low barrier of 28 kJ mol^{-1}, the OCC(O)OOH radical would dissociate fast to form $CO + CO_2 + OH$; an overall step equivalent to (11a). Alternatively, the ketoperoxy radical could pick up an H atom at the radical oxygen resulting in OCHC(O)OOH. The new O-H bond with a bond energy of 407 kJ mol^{-1} is reasonably strong; thus H might be abstracted from other species present including glyoxal. OCHC(O)OOH can decompose in a unimolecular step with a barrier of 87 kJ mol^{-1} to yield $HCO + CO_2 + OH$ or it can be converted to OCC(O)OOH by abstraction of H from the C-H bond. With a bond energy of 379 kJ mol^{-1} this bond is weaker than the O-H bond. However, da Silva predicts the association rate (11c) to decrease rapidly above 300 K, and these pathways are not expected to be important under the conditions of the present study.

8.3 Experimental

The thermal decomposition of glyoxal has been investigated behind shock waves with and without oxygen present in the reaction gas mixtures. All experiments were carried out in an electro-polished stainless steel shock tube that is described in detail elsewhere.[2] The shock tube has been operated using hydrogen or hydrogen/nitrogen mixtures as driver gas and 30 or 80 μm thick aluminium diaphragms. Concentration-time profiles of the glyoxal decomposition product HCO were measured by means of frequency modulation (FM) spectroscopy at a detection wavelength of $\lambda = 614.752$ nm. The experimental setup was very similar to the one used in our previous paper on the reaction HCO + O_2.[2] Details on the HCO detection scheme and the implementation of FM spectroscopy for quantitative measurements of radicals behind shock waves can be found elsewhere.[43,44] According to FM

theory, the measured signal I_{FM} is related to the absolute radical concentration c by the equation

$$I_{FM} = \frac{I_0}{2} \sigma_c \times c \times l \times \Delta f \times G.$$

Here, I_0 is the probe light intensity, σ_c the absorption cross section at line center, and l the absorption path length. Δf, the so-called FM factor, depends on the applied modulation frequency as well as the modulation depth and is calculated from the absorption line shape profile at the actual experimental temperature and pressure. Accurate line shape data and absorption cross sections have been adopted from Friedrichs et al.[43] The room temperature value of the absorption cross section is in excellent agreement (within 2%) with the accurate measurements of Flad et al.[45] Allowance was made for a small pressure broadening effect according to an assumed pressure broadening coefficient $\Delta v = 2.0 \times (T/298\,\mathrm{K})^{0.75}$ GHz bar^{-1}, hence similar to the one experimentally observed for NH$_2$.[46] G is the device-specific electronic gain factor of the FM spectrometer, which has to be determined separately. Its value has been re-measured and was found to be consistent with our previous determinations. We estimate the accuracy of the calculated HCO concentrations (including the error of the gain factor and the high temperature extrapolation of the HCO cross section) to be $\pm 20\%$.

Table 8.3: Experimental conditions and results.

$T/$ K	$\rho/10^{-6}$ mol cm^{-3}	x(glyoxal) %	$T/$ K	$\rho/10^{-6}$ mol cm^{-3}	x(glyoxal) %	x(O$_2$) ppm	$k_1/10^{12}$ cm^{3}mol^{-1}s^{-1}
	without O$_2$			with O$_2$			
incident shock wave			incident shock wave				
1299	3.87	1.01	1285	3.86	1.01	3185	7.3
1379	5.24	1.04	1294	3.86	1.01	6700	7.7
1398	3.94	1.01	1382	3.93	1.01	3185	11.3
1406	4.60	1.14	1432	3.96	1.01	6700	8.9
1466	3.98	1.01	1450	5.30	1.04	9415	13.6
1521	5.35	1.04	1481	4.66	1.14	7210	12.9
1757	3.95	1.01	1572	5.39	1.04	9415	19.6
			1677	4.09	1.01	6700	11.8
			1705	4.07	1.01	3185	13.2
reflected shock wave			reflected shock wave				
1382	9.80	1.05	1339	9.61	1.05	5045	9.3
1519	10.3	1.05	1340	10.0	1.05	7735	9.3
1539	10.4	1.05	1420	9.96	1.05	5045	13.7
1545	11.6	1.01	1431	10.0	1.04	7645	9.1
1618	10.7	1.05	1558	11.6	1.02	4880	15.5
			1660	10.8	1.05	9060	14.4
			1663	10.8	1.05	7735	11.7

Glyoxal was prepared by heating glyoxal trimeric dihydrate in the presence of P$_2$O$_5$ and was stored in a liquid nitrogen trap. Reaction gas mixtures were prepared manometrically and contained 1% glyoxal in argon. Such high glyoxal mole fractions were necessary to ensure detectable HCO concentration levels. In about half of the experiments, mole fractions of 3185 - 9415 ppm oxygen have been added using a flow system with mass flow controllers. Experiments have been performed behind incident

(corresponding to an average total density $\rho \approx 4.4 \times 10^{-6}$ mol cm^{-3}) and reflected ($\rho \approx 1.1 \times 10^{-5}$ mol cm^{-3}) shock waves in the temperature range 1299 K $< T <$ 1757 K. The experimental conditions of all 28 shock tube experiments, as calculated from the measured shock wave velocity and pre-shock conditions using a standard shock tube code with real gas correction, are outlined in Table 8.3. It is known that the vibrational relaxation/equilibration of oxygen is quite slow, about 100 μs at $T = 1500$ K and $p = 1$ bar in argon.[47] Therefore, in contrast to the translational and rotational degrees of freedom that are heated within 1 μs, the vibrational degrees of freedom are not in thermal equilibrium on the typical experimental timescales of $7 - 70$ μs present in this study. This has two consequences: On the one hand, the real initial temperatures behind the shock waves were somewhat higher than calculated by the standard shock tube code. Therefore, Table 8.3 lists a corrected, up to 10 K higher initial temperature assuming that the O_2 vibrational degree of freedom is not heated at all. On the other hand, as the actual O_2(v = 1)/O_2(v = 0) ratio during the experiment is lower than at thermal equilibrium (about 0.2 at $T = 1400$ K), the determined rate constant may be slightly biased by the different reactivities of O_2 in its $v = 0$ and $v = 1$ vibrational states. This non-equilibrium effect is difficult to address quantitatively and is typically neglected in the analysis of shock tube data. Within the scatter of the obtained rate constant data, and taking into account the very good agreement with our previous shock tube measurements (which were not affected due to a sufficiently long delay behind the shock wave arrival and glyoxal photolysis), we assume that the possible, presumably negative bias is not significant.

8.4 Results and Discussion

8.4.1 Branching ratio of glyoxal decomposition

Table 8.4: Previously reported channel branching ratios and total rate constants of the multi-channel thermal decomposition of glyoxal for typical experimental conditions behind the incident ($\rho = 4.43 \times 10^{-6}$ mol cm^{-3}) and reflected ($\rho = 1.05 \times 10^{-5}$ mol cm^{-3}) shock waves, according to Friedrichs et al.[19].

OCHCHO $\rightarrow$ products	$T = 1300$ K		$T = 1700$ K	
$\rho/$ (mol/cm^3)	1.05×10^{-5}	4.43×10^{-6}	1.05×10^{-5}	4.43×10^{-6}
ϕ (CH$_2$O + CO) %	48	56	38	47
ϕ (2 CO + H$_2$) %	29	28	27	29
ϕ (HCOH + CO) %	7	7	6	7
ϕ (2 HCO) %	16	9	29	17
$k_{2,\text{total}}/$s^{-1}	1.3×10^4	8.3×10^3	7.1×10^5	3.8×10^5

Experiments with glyoxal/argon mixtures without oxygen were performed to test the overall thermal glyoxal decomposition mechanism reported in the literature. According to Friedrichs et al.,[19] the channel branching of the multi-channel unimolecular decomposition of glyoxal is strongly dependent on the temperature and total density. The effect of total density and temperature on the channel branching ratio is illustrated in Table 8.4. Note the pronounced fall-off of the total rate constant $k_{2,\text{total}}$ ($\rho^{\text{reflected}}/\rho^{\text{incident}} = 2.5$, but $k_{2,\text{total}}^{\text{reflected}}/k_{2,\text{total}}^{\text{incident}} \approx 1.7$) and the significantly different importance of the

HCO channel (2d) at the two different temperatures ($\phi_{1700\ K}/\phi_{1300\ K} \approx 1.8$). Hence, the experiments behind the incident and reflected shock waves at overall different total densities provide a critical test of their rate constant data and RRKM/SACM/ME predictions.

Experimental HCO concentration-time profiles behind the reflected shock wave at three different temperatures are shown in Fig. 8.1a together with simulated profiles (thick curves). Fig. 8.1b illustrates the corresponding sensitivity analysis of the $T = 1519$ K experiment in order to identify the most important reactions. The numerical simulations were performed using the CHEMKIN-II package[48] and the SENKIN routine[49] based on the glyoxal oxidation mechanism outline above. Overall, the observation times of the HCO profiles were rather short and the initial increase of the HCO profiles were obscured by the strong Schlieren signal attributable to the passage of the shock wave through the detection laser beam. For a better comparison of the experimental and numerically simulated profiles, the experimental time resolution has been taken into account by convoluting the numerical simulation with an appropriate time response function (Gaussian, FWHM of 2-3 μs). Excluding the first few μs that are affected by the Schlieren signal (open symbols), both the absolute concentrations and the overall shapes of the reported concentration-time profiles are very well captured by the simulations. Toward low temperatures, the experimentally accessible temperature range was limited by too low intermediate concentrations, toward high temperatures by too short HCO lifetimes. The sensitivity analysis in Fig. 8.1b highlights the influence of the five most important reactions. Both the branching ratio of the OCHCHO decomposition as well as the rate constant of several secondary reactions have to be known to accurately predict the HCO profile. In fact, we were able to reproduce all measured HCO profiles without adjusting any rate constant data, initial glyoxal concentrations, or the temperature dependent HCO absorption cross section. From this high reproducibility we conclude that both the thermal glyoxal decomposition mechanism as well as the HCO detection scheme is highly reliable.

8.4.2   Rate of Reaction HCO+O$_2$

The rate constant of the reaction

$$HCO + O_2 \rightarrow CO + HO_2 \tag{1}$$

has been measured between 1285 K $\leq T \leq$ 1705 K at two different total densities of $\rho \approx 4.3 \times 10^{-6}$ mol/cm^3 behind the incident and $\rho \approx 1.0 \times 10^{-5}$ mol/cm^3 behind the reflected shock waves. The experimental conditions and the results for k_1 are summarized in Table 8.3. Next to 1% glyoxal, serving as a source of HCO radicals from reaction (2d), the reaction mixtures contained 3185–9415 ppm O$_2$. Fig. 8.2a illustrates two typical experimental HCO concentration-time profiles measured behind reflected shock waves at a temperature of 1339 K and 1558 K, respectively. Both experiments were carried out at similar densities ($\rho = 1.16$ and 0.96×10^{-6} mol/cm^3) and initial glyoxal (1.02% and 1.05%) and O$_2$ mole fractions (4880 ppm and 5045 ppm). The observed peak HCO concentration is about four times lower at the lower temperature. For the 1558 K experiment, the total HCO observation time is only about 40 μs, whereas HCO could be observed for > 200 μs at 1339 K. This behavior is well captured by the two simulated profiles (thick curves) using our glyoxal oxidation mechanism. Fig. 8.2b illustrates the results of the sensitivity analysis of the $T = 1339$ K experiment. It reveals
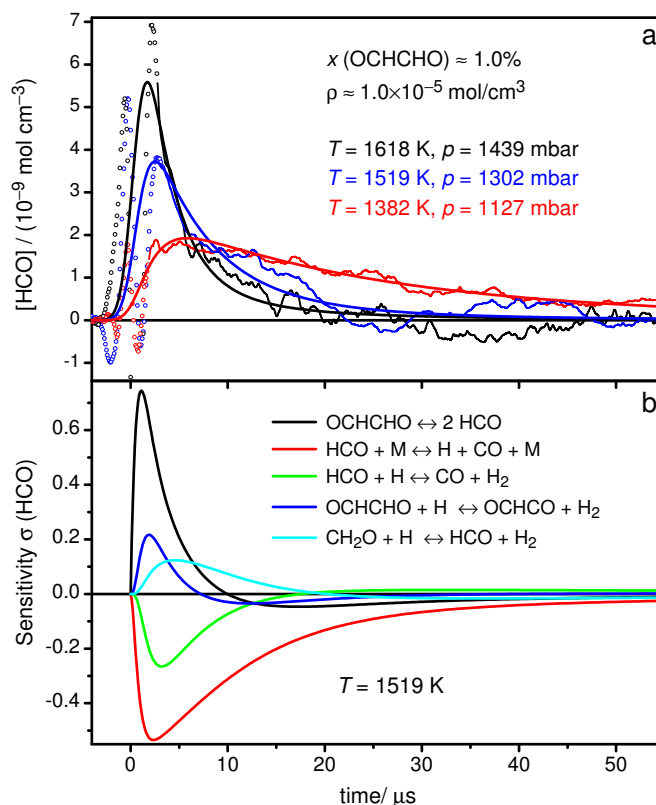
Figure 8.1: a: Three experimental HCO profiles at different temperatures behind reflected shock waves in comparison with numerically simulated profiles. Open circles mark the interfering Schlieren signals and do not contain information on HCO concentration. b: Corresponding HCO sensitivity analysis for $T = 1519$ K. The sensitivity coefficients are normalized with respect to the maximum HCO concentration over the time history, $\sigma(\text{HCO}) = 1/[\text{HCO}]_{\text{max}} \times \partial[\text{HCO}](t)/\partial \ln k$.

that the simulated absolute concentration levels are mainly determined by the branching ratio of the thermal decomposition of glyoxal, in particular the rate constants of the reaction (2b), and by the assumed rate constant for the target reaction (1). Other consecutive reactions of HCO and glyoxal are also important, but their rates have been validated together with the branching ratio by the shock tube measurements for mixtures without O$_2$ as outlined above. Hence it was possible to obtain a best-fit value for the rate constant of the reaction HCO + O$_2$ by adjusting exclusively k_1. The two dashed curves in Fig. 8.2a, corresponding to numerical simulations with k_1 set to $k_1 \times 2$ and $k_1 \div 2$, demonstrate the sensitivity of this procedure. Especially with respect to the HCO peak concentration, the effect of changing k_1 is very pronounced. Nevertheless, due to the moderate signal-to-noise ratio of the experiments, we estimate that the uncertainty of each individual k_1 value with $\pm 75\%$ is rather large.

The obtained k_1 values are depicted as red symbols in comparison with selected literature data in the Arrhenius plot shown in Fig. 8.3. The included red error bar corresponds to the $\pm 75\%$ uncertainty of a single data point; the 2σ standard deviation of the data with respect to the final Arrhenius fit (red curve) is about $\pm 40\%$. For a more complete comparison of available literature data and a critical
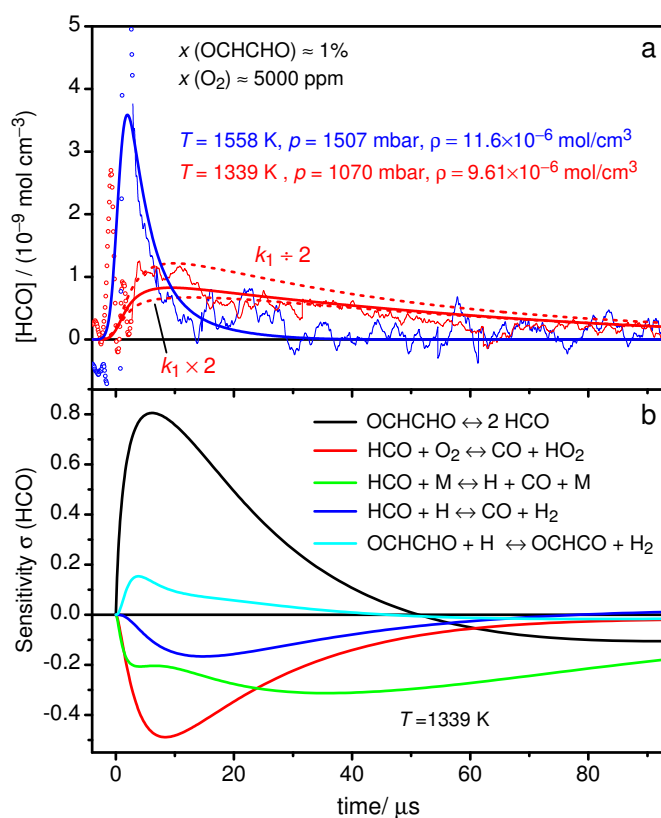
Figure 8.2: a: Two typical experimental HCO concentration-time profiles in comparison with simulations (thick curves). The simulated profiles have been convoluted with an appropriate response function in order to allow for a direct comparison of the experiment and simulation at short reaction times. Open circles mark the interfering Schlieren signals, which were excluded from the fit. b: Corresponding HCO sensitivity analysis for the experiment at $T = 1339$ K. Only the five most sensitive reactions are shown.

assessment of available room temperature data we refer to our previous publication[2] and the paper of De Sain et al.[50] Within the scatter of the data, the experiments behind the incident (open circles) and reflected shock waves (star symbols) are consistent, hence no dependence of the rate constant on the total density could be identified. In contrast, a weak positive temperature dependence is evident. Both the temperature dependence and the absolute rate constant values are in quantitative agreement with the high temperature extrapolation (blue dashed line) of our previous determination:[2]

$$k_1/(\text{cm}^3\text{mol}^{-1}\text{s}^{-1}) = 3.7 \times 10^{13} \times \exp\left(-13 \text{ kJ/mol}/RT\right)$$

The original data and error bars of the latter study are included as blue plus symbols. They had been determined using the 193 nm photolysis of glyoxal as a source of HCO radicals and their uncertainty, unlike the uncertainty of the experiments in this work, were mainly due to the assumed initial ratio of [H]/[HCO] from glyoxal photolysis. The very good agreement of these two independent studies points out the consistent modeling capabilities of our mechanism with regard to glyoxal photolysis and pyrolysis.

The recommended value from the GRI-Mech. 3.0[51] (line marked with black filled circles) is in agreement with the new high temperature results, but the temperature dependence is quite underestimated. The RRKM/VTST calculations of Hsu et al.[36] (curve marked with down triangle) underpredict the onset of the high-temperature direct abstraction channel resulting in about two times lower absolute k_1 values at temperatures around 1500 K. Other experimental data for intermediate temperatures and at room temperature[2,50,52,53] reveal a more or less temperature independent rate constant, which is consistent with the expected capture controlled process of the indirect abstraction channel with an initiating recombination step and a low-lying exit barrier to the products CO + HO$_2$. As a reasonable fit of the overall temperature dependence of the available data, an extended Arrhenius expression is recommended over the temperature range 295 K $< T <$ 1705 K (red curve):

$$k_1/(cm^3mol^{-1}s^{-1}) = 6.92 \times 10^6 \times T^{1.90} \times \exp(+5.73 \text{ kJ/mol}/RT)$$

The overall rate constant is independent of pressure. Even at room temperature, the collisionally deactivated recombination product HC(O)O$_2$ does not play a role provided that the pressure does not exceed several bar.[36]
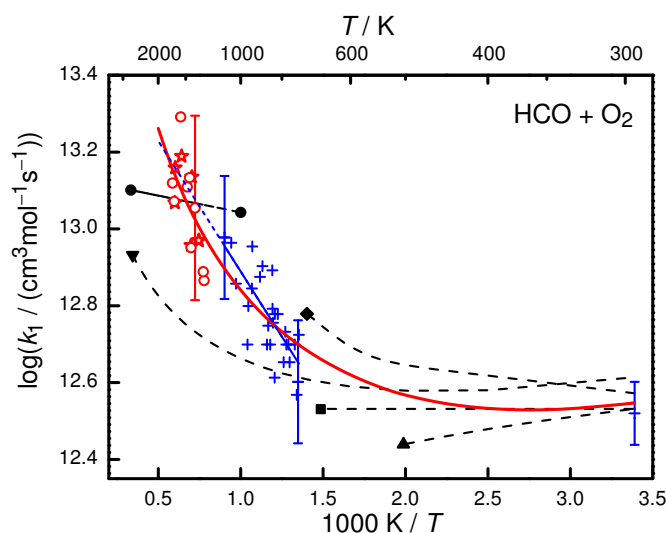
Figure 8.3: Arrhenius plot of the measured rate constants k_1 for the reaction HCO + O$_2$ of this work (incident wave ○, reflected wave ☆) in comparison with selected experimental data from Colberg and Friedrichs (+, blue line),[2] Veyret and Lesclaux (▲),[52] Timonen et al. (◆),[53] DeSain et al. (■),[50] the GRI-Mech 3.0 recommendation (●),[51] and the theoretical study of Hsu et al. (▼).[36] The red curve depicts the final recommended k_1 rate expression.

8.4.3 Model validation against literature data

To test the capacity of our mechanism we used it for the modeling of other available experimental literature data. In particular, the batch reactor experiments of Hay and Norrish[21] were of interest. Their study, which was based on manometric detection of the reaction progress and gas chromatographic

product analysis, should provide a detailed characterization of glyoxal oxidation with varying equivalence ratio at a nominal temperature of 603 K. At this intermediate temperature, HO$_2$ related oxidation reactions such as OCHCHO + HO$_2$ become important. However, we were not able to reconcile the results of Hay and Norrish with our present understanding of the reaction system. Using our mechanism, we were able to reproduce qualitatively the product yields and the overall shapes of the experimental concentration-time profiles – but in fact on a more than two orders of magnitude slower time scale. As a possible explanation, the hypotheses of a much higher yield of the OH radical forming channel (6), OCHCHO + HO$_2$ → HOCHO + CO + OH, was tested. As already stated above and further outlined in the Appendix, we actually recommend the low k_6 value calculated by da Silva[34] in our mechanism, which is two orders of magnitude smaller than the value reported by Niki et al.[41] In fact, setting k_6 to the much higher value of Niki et al. significantly reduces the mismatch of the overall reaction time scales, but the agreement with the reported product yields is seriously deteriorated. In particular, the high yield of H$_2$O$_2$ reported by Hay and Norrish is considerably underestimated. Further modeling attempts led us to the conclusion that the Hay and Norrish experiments presumably were not performed under isothermal conditions and that the fast observed experimental glyoxal consumption is at least partly due to an unidentified temperature increase of the reaction gas mixture. This uncertainty, along with the issue of potential surface effects in the reactor, makes these data less suitable for kinetic interpretation.

Another test for the glyoxal oxidation mechanism was the modeling of the photolysis experiments of glyoxal/oxygen mixtures performed by Colberg and Friedrichs.[2] Fig. 8.4 shows a comparison of an original experiment at $T = 857$ K taken from ref 2 with simulations of HCO concentration-time profiles with (solid curve) and without oxygen (dash-dotted curve) present in the reaction mixture. Oxygen addition significantly reduces the overall HCO yield and lifetime. The simulation is in perfect agreement with the experimental data. To further investigate the possibility of a significant OH forming channel of the reaction OCHCHO + HO$_2$, a simulation with the rate of reaction (6) increased to the Niki et al. value, $k_6 \times 200$, is shown as well (dotted curve). With $k_6 \times 200$, the influence of reaction (6) on the HCO concentration profile is negligible at short reaction times, but a factor of four higher HCO concentration is simulated at $t = 25$ μs. In this case, the simulated residual HCO concentration at long reaction times can be traced back to a steady regeneration of HCO radicals due to the combined reaction sequence (5) and (10), OCHCHO + OH → HCO + CO + H$_2$O. However, none of the original experiments of Colberg and Friedrichs showed this small but significant HCO concentration plateau at longer reaction times, hence further supporting the low OH yield from the reaction OCHCHO + HO$_2$ as predicted by da Silva and recommended by us.

8.5   Conclusions

A detailed glyoxal decomposition and oxidation mechanism has been compiled from literature data merging previous reports on glyoxal/oxygen photolysis at room and high temperature,[19] the branching ratios of glyoxal thermal decomposition,[2] and theoretical studies on the reaction of glyoxal + HO$_2$,[34] OCHCO + O$_2$,[35] and formic acid oxidation.[26]
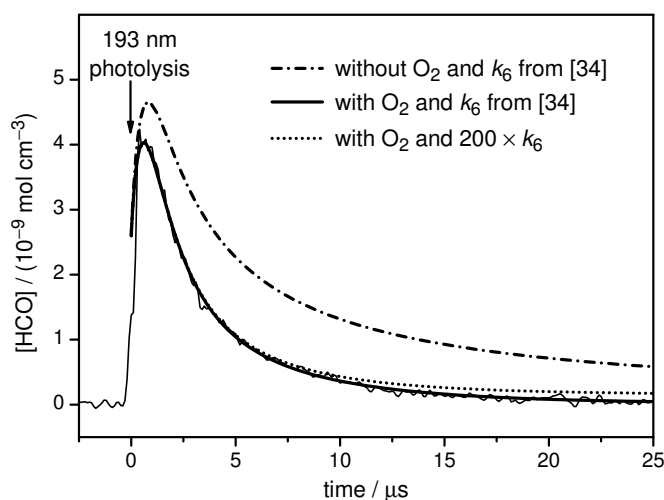
Figure 8.4: Photolysis experiment of Colberg and Friedrichs[2] at $T = 857$ K and $p = 1080$ mbar with 2% OCHCHO and 3160 ppm O$_2$ in the reaction mixture. Three different simulations are shown: without O$_2$ (dash-dotted curve) and with O$_2$ assuming either the rate constant for the reaction OCHCHO + HO$_2$ as reported by Niki et al.[41] (dotted curve) or by da Silva[34] (solid curve).

All HCO profiles from glyoxal decomposition behind shock waves could be very well simulated, both in terms of absolute HCO concentrations and signal shapes, using the glyoxal decomposition mechanism adopted from Colberg and Friedrichs[2] with branching fractions taken from Friedrichs et al.[19] The established glyoxal pyrolysis mechanism was able to predict the measured HCO concentration-time profiles of this work without any modifications. Moreover, by adding oxygen to the reaction mixtures, the rate constant for the reaction HCO + O$_2$ could be measured at temperatures 1285 K $\leq T \leq$ 1705 K, hence significantly extending the range of direct measurements toward higher temperatures. The results are in striking agreement with the previous shock tube/photolysis experiments of Colberg and Friedrichs.[2] The absolute values as well as the overall temperature dependence, which is stronger than predicted theoretically, could be confirmed.

A detailed reanalysis of previous experimental measurements on the reaction OCHCHO + HO$_2$ performed by Niki et al.[41] led us to the conclusion that the reported high OH yield can be traced back to a previously unidentified formation of the recombination product HOCH(OO)CHO and its secondary reaction with HO$_2$. The theoretically predicted, two orders of magnitude lower rate constant value for OH formation reported by da Silva[34] is also supported by a reassessment of the previous glyoxal/O$_2$ photolysis data from Colberg and Friedrichs.[2] Using the original high rate constant value of Niki et al., our glyoxal oxidation mechanism would predict HCO concentration plateau levels at long reaction times that have not been observed in the experiment.

Unfortunately, a further critical test of the performance of our mechanism at intermediate temperatures by comparing model predictions with the outcome of the glyoxal oxidation batch reactor experiments of Hay and Norrish[21] turned out to be unfeasible. Most probably those experiments were biased by an unidentified temperature increase in the reactor. Therefore, additional measurements of glyoxal

oxidation at intermediate temperatures are desirable and would offer a possibility to critically check the predicted important role of the reaction OCHCHO + HO$_2$ for the overall reaction progress.

Acknowledgments

Supporting Information

Detailed glyoxal oxidation reaction mechanism and pressure dependent rate constant data in PLOG format.

8.6 Appendix: On the OCHCHO + HO$_2$ Reaction

As discussed above, the reaction of OCHCHO with HO$_2$ is believed to be of importance for the generation of chain carriers in oxidation of glyoxal. Figure 8.5 compares the available rate constant data for the rate of OCHCHO + HO$_2$. According to the recent theoretical study by da Silva,[34] glyoxal reacts with HO$_2$ to form a hydroxyperoxy radical. At low temperatures the major reaction product is predicted to be collisionally deactivated HOCH(OO)CHO (7), but a secondary product channel yielding HOCHO and OH,

$$OCHCHO + HO_2 \rightarrow HOCHO + CO + OH, \tag{7}$$

has been proposed in earlier studies of glyoxal oxidation. The only experimental determination of the rate constant for the OH channel was reported by Niki et al.,[41] who derived a value more than two orders of magnitude larger than the theoretical estimate for k_7 by da Silva.[34] Figure 8.5 compares their value (open square) with the theoretical prediction of the rate constants for the different channels of the reaction OCHCHO + HO$_2$.

Due to the importance of the reaction of glyoxal with HO$_2$, it is worthwhile to take a closer look at the experimental results from Niki et al. that form the basis of their estimation of k_7. They conducted Cl-atom initiated oxidation studies of glyoxal oxidation, photolyzing a system of Cl$_2$ (100 ppm), OCHCHO (8-22 ppm), O$_2$ (93.3 mbar), and H$_2$ (840 mbar). The following sequence of reactions was intended to provide data on k_7: Cl$_2$ + hν → Cl + Cl, Cl + H$_2$ → HCl + H, H + O$_2$ (+M) → HO$_2$ (+M), OCHCHO + HO$_2$ → HOCHO + CO + OH (7), along with the side reaction HO$_2$ + HO$_2$ → H$_2$O$_2$ + O$_2$. Niki et al. used continuous UV light for 60 or 120 seconds to obtain sufficient photolysis of Cl$_2$. The results of the experiments are shown in Table 8.5. Results obtained for longer reaction times are neglected here, as Niki et al. reported a considerable loss of species by surface reactions.
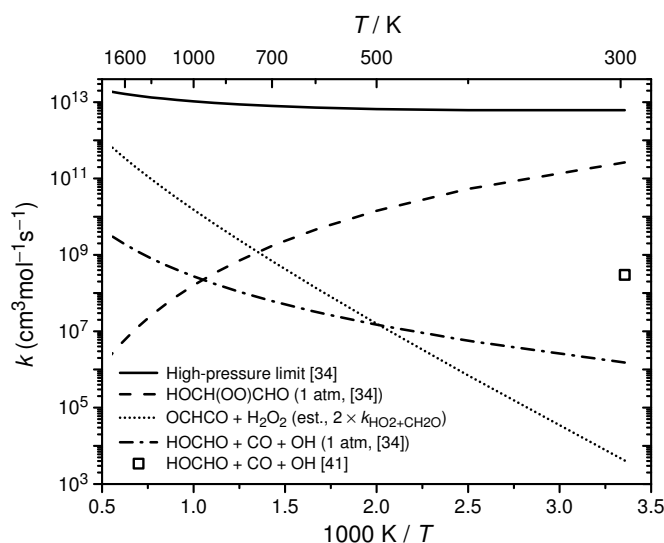
Figure 8.5: Arrhenius plot for the reaction OCHCHO + HO$_2$ → products. The curves denote the rate constants predicted theoretically by da Silva[34] for the total reaction at the high-pressure limit and for the recombination reaction (6) as well as the OH-producing channel (7) at 1.0 atm. The H-abstraction channel forming OCHCO + H$_2$O$_2$ (8) is an estimate by analogy to the reaction CH$_2$O + HO$_2$. The square symbol denotes the experimental result for the OH-producing channel (7) by Niki et al.[41]

Niki et al. estimated the HO$_2$ radical concentration from the equation,

$$\Delta[H_2O_2] = 2k_{HO2+HO2}[HO_2]^2 \times \Delta t$$

using the measured H$_2$O$_2$ concentration. Then, they calculated the rate constant for (7) from

$$\Delta[OCHCHO] = k_7[OCHCHO]_{average}[HO_2] \times \Delta t$$

deriving a room temperature of $k_7 = 3 \times 10^8$ cm^3 mol^{-1} s^{-1} (Fig. 8.5).

An up-to-date kinetic analysis of the system supports most of the assumptions made by Niki et al. Once formed by the sequence of reactions outlined by Niki et al., HO$_2$ reacts with glyoxal,

$$OCHCHO + HO_2 \rightarrow products,$$

or with itself,

$$HO_2 + HO_2 \rightarrow H_2O_2 + O_2$$
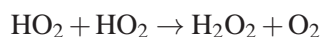
The major shortcoming of their analysis is the disregard of the formation of HOCH(OO)CHO, which according to da Silva is the dominating product of the glyoxal + HO$_2$ reaction. Provided the HOCH(OO)CHO adduct has a sufficiently long lifetime, this adduct may react with HO$_2$ in a secondary reaction. There are no experimental or theoretical data available for HOCH(OO)CHO + HO$_2$, but from analogy with other hydrocarbon peroxide radicals, the reaction is likely to have two product

131

channels,

$$HOCH(OO)CHO + HO_2 \rightarrow HOCH(O)CHO + O_2 + OH \qquad (13)$$

$$HOCH(OO)CHO + HO_2 \rightarrow HOCH(OOH)CHO + O_2 \qquad (14)$$

Dissociation of HOCH(O)CHO to HOCHO and HCO is 59 kJ mol^{-1} exothermic. A DFT estimate indicates a barrier to dissociation of merely $+1.0$ kJ mol^{-1}, which drops to -5.0 kJ mol^{-1} at the CBS-QB3 level of theory, so we believe that dissociation of HOCH(O)CHO is essentially instant, even at 298 K. For similar reactions of HOCH$_2$OO, CH$_3$C(O)OO, and CH$_3$C(O)CH$_2$OO with HO$_2$, branching fractions k_{OH}/k_{total} of 40%($\pm$25%) have been reported.[54,55,56] In the present work, we have assumed a branching fraction for HOCH(OO)CHO + HO$_2$ of 50%, together with an overall rate constant of $k_{13+14} = 6.0 \cdot 10^{12}$ cm^3 mol^{-1} s^{-1}, which is typical for this type of reaction.

Modeling of the experimental data from Niki et al. with the detailed reaction mechanism of the present work have been performed. Appropriate reactions of chlorine species have been added and the photolysis rate for Cl$_2$ was fitted such that the calculated concentration of HCl after 60 or 120 s matched reasonably the measured values. The results are shown (in parenthesis) in Table 8.5. Even though we employ a rate constant for k_7, which is about two orders of magnitude lower than derived by Niki et al., the agreement between measured and predicted concentrations is acceptable. In support of the present interpretation of the reaction system, Niki et al. reported the detection of a transient component, which they believed to be HOCH(OOH)CHO.

Table 8.5: Cl-atom initiated reaction in the OCHCHO/H$_2$/O$_2$ system. Photolysis of a mixture of Cl$_2$ (100 ppm), OCHCHO (8-22 ppm), O$_2$ (70 torr), and H$_2$ (630 torr). Experimental data are from Niki et al.[41] and modeling results (shown in parenthesis) from the present work.

[OCHCHO]$_0$ (ppm)	8.5	9.0	22.4
Irradiation time (s)	60	60	120
$-\Delta$[OCHCHO] (ppm)	0.68 (0.83)	0.71 (0.88)	2.14 (3.5)
[HCl] (ppm)	13.4 (12.6)	12.3 (12.6)	22.6 (21.4)
[HOCHO] (ppm)	0.34 (0.29)	0.40 (0.31)	1.9 (1.2)
[CO] (ppm)	0.90 (0.70)	1.05 (0.74)	4.55 (3.0)
[CO$_2$] (ppm)	0.22 (0.10)	0.17 (0.10)	0.53 (0.42)
[H$_2$O$_2$] (ppm)	4.9 (6.0)	5.4 (6.0)	10.5 (9.6)

References

[1] Q. Wang, C. Geng, S. Lu, W. Chen, and M. Shao. Emission factors of gaseous carbonaceous species from residential combustion of coal and crop residue briquettes. *Front. Environm. Sci. Eng.*, 7:66-76, 2013.

[2] M. Colberg and G. Friedrichs. Room Temperature and Shock Tube Study of the Reaction HCO + O$_2$ using the Photolysis of Glyoxal as an Efficient HCO Source. *J. Phys. Chem. A*, 110:160-170, 2006.

[3] J. G. Calvert, R. Atkinson, K. H. Becker, R. H. Kamens, J. H. Seinfeld, T. J. Wallington, and G. Yarwoog. *The Mechanism of Atmospheric Oxidation of Aromatic Hydrocarbons*, Oxford University Press, Oxford 2000.

[4] T. Stavrakou, J.-F. Müller, I. De Smedt, M. Van Roozendael, M. Kanakidou, M. Vreskoussis, F. Wittrock, A. Richter, and J. P. Burrows. The continental source of glyoxal estimated by the synergistic use of spaceborne measurements and inverse modelling. *Atmos. Chem. Phys.*, 9:8431-8446, 2009.

[5] J. M. Hay and R. G. W. Norrish. The oxidation of gaseous glyoxal. *Proc. Roy. Soc. Ser. A*, 288:17-38, 1965.

[6] T. M. Stevenson and C. F. H. Tipper. The photoinduced oxidation of acetylene. *Combust. Flame*, 11:35-48, 1967.

[7] J. M. Hay and D. Lyon. Alkyne Oxidation I. Acetylene Oxidation. *Proc. Roy. Soc. Ser. A*, 317:1-20, 1970.

[8] A. Williams and D. B. Smith. Combustion and oxidation of acetylene. *Chem. Rev.*, 70:267-293, 1970.

[9] M. U. Alzueta, M. Borruey, A. Callejas, A. Millera, and R. Bilbao. An experimental and modeling study of the oxidation of acetylene in a flow reactor. *Combust. Flame*, 152:377-386, 2008.

[10] M. Siese and C. Zetzsch. Addition of OH to acetylene and consecutive reactions of the adduct with O$_2$. *Z. Phys. Chem.*, 188:75 - 89, 1995.

[11] B. Bohn and C. Zetzsch. Formation of HO$_2$ from OH and C$_2$H$_2$ in the presence of O$_2$. *J. Chem. Soc. Faraday Trans.*, 94:1203-1210, 1998.

[12] L. Y. Yeung, M. J. Pennino, and A. M. Miller, and M. J. Elrod. Kinetics and Mechanistic Studies of the Atmospheric Oxidation of Alkynes. *J. Chem. Phys. A*, 109:1879-1889, 2005.

[13] A. Maranzana, G. Ghigo, G. Tonachini, and J. R. Barker. Tropospheric Oxidation of Ethyne and But-2-yne. 1. Theoretical Mechanistic Study. *J. Chem. Phys. A*, 112:3656-3665, 2008.

[14] A. Galano, L. G. Ruiz-Suarez, and A. Vivier-Bunge. On the mechanism of the OH initiated oxidation of acetylene in the presence of O$_2$ and NO$_x$. *Theor. Chem. Account*, 121:219-225, 2008.

[15] D. R. Glowacki, J. Lockhart, M. A. Blitz, J. Klippenstein, M. J. Pilling, S. H. Robertson, and P. W. Seakins. Interception of Excited Vibrational Quantum States by O$_2$ in Atmospheric Association Reactions. *Science*, 337:1066-1069, 2012.

[16] J. Lockhart, M. A. Blitz, D. E. Heard, P. W. Seakins, and R. J. Shannon. Mechanism of the Reaction of OH with Alkynes in the Presence of Oxygen. *J. Chem. Phys. A*, 117:5407-5418, 2013.

[17] E. W. R. Steacie, W. H. Hatcher, and J. F. Horwood. Kinetics of the decomposition of gaseous glyoxal. *J. Chem. Phys.*, 3:291-295, 1935.

[18] K. Saito, T. Kakumoto, and I. Murakami. Thermal unimolecular decomposition of glyoxal. *J. Phys. Chem.*, 88:1182-1187, 1984.

[19] G. Friedrichs, M. Colberg, J. Dammeier, T. Bentz, and M. Olzmann. HCO formation in the thermal unimolecular decomposition of glyoxal: Rotational and weak collision effects. *Phys. Chem. Chem. Phys.*, 10:6520-6533, 2008.

[20] E. W. R. Steacie, W. H. Hatcher, and J. F. Horwood. The Kinetics of the Oxidation of Gaseous Glyoxal. *J. Chem. Phys.*, 3:551-555, 1935.

[21] J. M. Hay, and R. G. W. Norrish. The Oxidation of Gaseous Glyoxal. *Proc. Roy. Soc. Ser. A*, 288:1-16, 1965.

[22] J. M. Hay. The competitive oxidation of formaldehyde and glyoxal. *J. Chem. Soc.*, 8:7388-7391, 1965.

[23] D. M. Newitt, L. M. Baxt, and V. V. Kelkar. The oxidation of aldehydes. Part I. The combustion zones of butaldehyde, isobutaldehyde, propaldehyde, acetaldehyde, glyoxal, and acraldehyde. *J. Chem. Soc.*, 1703-1710, 1939.

[24] J. H. Payne, and G. F. Lemon Jr. The Oxidation of Aldehydes with Hydrogen Peroxide. *J. Am. Chem. Soc.*, 63:226-228, 1941.

[25] J. H. Thomas. Gas-phase reactions of nitrogen dioxide. Part 2.−The oxidation of glyoxal. *Trans. Faraday Soc.*, 49:630-635, 1953.

[26] P. Marshall, and P. Glarborg. Ab Initio and Kinetic Modeling Studies of Formic Acid Oxidation. *Proc. Combust. Inst.*, 35:153-160, 2015.

[27] G. Friedrichs, D. F. Davidson, and R. K. Hanson. Int., Validation of a thermal decomposition mechanism of formaldehyde by detection of CH$_2$O and HCO behind shock waves. *J. Chem. Kinet.*, 36:157-169, 2004.

[28] C. L.Rasmussen, J. Hansen, P. Marshall, and P. Glarborg. Experimental measurements and kinetic modeling of CO/H$_2$/O$_2$/NO$_x$ conversion at high pressure. *Int. J. Chem. Kinet.*, 40:454-480, 2008.

[29] H. Hashemi, J. M. Christensen, S. Gersen, and P. Glarborg. Hydrogen Oxidation at High Pressure and Intermediate Temperatures: Experiments and Kinetic Modeling. *Proc. Combust. Inst.*, 35:553-560, 2015.

[30] A. Burcat and B. Ruscic. "*Third Millennium Ideal Gas and Condensed Phase Thermochemical Database for Combustion with Updates from Active Thermochemical Tables*", Report TAE960, Technion Israel Inst. of Technology, 16th September 2005.

[31] J. A. Montgomery Jr., M. J. Frisch, J. Ochterski, and G. A. Petersson. A complete basis set model chemistry. VI. Use of density functional geometries and frequencies. *J. Chem. Phys.*, 110:2822-2827, 1999.

[32] K. J. Feierabend, L. Zhu, R. K. Talukdar, and J. B. Burkholder. Rate Coefficients for the OH + HC(O)C(O)H (Glyoxal) Reaction between 210 and 390 K. *J. Phys. Chem. A*, 112:73-82, 2008.

[33] J. Lockhart, M. Blitz, D. Heard, P. Seakins, and R. Shannon. Kinetic Study of the OH + Glyoxal Reaction: Experimental Evidence and Quantification of Direct OH Recycling. *J. Phys. Chem. A*, 117:11027-11037, 2013.

[34] G. da Silva. Kinetics and Mechanism of the Glyoxal + HO$_2$ Reaction: Conversion of HO$_2$ to OH by Carbonyls. *J. Phys. Chem. A*, 115:291-297, 2011.

[35] G. da Silva. Hydroxyl radical regeneration in the photochemical oxidation of glyoxal: kinetics and mechanism of the HC(O)CO + O$_2$ reaction. *Phys. Chem. Chem. Phys.*, 12:6698-6705, 2010.

[36] C.-C. Hsu, M. Mebel, and M. C. Lin. Ab initio molecular orbital study of the HCO+O$_2$ reaction: Direct versus indirect abstraction channels. *J. Chem. Phys.*, 105:2346-2352, 1996.

[37] D. M. Koch, N. H. Khieu, and G. H. Peslherbe. Ab Initio Studies of the Glyoxal Unimolecular Dissociation Pathways. *J. Phys. Chem. A*, 105:3598-3604, 2001.

[38] J. W. Hepburn, R. J. Buss, L. J. Butler, and Y. T. Lee. Molecular beam study of the photochemistry of S$_1$ glyoxal. *J. Phys. Chem.*, 87:3638-3641, 1983.

[39] C. N. Plum, E. Sanhueza, R. Atkinson, W. P. L. Carter, and J. N. Pitts. Hydroxyl radical rate constants and photolysis rates of α−dicarbonyls. *J. Environ. Sci. Technol.*, 17:479-484, 1983.

[40] A. Galano, J. R. Alvarez-Idaboy, M. E. Ruiz-Santoyo, and A. Vivier-Bunge. Mechanism and kinetics of the reaction of OH radicals with glyoxal and methylglyoxal: A quantum chemistry + CVT/SCT approach.*Chem. Phys. Chem.*, 5:1379-1388, 2004.

[41] H. Niki, P. D. Maker, C. M. Savage, and L. P. Breitenbach. An FTIR study of the chlorine−atom−initiated reaction of glyoxal. *Int. J. Chem. Kinet.*, 17:547-558, 1985.

[42] J. J. Orlando and G. S. Tyndall. The atmospheric chemistry of the HC(O)CO radical. *Int. J. Chem. Kinet.*, 33:149-156, 2001.

[43] G. Friedrichs, J. T. Herbon, D. F. Davidson, and R. K. Hanson. Quantitative detection of HCO behind shock waves: The thermal decomposition of HCO. *Phys. Chem. Chem. Phys.*, 4:5778-5788, 2002.

[44] G. Friedrichs. Sensitive absorption methods for quantitative gas phase kinetic measurements. Part 1: Frequency Modulation Spectroscopy. *Z. Phys. Chem.*, 222:1-30, 2008.

[45] J. E. Flad, S. S. Brown, J. B. Burkholder, H. Stark, and A. R. Ravishankara. Absorption cross sections for the $\tilde{A}$ ^{2}A$''$ $(0,9^0,0) \leftarrow \tilde{X}$ ^{2}A$'$ $(0,0^1,0)$ band of the HCO radical. *Phys. Chem. Chem. Phys.*, 8:3636-3642, 2006.

[46] G. Friedrichs, M. Colberg, M. Fikri, Z. Huang, J. Neumann, and F. Temps. Validation of the Extended Simultaneous Kinetics and Ringdown Model by Measurements of the Reaction NH$_2$ + NO. *J. Phys. Chem. A*, 109:4785-4795, 2005.

[47] R. C. Millikan, and D. R. White. Vibrational energy exchange between N$_2$ and CO. The vibrational relaxation of nitrogen. *J. Chem. Phys.*, 39:98-101, 1963.

[48] R. J. Kee, F. M. Rupley, and J. A. Miller. *Chemkin II: A Fortran Chemical Kinetics Package for the Analysis of Gas Phase Chemical Kinetics*, Sandia Report SAND89–8009, Sandia National Laboratories, Livermore, CA, 1989.

[49] A. E. Lutz, R. J. Kee, and J. A. Miller. *Senkin: A Fortran Program for Predicting Homogeneous Gas Phase Chemical Kinetics With Sensitivity Analysis*, Sandia Report SAND87–8248, Sandia National Laboratories, Livermore, CA, 1990.

[50] J. D. DeSain, L. E. Jusinski, A. D. Ho, and C. A. Taatjes. Temperature dependence and deuterium kinetic isotope effects in the HCO (DCO) + O$_2$ reaction between 296 and 673 K. *Chem. Phys. Lett.*, 347:79-86, 2001.

[51] G. P. Smith, D. M. Golden, M. Frenklach, N. W. Moriarty, B. Eiteneer, M. Goldenberg, C. T. Bowman, R. K. Hanson, S. Song, W. C. Gardiner Jr., V. Lissianski, and Z. Qin. *GRI-Mech Version 3.0*, 1999, http://www.me.berkeley.edu/gri_mech, last accessed: 15.04.2015.

[52] B. Veyret and R. Lesclaux. Absolute rate constants for the reactions of the formyl radical HCO with oxygen and nitric oxide from 298 to 503 K. *J. Phys. Chem.*, 85:1918-1922, 1981.

[53] R. S. Timonen, E. Ratajczak, and D. Gutman. Kinetics of the reactions of the formyl radical with oxygen, nitrogen dioxide, chlorine, and bromine. *J. Phys. Chem.*, 92:651-655, 1988.

[54] A. S. Hasson, G. S. Tyndall, and J. J. Orlando. A Product Yield Study of the Reaction of HO$_2$ Radicals with Ethyl Peroxy (C$_2$H$_5$O$_2$), Acetyl Peroxy (CH$_3$C(O)O$_2$), and Acetonyl Peroxy (CH$_3$C(O)CH$_2$O$_2$) Radicals. *J. Phys. Chem. A*, 108:5979-5989, 2004.

[55] M. E. Jenkin, M. D. Hurley, and T. J. Wallington. Investigation of the radical product channel of the CH$_3$COO$_2$ + HO$_2$ reaction in the gas phase. *Phys. Chem. Chem. Phys.*, 9:3149-3162, 2007.

[56] M. E. Jenkin, M. D. Hurley, and T. J. Wallington. Investigation of the radical product channel of the CH$_3$C(O)CH$_2$O$_2$ + HO$_2$ reaction in the gas phase. *Phys. Chem. Chem. Phys.*, 10:4274-4280, 2008.

8.7   Supporting Information

CHEMKIN input file

This is the CHEMKIN input file used for modeling glyoxal thermal decomposition and oxidation at high and intermediate temperatures.

Be aware of the limited pressure and temperature validity ranges of some of the listed rate expressions. For example, the parametrization of thermal decomposition reactions of glyoxal is valid over the temperature range 800 K < T < 2500 K only; for modeling attempts at significantly lower temperatures (and hence very slow decomposition) this reactions should be commented out.

Most pressure dependent reaction are reported in terms of the PLOG formalism (commented out). Newer CHEMKIN versions automatically interpolate the appropriate rate constant values at the desired pressure, see X. Gou, J.A. Miller, W. Sun and Y. Ju (2001)

http://engine.princeton.edu/download/PLOG-documents/PLOG-software_distribution.pdf

Activation energies are specified in cal/mol units, pressures in atm.

! ******************** Glyoxal mechanism C/H/O/N ********************

! REFERENCES:
! [Anglada04]	Anglada, J. Am. Chem. Soc. 126:9809 (2004).
! [BacMac05]	Bacskay and Mackie, J. Phys. Chem. A 109:2019 (2005).
! [Baulch92]	Baulch et al., J. Phys. Chem. Ref. Data 21:403 (1992).
! [Baulch05]	Baulch et al., J. Phys. Chem. Ref. Data 34:757 (2005).
! [Burcat]	Burcat, Ruscic, Third Millenium Ideal gas and Condensed Physe Thermochemical
!	Database for Combustion with Updates from Active Thermochamical Tables,
!	Report TAE960, 16. Sept. 2005
! [Burke12]	Burke et al., Int. J. Chem. Kinet. 44:444 (2012).
! [Burke13]	Burke et al., Proc. Combust. Inst. 34:547 (2013).
! [Chang07]	Chang et al., J. Phys. Chem. A 111:6789 (2007).
! [ColFri06]	Colberg and Friedrichs, J. Phys. Chem. A 110:160 (2006).
! [daSilva10]	da Silva, Phys. Chem. Chem. Phys. 12:6698 (2010).
! [daSilva11]	da Silva, J. Phys. Chem. A 115:191 (2011).
! [Eiteneer98]	Eiteneer et al., J. Phys. Chem. A. 102:5196 (1998).
! [FabJan05]	Fabian and Janoschek, J. Mol. Struct.: THEOCHEM 713:227 (2005).
! [Feierab08]	Feierabend et al., J. Phys. Chem. A 112:73 (2008).
! [Fernandez08]	Fernandes et al., Phys. Chem. Chem. Phys. 10:4313 (2008).
! [FerVar02]	Fernandez-Ramos and Varandas, J. Phys. Chem. A 106:4077 (2002).
! [Friedr02]	Friedrichs et al., Int. J. Chem. Kinet. 34:374 (2002).
! [Friedr02b]	Friedrichs et al., Phys. Chem. Chem. Phys. 4:5778 (2002).
! [Friedr04]	Friedrichs et al., Int. J. Chem. Kinet. 36:157 (2004).
! [Friedr08]	Friedrichs et al., Phys. Chem. Chem. Phys. 10:6520 (2008).
! [GlaMar09]	Glarborg and Marshall, Chem. Phys. Lett. 475:40 (2009).
! [Golden98]	Golden et al., J. Phys. Chem. A 102:8598 (1998).
! [Hong10]	Hong et al., J. Phys. Chem. A 114:5718 (2010).
! [Hong11]	Hong et al., Proc. Comb. Inst. 33:309 (2011).
! [Irdam93]	Irdam et al., Int J Chem Kin 25:285 (1993).
! [Li04]	Li et al., Int. J. Chem. Kinet. 36:566 (2004).
! [MarGla15]	Marshall and Glarbog, Proc. Combust. Inst. 35:153 (2015).
! [Michael00]	Michael et al., Proc. Comb. Inst. 28:1471 (2000).
! [Michael02]	Michael et al., J. Phys. Chem. A 106:5297 (2002).
! [MicSut88]	Michael and Sutherland, J. Phys. Chem. 92:3853 (1988).
! [Mueller99]	Mueller et al., Int. J. Chem. Kinetic. 31:113 (1999).
! [RasGla08]	Rasmussen and Glarborg, Ind. Eng. Chem. Res. 47:6579 (2008) (supp. info).
! [Ruscic06]	Ruscic et al., J. Phys. Chem. A 110:6592 (2006).
! [SanKra12]	Sangwan and Krasnoperov, J. Phys. Chem. A 116: 11817 (2012).
! [Senosiain05]	Senosiain et al., Proc. Combust. Inst. 30:945 (2005).
! [SriMic06]	Srinivasan and Michael, Int. J. Chem. Kinet. 38:211 (2006).
! [Troe00]	Troe, Proc. Comb. Inst. 28:1463 (2000).
! [Troe11]	Troe, Combust. Flame 158:594 (2011).
! [TsaHam86]	Tsang and Hampson, J. Phys. Chem. Ref. Data, 15:1087 (1986).

! [Vasudevan05]   Vasudevan et al., Int. J. Chem. Kinet. 37:98 (2005).
! [You07]   You et al., J. Phys. Chem. A 111:4031 (2007).
! [Yu07]   Yu et al., J. Chem. Phys. 127:094302 (2007).
! [Yu08]   Yu et al., J. Chem. Phys. 129:244315 (2008).
! [YuFra08]   Yu and Francisco, J. Chem. Phys. 128:244315 (2008).
! [YuMuc06]   Yu and Muckerman, J. Phys. Chem. A 110:5312 (2006).
! [Zhou12]   Zhou et al., J. Phys. Chem. A 116:2089 (2012).

```
ELEMENTS
O H C CL N AR
END
SPECIES
OCHCHO OCHCO HOCHO HOCO OCHO HOCH(OO)CHO
HOCH(OOH)CHO CH2O HCO
H O OH H2 O2 HO2 H2O H2O2
CO CO2 AR N2
END


THERMO ALL
         300.00     1000.00     5000.00
OCHCO                C   2O   2H   1   G    350.000  2900.000  1000.00      1 ! this work
  0.49499388E+01 0.10163032E-01-0.55772010E-05 0.14572026E-08-0.14743475E-12    2
-0.96593808E+04 0.25798798E+01 0.33940561E+01 0.14362856E-01-0.88413766E-05     3
  0.16096129E-08 0.32038938E-12-0.92479810E+04 0.10592041E+02                   4
HOCH(OO)CHO  dummy C   2H   3O   4   0G    300.000  5000.000  1394.000      1 ! dummy
  0.15404761E+01 0.31924787E-01-0.29631306E-04 0.13499252E-07-0.23583024E-11    2
  0.17876151E+05 0.17757938E+02 0.15404761E+01 0.31924787E-01-0.29631306E-04    3
  0.13499252E-07-0.23583024E-11 0.17876151E+05 0.17757938E+02                   4
HOCH(OOH)CHO  dummy C   2H   3O   4   0G    300.000  5000.000  1394.000     1 ! dummy
  0.15404761E+01 0.31924787E-01-0.29631306E-04 0.13499252E-07-0.23583024E-11    2
  0.17876151E+05 0.17757938E+02 0.15404761E+01 0.31924787E-01-0.29631306E-04    3
  0.13499252E-07-0.23583024E-11 0.17876151E+05 0.17757938E+02                   4
HOCHO FORMIC ACID L 8/88H 2C   1O   2   0G    200.000  6000.000  1000.      1 ! [Burcat]
  0.46138316E+01 0.64496364E-02-0.22908251E-05 0.36716047E-09-0.21873675E-13    2
-0.47514850E+05 0.84788383E+00 0.38983616E+01-0.35587795E-02 0.35520538E-04     3
-0.43849959E-07 0.17107769E-10-0.46770609E+05 0.73495397E+01-0.45531246E+05     4
OCHO                 1104 C   1H   1N   0O   2G    298.150  3000.000  1000.00   1 ! [FabJan05]
  4.41052368E+00 7.50888367E-03-4.25889679E-06 1.12761124E-09-1.14144138E-13    2
-1.70297531E+04 3.43148293E+00 3.62860375E+00 8.12496033E-03-1.41560718E-06     3
-3.27951824E-09 1.61553900E-12-1.67477889E+04 7.83169538E+00                    4
AR        BUR0302 L 6/88AR   1    0    0    0G    200.00   6000.00   1000.       1
  0.25000000E+01 0.00000000E+00 0.00000000E+00 0.00000000E+00 0.00000000E+00    2
-0.74537500E+03 0.43796749E+01 0.25000000E+01 0.00000000E+00 0.00000000E+00     3
  0.00000000E+00 0.00000000E+00-0.74537500E+03 0.43796749E+01 0.00000000E+00    4
CH2O             L 8/88H 2C   1O   1   0G    200.00   6000.00   1000.       1 ! [Burcat]
  0.31694807E+01 0.61932742E-02-0.22505981E-05 0.36598245E-09-0.22015410E-13    2 ! H298 =-25.95 kcal/mol
-0.14478425E+05 0.60423533E+01 0.47937036E+01-0.99081518E-02 0.37321459E-04     3 ! S298 = 52.28 cal/mol/K
-0.37927902E-07 0.13177015E-10-0.14308955E+05 0.60288702E+00-0.13059098E+05     4
CO               RUS 79C   1O   1    0    0G    200.00   6000.00   1000.       1 ! [Burcat]
  0.30484859E+01 0.13517281E-02-0.48579405E-06 0.78853644E-10-0.46980746E-14    2 ! H298 =-26.41 kcal/mol
-0.14266117E+05 0.60170977E+01 0.35795335E+01-0.61035369E-03 0.10168143E-05     3 ! S298 = 47.24 cal/mol/K
  0.90700586E-09-0.90442449E-12-0.14344086E+05 0.35084093E+01-0.13293628E+05    4
CO2              L 7/88C   1O   2    0    0G    200.00   6000.00   1000.       1 ! [Burcat]
  0.46365111E+01 0.27414569E-02-0.99589759E-06 0.16038666E-09-0.91619857E-14    2 ! H298 =-94.04 kcal/mol
-0.49024904E+05-0.19348955E+01 0.23568130E+01 0.89841299E-02-0.71220632E-05     3 ! S298 = 51.09 cal/mol/K
  0.24573008E-08-0.14288548E-12-0.48371971E+05 0.99009035E+01-0.47328105E+05    4
H                L 6/94H   1    0    0    0G    200.00   6000.00   1000.       1 ! [Burcat]
  0.25000000E+01 0.00000000E+00 0.00000000E+00 0.00000000E+00 0.00000000E+00    2 ! H298 = 52.10 kcal/mol
  0.25473660E+05-0.44668285E+00 0.25000000E+01 0.00000000E+00 0.00000000E+00    3 ! S298 = 27.42 cal/mol/K
```

```
    0.00000000E+00 0.00000000E+00 0.25473660E+05-0.44668285E+00 0.26219035E+05  4
HCO             T 5/03C  1H  1O  1   0G   200.00  6000.00   1000.      1 ! [Burcat]
   3.92001542E+00 2.52279324E-03-6.71004164E-07 1.05615948E-10-7.43798261E-15    2 ! H298 = 42.296 kJ/mol
   3.65008461E+03 3.58077496E+00 4.23754610E+00-3.32075257E-03 1.40030264E-05    3 ! S298 = 53.60 cal/mol/K
  -1.34239995E-08 4.37416208E-12 3.86906718E+03 3.30835309E+00                   4
HOCO           FAB/JAN05C  1O  2H  1   0G   200.00  3000.00   998.402  1 ! [FabJan05]
   4.63988707E+00 5.66362726E-03-2.67855311E-06 6.17048884E-10-5.60953531E-14    2 ! H298 =-44.33 kcal/mol
  -2.40527335E+04 1.90175132E+00 2.82191157E+00 9.66218175E-03-2.78560177E-06    3 ! S298 = 60.07 cal/mol/K, Cp
  -4.12692493E-09 2.61472072E-12-2.35465218E+04 1.14284719E+01                   4 ! (polyfit [RasGla08])
HO2             L 5/89H  1O  2  0   0G   200.00  6000.00   1000.      1 ! [ATcT(Ruscic06)]
   4.17226590E+00 1.88120980E-03-3.46292970E-07 1.94685160E-11 1.76091530E-16    2 !H298 = 12.296 kJ/mol
   3.02010736E+01 2.95697380E+00 4.30178800E+00-4.74902010E-03 2.11579530E-05    3 ! [Burcat]
  -2.42759610E-08 9.29206700E-12 2.63190983E+02 3.71587740E+00                   4 ! S298 = 54.75 cal/mol/K, Cp
H2 REF ELEMENT RUS 78H  2  0  0   0G   200.00  6000.00   1000.      1 ! [Burcat]
   0.29328305E+01 0.82659802E-03-0.14640057E-06 0.15409851E-10-0.68879615E-15    2 ! H298 = 0
  -0.81305582E+03-0.10243164E+01 0.23443029E+01 0.79804248E-02-0.19477917E-04    3 ! S298 = 31.23 cal/mol/K
   0.20156967E-07-0.73760289E-11-0.91792413E+03 0.68300218E+00 0.00000000E+00    4
H2O             L 5/89H  2O  1  0   0G   200.00  6000.00   1000.      1 ! [Burcat]
   0.26770389E+01 0.29731816E-02-0.77376889E-06 0.94433514E-10-0.42689991E-14    2 ! H298 =-57.79 kcal/mol
  -0.29885894E+05 0.68825500E+01 0.41986352E+01-0.20364017E-02 0.65203416E-05    3 ! S298 = 45.13 cal/mol/K
  -0.54879269E-08 0.17719680E-11-0.30293726E+05-0.84900901E+00-0.29084817E+05    4
H2O2            T 8/03H  2O  2  0   0G   200.00  6000.00   1000.      1 ! [ATcT(RUS/PIN06)]
   4.57977305E+00 4.05326003E-03-1.29844730E-06 1.98211400E-10-1.13968792E-14    2 ! H298 =-135.77 kJ/mol
  -1.79847939E+04 6.64969660E-01 4.31515149E+00-8.47390622E-04 1.76404323E-05    3 ! [Burcat]
  -2.26762944E-08 9.08950158E-12-1.76843601E+04 3.27373216E+00                   4 ! S298 = 56.05 cal/mol/K, Cp
N2       BUR0302 G 8/02N  2.  0.  0.  0.G   200.00  6000.00   1000.      1
   2.95257637E+00 1.39690040E-03-4.92631603E-07 7.86010195E-11-4.60755204E-15    2
  -9.23948688E+02 5.87188762E+00 3.53100528E+00-1.23660988E-04-5.02999433E-07    3
   2.43530612E-09-1.40881235E-12-1.04697628E+03 2.96747038E+00 0.00000000E+00    4
O               L 1/90O  1  0  0   0G   200.00  6000.00   1000.      1 ! [Burcat]
   2.54363697E+00-2.73162486E-05-4.19029520E-09 4.95481845E-12-4.79553694E-16    2 ! H298 = 59.55 kcal/mol
   2.92260120E+04 4.92229457E+00 3.16826710E+00-3.27931884E-03 6.64306396E-06    3 ! S298 = 38.49 cal/mol/K
  -6.12806624E-09 2.11265971E-12 2.91222592E+04 2.05193346E+00 2.99687009E+04    4
OCHCHO  Glyoxal  g 3/02C  2.H  2.O  2.  0.G   200.00  6000.00   1000.      1! [Burcat]
   8.72506895E+00 6.33096819E-03-2.35574814E-06 3.89782853E-10-2.37486912E-14    2 ! drawn 6/2009
  -2.91024131E+04-2.03903909E+01 4.68412461E+00 4.78012819E-04 4.26390768E-05    3
  -5.79018239E-08 2.31669328E-11-2.71985007E+04 4.51187184E+00-2.55074562E+04    4
O2 REF ELEMENT RUS 89O  2  0  0   0G   200.00  6000.00   1000.      1 ! [Burcat]
   3.66096083E+00 6.56365523E-04-1.41149485E-07 2.05797658E-11-1.29913248E-15    2 ! H298 = 0
  -1.21597725E+03 3.41536184E+00 3.78245636E+00-2.99673415E-03 9.84730200E-06    3 ! S298 = 49.03 cal/mol/K
  -9.68129508E-09 3.24372836E-12-1.06394356E+03 3.65767573E+00 0.00000000E+00    4
OH              IU3/03O  1H  1  0   0G   200.00  6000.00   1000.      1 ! [ATcT(RUS/PIN06)]
   2.83853033E+00 1.10741289E-03-2.94000209E-07 4.20698729E-11-2.42289890E-15    2 ! H298 = 37.344 kJ/mol
   3.70056220E+03 5.84513094E+00 3.99198424E+00-2.40106655E-03 4.61664033E-06    3 ! [Burcat]
  -3.87916306E-09 1.36319502E-12 3.37165248E+03-1.03814059E-01                   4 ! S298 = 43.91 cal/mol/K, Cp
END
```

REACTIONS
! **
! H2/O2 subset *
! **

H+O2=O+OH	1.0E14	0.000	15286	! [Hong11]
O+H2=OH+H	3.8E12	0.000	7948	! [Baulch05]
DUPLICATE				
O+H2=OH+H	8.8E14	0.000	19175	! [Baulch05]
DUPLICATE				
OH+H2=H+H2O	2.2E08	1.510	3430	! [MicSut88]
OH+OH=O+H2O	1.4E07	1.689	-1167	! [SanKra12]
DUPLICATE				
OH+OH=O+H2O	-2.7E10	0.567	0	! [SanKra12]

```
DUPLICATE
H2+M=H+H+M                                      4.6E19  -1.400 104380! [TsaHam86]
H2/2.5/ H2O/12/ CO/1.9/ CO2/3.8/ AR/0.0/
H2+AR=H+H+AR                                    5.8E18  -1.100 104380! [TsaHam86]
H+O+M=OH+M                                      4.7E18  -1.000 0
H2/2.5/ H2O/12/ AR/0.75/ CO/1.9/ CO2/3.8/                        ! [TsaHam86]
O+O+M=O2+M                                      1.9E13   0.000 -1788 ! [TsaHam86]
H2/2.5/ H2O/12/ AR/0.0/ CO/1.9/ CO2/3.8/
H2O+M = H+OH+M                                  6.1E27  -3.322 120790! [SriMic06]
H2/3.0/ H2O/0.0/ N2/2.0/ O2/1.5/ CO/1.9/ CO2/3.8/               ! [Michael02][Li04]
H2O+H2O = H+OH+H2O                              1.0E26  -2.440 120180! [SriMic06]
!===========================================================
! MAIN BATH GAS IS N2 (comment this reaction otherwise)
!H+O2(+M)=HO2(+M)                               4.7E12   0.440  0     !
! LOW/6.366E+20 -1.72 5.248E+02/
! TROE/0.5 1E-30 1E+30/
! H2/2.0/ H2O/14/ O2/0.78/ CO/1.9/ CO2/3.8/ AR/0.67/
!===========================================================
! MAIN BATH GAS IS AR (comment this reaction otherwise)
H+O2(+M)=HO2(+M)                                4.7E12   0.440  0     !
LOW/9.042E+19 -1.50 4.922E+02/
TROE/0.5 1E-30 1E+30/
H2/3.0/ H2O/21/ O2/1.1/ CO/2.7/ CO2/5.4/ N2/1.5/
!===========================================================
! High-pressure limit from [Troe00]
! Low-pressure limit from [Michael02]
! Centering factors from [Fernandez08]
HO2+H=H2+O2                                     2.8E06   2.090 -1451 ! [Michael00], scaled by 0.75 [Burke12]
HO2+H=OH+OH                                     7.1E13   0.000  295   ! [Mueller99]
HO2+H=H2O+O                                     1.4E12   0.000  0     ! [Baulch05]
HO2+O=O2+OH                                     2.9E10   1.000 -724  ! [FerVar02], scaled by 0.60 [Burke12]
HO2+OH = H2O+O2                                 1.9E20  -2.490 584   ! [Burke13]
DUPLICATE
HO2+OH = H2O+O2                                 1.2E09   1.240 -1310 ! [Burke13]
DUPLICATE !
HO2+HO2=H2O2+O2                                 1.2E09   0.7712 -1825 ! [Zhou12]
DUPLICATE
HO2+HO2=H2O2+O2                                 1.3E12   0.2950 7397  ! [Zhou12]
DUPLICATE
H2O2(+M) = OH+OH(+M)                            2.0E+12  0.9000 48749 ! [Troe11]
LOW/2.49E24 -2.30 4.8749E+04/
TROE/0.43 1E-30 1E+30/
AR/1.0/ H2O/7.5/ CO2/1.6/ N2/1.5/ O2/1.2/ H2O2/7.7/ H2/3.7/ CO/2.8/
! Efficiencies for H2 and CO from [Li04]
H2O2+H=H2O+OH                                   2.4E13   0.000  3970  ! [TsaHam86]
H2O2+H=HO2+H2                                   4.8E13   0.000  7950  ! [TsaHam86]
H2O2+O=HO2+OH                                   9.6E06   2.000  3970  ! [TsaHam86]
H2O2+OH=HO2+H2O                                 1.7E12   0.000  318   ! [Hong10]
DUPLICATE
H2O2+OH=HO2+H2O                                 7.6E13   0.000  7270  ! [Hong10]
DUPLICATE
! *****************************************************************
! CO/CO2 subset *
! *****************************************************************
CO+O(+M)=CO2(+M)                               1.8E10   0.000  2384  ! [Mueller 99]
LOW /1.35E24 -2.79 4191/
TROE /1.0 1E-30 1E30 1E30/
H2/2.5/ H2O/12/ CO/1.9/ CO2/3.8/
CO+OH=CO2+H                                     8.7E05   1.730 -685  ! 1000Torr [Senosiain05]
! PLOG/ 0.01315                                2.1E05   1.900 -1064/
! PLOG/ 0.1315                                 2.5E05   1.880 -1043/
```

! PLOG/ 1.315	8.7E05	1.730	-685/		
! PLOG/ 13.158	6.8E06	1.480	48/		
! PLOG/ 131.58	2.3E07	1.350	974/		
CO+OH=HOCO	2.0E20	-3.500	1309	!	1000Torr [Senosiain05]
! PLOG/ 0.013158	1.7E15	-2.680	859/		
! PLOG/ 0.13158	5.9E18	-3.350	887/		
! PLOG/ 1.3158	2.6E20	-3.500	1309/		
! PLOG/ 13.158	7.1E20	-3.320	1763/		
! PLOG/ 131.58	1.1E20	-2.780	2056/		
CO+HO2=CO2+OH	1.6E05	2.180	17943	!	[You07]
CO+O2=CO2+O	4.7E12	0.000	60500	!	[BacMac05]
CO+H2O2=HOCO+OH	3.6E04	2.500	28660	!	[GlaMar09]
HOCO(+M)=CO2+H(+M)	8.2E11	0.413	35335	!	[Golden98]
LOW / 6.0E26 -3.148 37116 /					
TROE / 0.39 1.0E-30 1.0E30 /				!	Fc = 0.39
HOCO+H=CO2+H2	3.1E17	-1.3475555		!	[YuFra08][MarGla15], 300-1000K fit
HOCO+H=CO+H2O	6.0E15	-0.525	2125	!	[YuFra08][MarGla15], 300-1000K fit
HOCO+O=CO2+OH	9.0E12	0.000	0	!	[Yu07]
HOCO+OH=CO2+H2O	4.6E12	0.000	-89	!	[Yu07]
DUPLICATE					
HOCO+OH=CO2+H2O	9.5E06	2.000	-89	!	[Yu07]
DUPLICATE					
HOCO+HO2=CO2+H2O2	4.0E13	0.000	0	!	[Yu08]
HOCO+O2=CO2+HO2	4.0E09	1.000	0	!	[YuMuc06][MarGla15]
! **					
! CH2O subset *					
! **					
CH2O=HCO+H	5.62E35	-6.87	97877	!	1.0bar, 1400K - 3000K, [Friedr04] refitted
!PLOG/ 9.869E-4	1.78E41	-9.18	109510/		
!PLOG/ 9.869E-3	4.39E38	-8.20	105298/		
!PLOG/ 9.869E-2	2.44E35	-7.06	100144/		
!PLOG/ 9.869E-1	5.62E35	-6.87	97877/		
!PLOG/ 9.869E-0	1.12E38	-7.19	96816/		
!PLOG/ 9.869E+1	1.33E40	-7.45	99278/		
CH2O=H2+CO	2.28E42	-8.74	95817	!	1.0bar, 1400K - 3000K, [Friedr04] refitted
!PLOG/ 9.869E-4	1 84E42	-9.58	96387/		
!PLOG/ 9.869E-3	3.89E41	-9.10	94928/		
!PLOG/ 9.869E-2	3.00E41	-8.78	94716/		
!PLOG/ 9.869E-1	2.28E42	-8.74	95817/		
!PLOG/ 9.869E-0	9.16E43	-8.99	97781/		
!PLOG/ 9.869E+1	5.33E42	-8.50	98240/		
CH2O+H=HCO+H2	5.7E07	1.900	2747	!	[Irdam93] [Friedr02]
CH2O+O=HCO+OH	4.2E11	0.570	2760	!	[Baulch05]
CH2O+O2=HCO+HO2	2.4E05	2.500	36461	!	[Baulch05]
CH2O+OH=HCO+H2O	7.8E07	1.630	-1055	!	[Vasudevan05]
CH2O+HO2=HCO+H2O2	4.1E04	2.500	10206	!	[Eiteneer98]
HCO+M=H+CO+M	4.8E17	-1.200	17720	!	[Friedr02b]
HCO+H=CO+H2	1.1E14	0.000	0	!	[Friedr02b]
HCO+O=CO+OH	3.0E13	0.000	0	!	[Baulch02]
HCO+O=CO2+H	3.0E13	0.000	0	!	[Baulch02]
HCO+OH=CO+H2O	1.1E14	0.000	0	!	[Baulch05]
HCO+O2=CO+HO2	6.92E06	1.900	-1370	!	this work, 295-1705K, <5bar
HCO+HO2=CO2+OH+H	3.0E13	0.000	0	!	[TsaHam86]
HCO+HCO=CO+CH2O	2.7E13	0.000	0	!	[Friedr02b]
! **					
! OCHCHO subset *					
! **					
OCHCHO=CH2O+CO	8.04E55	-12.6	76713	!	1.0bar, 800K-2500K, [Friedr08] refitted
DUPLICATE					
!PLOG/ 0.009869	4.17E53	-12.5	70845/		
!PLOG/ 0.04935	5.12E54	-12.6	73012/		

!PLOG/ 0.09869	1.03E55	-12.6	73877/		
!PLOG/ 0.4935	4.50E55	-12.6	75869/		
!PLOG/ 0.9869	8.04E55	-12.6	76713/		
!PLOG/ 4.935	1.05E55	-12.2	77643/		
!PLOG/ 9.869	5.48E56	-12.6	79964/		
OCHCHO=CO+CO+H2	6.12E57	-13.1	80147	!	1.0bar, 800K-2500K, [Friedr08] refitted
!PLOG/ 0.009869	6.02E51	-12.1	71854/		
!PLOG/ 0.04935	1.43E54	-12.5	74751/		
!PLOG/ 0.09869	1.78E55	-12.7	76137/		
!PLOG/ 0.4935	1.31E57	-13.0	78972/		
!PLOG/ 0.9869	6.12E57	-13.1	80147/		
!PLOG/ 4.935	5.79E57	-12.9	81871/		
!PLOG/ 9.869	3.42E59	-13.3	84294/		
OCHCHO=CH2O+CO	2.62E57	-13.2	79754	!	1.0bar, 800K-2500K, [Friedr08] refitted
DUPLICATE				!	CH2O = HCOH, see text
!PLOG/ 0.009869	8.36E52	-12.6	72393/		
!PLOG/ 0.04935	8.25E54	-12.9	75113/		
!PLOG/ 0.09869	4.37E55	-13.0	76257/		
!PLOG/ 0.4935	1.32E57	-13.2	78851/		
!PLOG/ 0.9869	2.62E57	-13.2	79754/		
!PLOG/ 4.935	1.00E57	-12.9	81161/		
!PLOG/ 9.869	5.69E59	-13.3	83539/		
OCHCHO=HCO+HCO	1.89E57	-12.8	84321	!	1.0bar, 800K-2500K, [Friedr08] refitted
!PLOG/ 0.009869	1.03E42	-9.7	73534/		
!PLOG/ 0.04935	6.02E48	-11.1	77462/		
!PLOG/ 0.09869	1.65E51	-11.6	79111/		
!PLOG/ 0.4935	5.33E55	-12.5	82774/		
!PLOG/ 0.9869	1.89E57	-12.8	84321/		
!PLOG/ 4.935	2.22E59	-13.1	87258/		
!PLOG/ 9.869	2.99E60	-13.3	88993/		
OCHCHO+H=OCHCO+H2	5.4E13	0.000	4302	!	[ColFri06]
OCHCHO+O=OCHCO+OH	4.2E11	0.570	2760	!	est., 2k(CH2O+O)
OCHCHO+OH=OCHCO+H2O	4.0E06	2.000	-1630	!	[Feierab08]
OCHCHO+HO2=>HOCH(OO)CHO	1.3E31	-7.532	1440	!	1.0atm [daSilva11]
HOCH(OO)CHO => OCHCHO+HO2	1.9E29	-5.781	15790	!	1.0 atm [daSilva11]
HOCH(OO)CHO => HOCHO+CO+OH	1.6E10	0.051	15190	!	1.0 atm [daSilva11]
!HOCH(OO)CHO+HO2=>HOCHO+HCO+O2+OH	3.0E12	0.000	0	!	est., 298K, see text
!HOCH(OO)CHO+HO2=>HOCH(OOH)CHO+O2	3.0E12	0.000	0	!	est., 298K, see text
OCHCHO+HO2=OCHCO+H2O2	8.2E04	2.500	10206	!	est., 2k(CH2O+HO2)
OCHCHO+O2=OCHCO+HO2	4.8E05	2.500	36461	!	est., 2k(CH2O+O2)
OCHCHO+HO2=HOCHO+CO+OH	3.3E-4	3.995	300	!	1.0 atm [daSilva11]
OCHCO=HCO+CO	4.1E14	0.000	8765	!	1.0atm [daSilva10]
! PLOG/ 0.01	3.8E12	0.000	8610/		
! PLOG/ 0.1	3.8E13	0.000	8665/		
! PLOG/ 1.0	4.1E14	0.000	8765/		
! kinf	1.1E14	0.133	10140	!	
OCHCO+O2=CO+CO2+OH	3.3E14	0.000	2075	!	1.0atm [daSilva10]
! PLOG/ 0.01	1.6E14	0.000	1540/		
! PLOG/ 0.1	1.1E14	0.000	1300/		
! PLOG/ 1.0	3.3E14	0.000	2075/		
! kinf	3.4E04	1.929	344		
HOCHO(+M)=CO+H2O(+M)	7.5E14	0.000	68710	!	[Chang07]
LOW /4.1E15 0 52980/					
HOCHO(+M)=CO2+H2(+M)	4.5E13	0.000	68240	!	[Chang07]
LOW /1.7E15 0 51110/					
HOCHO+H=HOCO+H2	2.3E02	3.272	4858	!	[MarGla15]
HOCHO+H=OCHO+H2	4.2E05	2.255	14091	!	[MarGla15]
HOCHO+O=HOCO+OH	5.1E01	3.422	4216	!	[MarGla15]
HOCHO+O=OCHO+OH	1.7E05	2.103	9880	!	[MarGla15]
HOCHO+OH=HOCO+H2O	7.8E-6	5.570	-2365	!	[Anglada04][MarGla15]
HOCHO+OH=OCHO+H2O	4.9E-5	4.910	-5067	!	[Anglada04][MarGla15]

```
HOCHO+HO2=HOCO+H2O2          4.7E-1  3.975  16787  !  [MarGla15]
HOCHO+HO2=OCHO+H2O2          3.9E01  3.080  25206  !  [MarGla15]
HOCO+HO2=HOCHO+O2            4.0E11  0.000  0      !  [Yu08]
HOCHO+O2=OCHO+HO2            3.0E13  0.000  63000  !  [MarGla15]
OCHO=CO2+H                   1.0E10  0.000  0      !  [MarGla15]
OCHO+O2=CO2+HO2              5.0E13  0.000  0      !  [MarGla15]
END
```

9 Summary and outlook

High-temperature rate constants of five bimolecular reactions of NCN, HNO, and HCO have been measured at high temperatures. These molecules are short-lived flame intermediates that play important roles for NO_x pollutant formation (NCN and HNO) and the overall oxidation rate (HCO) in flames. Combustion-relevant experimental conditions have been generated by the shock wave method.

NCN reactions: Narrow-bandwidth UV laser difference absorption spectroscopy has been applied for the detection of NCN concentration-time profiles. The measurements have been performed at a transition at $\tilde{\nu} = 30383.11$ cm^{-1} ($\lambda \approx 329$ nm) corresponding to a superposition of the $^3\Pi_1$ subband of the $\tilde{A}^3\Pi_u(000) - \tilde{X}^3\Sigma_g(000)$ transition and the Q$_1$ band head of the vibrationally hot Renner-Teller split vibronic $^3\Sigma^+(010) - ^3\Pi(010)$ transition. At high temperatures, the (010) vibrational state is significantly populated resulting in a comparably high absorption cross section suitable for a sensitive detection scheme.

For the first time, direct rate constant measurements have been performed for the reactions NCN + H, NCN + H$_2$ and NCN + O$_2$ over a wide temperature and pressure range (see Fig. 9.1). NCN radicals were generated from the thermal decomposition of NCN$_3$ in shock tube experiments. The highly explosive and very toxic NCN$_3$ has been synthesized in high purity and storage mixtures of NCN$_3$ in argon were used within a few days since a slow decomposition/polymerization takes place. The pyrolysis of ethyl iodide (C$_2$H$_5$I) was used as H atom source for the investigation of the reaction NCN + H. The rate constant of this reaction has been determined between temperatures 962 K $< T <$ 2425 K. The obtained rate constant can be best represented by the combination of two Arrhenius expressions, corresponding to two reaction channels yielding either CH + N$_2$ or HCN + N. By a detailed analysis of the data in comparison with literature data, the temperature dependent branching ratio for the reaction NCN + H as well as a consistent value for the NCN enthalpy of formation $\Delta_r H^\circ_{298K} = 450$ kJ/mol were determined.

The rate constant of the reaction NCN + H$_2$, which has so far been neglected in detailed reaction mechanisms for NO_x formation, has been measured under accurately pseudo first-order reaction conditions. From different possible product channels for this reaction, the obtained Arrhenius activation energy as well as mechanistic considerations are most consistent with a direct abstraction channel yielding the products HNCN + H. Further, in cooperation with N. Lamoureux and P. Desgroux (Université Lille 1, France), the reaction NCN + H$_2$ and additionally secondary reactions have been implemented

143

into the detailed GDFkin3.0_NCN mechanism for the simulation of low pressure $CH_4/O_2/N_2$-flames. Significant differences have been observed for the overall NO yields with the updated mechanism at two different flame conditions.

For $NCN + O_2$, high-temperature rate expressions used in flame modeling mechanisms differ by five orders of magnitude (at $T = 1500$ K). Depending on the assumed rate constant value, this reaction was reported to be either very important or dispensable for flame modeling. To resolve the role of the reaction $NCN + O_2 \rightarrow NCO + NO$ for prompt-NO modeling in flames, the rate expression was determined experimentally at temperatures between 1577 K $\leq T \leq$ 2492 K. The measurements confirmed that the reaction is rather slow and hence does play a minor role for NCN modeling in flames.

The measured rate constants for bimolecular NCN reactions of this work (red curves) are displayed in the Arrhenius plot in Fig. 9.1 together with previously determined rate constant data (black curves) from the Kiel shock tube group.
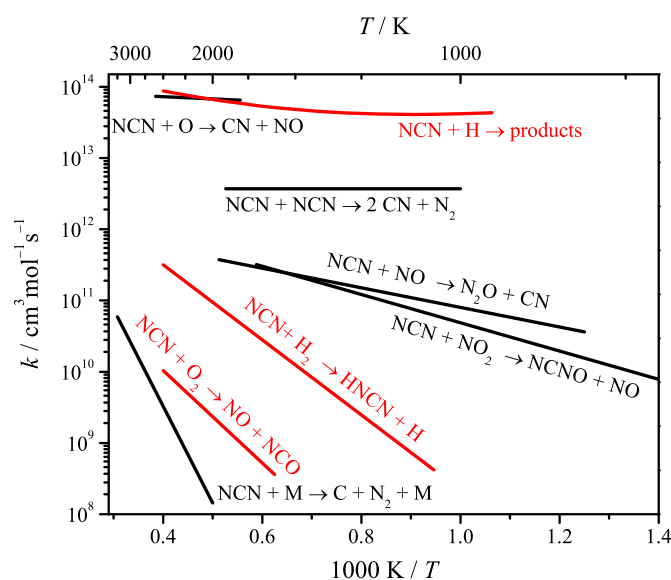
Figure 9.1: Arrhenius plot of bimolecular NCN rate constants measured with the Kiel shock tube setup. Rate constants measured in this work are labled with red color.

HNO detection and the reaction HNO + O$_2$: HNO has been measured for the first time behind shock waves using the very sensitive absorption based FM spectroscopy. HNO concentrations of about 200 ppm were generated from the 193 nm UV photolysis of glyoxal/NO mixtures, initially yielding HCO radicals followed by the reaction $HCO + NO \rightarrow HNO + CO$. HNO FM spectra of the $\tilde{A}^1A''$ - $\tilde{X}^1A'$ transition and concentration-time profiles have been detected at three different wavelengths around 618 and 625 nm. An HNO formation mechanism has been compiled from available literature data. Further, by monitoring HCO and HNO concentration time profiles at similar reaction conditions, the temperature dependent HNO absorption cross section has been determined, allowing us to perform quantitative HNO measurements at high temperatures. Based on this results and by adding specific amounts of O_2 to the reaction mixtures, the reaction $HNO + O_2 \rightarrow NO + HO_2$ has been directly measured. The obtained rate constant data are about two to three orders of magnitude higher than

144

frequently used literature data.

Glyoxal oxidation and HCO + O$_2$: HCO concentration-time profiles have been measured by FM spectroscopy. The pyrolysis of glyoxal was used as HCO source. The applied mechanism for the thermal decomposition was developed from former experiments in our working group. By adding O$_2$ to the glyoxal reaction mixtures, the rate constant of the reaction HCO + O$_2$ → CO + HO$_2$ could be determined. Moreover, the capability of a detailed glyoxal oxidation mechanism assembled from available literature data was tested. The outcome of the experiments of this work concerning the glyoxal decomposition and the temperature dependent k_{HCO+O_2} values were in very good agreement with former findings. Together with P. Glarborg (Technical University of Denmark) and P. Marshall (University of North Texas) an extensive glyoxal oxidation mechanism was assembled from available literature data and validated by the shock tube measurements.

Outlook: The established experimental setups for time-resolved measurements of NCN and HNO concentration profiles behind shock waves should be used to study other important reactions of these species. For example, experimental rate constant data for the reactions of NCN with the important flame intermediates OH, CN, C and N atoms are still missing for a complete high temperature NCN submechanism. Also detection schemes for the possible reaction products of NCN reactions should be considered. For example, in order to confirm the formation of HNCN + H from NCN + H$_2$, H-ARAS (at $\lambda = 121.6$ nm) could by applied. Also the reported temperature dependent product branching ratio for NCN + H needs to be experimentally verified, for example by the detection of CH (laser absorption around $\lambda = 430$ nm) and N atoms (N-ARAS at $\lambda = 119.9$ nm). The reactions NCN + O, NCN + N, NCN + C and NCN + NCN are supposed to form CN radicals; therefore ongoing CN measurements (M.Sc. thesis of S. Hesse) by means of FM spectroscopy are important to verify these assumed reaction products.

The overall aim of this work was to contribute to the implementation of a complete NCN submechanism into existing combustion mechanisms. Such a submechanism should be based on directly measured rate constants including branching ratios as well as temperature and pressure dependences. Continued cooperation with flame modeling groups is important to test and improve the capability and reliability of such mechanisms for NO$_x$ modeling.

In the case of HNO, a lot of experimental kinetic data at combustion relevant temperatures are still missing. Even the rate constants for reactions with common flame intermediates like OH, O and H atoms are not accurately known. To observe these probably fast reactions, the HNO detection scheme, established in this work, needs further optimization in order to improve the signal-to-noise ratio. One possibility is to use an EOM capable of generating higher modulation indices M, another is to search for alternative, more direct HNO generation schemes.

Danksagungen

Selbstständigkeitserklärung

Hiermit erkläre ich, Nancy Faßheber, an Eides statt, dass ich die vorliegende Arbeit selbstständig und nur unter Verwendung der angegebenen Hilfsmittel angefertigt habe. Inhalt und Form dieser Arbeit sind, abgesehen von der Beratung durch meinen Doktorvater Prof. Dr. Gernot Friedrichs, selbstständig erarbeitet worden. Die Arbeit entstand unter Einhaltung der Regeln guter wissenschaftlicher Praxis der Deutschen Forschungsgemeinschaft. Dies ist mein erster Promotionsversuch und weder die gesamte Arbeit noch Teile davon habe ich im Rahmen eines Prüfungsverfahrens eingereicht. Sie wurde in ihrer Gesamtheit nicht veröffentlicht und auch nicht zur Veröffentlichung eingereicht. Teile dieser Arbeit wurden in fachwissenschaftlichen Zeitschriften veröffentlicht, dies bezieht sich auf die folgenden Kapitel:

– Kapitel 4:

N. Faßheber, J. Dammeier, and G. Friedrichs, Direct measurements of the total rate constant of the reaction NCN + H and implications for the product branching ratio and the enthalpy of formation of NCN, *Phys. Chem. Chem Phys.* **2014**, 16, 11647-11657.

– Kapitel 5:

N. Faßheber, N. Lamoureux, and G. Friedrichs, The rate constant of the reaction NCN + H_2 and its impact on NCN and NO concentrations in low pressure CH_4/O_2/N_2-flames, *Phys. Chem. Chem Phys.* **2015**, 17, 15876-15886.

– Kapitel 6:

N. Faßheber and G. Friedrichs, Shock tube measurements of the rate constant of the reaction NCN + O_2, *Int. J. Chem. Kinet.* **2015**, 47, 586-595.

– Kapitel 8:

N. Faßheber, G. Friedrichs, P. Marshall, and P. Glarborg, Glyoxal oxidation mechanism: Implications for the reactions HCO + O_2 and OCHCHO + HO_2, *J. Chem. Phys. A* **2015**, 119, 7305-7315.

Kiel, Mai 2015

_____

Nancy Faßheber

Curriculum Vitae

Personal data

Name:	Nancy Faßheber
Nationality:	German
Date of birth:	5th of May, 1986
Place of birth:	Röbel/ Müritz
Address:	Knooper Weg 122, 24105 Kiel, Germany

Education

July 2014:	Measurements at the Swiss Light Source
since 2011:	Doctoral candidate of Prof. Dr. G. Friedrichs, Shock tube lab at the Institut für Physikalische Chemie at the Christian-Albrechts-Universität zu Kiel
December 2010:	Diploma Thesis: Stoßwellenuntersuchungen zur Bestimmung der Hochtemperatur-Geschwindigkeitskonstanten der Reaktionen NCN + H und NCN + H_2
2005 - 2010:	Chemistry studies (Diploma) at the Christian-Albrechts-Universität zu Kiel
2005:	Abitur (university-entrance diploma)
1996 - 2005:	Joliot-Curie-Gymnasium, Röbel/Müritz
1992 - 1996:	Grundschule 1, Röbel/Müritz

Publications

- **N. Faßheber** and G. Friedrichs, Shock tube measurements of the rate constant of the reaction NCN + O_2, *Int. J. Chem. Kinet.* **2015**, 47, 586-595, DOI: 10.1002/kin.20932.

- **N. Faßheber**, N. Lamoureux, and G. Friedrichs, The rate constant of the reaction NCN + H_2 and its impact on NCN and NO concentrations in low pressure $CH_4/O_2/N_2$-flames, *Phys. Chem. Chem Phys.* **2015**, 17, 15876-15886, DOI: 10.1039/C5CP01414J.

- **N. Faßheber**, G. Friedrichs, P. Marshall, and P. Glarborg, Glyoxal oxidation mechanism: Implications for the reactions HCO + O_2 and OCHCHO + HO_2, *J. Chem. Phys. A* **2015**, 119, 7305-7315, DOI: 10.1021/jp512432q.

- **N. Faßheber**, J. Dammeier, and G. Friedrichs, Direct measurements of the total rate constant of the reaction NCN + H and implications for the product branching ratio and the enthalpy of formation of NCN, *Phys. Chem. Chem Phys.* **2014**, 16, 11647-11657, DOI: 10.1039/C4CP01107D, selected as ***Hot Article***

- **N. Faßheber**, G. Friedrichs, and J. Dammeier, Direct High Temperature Measurements of NCN Reactions, *Bunsen-Mag.* **2012**, 5, 202.

- J. Dammeier, **N. Faßheber**, and G. Friedrichs, Direct Measurements of the High Temperature Rate Constants of the Reactions NCN + O, NCN + NCN, and NCN + M, *Phys. Chem. Chem Phys.* **2012**, 14, 1030-1037, DOI: 10.1039/c1cp22123j. ***Cover Article***

Presentations

- **N. Faßheber**, Wo Rauch ist, ist auch Feuer: Neuigkeiten zur Stickoxidbildung in Flammen, Talk, *Christmas Colloquium*, Kiel University, Department of Chemistry, Kiel, Germany, December 2014.

- **N. Faßheber**, G. Friedrichs, First direct high temperature measurements of the reaction HNO + O_2 behind shock waves, Poster, *35th International Symposium on Combustion*, San Francisco, USA, August 2014.

- **N. Faßheber** G. Friedrichs, Quantitative high temperature detection of HNO and first direct measurement of the reaction HNO + O_2 behind shock waves, Poster, *Annual Meeting of the German Bunsen Society of Physical Chemistry*, Hamburg, Germany, May 2014.

- G. Friedrichs, J. Dammeier, **N. Faßheber**, Issues of NO formation in flames via the NCN radical pathway: Rate constants, absorption cross section, and thermochemistry, Talk, *32nd International Symposium on Free Radicals*, Potsdam, Germany, July 2013.

- **N. Faßheber**, G. Friedrichs, Glyoxal photolysis as a quantitative source of HNO studied by frequency modulation spectroscopy, Poster, *32nd International Symposium on Free Radicals*, Potsdam, Germany, July 2013. ***PCCP Poster Prize***

- **N. Faßheber**, G. Friedrichs, Direct high temperature measurements of the reactions $NCN + O_2$ and $NCN + H_2$, Poster, *34th International Symposium on Combustion*, Warsaw, Poland, August 2012.

- **N. Faßheber**, J. Dammeier, G. Friedrichs, Building a new submechanism for prompt-NO formation: Direct measurements of high temperature NCN reactions, Poster, *Annual Meeting of the German Bunsen Society of Physical Chemistry*, Leipzig, Germany, May 2012. ***PCCP Hot Topic Poster Prize***

- G. Friedrichs, J. Dammeier, **N. Faßheber**, Shock tube study on the reactions NCN + H and NCN + O, Talk, *7th International Conference on Chemical Kinetics*, MIT, Cambridge, USA, July 2011.

- **N. Faßheber**, J. Dammeier, G. Friedrichs, Experimental study on the reactions NCN + NO / NO_2 and NCN + H / H_2 behind shock waves, Poster, *Annual Meeting of the German Bunsen Society of Physical Chemistry*, Berlin, Germany, June 2011.